

UNIVERSITY OF ZAGREB
FACULTY OF MECHANICAL ENGINEERING AND NAVAL
ARCHITECTURE

Boundary Layer Method for Unsteady Aerodynamic Loads Determination

DOCTORAL THESIS

FRANE MAJIĆ

ZAGREB, 2010.



University of Zagreb
Faculty of Mechanical Engineering and
Naval Architecture

Boundary Layer Method for Unsteady Aerodynamic Loads Determination

DOCTORAL THESIS

Supervisor:

Dr. sc. Ralph Voss

Frane Majić, dipl. ing.

ZAGREB, 2010.

Bibliography data

UDC: 532.511:532.517.2:532.517.3:532.517.4:
532.526:533.6.011.3:533.6.011.7:533.6.013.2:
533.6.013.04:533.6.013.13

Keywords: viscous-inviscid coupling, viscous flow, Euler equations, transpiration velocity, computational fluid dynamics, mach number, airfoil, shock-wave, airfoil pressure coefficient distribution

Scientific area: Technical sciences

Scientific field: Aviation, rocket and outer-space technology

Institution: Faculty of Mechanical Engineering and Naval Architecture

Supervisor: Dr. sc. Ralph Voss

Number of pages: 134

Number of figures: 78

Number of tables: 9

Number of references: 45

Date of oral examination: 24. May 2010.

Jury members: Prof. dr. sc. Zdravko Terze,
Dr. sc. Ralph Voss,
Prof. dr. sc. Zdravko Virag,
Prof. dr. sc. Zoran Milas,
Doc. dr. sc. Milan Vrdoljak

Archive: Faculty of Mechanical Engineering and Naval Architecture,
University of Zagreb

First of all I would like to thank to my supervisors dr. sc. Ralph Voss and prof. dr. sc. Zdravko Virag for all the time they spent to unselfishly share their huge knowledge and experience in CFD with me. Thanks to doc. dr. sc. Milan Vrdoljak for the usefull comments and the unselfish assistance in mastering LaTeX. Thanks to Ante Šoda who was always there to remind me for the timetable of my PhD's milestones. Also, thanks to Ante Šoda and Jens Nitzsche for the help in using Tau code during my stay in DLR in Göttingen, where majority of this work was done. Thanks to my friend Heiko Uhlemann for the company and help during my stay in Göttingen. Thanks to Heiko Uhlemann, Ante Šoda, Jens Nitzsche and Claudio Manini for the time we spent in "6 Millionen Dollar Club" and other nice places in Göttingen discussing the CFD and Aerodynamics. Finally, thanks to my parents, my sister, and to Helena and Mislav for their support and patience.

Contents

Contents	iv
Preface	vi
Summary	viii
Sažetak	ix
Nomenclature	x
List of Figures	xiv
List of Tables	xx
1. Introduction	1
1.1. Motivation	1
1.2. Overview of Previous Work	4
1.3. Objective and Hypothesis of Research	7
2. Viscous-Inviscid Interaction	8
2.1. Viscous-Inviscid Interaction Method	8
3. Inviscid Model	11
3.1. Coordinates Transformation	11
3.2. Euler Equations	14
3.3. The Vector Flux Splitting	15
3.4. Solution Procedure for Euler Equations	21

3.5. Boundary Conditions and Contour Pressure Determination	22
4. Boundary layer	28
4.1. Boundary Layer Concept	28
4.2. Boundary Layer in Transonic Flow	30
4.3. Integral Compressible Boundary Layer Equations by Drela	31
4.4. Solution Procedure for Boundary Layer Equations	35
4.5. Transition	38
5. Results	40
5.1. Computational Grid	41
5.2. Grid Convergence	42
5.3. Steady Results	60
5.3.1. NACA0012 Airfoil	60
5.3.2. NACA64A010 Airfoil	68
5.3.3. NLR7301 Airfoil	73
5.4. Unsteady Results	77
5.4.1. NACA0012 Airfoil	78
5.4.2. NACA64A010 Airfoil	83
6. Conclusion	88
7. Conclusion of the Doctoral Dissertation	92
A. Derivation of Boundary Condition	93
References	109
Curriculum vitae	114

Preface

This work was made at the Faculty of Mechanical Engineering and Naval Architecture in Zagreb, and at the Institute of Aeroelasticity which is part of DLR (Deutsches Zentrum für Luft- und Raumfahrt) in Göttingen.

Flutter phenomenon of aerodynamic surfaces of aircraft, which has to be investigated for each new aircraft design or structural modification of existing aircraft, is still important topic of research in aeroelasticity, and especially for aircraft in transonic flight.

One way to check aeroelastic behaviour of the aircraft are computational methods which are capable to carry out big amount of calculations before in flight checks, and the other way are wind tunnel experiments. Direct simulation of fluid-structure interaction in time domain, using the most precise methods for loads calculations, requires extremely high needs for computational resources.

As the main effort is needed for the part of unsteady loads determination, more efficient methods are developed for flutter boundary prediction. Loads determination comprises the unsteady flow calculation around aircraft which performs oscillatory motions with different elastic modes and different frequencies. Because of small computational and time requirements for loads analysis, panel method with doublets called doublet-lattice method (DLM) is widely used. One of the DLM method shortages is inability to resolve strong shocks in transonic region. Simulations of Reynolds averaged Navies-Stokes (RANS) equations for flutter analysis give more precise results, but also require big computational and time resources, and because of that are not first choice for preliminary design phase.

Between these two extremes, viscous-inviscid interaction methods like Euler with boundary layer are good compromise. Solving Euler equations it is possible to resolve shocks, and coupling with boundary layer equations gives balance between flow model and computational efficiency. Viscous-inviscid interaction methods give results that are comparable with RANS results, but computational time is several times less and this gives them advantage for fast flutter analysis.

Zagreb, March 2010.

Frane Majić, dipl. ing.

Summary

In this work a simple and accurate method for two-dimensional unsteady aerodynamic load determination on airfoil is developed. The method employs viscous-inviscid coupling. The inviscid flow is governed by the unsteady Euler equations solved by finite volume method on moving C-type rigid grid, while viscous flow is governed by steady boundary layer integral equations. The Euler equations are solved in conservative form, in transformed body-fitted coordinates. The viscous-inviscid coupling is performed by transpiration velocity incorporated in the boundary condition on airfoil. Therefore, the method requires no grid deformation for the boundary layer influence inclusion. The transition is predicted by the e^n method. The viscous-inviscid method is focused on subsonic and transonic flows, at high Reynolds number, with shock-wave appearance. The steady and unsteady test cases for three characteristic airfoils are performed, namely NACA 0012, NACA64A010, NLR 7301. The results are compared with experimental data and with unsteady RANS calculations. The method gives results which are in good agreement with experimental data and with calculated unsteady RANS results. Problems in convergence the method has in the test cases with separation. The method is applicable in the design processes where unsteady loads are required within reasonable time and with accuracy comparable with RANS methods.

Keywords: viscous-inviscid coupling, viscous flow, Euler equations, transpiration velocity, computational fluid dynamics, mach number, airfoil, shock-wave, airfoil pressure coefficient distribution

Sažetak

U ovom radu razvijena je jednostavna i precizna metoda za određivanje nestacionarnih aerodinamičkih opterećenja za dvodimenzionalno strujanje oko aeroprofila. Metoda koristi princip sprezanja viskoznog i neviskoznog dijela strujanja. Neviskozni dio strujanja je opisan nestacionarnim Eulerovim jednadžbama koje su riješene pomoću metode kontrolnih volumena na pomičnoj nedeformabilnoj mreži C-tipa. Viskozni dio strujanja je opisan integralnim jednadžbama graničnog sloja za stacionarno strujanje koje su riješene Runge-Kutta metodom četvrtog reda. Eulerove jednadžbe su riješene u konzervativnom obliku, u transformiranim prijanjajućim koordinatama. Sprezanje viskoznog i neviskoznog dijela strujanja je izvedeno pomoću transpiracijske brzine koje je uključena u rubni uvjet na aeroprofilu. Iz tog razloga metoda ne zahtijeva deformaciju mreže da bi se uključio utjecaj graničnog sloja. Položaj tranzicije graničnog sloja je predviđen pomoću metode e^n . Metoda viskozno-neviskoznog sprezanja je usmjerena na podzvučno i kroz-zvučno strujanje pri velikim Reynoldsovima brojevima, s pojavom udarnog vala. Izvršeni su proračuni za stacionarno i nestacionarno strujanje, za tri karakteristična aeroprofila NACA 0012, NACA64A010 i NLR 7301. Rezultati su uspoređeni s eksperimentalnim podacima i s nestacionarnim RANS proračunima. Metoda daje rezultate koji se dobro slažu s eksperimentalnim podacima i s proračunatim nestacionarnim RANS rezultatima. U slučajevima strujanja s odvajanjem, metoda pokazuje probleme s konvergencijom. Metoda je primjenjiva u procesima razvoja gdje se zahtijeva proračun nestacionarnih opterećenja unutar prihvatljivog vremena računanja i s preciznošću koja je usporediva s RANS metodama.

Ključne riječi: viscous-inviscid coupling, viscous flow, Euler equations, transpiration velocity, computational fluid dynamics, mach number, airfoil, shock-wave, airfoil pressure coefficient distribution

Nomenclature

Latin

A, B	jacobians of Euler equations	15
c	airfoil chord length, [m]	7
C_D	dissipation coefficient, [1]	31
C_f	friction coefficient, [1]	31
c_l	local lift coefficient, [1]	7
c_n	normal force coefficient, [1]	43
C_p	pressure coefficient, [1]	43
C_τ	shear coefficient, [1]	35
e	total energy per unit mass, [J/kg]	14
F, G	flux vectors of conservative variables	14
H	shape parameter,[1]	31
H_k	kinematic shape parameter, [1]	33
h	total enthalpy per unit mass, [J/kg]	15
H^*	kinetic energy shape parameter, [1]	31
H^{**}	density shape parameter,[1]	31
J	determinant of Jacobi matrix of coordinate transformation, [1]	14
L	reference length, [m]	77
Ma	Mach number	79
Ma _e	Mach number at the boundary layer edge, [1]	31
p	pressure, [Pa]	14
p_m	mean pressure for unsteady pressure oscillation, [Pa]	77

p_o	pressure perturbation magnitude in unsteady flow, [Pa]	77
p_s	pressure for steady mean condition, [Pa]	78
p_T	total pressure, [Pa]	26
Q	vector of conservative variables	14
Re	Reynolds number referenced by airfoil chord	79
Re_θ	Reynolds number referenced by momentum thickness	39
S	entropy, [J/K]	26
s	curvilinear coordinate in boundary layer equations, [m]	31
t	physical time, [s]	77
T_F	local rotation matrix for F flux	18
T_G	local rotation matrix for G flux	18
τ_w	tangential stress on viscous wall, [Pa]	31
u	x-direction velocity component, [m/s]	14
U	max. velocity in boundary layer in direction of viscous wall, [m/s]	29
u_e	velocity magnitude at the boundary layer edge, [m/s]	23
U_∞	free stream velocity magnitude, [m/s]	77
v	y-direction velocity component, [m/s]	14
\vec{v}	fluid velocity vector, [m/s]	23
V	maximum velocity in boundary layer in direction perpendicular to viscous wall, [m/s]	29
\vec{v}_b	velocity vector of boundary (airfoil contour), [m/s]	23
v_{norm}	fluid velocity magnitude normal to outer domain boundary, [m/s]	26
\vec{v}_t	transpiration velocity vector of boundary layer, [m/s]	23
v_{tang}	fluid velocity magnitude along outer domain boundary, [m/s]	26
x, y, z	cartesian coordinates, [m]	14
x_α	rotational axis distance from leading edge, [m]	83

Greek

α	angle of attack, [°]	43
α_m	mean angle of attack, [°]	53
α_o	pitch amplitude, [°]	53
β	underrelaxation factor, [1]	10
γ	specific heats ratio, [1]	14

δ	boundary layer thickness, [m]	30
δ^*	displacement thickness, [m]	31
δ^{**}	density thickness, [1]	32
μ	dynamic viscosity, [Pas]	31
η	curvilinear coordinate, [m]	31
θ	momentum thickness, [m]	31
θ^*	kinetic energy thickness, [1]	32
ν	kinematic viscosity, [m ² /s]	60
ν_t	turbulent kinematic viscosity, [m ² /s]	60
ξ	curvilinear coordinate, [m]	31
ρ	density, [kg/m ³]	14
φ	phase shift, [rad]	77
ϕ	phase angle, [rad]	79
ω	angular frequency, [rad/s]	77
ω^*	reduced frequency, [1]	53

Subscripts

ξ	derivaton with respect to ξ	25
η	derivaton with respect to η	25
L	lower side of airfoil	43
τ	derivaton with respect to τ	25
U	upper side of airfoil	43
w	viscous wall value	31
∞	free stream value	79

Superscripts

*	normalized value	29
\wedge	normalized metric coefficients	17
\sim	transformed variables in body-fitted coordinates	17
-	transformed variable	25

Abbreviations

AIC	Aerodynamic influence coefficients	4
BL	Boundary layer	8

CAP-TSD	Computational Aeroelasticity Program - Transonic Small Disturbance	5
CFD	Computational fluid dynamics	4
CPU	Central processing unit	75
MUSCL	Monotone upstream-centered scheme for conservation laws	21
RANS	Reynolds averaged Navier-Stokes equations	4
RK	Runge-Kutta method	36
SDE	Small disturbance Euler equations	6
URANS	Unsteady Reynolds averaged Navier-Stokes equations	79

List of Figures

1.1	Transonic dip	2
2.1	The scheme of direct coupling method of viscous-inviscid interaction	10
3.1	Body-fitted curvilinear coordinates about airfoil contour	12
3.2	Curvilinear to cartesian grid mapping	13
3.3	Covariant and contravariant velocities	19
3.4	Control volume interfaces	22
3.5	Transpiration velocity on airfoil surface	24
3.6	Pressure in the control volume adjacent to airfoil contour	25
3.7	Velocities at the outer domain boundary	27
4.1	Boundary layer main stations and subintervals	37
4.2	The algorithm for the integration of boundary layer equations	38
5.1	Computational grid around airfoil NACA0012 obtained by elliptic grid generator	41
5.2	Close view of grid around airfoil NACA0012 contour	41
5.3	Grid 100X30; grid convergence test for steady solution for NACA0012 airfoil at $\alpha = 1^\circ$, $Ma = 0.77$; 10, 40, 80 are chord lengths from airfoil to outer boundary	44
5.4	Grid 100X30; difference between solutions for distances 10 and 40 chord lengths and solution for distance 80 chord lengths, in percent of constant finest solution (80 chord lengths); NACA0012 airfoil at $\alpha = 1^\circ$, $Ma = 0.77$	45

5.5	Grid 160X30; grid convergence test for steady solution for NACA0012 airfoil at $\alpha = 1^\circ$, $Ma = 0.77$; 10, 40, 80 are chord lengths from airfoil to outer boundary	45
5.6	Grid 160X30; difference between solutions for distances 10 and 40 chord lengths and solution for distance 80 chord lengths, in percent of constant finest solution (80 chord lengths); NACA0012 airfoil at $\alpha = 1^\circ$, $Ma = 0.77$	46
5.7	Grid 160X60; grid convergence test for steady solution for NACA0012 airfoil at $\alpha = 1^\circ$, $Ma = 0.77$; 10, 40, 80 are chord lengths from airfoil to outer boundary	46
5.8	Grid 160X60; difference between solutions for distances 10 and 40 chord lengths and solution for distance 80 chord lengths, in percent of constant finest solution (80 chord lengths); NACA0012 airfoil at $\alpha = 1^\circ$, $Ma = 0.77$	47
5.9	Grid 240X60; grid convergence test for steady solution for NACA0012 airfoil at and $\alpha = 1^\circ$, $Ma = 0.77$; 10, 40, 80 are chord lengths from airfoil to outer boundary	47
5.10	Grid 240X60; difference between solutions for distances 10 and 40 chord lengths and solution for distance 80 chord lengths, in percent of constant finest solution (80 chord lengths); NACA0012 airfoil at $\alpha = 1^\circ$, $Ma = 0.77$	48
5.11	Grid 320X60; grid convergence test for steady solution for NACA0012 airfoil at and $\alpha = 1^\circ$, $Ma = 0.77$; 10, 40, 80 are chord lengths from airfoil to outer boundary	48
5.12	Grid 320X60; difference between solutions for distances 10 and 40 chord lengths and solution for distance 80 chord lengths, in percent of constant finest solution (80 chord lengths); NACA0012 airfoil at $\alpha = 1^\circ$, $Ma = 0.77$	49
5.13	Grid convergence test for different grid densities for distance of 80 chord lengths from outer domain boundary to airfoil; NACA0012 airfoil at $\alpha = 1^\circ$, $Ma = 0.77$	49
5.14	Differences between solutions obtained by grids stated in the figure's legend and grid 320X60 with 80 chord lengths from outer domain boundary to airfoil, for NACA0012 at $\alpha = 1^\circ$, $Ma = 0.77$	50
5.15	Grid convergence test for NACA0012 airfoil at $\alpha = 5^\circ$, $Ma = 0.77$	50
5.16	Differences between solutions obtained by grids stated in the figure's legend and grid 320X60 with 80 chord lengths from outer domain boundary to airfoil, for NACA0012 at $\alpha = 5^\circ$, $Ma = 0.77$	51

5.17	Grid 100X30; convergence test for unsteady solution; 10, 40 and 80 are chord lengths from airfoil to outer domain boundary; NACA0012 airfoil at $Ma = 0.77$, $\alpha_m = 0^\circ$, $\alpha_o = 1^\circ$	53
5.18	Grid 100X30; difference between solutions for distances 10 and 40 chord lengths and solution for distance 80 chord lengths; NACA0012 airfoil at $Ma = 0.77$, $\alpha_m = 0^\circ$, $\alpha_o = 1^\circ$	54
5.19	Grid 160X30; convergence test for unsteady solution; 10, 40 and 80 are chord lengths from airfoil to outer domain boundary; NACA0012 airfoil at $Ma = 0.77$, $\alpha_m = 0^\circ$, $\alpha_o = 1^\circ$	54
5.20	Grid 160X30; difference between solutions for distances 10 and 40 chord lengths and solution for distance 80 chord lengths; NACA0012 airfoil at $Ma = 0.77$, $\alpha_m = 0^\circ$, $\alpha_o = 1^\circ$	55
5.21	Grid 160X60; convergence test for unsteady solution; 10, 40 and 80 are chord lengths from airfoil to outer domain boundary; NACA0012 airfoil at $Ma = 0.77$, $\alpha_m = 0^\circ$, $\alpha_o = 1^\circ$	55
5.22	Grid 160X60; difference between solutions for distances 10 and 40 chord lengths and solution for distance 80 chord lengths; NACA0012 airfoil at $Ma = 0.77$, $\alpha_m = 0^\circ$, $\alpha_o = 1^\circ$	56
5.23	Grid 240X60; convergence test for unsteady solution; 10, 40 and 80 are chord lengths from airfoil to outer domain boundary; NACA0012 airfoil at $Ma = 0.77$, $\alpha_m = 0^\circ$, $\alpha_o = 1^\circ$	56
5.24	Grid 240X60; difference between solutions for distances 10 and 40 chord lengths and solution for distance 80 chord lengths; NACA0012 airfoil at $Ma = 0.77$, $\alpha_m = 0^\circ$, $\alpha_o = 1^\circ$	57
5.25	Grid 320X60; convergence test for unsteady solution; 10, 40 and 80 are chord lengths from airfoil to outer domain boundary; NACA0012 airfoil at $Ma = 0.77$, $\alpha_m = 0^\circ$, $\alpha_o = 1^\circ$	57
5.26	Grid 320X60; difference between solutions for distances 10 and 40 chord lengths and solution for distance 80 chord lengths; NACA0012 airfoil at $Ma = 0.77$, $\alpha_m = 0^\circ$, $\alpha_o = 1^\circ$	58
5.27	NACA0012 steady pressure coefficient distribution at $Ma = 0.504$, $Re = 2.93 \cdot 10^6$, $\alpha = 4.06^\circ$	62

5.28	NACA0012 boundary layer integral values for upper surface at $Ma = 0.504$, $Re = 2.93 \cdot 10^6$, $\alpha = 4.06^\circ$	62
5.29	NACA0012 boundary layer integral values for lower surface at $Ma = 0.504$, $Re = 2.93 \cdot 10^6$, $\alpha = 4.06^\circ$	63
5.30	NACA0012 steady pressure coefficient distribution for upper surface at $Ma =$ 0.756 , $Re = 4.01 \cdot 10^6$, $\alpha = -0.01^\circ$	64
5.31	NACA0012 steady pressure coefficient distribution for lower surface at $Ma =$ 0.756 , $Re = 4.01 \cdot 10^6$, $\alpha = -0.01^\circ$	64
5.32	NACA0012 boundary layer integral values for lower surface at $Ma = 0.756$, $Re = 4.01 \cdot 10^6$, $\alpha = -0.01^\circ$	65
5.33	NACA0012 steady pressure coefficient distribution for upper surface at $Ma =$ 0.803 , $Re = 4.09 \cdot 10^6$ and $\alpha = 0.05^\circ$	66
5.34	NACA0012 steady pressure coefficient distribution for lower surface at $Ma =$ 0.803 , $Re = 4.09 \cdot 10^6$ and $\alpha = 0.05^\circ$	66
5.35	NACA0012 boundary layer integral values for lower side at $Ma = 0.803$, $Re =$ $4.09 \cdot 10^6$, $\alpha = 0.05^\circ$	67
5.36	NACA64A010 computational grid; A far-field boundary is placed 40 chord lengths away from profile.	68
5.37	NACA64A010 steady pressure coefficient distribution for upper side at $Ma =$ 0.49 , $Re = 2.52 \cdot 10^6$, $\alpha = -0.01^\circ$	70
5.38	NACA64A010 steady pressure coefficient distribution for upper side at $Ma =$ 0.502 , $Re = 1.0 \cdot 10^7$, $\alpha = -0.22^\circ$	70
5.39	NACA64A010 boundary layer integral values for upper side at $Ma = 0.49$, $Re = 2.52 \cdot 10^6$, $\alpha = -0.01^\circ$	70
5.40	NACA64A010 boundary layer integral values for upper side at $Ma = 0.502$, $Re = 1.0 \cdot 10^7$, $\alpha = -0.22^\circ$	70
5.41	NACA64A010 pressure coefficient distribution for upper (left) and lower side (right) at $Ma = 0.796$, $Re = 12.56 \cdot 10^6$, $\alpha = -0.21^\circ$	71
5.42	NACA64A010 boundary layer integral values for upper surface at $Ma = 0.796$, $Re = 12.56 \cdot 10^6$, $\alpha = -0.21^\circ$	72
5.43	NACA64A010 boundary layer integral values for lower surface at $Ma = 0.796$, $Re = 12.56 \cdot 10^6$, $\alpha = -0.21^\circ$	72

5.44	NLR7301; Computational grid. A far-field boundary is placed 40 chord lengths away from profile.	74
5.45	NLR7301 steady pressure coefficient distribution at $Ma = 0.299$, $Re = 1.1 \cdot 10^6$, $\alpha = 0.3966^\circ$	75
5.46	NLR7301 steady pressure coefficient distribution at $Ma = 0.599$, $Re = 1.9 \cdot 10^6$, $\alpha = 0.3832^\circ$	75
5.47	Example of unsteady variation of airfoil angle of attack and pressure	78
5.48	NACA0012 unsteady pressure coefficient distribution at phase angle $\phi = 25.34^\circ$ for $Ma = 0.755$, $Re = 5.5 \cdot 10^6$, $\alpha_m = 0.016^\circ$, $\alpha_o = 2.51^\circ$, $\omega^* = 0.1628$	80
5.49	NACA0012 unsteady pressure coefficient distribution at phase angle $\phi = 67.80^\circ$ for $Ma = 0.755$, $Re = 5.5 \cdot 10^6$, $\alpha_m = 0.016^\circ$, $\alpha_o = 2.51^\circ$, $\omega^* = 0.1628$	80
5.50	NACA0012 unsteady pressure coefficient distribution at phase angle $\phi = 127.40^\circ$ for $Ma = 0.755$, $Re = 5.5 \cdot 10^6$, $\alpha_m = 0.016^\circ$, $\alpha_o = 2.51^\circ$, $\omega^* = 0.1628$	80
5.51	NACA0012 unsteady pressure coefficient distribution at phase angle $\phi = 168.42^\circ$ for $Ma = 0.755$, $Re = 5.5 \cdot 10^6$, $\alpha_m = 0.016^\circ$, $\alpha_o = 2.51^\circ$, $\omega^* = 0.1628$	80
5.52	NACA0012 unsteady pressure coefficient distribution at phase angle $\phi = 210.29^\circ$ for $Ma = 0.755$, $Re = 5.5 \cdot 10^6$, $\alpha_m = 0.016^\circ$, $\alpha_o = 2.51^\circ$, $\omega^* = 0.1628$	81
5.53	NACA0012 unsteady pressure coefficient distribution at phase angle $\phi = 255.14^\circ$ for $Ma = 0.755$, $Re = 5.5 \cdot 10^6$, $\alpha_m = 0.016^\circ$, $\alpha_o = 2.51^\circ$, $\omega^* = 0.1628$	81
5.54	NACA0012 unsteady pressure coefficient distribution at phase angle $\phi = 306.56^\circ$ for $Ma = 0.755$, $Re = 5.5 \cdot 10^6$, $\alpha_m = 0.016^\circ$, $\alpha_o = 2.51^\circ$, $\omega^* = 0.1628$	81
5.55	NACA0012 unsteady pressure coefficient distribution at phase angle $\phi = 347.20^\circ$ for $Ma = 0.755$, $Re = 5.5 \cdot 10^6$, $\alpha_m = 0.016^\circ$, $\alpha_o = 2.51^\circ$, $\omega^* = 0.1628$	81
5.56	Normal force coefficient and instantaneous angle of attack as a function of phase angle in one period, for NACA0012 airfoil at $Ma = 0.755$, $Re = 5.5 \cdot 10^6$, $\alpha_m = 0.016^\circ$, $\alpha_o = 2.51^\circ$, $\omega^* = 0.1628$. The lag between normal force coefficient and pitch motion of airfoil (angle of attack) can be seen	82
5.57	Normal force coefficient as a function of instantaneous angle of attack for NACA0012 airfoil at $Ma = 0.755$, $Re = 5.5 \cdot 10^6$, $\alpha_m = 0.016^\circ$, $\alpha_o = 2.51^\circ$, $\omega^* = 0.1628$	82
5.58	NACA64A010 unsteady pressure coefficient distribution at phase angle $\phi = 45.00^\circ$ for $Ma = 0.797$, $Re = 12.4 \cdot 10^6$, $\alpha_m = -0.08^\circ$, $\alpha_o = 2.00^\circ$, $\omega^* = 0.202$	84

5.59	NACA64A010 unsteady pressure coefficient distribution at phase angle $\phi = 90.00^\circ$ for $\text{Ma} = 0.797$, $\text{Re} = 12.4 \cdot 10^6$, $\alpha_m = -0.08^\circ$, $\alpha_o = 2.00^\circ$, $\omega^* = 0.202$.	84
5.60	NACA64A010 unsteady pressure coefficient distribution at phase angle $\phi = 135.00^\circ$ for $\text{Ma} = 0.797$, $\text{Re} = 12.4 \cdot 10^6$, $\alpha_m = -0.08^\circ$, $\alpha_o = 2.00^\circ$, $\omega^* = 0.202$	85
5.61	NACA64A010 unsteady pressure coefficient distribution at phase angle $\phi = 180.00^\circ$ for $\text{Ma} = 0.797$, $\text{Re} = 12.4 \cdot 10^6$, $\alpha_m = -0.08^\circ$, $\alpha_o = 2.00^\circ$, $\omega^* = 0.202$	85
5.62	NACA64A010 unsteady pressure coefficient distribution at phase angle $\phi = 225.00^\circ$ for $\text{Ma} = 0.797$, $\text{Re} = 12.4 \cdot 10^6$, $\alpha_m = -0.08^\circ$, $\alpha_o = 2.00^\circ$, $\omega^* = 0.202$	85
5.63	NACA64A010 unsteady pressure coefficient distribution at phase angle $\phi = 270.00^\circ$ for $\text{Ma} = 0.797$, $\text{Re} = 12.4 \cdot 10^6$, $\alpha_m = -0.08^\circ$, $\alpha_o = 2.00^\circ$, $\omega^* = 0.202$	85
5.64	NACA64A010 unsteady pressure coefficient distribution at phase angle $\phi = 315.00^\circ$ for $\text{Ma} = 0.797$, $\text{Re} = 12.4 \cdot 10^6$, $\alpha_m = -0.08^\circ$, $\alpha_o = 2.00^\circ$, $\omega^* = 0.202$	86
5.65	NACA64A010 unsteady pressure coefficient distribution at phase angle $\phi = 360.00^\circ$ for $\text{Ma} = 0.797$, $\text{Re} = 12.4 \cdot 10^6$, $\alpha_m = -0.08^\circ$, $\alpha_o = 2.00^\circ$, $\omega^* = 0.202$	86
5.66	Normal force coefficient and instantaneous angle of attack as a function of phase angle in one period, for NACA64A010 airfoil at $\text{Ma} = 0.797$, $\text{Re} = 12.4 \cdot 10^6$, $\alpha_m = -0.08^\circ$, $\alpha_o = 2.00^\circ$, $\omega^* = 0.202$	87
5.67	Normal force coefficient as a function of instantaneous angle of attack for NACA64A010 airfoil at $\text{Ma} = 0.797$, $\text{Re} = 12.4 \cdot 10^6$, $\alpha_m = -0.08^\circ$, $\alpha_o = 2.00^\circ$, $\omega^* = 0.202$	87

List of Tables

5.1	Tested computational grids	42
5.2	Converged normal force coefficient results for steady cases	52
5.3	Converged normal force coefficient results for the unsteady cases	59
5.4	NACA0012 steady test cases	61
5.5	NACA64A010 steady test cases	69
5.6	NLR7301 steady test cases	73
5.7	Summarized steady test cases	76
5.8	NACA0012 unsteady test case	79
5.9	NACA64A010 unsteady test case	83

1 Introduction

1.1. Motivation

The phenomenon of aircraft flutter, which has to be investigated for each new aircraft design or structural modification of existing aircraft, is still one of the current important research topics in aeroelasticity, especially for transonic speed flights. This phenomenon is aeroelastic problem, determined by the interaction of the elastic, damping and inertial forces of the structure and the unsteady aerodynamic forces generated by oscillatory motion of the structure itself. Such oscillatory motion can lead to a progressive increase in amplitude of vibration, ending in a disintegration of the structure. For a given configuration of an aircraft structure the unsteady aerodynamic forces increase rapidly with flight speed, while the elastic, damping and inertia forces remain unchanged. From this reason there exists a critical flight speed (flutter speed) above which flutter¹ occurs.

Actually, every manned flying machine has to undergo some kind of aeroelastic analysis before flight, because flutter and other aeroelastic phenomenon in flight envelope of the aircraft have to be avoided without exception. There are three ways to examine the aeroelastic behavior of the aircraft: flight testing, wind-tunnel testing, and analysis by computational methods. Flight and wind-tunnel testings can be performed earliest in late phase of aircraft design process, because these testing are very expensive. Moreover, because of need for testing of more different aircraft or aerodynamic surface configurations, fabrication of different wind-tunnel models and different aircraft prototypes would be huge time and financial burden in aircraft testing process. Therefore,

¹Self-induced oscillation of coupled aeroelastic system due to the mutual interaction between structural (elastic, inertial and damping) forces and unsteady aerodynamic forces.

a much cheaper solutions are computational methods where many computational test cases can be performed before flight or wind-tunnel tests.

In the transonic speed range, aeroelastic analysis becomes significantly more complicated. Under these conditions, shock waves can form and disappear as the aircraft undergoes unsteady, structurally flexible motion. In addition, regions of separated flow can appear and disappear as these shock waves strengthen and weaken. These are highly nonlinear phenomena that can have essential impact on the aeroelastic behavior of aircraft. The appearance of shock waves on the aircraft aerodynamic surfaces can cause a further drop in flutter boundary in the range of transonic speed. This drop is called transonic dip (see Fig. 1.1). The important feature of the transonic dip is the bottom of the dip, which defines the minimum flutter speed at which flutter can occur across the flight envelope of the aircraft. The flutter speed represents some critical speed at which the structure sustains oscillations following some initial disturbance. Below this speed the oscillations are damped, whereas above it one of the modes becomes negatively damped and unstable oscillations occur, unless some form of nonlinearity bounds the motion [1].

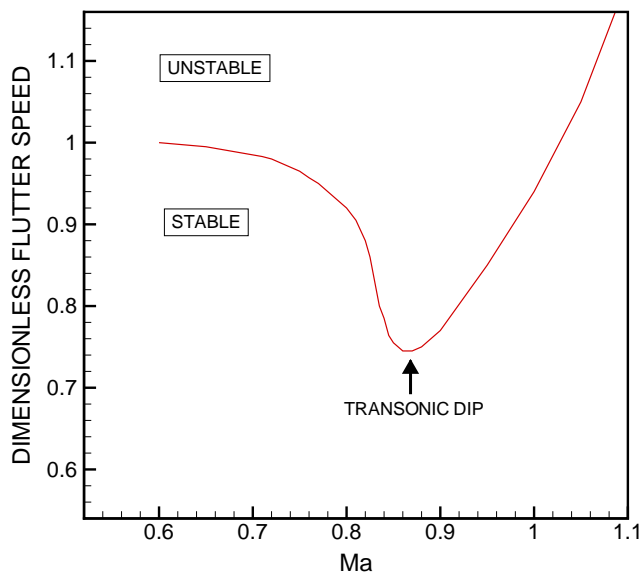


Figure 1.1: Transonic dip

The flutter analysis by linear aerodynamic methods typically predict the flutter boundary adequately at subsonic and supersonic speeds, but in transonic speed range it

predicts a higher flutter speed than experiment [2]. The flutter boundary could be obtained by inviscid unsteady aerodynamics analysis, e.g. solving unsteady transonic small disturbance potential flow, full potential flow, or Euler equations of motions. Although these methods have capability of capturing shock waves in the flow and transonic dip, they predict significantly lower flutter speed at the bottom of the transonic dip because they do not involve viscous effects in the calculations. Viscous effects which act in the form of significant boundary layer thickening and shock-induced flow separation are responsible for better defining the bottom of the transonic dip.

For the flutter analysis, some arbitrary motion of the airfoil is not so often used but the harmonic motion for a single oscillation frequency is of more interest. The objective of such analysis is to determine the flight conditions that correspond to the flutter boundary (stability boundary), for which one of the modes of motion has a simple harmonic time dependency [3]. In the linear flutter analysis it is presumed that the solution involves simple harmonic motion and also excitation force and moment have harmonic behavior. With this assumption the equations of motion are then cast into eigenvalue problem in frequency domain and solved for complex eigenvalues. From this eigenvalues it can be concluded about stable or unstable oscillations of the airfoil. The classical flutter analysis cannot provide any definitive measure of flutter stability other than the location of the stability boundary. Despite this weakness of the method, its primary strength is that it needs only the unsteady airloads for simple harmonic motion of the airfoil.

The direct simulation of fluid-structure coupling in the time domain, adopting the most precise modeling techniques for computation of fluid loads, requires extremely high computational effort. As the main effort is needed for the part of computing unsteady aerodynamic loads, more efficient methods have been developed for the task of predicting only the flutter boundary, which is the state of equilibrium between dynamic structural forces and induced aerodynamic forces. The aerodynamic part of the solution procedure then comprises the computation of unsteady aerodynamic flows around the aircraft structures performing oscillatory dynamic motions in different known elastic geometrical modes and with different frequencies.

For this purpose the doublet-lattice method is still present in actual design analysis because of low computer time consumption and simple setting procedure of computational problem. One of the method lacks is inability of capturing strong shocks in

transonic flows. RANS simulation for flutter analysis gives much more accurate results, but it uses large amount of computational time and hence is not first choice for preliminary design. In addition, RANS needs large grids with high resolution and the problem setting is much more demanding. RANS is also limited with uncertainties in turbulence modeling, difficulties in high quality grid generation and difficulties with grid deformation algorithm in unsteady flows [4].

In preliminary aeroelastic design process, engineers that are not experts in computational fluid dynamics (CFD), but other fields like finite element structural modeling or flight controls, should also be able to use CFD methods. This requires that CFD methods be robust and more automated than current RANS codes. Between these extremes, viscous-inviscid interaction methods such as Euler with viscous boundary layer correction is a good compromise. Euler methods are capable of resolving strong shocks and with boundary layer coupling they are good balance between flow model and computational efficiency. The viscous-inviscid interaction methods give results comparable to RANS solvers, but computer time is several times smaller and this gives appreciable advantage for fast flutter analysis in design process.

This work is dedicated for improvement of such viscous-inviscid interaction method with unsteady Euler as an inviscid solver and a solver of integral boundary-layer equations for thin viscous region, with interaction by transpiration velocity concept.

1.2. Overview of Previous Work

The earliest works in unsteady aerodynamics connected to flutter analysis were made in 1930's and 1940's. Strip theory aerodynamics was long time the most used aerodynamic tool for prediction of unsteady aerodynamic loads [5]. In this approximation theory one considers each spanwise segment as it were a portion of an infinite span wing with uniform spanwise properties.

During 1960's remarkable unsteady aerodynamic tool was developed, namely doublet-lattice method [6]. Further development of this method was to allow handling of non-planar aerodynamic surfaces with bodies [7]. This method produced one important contribution to flutter analysis, aerodynamic influence coefficients (AICs). AICs relate the lift on each element of aerodynamic surfaces and displacements (related to translation and rotation) and also the dynamic pressure. More recently, Rodden et al. continued

to refine the doublet-lattice method [8]. These enhancements were the replacement of the approximation of the numerators of the incremental kernels and improved approximation to the integrand in the integral in the kernel. The doublet-lattice method has been in use for over 30 years and has become a standard for production flutter analysis. There are some features that are responsible for the long life of the method. First, the method is accurate enough for production flutter analysis, except in transonic regime and when there exist separation. Second, the method has small calculation time and produces AICs. Third, the method has ability to model fairly complex geometry and does not have the need for grid generation. The method has lifting surfaces that are simply replaced with series of panels. All this gives final important feature that is, user friendly code.

Among methods based on various forms of the potential flow equation with boundary layer correction, which have shown good results for unsteady calculations without large computational resources and less working hours in setting up the problem, the CAP-TSD [9] code is widely used. This code has many advantages over a RANS code: ease in grid generation, no need for moving grid and less demand for computational resources. Despite the use of vortex and entropy corrections, the assumptions in CAP-TSD code limits its applicability to irrotational flows with weak shocks. Edwards [10] used CAP-TSD code with a lag-entrainment integral boundary layer method for computation of unsteady transonic flows involving separation and reattachment. Also, Edwards showed the self-excited shock-induced oscillations (buffet). Cebeci et al. [11] have shown an interactive boundary layer method for multielement airfoils at low and moderate Reynolds numbers. In this method inviscid part of flow is solved by the Hess Smith panel method, while viscous boundary layer flow is solved by the compressible boundary layer equations (mass, momentum and energy) for laminar and turbulent flows and, with the algebraic eddy viscosity and turbulent Prandtl number formulation of Cebeci and Smith [12]. Mangler and Catherall [13] in their work showed the method which gave the solution of the boundary layer equations near a separation point for steady incompressible laminar two-dimensional flow. The boundary layer equations are solved in a regular direct mode until the separation point is reached. After the separation point displacement thickness is prescribed, and then the pressure gradient is calculated. They obtained solutions for reversed flow, namely for small separation bubbles inside boundary layer.

Because methods that solve Euler equations are capable of resolving strong shocks

and transporting vortices correctly, many researchers have investigated interactive boundary layer methods using the Euler equations [14, 15]. However, many researchers have focused on steady calculations. Drela [16] has used Euler equations for inviscid field and integral boundary layer formulation for thin viscous region in neighborhood of the airfoil. Transition prediction is based on the Orr-Sommerfeld equation formulation (e^N method) and incorporated into two-equation, integral, laminar/turbulent boundary layer analysis. The viscous formulation is fully coupled with the inviscid flow that is governed by a streamline-based Euler formulation. The entire non-linear coupled system of equations is solved by Newton solution procedure.

Recently, Zhang [17] demonstrated an efficient Euler method with boundary-layer correction suitable for the airplane wing flutter. The thickness of the wing as well as its small-scale motion is simulated by approximated boundary conditions implemented on the stationary wing chord plane. Therefore, non-moving Cartesian grid is used for unsteady simulations of airplane wing.

In aeroelastic applications, where a high number of parameters such as different natural modes, angles of attack, Mach numbers, frequency, etc. must be investigated, methods that solve unsteady aerodynamic problem in frequency domain are introduced. Especially, these methods are suitable for simulations at low reduced frequencies. The same simulations in time domain are time consuming because a periodic state can be achieved after calculating a number of cycles. Recently, a numerical method based on such alternative approach, namely, on solution of small disturbance Euler equations (SDE) is presented [18]. Assuming harmonic behavior of unsteadiness (unsteady variables), they yield a set of linear variable coefficient equations for the complex amplitude of the field quantities. The unsteady problem is reduced to a steady-state problem for the perturbation part. The non-linear flow physics is contained in steady reference solution which is needed for linearized solution. The unsteady loads can be evaluated directly and used within the standard modal flutter calculations. Overall, the method shows good results, but in flows with shocks, pressure distribution shows remarkable differences in comparison with non-linear Euler solution. The same linearization is made for Navier-Stokes equations by Pechloff [19]. In this work also the linearization of Spalart-Allmaras one-equation turbulence model was made.

Recently, some papers are published that analyze coupling of RANS equations with boundary layer [20, 21, 22]. These papers demonstrated the prediction of transition

region with the aim to construct laminar airfoils and to reduce the drag.

1.3. Objective and Hypothesis of Research

The effective surface displacement approach describes the concept of the viscous-inviscid interaction. This approach can be employed in high Reynolds number flows where viscous effects are contained in thin boundary layer region. As the boundary layer thickness changes in unsteady flows, a new grid must be generated for the inviscid computation after each interaction. A method which avoids this difficulty is the method of equivalent sources proposed by Lighthill [23]. Changes of boundary-layer mass defect is used to impose the sources or sinks on solid surface of airfoil. The blowing or suction effect of the injected flow simulates the displacement action of the boundary-layer on the outer inviscid flow. In this work attempt is made to incorporate momentum contribution of the injected flow for the interaction with Euler equations. Momentum equation in direction perpendicular to airfoil surface is solved with incorporation of boundary layer blowing effect on inviscid flow. All calculations are made on body-fitted curvilinear grid with orthogonality condition on airfoil surface.

The aim and hypothesis of the thesis is to show that approach with incorporation of momentum from boundary layer into momentum equation in direction normal to airfoil will give results that are comparable with more precise today available methods. The method should be accurate enough to be usable as aerodynamic tool in routine aeroelastic checks, and also should give good results in transonic region where the shock waves are appearing.

2 Viscous-Inviscid Interaction

At high Reynolds number flows, where inertial forces are more significant than viscous forces, Prandtl [24] showed how Navier-Stokes equations could be simplified to yield approximate solution. In such flow cases viscous effects are confined in thin region close to viscous wall, called boundary layer. Therefore, such flows can be decomposed in two regions. First region is the field away from boundaries, where viscous effects at high Reynolds number can be neglected. Second region is thin boundary layer region where viscous effects are confined.

2.1. Viscous-Inviscid Interaction Method

In this work viscous-inviscid interaction of boundary layer integral equations and Euler equations is made by the transpiration velocity concept. The transpiration velocity changes the slope of the net velocity at the boundary and in such way represents displacement thickness of boundary layer and influence of boundary layer on inviscid flow outside the boundary layer. The transpiration velocity concept is proposed by Lighthill in [23] as equivalent sources concept. From the integration of continuity equation for incompressible flow, from wall surface to the outer edge of boundary layer $\delta(x)$, it follows:

$$v = \int_0^{\delta(x)} \frac{\partial v}{\partial y} dy = - \int_0^{\delta(x)} \frac{\partial u}{\partial x} dy. \quad (2.1)$$

x and y are coordinates along and perpendicular to the wall respectively, and u and v are corresponding velocity components. When the velocity u_e at the boundary layer

edge ($y = \delta(x)$) is introduced in the second integral, then the following expression for the velocity v is obtained:

$$v = -\frac{du_e}{dx}\delta + \frac{d}{dx} \int_0^{\delta(x)} (u_e - u) dy \quad (2.2)$$

The first term in (2.2) is that which would be present in the irrotational flow around the body, and the second is the additional velocity due to the boundary layer existence. The second term, which represents transpiration velocity, can be rearranged to contain displacement thickness:

$$v_t = \frac{d}{dx} \int_0^{\infty} u_e \left(1 - \frac{u}{u_e}\right) dy = \frac{d}{dx} (u_e \delta^*). \quad (2.3)$$

In this work the viscous-inviscid interaction is made in direct mode. There are other possible ways for the viscous-inviscid interaction, namely inverse, semi inverse and simultaneous. In the direct method, used in this work, the output from inviscid solver, which are velocity or pressure at the boundary edge, are used as the input in the viscous solver of boundary layer equations. The output from the viscous solver is displacement thickness, or transpiration velocity derived from the displacement thickness, which is then used as input in inviscid solver to update the boundary condition of inviscid flow. The used scheme of direct coupling method is presented in Fig. 2.1. The advantage of such coupling method is its speed and simplicity in the application. The disadvantage of the the direct method is inability to simulate separated flows, because of the appearance of a singularity in the boundary layer equations which is called Goldstein's singularity [25].

In the inverse method, the viscous and inviscid equations are solved in the reverse mode. The boundary layer equations are solved for the unknown pressure from the displacement thickness as the input, while inviscid equations are solved for the required displacement thickness from the pressure distribution of boundary layer. The calculated displacement thickness serves as input to the boundary layer solver.

The compromise between direct and inverse methods is semi inverse method. In this method the inviscid equations are solved as in direct mode, while boundary layer equations are solved as in the inverse mode. The both viscous and inviscid regions are solved for the unknown velocity distribution at the boundary layer edge from the displacement thickness. The two velocity distributions are compared and according

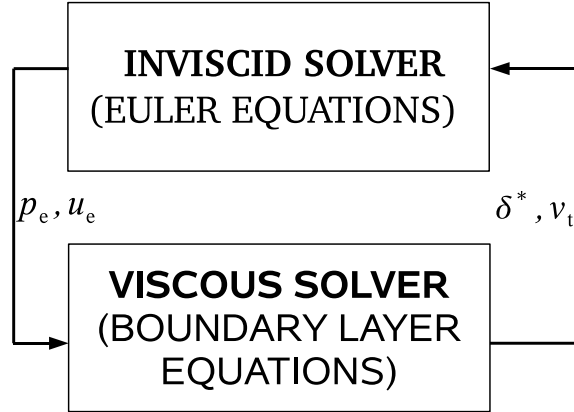


Figure 2.1: The scheme of direct coupling method of viscous-inviscid interaction

to this difference, new displacement thickness is determined. The convergence with relaxation is performed until velocity distributions from two flow region are in agreement.

In the simultaneous method, the inviscid equations are simultaneously solved with viscous equations. The both set of equations are written together and solved as one system.

The coupling method by the transpiration velocity showed strong solution oscillations at the near separation test cases, and at the position of sudden thickening of boundary layer thickness. To reduce such oscillatory behavior of solution and to reach monotone converged solution, the underrelaxation method was used. The underrelaxation is performed on the transpiration velocity, by the following expression:

$$v_t = v_t^o + \beta (v_t^n - v_t^o). \quad (2.4)$$

The superscripts o and n represent the old and the new solution of transpiration velocity magnitude in the iterations of viscous-inviscid coupling respectively. β represents underrelaxation factor and it is smaller than one. At the initial calculation step when transpiration velocity magnitude is calculated for the first time, the old solution of transpiration velocity magnitude is equal to zero. Left hand of equation (2.4) is resulting transpiration velocity magnitude and in new iteration step it serves as the old solution in the subsequent iteration.

3 Inviscid Model

In this chapter inviscid compressible fluid dynamics equations will be derived. The method of solving these equations will be described and also the transformation of body-fitted (physical) grid to Cartesian (calculation) grid. The boundary conditions will be described on outer domain boundary as well as on the airfoil contour boundary. The incorporation of boundary layer influence by transpiration velocity in boundary condition on airfoil will be described.

3.1. Coordinates Transformation

In the case of flows around curved bodies like airfoils, the structured grids in curvilinear body-fitted coordinates can be used. Such grids are suitable because of their structured nature and better performance of codes optimized for such grid type. In Fig. 3.1 body-fitted coordinate system is shown on two dimensional structured grid around airfoil with curvilinear axes ξ and η .

Structured grid in such coordinate system can be very easily transformed into Cartesian grid in Cartesian coordinate system, which numerically simplifies the solution calculation by application of control volume method. Mapping functions from Cartesian system (x, y, t) into curvilinear body-fitted coordinate system (ξ, η, τ) can be written in the following form:

$$\begin{aligned}\xi &= \xi(x, y, t) \\ \eta &= \eta(x, y, t) \\ \tau &= t.\end{aligned}\tag{3.1}$$

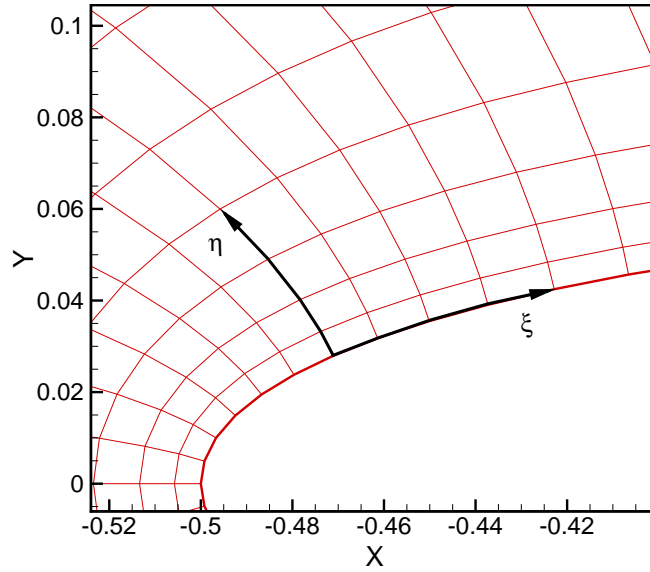


Figure 3.1: Body-fitted curvilinear coordinates about airfoil contour

In Fig. 3.2 characteristic points (from A to F) in the curvilinear structured grid around airfoil are shown. Point A is at the trailing edge on lower surface and point F is at the trailing edge on upper surface. In the same figure these points are shown in the physical plane (down left) and in the mapped plane (down right). The airfoil surface which is represented by line between A and F, is in mapped plane represented by straight line between points A and F (shown bolded). Between these two grid representations of field around airfoil, mapping functions exist which are written in equations (3.1)

In the transformation of Euler equations from Cartesian coordinates to curvilinear coordinates the metric coefficients that come from grid transformation have to be calculated (see section 3.3.). This transformations can be expressed from functions written in (3.1). From these expressions the derivations with respect to Cartesian coordinates and physical time can be written as follows:

$$\begin{aligned}
 \frac{\partial}{\partial x} &= \xi_x \frac{\partial}{\partial \xi} + \eta_x \frac{\partial}{\partial \eta} + \tau_x \frac{\partial}{\partial \tau} \\
 \frac{\partial}{\partial y} &= \xi_y \frac{\partial}{\partial \xi} + \eta_y \frac{\partial}{\partial \eta} + \tau_y \frac{\partial}{\partial \tau} \\
 \frac{\partial}{\partial t} &= \xi_t \frac{\partial}{\partial \xi} + \eta_t \frac{\partial}{\partial \eta} + \tau_t \frac{\partial}{\partial \tau}
 \end{aligned} \tag{3.2}$$

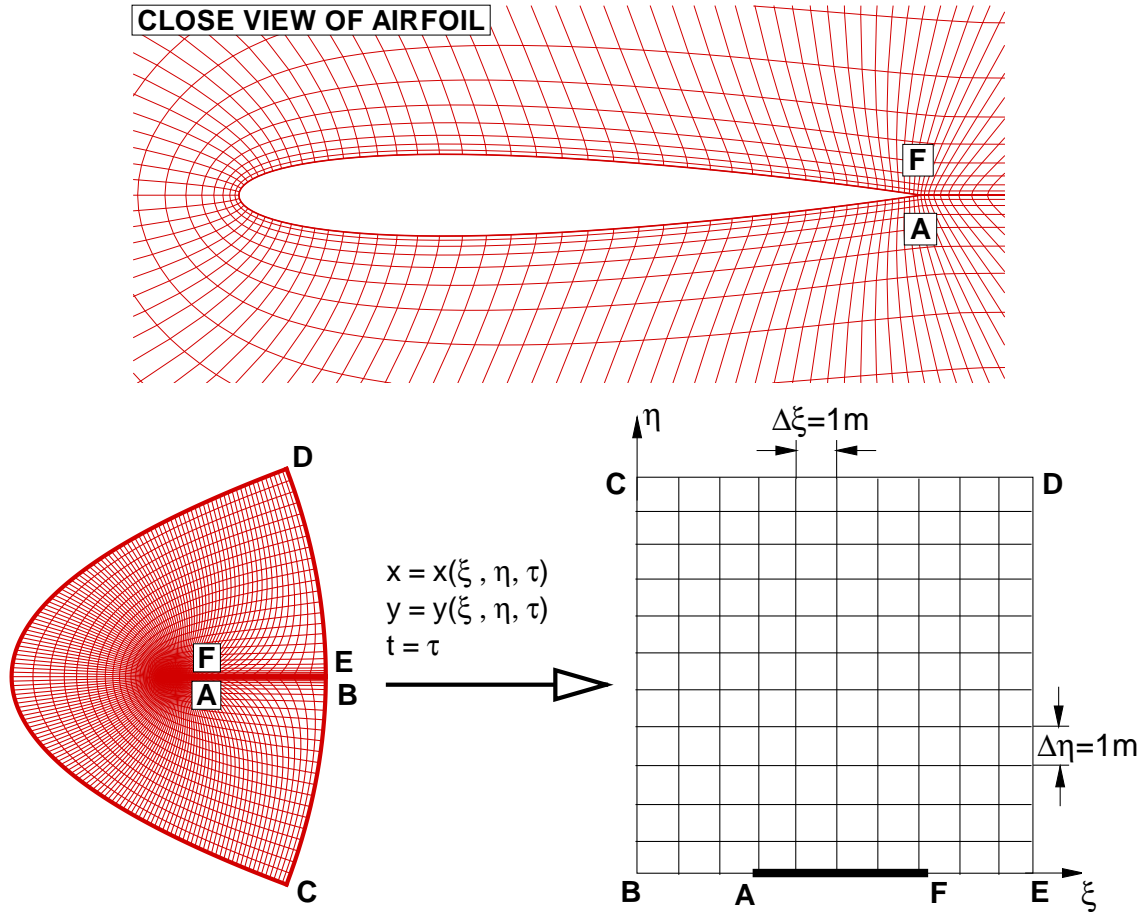


Figure 3.2: Curvilinear to cartesian grid mapping

Subscripts in expressions (3.2) and subsequent expressions represent partial derivation with respect to the variable in the subscript. Metric transformation coefficients are given according to following expressions:

$$\begin{aligned}
 \xi_x &= J^{-1}y_\eta & \eta_x &= -J^{-1}y_\xi & \tau_x &= 0 \\
 \xi_y &= -J^{-1}x_\eta & \eta_y &= J^{-1}x_\xi & \tau_y &= 0 \\
 \xi_t &= 0 & \eta_t &= 0 & \tau_t &= 1
 \end{aligned} \tag{3.3}$$

where J is the determinant of Jacobi matrix and equals:

$$J = \left| \frac{\partial(x, y, t)}{\partial(\xi, \eta, \tau)} \right| = \begin{vmatrix} x_\xi & y_\xi & 0 \\ x_\eta & y_\eta & 0 \\ x_\tau & y_\tau & 1 \end{vmatrix} = x_\xi y_\eta - y_\xi x_\eta \quad (3.4)$$

3.2. Euler Equations

In the flows around streamlined bodies like airfoils, at high Reynolds numbers, viscous effects are only significant in thin region close to airfoil called boundary layer. In such flows, the region around airfoil (except the boundary layer in the close vicinity of airfoil where viscous effect are not negligible) is possible to solve by Euler equations. In this work inviscid flow is calculated by Euler equations in body-fitted coordinates.

Euler equations describe unsteady, inviscid, compressible, anisotropic and rotational flow. Such form of the equations represents nonlinear hyperbolic conservative laws in which effects of mass forces, viscous stresses and heat fluxes are neglected. For such form of equations Riemann solvers and upwind methods are directly applicable.

There are different forms of Euler equations. Written in two dimensional Cartesian coordinates and conservation differential form, Euler equations have following form:

$$\frac{\partial \mathbf{Q}}{\partial t} + \frac{\partial \mathbf{F}(\mathbf{Q})}{\partial x} + \frac{\partial \mathbf{G}(\mathbf{Q})}{\partial y} = 0 \quad (3.5)$$

where vectors \mathbf{Q} , \mathbf{F} and \mathbf{G} equal

$$\mathbf{Q} = \begin{bmatrix} \rho \\ \rho u \\ \rho v \\ \rho e \end{bmatrix} \quad \mathbf{F} = \begin{bmatrix} \rho u \\ \rho u^2 + p \\ \rho uv \\ \rho uh \end{bmatrix} \quad \mathbf{G} = \begin{bmatrix} \rho v \\ \rho vu \\ \rho v^2 + p \\ \rho vh \end{bmatrix}. \quad (3.6)$$

In vectors expressed by (3.6), e is specific total energy (per unit mass)

$$e = \frac{1}{\gamma - 1} \frac{p}{\rho} + \frac{1}{2} (u^2 + v^2) \quad (3.7)$$

and h is specific total enthalpy (per unit mass).

$$h = \frac{\gamma}{\gamma - 1} \frac{p}{\rho} + \frac{1}{2} (u^2 + v^2) \quad (3.8)$$

3.3. The Vector Flux Splitting

The schemes based on central space discretizations, associated with the spatial flux terms in subsonic flow, have a symmetry with respect to a change in sign of the eigenvalues (characteristic speed) which does not distinguish upstream from downstream influences. Hence the physical propagation of perturbations along characteristics, typical of hyperbolic equations, is not considered in the definition of such numerical model. Therefore, in the numerical implementation of this work, the method of the vector flux splitting is used. This method belongs to the family of upwind methods which take into account the perturbation propagation direction. The background of the flux vector splitting method is given in report of Steger and Warming [26].

System of equations (3.5) can be written in the form of matrices in the following way:

$$\frac{\partial \mathbf{Q}}{\partial t} + \mathbf{A}(\mathbf{Q}) \frac{\partial \mathbf{Q}}{\partial x} + \mathbf{B}(\mathbf{Q}) \frac{\partial \mathbf{Q}}{\partial y} = 0 \quad (3.9)$$

where

$$\mathbf{A}(\mathbf{Q}) = \frac{\partial \mathbf{F}}{\partial \mathbf{Q}} \quad \text{and} \quad \mathbf{B}(\mathbf{Q}) = \frac{\partial \mathbf{G}}{\partial \mathbf{Q}}. \quad (3.10)$$

Coefficients in matrices \mathbf{A} and \mathbf{B} are functions of vector \mathbf{Q} , therefore the system of equations (3.9) is nonlinear. Matrices \mathbf{A} and \mathbf{B} are called Jacobi matrices (Jacobians) and have following form:

$$\mathbf{A}(\mathbf{Q}) = \frac{\partial \mathbf{F}}{\partial \mathbf{Q}} = \begin{bmatrix} \partial f_1 / \partial q_1 & \partial f_1 / \partial q_2 & \partial f_1 / \partial q_3 & \partial f_1 / \partial q_4 \\ \partial f_2 / \partial q_1 & \partial f_2 / \partial q_2 & \partial f_2 / \partial q_3 & \partial f_2 / \partial q_4 \\ \partial f_3 / \partial q_1 & \partial f_3 / \partial q_2 & \partial f_3 / \partial q_3 & \partial f_3 / \partial q_4 \\ \partial f_4 / \partial q_1 & \partial f_4 / \partial q_2 & \partial f_4 / \partial q_3 & \partial f_4 / \partial q_4 \end{bmatrix} \quad (3.11)$$

$$\mathbf{B}(\mathbf{Q}) = \frac{\partial \mathbf{G}}{\partial \mathbf{Q}} = \begin{bmatrix} \partial g_1 / \partial q_1 & \partial g_1 / \partial q_2 & \partial g_1 / \partial q_3 & \partial g_1 / \partial q_4 \\ \partial g_2 / \partial q_1 & \partial g_2 / \partial q_2 & \partial g_2 / \partial q_3 & \partial g_2 / \partial q_4 \\ \partial g_3 / \partial q_1 & \partial g_3 / \partial q_2 & \partial g_3 / \partial q_3 & \partial g_3 / \partial q_4 \\ \partial g_4 / \partial q_1 & \partial g_4 / \partial q_2 & \partial g_4 / \partial q_3 & \partial g_4 / \partial q_4 \end{bmatrix} \quad (3.12)$$

where f_i , g_i and q_i are components of vectors \mathbf{F} , \mathbf{G} and \mathbf{Q} respectively, for $i = 1, 2, 3, 4$.

Eigenvalues λ_i of matrix \mathbf{A} are solutions of characteristic polynomial

$$|\mathbf{A} - \lambda\mathbf{I}| = \det(\mathbf{A} - \lambda\mathbf{I}) = 0 \quad (3.13)$$

where \mathbf{I} is unit matrix. In analogous way the same is valid for matrix \mathbf{B} . Physically, the eigenvalues represent propagation velocities of disturbances, and the system of hyperbolic equations has all real eigenvalues.

In the algorithm of flux vector splitting, the flux vectors \mathbf{F} and \mathbf{G} are divided into positive contributions $\mathbf{F}^+, \mathbf{G}^+$ and negative contributions $\mathbf{F}^-, \mathbf{G}^-$:

$$\begin{aligned} \mathbf{F} &= \mathbf{F}^+ + \mathbf{F}^- \\ \mathbf{G} &= \mathbf{G}^+ + \mathbf{G}^- \end{aligned} \quad (3.14)$$

The flux vectors are splitted in such way that Jacobian matrices $\partial\mathbf{F}^+/\partial\mathbf{Q}$ and $\partial\mathbf{G}^+/\partial\mathbf{Q}$ have only positive, and Jacobian matrices $\partial\mathbf{F}^-/\partial\mathbf{Q}$ and $\partial\mathbf{G}^-/\partial\mathbf{Q}$ have only negative eigenvalues. According to this splitting, the equation (3.9) has now in Cartesian coordinates following form:

$$\frac{\partial\mathbf{Q}}{\partial t} + \frac{\partial\mathbf{F}^+}{\partial\mathbf{Q}} \frac{\partial\mathbf{Q}}{\partial x} + \frac{\partial\mathbf{F}^-}{\partial\mathbf{Q}} \frac{\partial\mathbf{Q}}{\partial x} + \frac{\partial\mathbf{G}^+}{\partial\mathbf{Q}} \frac{\partial\mathbf{Q}}{\partial y} + \frac{\partial\mathbf{G}^-}{\partial\mathbf{Q}} \frac{\partial\mathbf{Q}}{\partial y} = 0 \quad (3.15)$$

Because of such flux splitting, the numerical calculation of spatial derivations of $\mathbf{F}^+, \mathbf{G}^+$ and $\mathbf{F}^-, \mathbf{G}^-$ has to be conducted with backward and forward differencing respectively.

Flux splitting is made with respect to the one-dimensional Mach number $M_x = u/a$ i $M_y = v/a$. For subsonic flow, where $|M_x| < 1$ for \mathbf{F} and $|M_y| < 1$ for \mathbf{G} , the flux splitting of \mathbf{F} and \mathbf{G} is made according to Van Leer [27] as follows:

$$\mathbf{F}^\pm = \begin{bmatrix} \pm \frac{\rho a}{4} (1 \pm M_x)^2 \\ \frac{a}{\gamma} [(\gamma - 1) M_x \pm 2] f_1^\pm \\ v f_1^\pm \\ \frac{\gamma^2}{2(\gamma^2 - 1)} \frac{(f_2^\pm)^2}{f_1^\pm} + \frac{v^2}{2} f_1^\pm \end{bmatrix} \quad (3.16)$$

where f_1^\pm and f_2^\pm represent first and second member of vector \mathbf{F}^\pm respectively.

$$\mathbf{G}^{\pm} = \begin{bmatrix} \pm \frac{\rho a}{4} (1 \pm M_y)^2 \\ u g_1^{\pm} \\ \frac{a}{\gamma} [(\gamma - 1) M_y \pm 2] g_1^{\pm} \\ \frac{\gamma^2}{2(\gamma^2 - 1)} \frac{(g_3^{\pm})^2}{g_1^{\pm}} + \frac{u^2}{2} g_1^{\pm} \end{bmatrix} \quad (3.17)$$

Members g_1^{\pm} and g_3^{\pm} in (3.17) represent first and third member of vector \mathbf{G}^{\pm} respectively.

For supersonic flow, where $|M_x| > 1$ for \mathbf{F} and $|M_y| > 1$ for \mathbf{G} , it follows:

$$\begin{aligned} \mathbf{F}^+ &= \mathbf{F}, \quad \mathbf{F}^- = 0 & \text{for } M_x \geq +1 \\ \mathbf{F}^+ &= 0, \quad \mathbf{F}^- = \mathbf{F} & \text{for } M_x \leq -1 \end{aligned} \quad (3.18)$$

$$\begin{aligned} \mathbf{G}^+ &= \mathbf{G}, \quad \mathbf{G}^- = 0 & \text{for } M_y \geq +1 \\ \mathbf{G}^+ &= 0, \quad \mathbf{G}^- = \mathbf{G} & \text{for } M_y \leq -1 \end{aligned} \quad (3.19)$$

As the numerical calculations in this work are performed in body-fitted coordinates, it is needed to transform the Euler equations from Cartesian coordinates (x, y, t) into body-fitted coordinates (ξ, η, τ) . The Euler equations transformed in body-fitted coordinates and in conservative form are written in following equation:

$$\frac{\partial \tilde{\mathbf{Q}}}{\partial \tau} + \frac{\partial \tilde{\mathbf{F}}}{\partial \xi} + \frac{\partial \tilde{\mathbf{G}}}{\partial \eta} = 0 \quad (3.20)$$

where $\tilde{\mathbf{Q}}$ and $\tilde{\mathbf{F}}, \tilde{\mathbf{G}}$ are transformed vector of conservative variables and flux vectors respectively:

$$\begin{aligned} \tilde{\mathbf{Q}} &= J\mathbf{Q} \\ \tilde{\mathbf{F}} &= (-y_{\eta}x_{\tau} + x_{\eta}y_{\tau})\mathbf{Q} + y_{\eta}\mathbf{F} - x_{\eta}\mathbf{G} \\ \tilde{\mathbf{G}} &= (-x_{\xi}y_{\tau} + y_{\xi}x_{\tau})\mathbf{Q} + y_{\xi}\mathbf{F} - x_{\xi}\mathbf{G} \end{aligned} \quad (3.21)$$

In equations (3.21) and following equations in this work, indexes ξ, η and τ represent derivatives of Cartesian coordinates with respect to the curvilinear body-fitted coordinates. J represents the Jacobian of the grid transformation. The equation (3.20) has not the same structure as the equation (3.5) and is not appropriate for the described flux splitting. Correct splitting of transformed flux vectors (3.21) is performed in such way

that the flux vectors $\tilde{\mathbf{F}}$ and $\tilde{\mathbf{G}}$ are written as the product of the local rotation matrix and modified flux vector what is described in [28]. Such modified flux vectors have now the same form as the flux vectors in Cartesian coordinates but contain transformed instead of Cartesian velocities. The flux vectors written in this form equal:

$$\begin{aligned}\tilde{\mathbf{F}}(\tilde{\mathbf{Q}}) &= \sqrt{x_\eta^2 + y_\eta^2} \mathbf{T}_F \bar{\mathbf{F}}(\bar{\mathbf{Q}}) \\ \tilde{\mathbf{G}}(\tilde{\mathbf{Q}}) &= \sqrt{x_\xi^2 + y_\xi^2} \mathbf{T}_G \bar{\mathbf{G}}(\bar{\mathbf{Q}})\end{aligned}\tag{3.22}$$

where the fluxes now have the same form as in Cartesian coordinates, but with transformed velocities.

$$\bar{\mathbf{Q}} = \rho \begin{bmatrix} 1 \\ \bar{u} \\ \bar{v} \\ \bar{e} \end{bmatrix}\tag{3.23}$$

$$\bar{\mathbf{F}} = \rho \begin{bmatrix} \bar{u} \\ \bar{u}^2 + \frac{a^2}{\gamma} \\ \bar{u}\bar{v} \\ \bar{u}\bar{h} \end{bmatrix}\tag{3.24}$$

$$\bar{\mathbf{G}} = \rho \begin{bmatrix} \bar{v} \\ \bar{u}\bar{v} \\ \bar{v}^2 + \frac{a^2}{\gamma} \\ \bar{v}\bar{h} \end{bmatrix}\tag{3.25}$$

Transformed velocities in the flux vector $\bar{\mathbf{F}}$ are equal:

$$\begin{aligned}\bar{u} &= \hat{y}_\eta(u - x_\tau) - \hat{x}_\eta(v - y_\tau) \\ \bar{v} &= \hat{x}_\eta(u - x_\tau) + \hat{y}_\eta(v - y_\tau)\end{aligned}\tag{3.26}$$

while in the flux vector $\bar{\mathbf{G}}$ are equal

$$\begin{aligned}\bar{u} &= \hat{x}_\xi(u - x_\tau) + \hat{y}_\xi(v - y_\tau) \\ \bar{v} &= -\hat{y}_\xi(u - x_\tau) + \hat{x}_\xi(v - y_\tau).\end{aligned}\tag{3.27}$$

The velocity \bar{u} in the flux vector $\bar{\mathbf{F}}$ represent net velocity perpendicular to coordinate line $\xi = \text{const.}$ and velocity \bar{v} net velocity along coordinate line $\xi = \text{const.}$, i.e. covariant and contravariant velocity components at face $\xi = \text{const.}$ respectively. In the flux vector $\bar{\mathbf{G}}$ velocity \bar{u} represents net velocity along the coordinate line $\eta = \text{const.}$ and velocity \bar{v} is net velocity perpendicular to coordinate line $\eta = \text{const.}$, i.e. contravariant and covariant velocity components at face $\eta = \text{const.}$ respectively. These velocities are depicted in Fig. 3.3.

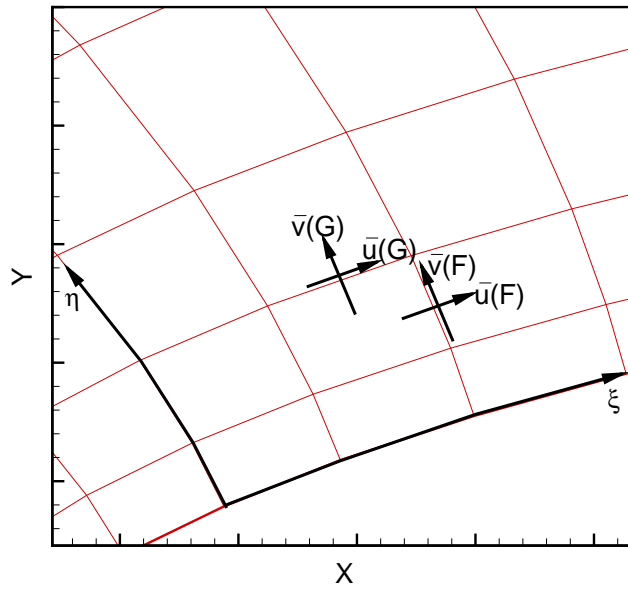


Figure 3.3: Covariant and contravariant velocities

The metric coefficients \hat{x}_η , \hat{y}_η , \hat{x}_ξ and \hat{y}_ξ are normalized as follows:

$$\begin{aligned}
 \hat{x}_\eta &= \frac{x_\eta}{\sqrt{x_\eta^2 + y_\eta^2}} \\
 \hat{y}_\eta &= \frac{y_\eta}{\sqrt{x_\eta^2 + y_\eta^2}} \\
 \hat{x}_\xi &= \frac{x_\xi}{\sqrt{x_\xi^2 + y_\xi^2}} \\
 \hat{y}_\xi &= \frac{y_\xi}{\sqrt{x_\xi^2 + y_\xi^2}}
 \end{aligned} \tag{3.28}$$

Transformed total energy \bar{e} and total enthalpy \bar{h} have the same form but include tran-

sformed velocities:

$$\bar{e} = \frac{a^2}{\gamma(\gamma - 1)} + \frac{1}{2}(\bar{u}^2 + \bar{v}^2) \quad (3.29)$$

$$\bar{h} = \frac{a^2}{\gamma - 1} + \frac{1}{2}(\bar{u}^2 + \bar{v}^2). \quad (3.30)$$

Local rotation matrices \mathbf{T}_F and \mathbf{T}_G have following form:

$$\mathbf{T}_F = \begin{bmatrix} 1 & 0 & 0 & 0 \\ x_\tau & \hat{y}_\eta & \hat{x}_\eta & 0 \\ y_\tau & -\hat{x}_\eta & \hat{y}_\eta & 0 \\ \frac{x_\tau^2 + y_\tau^2}{2} & \hat{y}_\eta x_\tau - \hat{x}_\eta y_\tau & \hat{x}_\eta x_\tau + \hat{y}_\eta y_\tau & 1 \end{bmatrix} \quad (3.31)$$

$$\mathbf{T}_G = \begin{bmatrix} 1 & 0 & 0 & 0 \\ x_\tau & \hat{x}_\xi & -\hat{y}_\xi & 0 \\ y_\tau & \hat{y}_\xi & \hat{x}_\xi & 0 \\ \frac{x_\tau^2 + y_\tau^2}{2} & \hat{x}_\xi x_\tau + \hat{y}_\xi y_\tau & \hat{x}_\xi y_\tau - \hat{y}_\xi x_\tau & 1 \end{bmatrix} \quad (3.32)$$

Now, the vector flux splitting on $\tilde{\mathbf{F}}$ and $\tilde{\mathbf{G}}$ can be performed in the same way as splitting of fluxes \mathbf{F} and \mathbf{G} in (3.16) and (3.17):

$$\tilde{\mathbf{F}}^\pm = \sqrt{x_\eta^2 + y_\eta^2} \mathbf{T}_F \bar{\mathbf{F}}^\pm \quad (3.33)$$

$$\tilde{\mathbf{G}}^\pm = \sqrt{x_\xi^2 + y_\xi^2} \mathbf{T}_G \bar{\mathbf{G}}^\pm \quad (3.34)$$

where the flux vectors $\bar{\mathbf{F}}^\pm$ and $\bar{\mathbf{G}}^\pm$ are calculated in same way like splitted vectors in Cartesian coordinates written in expressions (3.16) and (3.17), but in place of Mach numbers Ma_x and Ma_y come Mach numbers Ma_ξ and Ma_η which are calculated by transformed velocities:

$$\begin{aligned} \text{Ma}_\xi &= \frac{\bar{u}}{a} \\ \text{Ma}_\eta &= \frac{\bar{v}}{a} \end{aligned} \quad (3.35)$$

3.4. Solution Procedure for Euler Equations

Now, Euler equations in body-fitted coordinates with splitted flux vectors have following form:

$$\frac{\partial \tilde{\mathbf{Q}}}{\partial \tau} + \frac{\partial \tilde{\mathbf{F}}^+}{\partial \xi} + \frac{\partial \tilde{\mathbf{F}}^-}{\partial \xi} + \frac{\partial \tilde{\mathbf{G}}^+}{\partial \eta} + \frac{\partial \tilde{\mathbf{G}}^-}{\partial \eta} = 0 \quad (3.36)$$

The equation (3.36) is discretized and solved in the explicit way:

$$\begin{aligned} \tilde{\mathbf{Q}}^{n+1}(i, j) = \tilde{\mathbf{Q}}^n(i, j) - \Delta\tau & \left[\frac{\tilde{\mathbf{F}}^+(i+1/2, j) - \tilde{\mathbf{F}}^+(i-1/2, j)}{\Delta\xi} \right. \\ & + \frac{\tilde{\mathbf{F}}^-(i+1/2, j) - \tilde{\mathbf{F}}^-(i-1/2, j)}{\Delta\xi} \\ & + \frac{\tilde{\mathbf{G}}^+(i, j+1/2) - \tilde{\mathbf{G}}^+(i, j-1/2)}{\Delta\eta} \\ & \left. + \frac{\tilde{\mathbf{G}}^-(i, j+1/2) - \tilde{\mathbf{G}}^-(i, j-1/2)}{\Delta\eta} \right]^n \end{aligned} \quad (3.37)$$

where indices (i, j) represent concerned control volume. The indices $(i+1/2, j)$ and $(i-1/2, j)$ represent two control volume interfaces on lines $\xi = \text{const.}$, and indices $(i, j+1/2)$ and $(i, j-1/2)$ represent two control volume interfaces on lines $\eta = \text{const.}$ (see Fig. 3.4). Superscripts $n+1$ and n represent old and new time step respectively. Spatial step, difference between two coordinate lines in two directions ($\Delta\xi$ and $\Delta\eta$) are arbitrary chosen and equal $\Delta\xi = \Delta\eta = 1\text{m}$. Spatial derivations are approximated by MUSCL scheme (MUSCL - *Monotone Upstream-centered Scheme for Conservation Laws*), where the fluxes at the control volume interfaces are calculated directly by forward or backward extrapolation of solution vector \mathbf{Q} depending it is positive or negative flux contributions respectively. Generally, formula for splitted fluxes calculation follows:

$$\begin{aligned} \tilde{\mathbf{F}}^\pm(i-1/2, j) &= \tilde{\mathbf{F}}^\pm \left(\mathbf{Q}_{i-\frac{1}{2}, j}^\mp, m_{i-\frac{1}{2}, j} \right) \\ \tilde{\mathbf{F}}^\pm(i+1/2, j) &= \tilde{\mathbf{F}}^\pm \left(\mathbf{Q}_{i+\frac{1}{2}, j}^\mp, m_{i+\frac{1}{2}, j} \right) \\ \tilde{\mathbf{G}}^\pm(i, j-1/2) &= \tilde{\mathbf{G}}^\pm \left(\mathbf{Q}_{i, j-\frac{1}{2}}^\mp, m_{i, j-\frac{1}{2}} \right) \\ \tilde{\mathbf{G}}^\pm(i, j+1/2) &= \tilde{\mathbf{G}}^\pm \left(\mathbf{Q}_{i, j+\frac{1}{2}}^\mp, m_{i, j+\frac{1}{2}} \right) \end{aligned} \quad (3.38)$$

where m represents all geometric members included in body-fitted coordinates transformation, i.e. metric coefficients. The subscripts $i - 1/2$, $i + 1/2$, $j - 1/2$ and $j + 1/2$ in expressions (3.38) represent control volume interfaces as noted above. Extrapolated values of solution vectors \mathbf{Q} are obtained by help of second order approximations (here only for ξ direction):

$$\begin{aligned} \mathbf{Q}_{i+\frac{1}{2},j}^- &= \mathbf{Q}_{i,j} + 0.5(\mathbf{Q}_{i,j} - \mathbf{Q}_{i-1,j}) \\ \mathbf{Q}_{i+\frac{1}{2},j}^+ &= \mathbf{Q}_{i+1,j} + 0.5(\mathbf{Q}_{i+1,j} - \mathbf{Q}_{i+2,j}) \end{aligned} \quad (3.39)$$

where again $i - 1$, i , $i + 1$, $i + 2$ represent indices of control volume centers and $i + \frac{1}{2}$ index of right control volume face in ξ direction. Analogously is valid for η direction.

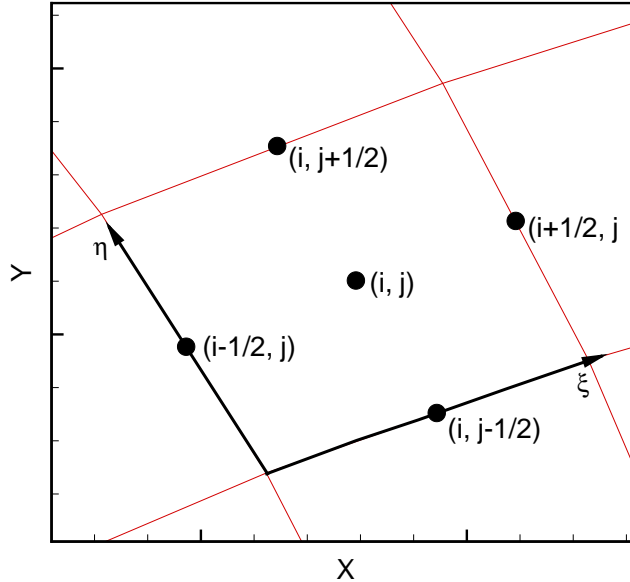


Figure 3.4: Control volume interfaces

3.5. Boundary Conditions and Contour Pressure Determination

Boundary condition on airfoil contour is imposed in inviscid part of flow solver. Boundary condition on airfoil contour is given by zero flow through airfoil contour, or by existence only the tangential velocity on contour. Mathematically, this boundary condition can be written by the following:

$$(\vec{v} - \vec{v}_b - \vec{v}_t) \cdot \vec{n} = 0 \quad (3.40)$$

where \vec{v} is fluid velocity, \vec{v}_b is prescribed velocity of boundary (airfoil contour), \vec{v}_t is transpiration velocity resulted from boundary layer existence, and \vec{n} is unit normal vector on airfoil contour. Transpiration velocity represents effect of boundary layer thickening, and actually by transpiration velocity boundary layer model is coupled with inviscid flow model. Transpiration velocity model is derived in [23] for incompressible flow under the name equivalent sources. With the same procedure the expression for transpiration velocity for compressible flow can be derived:

$$\rho_e v_t = \frac{d(\rho_e u_e \delta^*)}{ds} \quad (3.41)$$

where v_t represents transpiration velocity magnitude in direction perpendicular to airfoil contour, δ^* displacement thickness (defined by eq. (4.9)), and s is curvilinear coordinate going along airfoil contour from stagnation point to trailing edge. u_e and ρ_e are velocity magnitude and density at the boundary layer edge. The equation (3.41) represents the strength (mass flow rate per unit area) of additional outflow due to the boundary layer existence. Transpiration velocity is separately calculated for upper and lower surface from stagnation point of airfoil. In Fig. 3.5 the transpiration velocity vectors are shown perpendicular to upper surface of airfoil.

Boundary condition (3.40) can be rearranged by derivating it, which gives following equation:

$$\frac{D\vec{v}}{Dt} \cdot \vec{n} - \frac{D(\vec{v}_b + \vec{v}_t)}{Dt} \cdot \vec{n} + (\vec{v} - \vec{v}_b - \vec{v}_t) \cdot \frac{D\vec{n}}{Dt} = 0. \quad (3.42)$$

First member in equation (3.42) represents left hand of momentum equation in direction of unit normal \vec{n} :

$$\frac{D\vec{v}}{Dt} \cdot \vec{n} = -\frac{1}{\rho} \text{grad} p \cdot \vec{n}. \quad (3.43)$$

When equations (3.42) and (3.43) are combined, new momentum equation in direction of unit normal to airfoil contour follows:

$$\rho \left\{ \frac{D\vec{n}}{Dt} \cdot (\vec{v} - \vec{v}_b - \vec{v}_t) - \frac{D(\vec{v}_b + \vec{v}_t)}{Dt} \cdot \vec{n} \right\} = \text{grad} p \cdot \vec{n}. \quad (3.44)$$

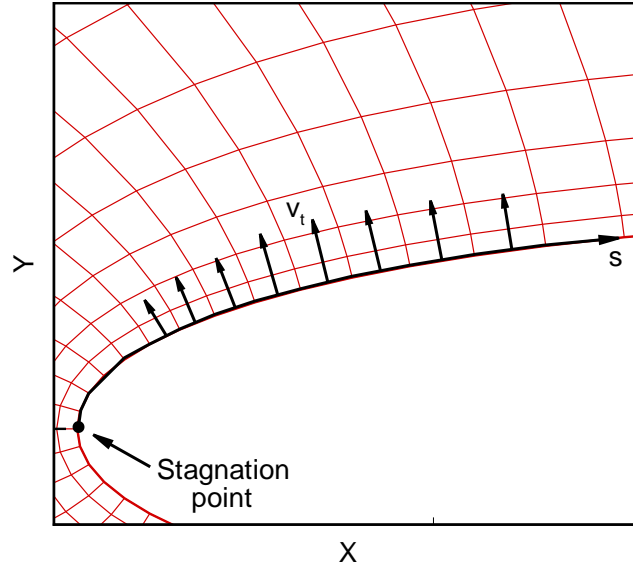


Figure 3.5: Transpiration velocity on airfoil surface

In equation (3.44) boundary layer effect is coupled with inviscid flow solver by transpiration velocity. Equation (3.44) can be expressed on airfoil contour to calculate pressure gradient in normal direction. Determining pressure gradient on airfoil contour, pressure on contour can accurately be determined from pressure in adjacent control volumes. Pressure on contour p_1 can then be calculated by:

$$p_1 = p_2 - \frac{\Delta\eta}{2} \text{grad}p \cdot \vec{n} \quad (3.45)$$

where p_2 is pressure in first control volume center adjacent to airfoil contour, and one half came from the fact that length of volume cell in η direction is equal $\Delta\eta = 1\text{m}$ (see fig. (3.6)). The same is valid for ξ direction where $\Delta\xi = 1\text{m}$.

Equation (3.44) should be transformed to appropriate coordinate system. Complete calculation of inviscid flow solver is made in body-fitted curvilinear coordinates (ξ, η, τ) . τ is transformed time which is equal to physical time t . Grid around airfoil is C-type grid generated by condition that coordinate lines $\xi = \text{konst.}$ (see Fig. 3.1) are perpendicular to airfoil contour. Line $\eta = \text{konst.}$ coincide with airfoil contour. According to these conditions, transformation of equation (3.44) into body-fitted coordinate system gives following equation (complete derivation of boundary condition is presented in appendix A.):

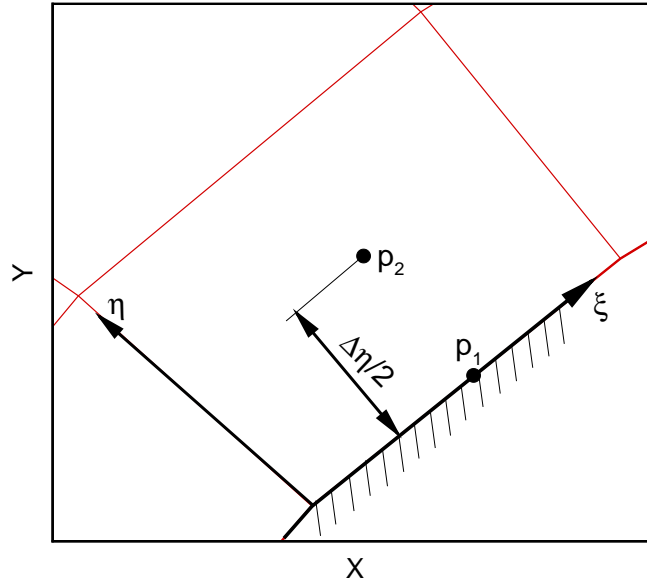


Figure 3.6: Pressure in the control volume adjacent to airfoil contour

$$\frac{\partial p}{\partial \eta} (x_\xi^2 + y_\xi^2) = \frac{\partial p}{\partial \xi} (x_\xi x_\eta + y_\xi y_\eta) + \rho \left\{ J \left[\frac{\bar{u}^2}{(x_\xi^2 + y_\xi^2)} (y_\xi x_{\xi\xi} - x_\xi y_{\xi\xi}) + \frac{2\bar{u}}{\sqrt{x_\xi^2 + y_\xi^2}} (y_\xi x_{\tau\xi} - x_\xi y_{\tau\xi}) + x_{\tau\tau} y_\xi - y_{\tau\tau} x_\xi \right] + (y_\xi v_{tx\xi} - x_\xi v_{ty\xi}) (y_\eta (u - x_\tau) - x_\eta (v - y_\tau)) + J (v_{tx\tau} y_\xi - v_{ty\tau} x_\xi) \right\} \quad (3.46)$$

In equation (3.46), velocity \bar{u} is covariant velocity on $\eta = \text{konst.}$ side of control volume defined according to expression (3.27) and J is Jacobian defined according to equation (3.4). Metric coefficients x_ξ , y_ξ , x_η , y_η , $x_{\xi\xi}$, $y_{\xi\xi}$ are grid constants where indexes represent derivation with respect to indexed values. Grid velocities are represented by members x_τ and y_τ . Last member in equation (3.46) take into account unsteady behaviour of coupling mechanism through time derivation of transpiration velocity components v_{tx} and v_{ty} . From equation (3.46) one can directly calculate pressure gradient in direction perpendicular to airfoil, namely $\partial p / \partial \eta$.

On the outer domain boundaries, characteristic boundary conditions were used. With such boundary conditions, the flow is concerned as locally one-dimensional and derivations along boundaries can be neglected ($\partial(\) / \partial \xi \rightarrow 0$). From generalized Riemman

invariants [29] for hyperbolic system of equations, expressions valid along disturbance propagation direction can be derived:

$$\begin{aligned} \frac{dS}{dt} = 0 & \quad \text{along} \quad C^0 : \frac{dx}{dt} = v_{\text{norm}} \\ \frac{dv_{\text{norm}}}{dt} \pm \frac{1}{\rho a} \frac{dp}{dt} = 0 & \quad \text{along} \quad C^\pm : \frac{dx}{dt} = v_{\text{norm}} \pm a \end{aligned} \quad (3.47)$$

where S is entropy, a is local speed of sound and v_{norm} is local velocity perpendicular to outer domain boundary respectively. C^0 and C^\pm represent three characteristics of disturbance propagation on outer domain boundary. With assumption of isentropic flow, last equation in (3.47) can be transformed to the following:

$$\frac{d}{dt}(R^\pm) = 0 \quad \text{along} \quad \frac{dx}{dt} = v_{\text{norm}} \pm a \quad (3.48)$$

where R^\pm are Riemman invariants

$$R^\pm = v_{\text{norm}} \pm \frac{2a}{\gamma - 1}. \quad (3.49)$$

Characteristic equation (3.49) is used to update variable values on the domain boundary in the new time step. For two-dimensional case number of variables equals four, namely ρ , u , v , p . Because of that, also four independent equations are needed. For subsonic inflow on outer domain boundary, where velocity component normal to boundary $v_{\text{norm}} < 0$, following expressions are valid:

$$\begin{aligned} R^+ &= R^+(\infty) \\ R^- &= R^-(F) \\ v_{\text{tang}} &= v_{\text{tang}}(\infty) \\ p_T &= p_T(\infty). \end{aligned} \quad (3.50)$$

In equation (3.50) symbols ∞ and F represent free stream value and flow field value of interior domain respectively. v_{tang} is fluid velocity along outer domain boundary and p_T is total pressure. In Fig. 3.7, the fluid velocity components on the outer domain boundary are showed. In the same way as for inflow, for subsonic outflow on outer domain boundary where velocity component in normal direction to boundary $v_{\text{norm}} > 0$, following expressions are valid:

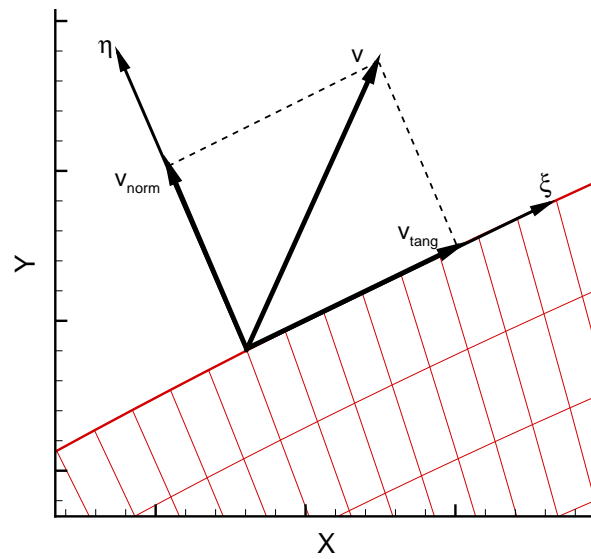


Figure 3.7: Velocities at the outer domain boundary

$$\begin{aligned}
 R^+ &= R^+(F) \\
 R^- &= R^-(\infty) \\
 v_{\text{tang}} &= v_{\text{tang}}(F) \\
 p_T &= p_T(F)
 \end{aligned}
 \tag{3.51}$$

Again, symbol F represents that variables are locally extrapolated from interior domain, and symbol ∞ represents that variable values are calculated from free stream value.

4 | **Boundary layer**

In this chapter, the integral compressible boundary layer equations used in the viscous-inviscid coupling are presented. Along with these equations, the relationships for closing the system of integral boundary layer equations are also presented. There are several descriptions of boundary layer implemented in the literature, like integral boundary layer equations and differential boundary layer equations. In this work integral boundary layer description made by Drela and Giles [16] is used.

4.1. **Boundary Layer Concept**

In the flows at high Reynolds number or with very small viscosity fluid, complete flow field can be divided into two regions. First is thin region close to viscous wall called boundary layer where viscous forces are dominant, and velocity gradient normal to wall ($\partial u/\partial y$) is very large. Second is region away from boundary layer where inertial forces are dominant and viscous forces are negligible, that is where velocity gradients are negligible. The simplification of such limiting flow cases is firstly shown by Prandtl [24].

In [30] it is shown the assessment of members in Navier-Stokes equations for two dimensional case, in the limiting flow case when Reynolds number $Re \rightarrow \infty$. After the assessment of the order of magnitude of members in the momentum equations in direction along and perpendicular to viscous wall follows:

$$u^* \frac{\partial u^*}{\partial x^*} + v^* \frac{\partial u^*}{\partial y^*} = -\frac{\partial p^*}{\partial x^*} + \frac{1}{Re} \frac{\partial^2 u^*}{\partial x^{*2}} + \frac{\partial^2 u^*}{\partial y^{*2}} \quad (4.1)$$

$$\frac{1}{\text{Re}} \left(u^* \frac{\partial v^*}{\partial x^*} + v^* \frac{\partial u^*}{\partial y^*} \right) = -\frac{\partial p^*}{\partial y^*} + \frac{1}{\text{Re}^2} \frac{\partial^2 v^*}{\partial x^{*2}} + \frac{1}{\text{Re}} \frac{\partial^2 v^*}{\partial y^{*2}} \quad (4.2)$$

In equations (4.1) and (4.2) superscript * represents normalized quantities. Coordinate x along viscous wall is normalized by characteristic length which is much bigger than boundary layer thickness, usually the airfoil chord length c is taken. Coordinate y perpendicular to viscous wall is normalized by boundary layer thickness δ . Velocity u in direction of viscous wall is normalized by maximum velocity in the boundary layer U in the same direction, while Velocity v is normalized by maximum velocity in boundary layer V in the direction perpendicular to viscous wall y . Pressure is normalized by ρU^2 .

When the Reynolds number goes to high values, the members with coefficients $1/\text{Re}$ and $1/\text{Re}^2$ in equations (4.1) and (4.2) tend to zero. From this assessment follows that dominant momentum transport is along wall direction (4.4), and from momentum equation in normal to wall direction (4.5) follows that there is no pressure change along normal to wall direction. Such system of steady boundary layer equations derived by process $\text{Re} \rightarrow \infty$ is given in equations (4.3) – (4.5) which are called Prandtl's boundary layer equations. Here, the coordinates x and y are along and perpendicular direction of wall boundary respectively.

$$\frac{\partial u^*}{\partial x^*} + \frac{\partial v^*}{\partial y^*} = 0 \quad (4.3)$$

$$u^* \frac{\partial u^*}{\partial x^*} + v^* \frac{\partial u^*}{\partial y^*} = -\frac{\partial p^*}{\partial x^*} + \frac{\partial^2 u^*}{\partial y^{*2}} \quad (4.4)$$

$$0 = -\frac{\partial p^*}{\partial y^*}. \quad (4.5)$$

The equations (4.4) and (4.5) show apparent reduction in complexity with respect to the Navier-Stokes equations. From the momentum equation (4.5) follows that pressure in boundary layer is independent of direction normal to the wall, that is the pressure is constant across the boundary layer height and equals to the pressure of outer inviscid flow. The boundary conditions for the system (4.3) – (4.5) is given by:

$$\begin{aligned} y^* = 0 & \quad \rightarrow \quad u^* = 0, \quad v^* = 0 \\ y^* \rightarrow \infty & \quad \rightarrow \quad u^*(x^*) = u_e^*(x^*) \end{aligned} \quad (4.6)$$

where u_e^* represents the normalized velocity of the flow at the outer boundary layer edge. The system of boundary layer equations (4.3) – (4.6) is of parabolic type. This has good property that outer inviscid velocity field $u_e(x)$, which dictates the boundary layer behavior, has the influence only on the flow downstream. This means that boundary layer equations can be solved by marching procedure.

The Prandtl's equations are derived without the influence of the wall curvature. In [31] it is shown that the wall curvature has no effect as long as the curvature radius is bigger than the characteristic length, that is much bigger than boundary layer thickness δ . In this work viscous-inviscid method is applied on airfoils which usually have leading edge with large curvature. Usually such geometry is confined only in the small length of airfoil chord. Because of that property, the integration of boundary layer equations is not started at the stagnation point, but is postponed 5% of airfoil chord length.

In many practical applications interest is not in velocity distribution within boundary layer, but in integral variables that change with coordinate along wall boundary. Such integral variables are obtained by integrating the momentum equation over the boundary layer thickness. Such approach is employed also in this work.

4.2. Boundary Layer in Transonic Flow

In transonic flow over an airfoil the pocket of supersonic flow appears which is terminated by a shock-wave. Through shock-wave, pressure and density undergo a sudden increase. Also, shock-wave has foot point in the boundary layer on the airfoil surface, and the pressure rise in the boundary layer has big impact on its evolution. Depending on its history at the station under consideration, a boundary layer shows a more or less strong tendency to separate from the airfoil surface. The parameters that determine the station of separation are the Reynolds number of the flow, surface geometry, roughness and the distance from the boundary layer origin [32]. This tendency is greatly enhanced on a convex surface, because of the destabilizing pressure gradient in the flow away from the surface, whereas the opposite pressure gradient on a concave surface stabilizes the boundary layer by compressing it. This is the normal situation in supersonic flows.

When a shock wave intersects the boundary layer, its strength decreases steadily as it proceeds into the layer, and it becomes a Mach line at the streamline where the flow is sonic. The high pressure behind the shock wave provides a steep adverse pressure gradi-

ent that makes itself felt upstream through the subsonic portion of the layer. Transition to turbulent boundary layer or flow separation may result, depending on the intensity of the adverse gradient, that is, on the intensity of the shock.

Intuitively, it is logical that the thicker the subsonic portion of the boundary layer, the farther upstream the effects of the adverse gradient will be felt. Also, $\partial u/\partial y$ near $y = 0$ will be small for a thick subsonic portion, and hence a small adverse gradient (small shock intensity) will suffice to cause flow separation. In general, a laminar boundary layer will have a thicker subsonic portion than the turbulent layer.

The consequences of transition that are of practical importance are the following:

- Since $(\partial u/\partial y)_w$ is greater for the turbulent than the laminar layer, the shearing stress $\tau_w = \mu(\partial u/\partial y)_w$ will increase greatly through the transition region
- There will be corresponding increase in the heat transfer rate at the wall
- Flow separation will be delayed because $(\partial u/\partial y)_w$ is greater in the turbulent layer

4.3. Integral Compressible Boundary Layer Equations by Drela

The boundary layer equations and additional relationship employed in the viscous-inviscid method of this work are taken from the work of Mark Drela [14], who obtained excellent results for steady transonic flows. The boundary layer equations in integral form which will be solved in this work are the well-known von Karman integral equation, which represents the momentum equation,

$$\frac{d\theta}{ds} = \frac{C_f}{2} - (H + 2 - \text{Ma}_e^2) \frac{\theta}{u_e} \frac{du_e}{ds}, \quad (4.7)$$

and kinetic energy equation, also known as shape parameter equation

$$\frac{dH^*}{ds} = \frac{2C_D}{\theta} - \frac{H^* C_f}{\theta} - \left(\frac{2H^{**}}{H^*} + 1 - H \right) \frac{H^*}{u_e} \frac{du_e}{ds}. \quad (4.8)$$

The variable s represents one-dimensional curvilinear coordinate along airfoil contour and index e represents values of variables at the boundary layer edge. The variable s

begins from stagnation point and goes separately on upper and lower airfoil side toward trailing edge. In equations (4.7) and (4.8) the variable s is introduced because the two coordinates s and ξ have different origin and different length. The variable s is physical coordinate while the coordinate ξ is not. The boundary layer equations (4.7) and (4.8) are valid for steady flow, and such are used in the viscous-inviscid method developed in this work.

The integral variables in equations (4.7) and (4.8) are defined as follows:

- displacement thickness

$$\delta^* = \int_0^{\infty} \left(1 - \frac{\rho u}{\rho u_e}\right) d\eta \quad (4.9)$$

- momentum thickness

$$\theta = \int_0^{\infty} \left(1 - \frac{u}{u_e}\right) \frac{\rho u}{\rho u_e} d\eta \quad (4.10)$$

- friction coefficient

$$C_f = \frac{2\tau_w}{\rho_e u_e^2} \quad (4.11)$$

- kinetic energy thickness

$$\theta^* = \int_0^{\infty} \left(1 - \left(\frac{u}{u_e}\right)^2\right) \frac{\rho u}{\rho u_e} d\eta \quad (4.12)$$

- density thickness

$$\delta^{**} = \int_0^{\infty} \left(1 - \frac{\rho}{\rho_e}\right) \frac{u}{u_e} d\eta \quad (4.13)$$

- dissipation coefficient

$$C_D = \frac{1}{\rho_e u_e^3} \int_0^{\infty} \tau \frac{\partial u}{\partial \eta} d\eta. \quad (4.14)$$

Also, the shape parameters are defined as follows:

$$H = \frac{\delta^*}{\theta} \quad H^* = \frac{\theta^*}{\theta} \quad H^{**} = \frac{\delta^{**}}{\theta} \quad (4.15)$$

The momentum and shape parameter equations (4.7) and (4.8) are valid for both laminar and turbulent boundary layers, as well as for free wakes. These equations contain more than two independent variables and hence some assumptions about the additional unknowns will have to be made. There are four additional unknown variables: C_f , C_D , H^* , H^{**} . All closure equations are expressed, between others, in terms of kinematic shape parameter which is defined with constant density across the boundary layer. Compressible and incompressible velocity profiles have nearly the same shapes which suggests that in compressible flow the additional closure equations should be based on the kinematic shape parameter, which depends only on velocity profile. Whitfield [33] proposed an empirical expression for H_k in terms of conventional shape parameter and boundary layer edge Mach number:

$$H_k = \frac{H - 0.29\text{Ma}_e^2}{1 + 0.113\text{Ma}_e^2}. \quad (4.16)$$

This parameter is used for both laminar and turbulent flows.

For laminar flow, closure equations are defined as in [14]:

- Kinetic energy shape parameter

$$H^* = \frac{H_k^* + 0.028\text{Ma}_e^2}{1 + 0.014\text{Ma}_e^2} \quad (4.17)$$

where

$$H_k^* = \begin{cases} 1.515 + 0.076 \frac{(H_k - 4)^2}{H_k}, & H_k < 4 \\ 1.515 + 0.04 \frac{(H_k - 4)^2}{H_k}, & H_k > 4 \end{cases} \quad (4.18)$$

- Friction coefficient (wall shear coefficient)

$$\text{Re}_\theta \frac{C_f}{2} = \begin{cases} -0.067 + 0.01977 \frac{(7.4 - H_k)^2}{H_k - 1}, & H_k < 7.4 \\ -0.067 + 0.022 \left(1 - \frac{1.4}{H_k - 6}\right)^2, & H_k > 7.4 \end{cases} \quad (4.19)$$

- Dissipation coefficient

$$\text{Re}_\theta \frac{2C_D}{H^*} = \begin{cases} 0.207 + 0.00205 (4 - H_k)^{5.5}, & H_k < 4 \\ 0.207 - 0.003 (H_k - 4)^2, & H_k > 4 \end{cases} \quad (4.20)$$

- Density thickness shape parameter

$$H^{**} = \left(\frac{0.064}{H_k - 0.8} + 0.251 \right) \text{Ma}_e^2 \quad (4.21)$$

Expression (4.21) for density thickness shape parameter will be used for both laminar and turbulent flows.

For turbulent flow, closure equations are derived on the fact of two layer structure. For turbulent flow, closure equations are defined as in [14]:

- Friction coefficient (wall shear coefficient)

$$F_c C_f = \frac{0.3e^{-1.33H_k}}{\left[\log_{10} \left(\frac{\text{Re}_\theta}{F_c} \right) \right]^{1.74+0.31H_k}} + 0.00011 \left[\tanh \left(4 - \frac{H_k}{0.875} \right) - 1 \right] \quad (4.22)$$

where

$$F_c = (1 + 0.2\text{Ma}_e^2)^{1/2} \quad (4.23)$$

- Kinetic energy shape parameter

$$H^* = \frac{H_k^* + 0.028\text{Ma}_e^2}{1 + 0.014\text{Ma}_e^2} \quad (4.24)$$

where

$$H_k^* = \begin{cases} 1.505 + \frac{4}{\text{Re}_\theta} + \left(0.165 - \frac{1.6}{\sqrt{\text{Re}_\theta}} \right) \frac{(H_0 - H_k)^{1.6}}{H_k}, & H_k < H_0 \\ 1.505 + \frac{4}{\text{Re}_\theta} + (H_k - H_0)^2 \left[\frac{0.04}{H_k} + 0.007 \frac{\ln(\text{Re}_\theta)}{\left(H_k - H_0 + \frac{4}{\ln(\text{Re}_\theta)} \right)^2} \right], & H_k > H_0 \end{cases} \quad (4.25)$$

and

$$H_0 = 3 + \frac{400}{\text{Re}_\theta}. \quad (4.26)$$

- Dissipation coefficient (non-equilibrium)

$$\frac{2C_D}{H^*} = \frac{C_f}{2} \left(\frac{4}{H_k} - 1 \right) \frac{1}{3} + \frac{2}{H^*} C_\tau (1 - U_s) \quad (4.27)$$

where shear coefficient is calculated from the lag equation:

$$\frac{\delta}{C_\tau} \frac{dC_\tau}{ds} = 4.2 \left(C_{\tau_{\text{eq}}}^{0.5} - C_\tau^{0.5} \right) \quad (4.28)$$

and expression for δ is equal

$$\delta = \theta \left(3.15 + \frac{1.72}{H_k - 1} \right) + \delta^* \quad (4.29)$$

Shear stress coefficient C_τ is non-dimensional quantity defined by

$$C_\tau = \frac{(-\overline{u'v'})_{\text{max}}}{u_e^2} \quad (4.30)$$

where $-\overline{u'v'}$ is Reynolds stress. Non-dimensional slip velocity U_s and the equilibrium shear stress coefficient $C_{\tau_{\text{eq}}}$ in equation (4.24) are defined by

$$U_s = \frac{H^*}{6} \left(\frac{4}{H_k} - 1 \right) \quad (4.31)$$

and

$$C_{\tau_{\text{eq}}} = \frac{H^*}{2} \frac{0.03}{1 - U_s} \left(\frac{H_k - 1}{H_k} \right)^3 \quad (4.32)$$

4.4. Solution Procedure for Boundary Layer Equations

The boundary layer equations (4.7) and (4.8) employed in this work were solved by fourth order Runge-Kutta method. The two equations contain two dependent variables θ and H^* , and four additional unknown variables C_f , H , C_D and H^{**} . These unknown variables are calculated by the additional relationships. The additional relationships, which are used to close the system of equations, are written in the section 4.3..

The input values to the boundary layer equations are fluid velocity $u_e(s)$ and Mach number $\text{Ma}_e(s)$ distribution at the edge of boundary layer, which is a function of distance

from stagnation point along airfoil surface. These distributions are output of inviscid part of flow, taken at the position of airfoil surface.

Integration of the boundary layer equations starts from the initial solution for the flat plate in laminar flow. The boundary layer variables for the initial solution were obtained from Blasius [34] solution:

- Boundary layer thickness

$$\delta = 5\sqrt{\frac{\nu s}{U_\infty}} \quad (4.33)$$

- Displacement thickness

$$\delta^* = 1.7208\sqrt{\frac{\nu s}{U_\infty}} \quad (4.34)$$

- Momentum thickness

$$\theta = 0.664\sqrt{\frac{\nu s}{U_\infty}} \quad (4.35)$$

- Friction coefficient

$$C_f = \frac{0.664}{\text{Re}_s} \quad (4.36)$$

where Re_s represents Reynolds number with reference length s measured from the leading edge to the certain point along plate.

The main spatial nodes for the integration of boundary layer equations along s -coordinate coincide with the position of control volume side centers at airfoil surface (see Fig. 4.1). At these nodes (nodes i and $i + 1$ in the fig. 4.1) the values of variables u_e and M_e are overtaken from the inviscid flow at the airfoil surface. For the more accurate integration the distance between two main nodes is divided into twenty subintervals (not shown all in the fig. 4.1). The integration procedure is the same for subintervals as for the main nodes, but the values from the inviscid flow are interpolated from main nodes to the subinterval nodes.

The boundary layer integration is started at the 5% airfoil chord to avoid the stagnation point and big curvature (small radius) in the vicinity of the leading edge. The solution at this distance is assumed to be equal solution of Blasius for flat plate. After this point starts the boundary layer model of Drela.

In Fig. 4.2 the algorithm for the boundary layer equations integration is presented. This algorithm shows the integration by fourth order Runge-Kutta method between two

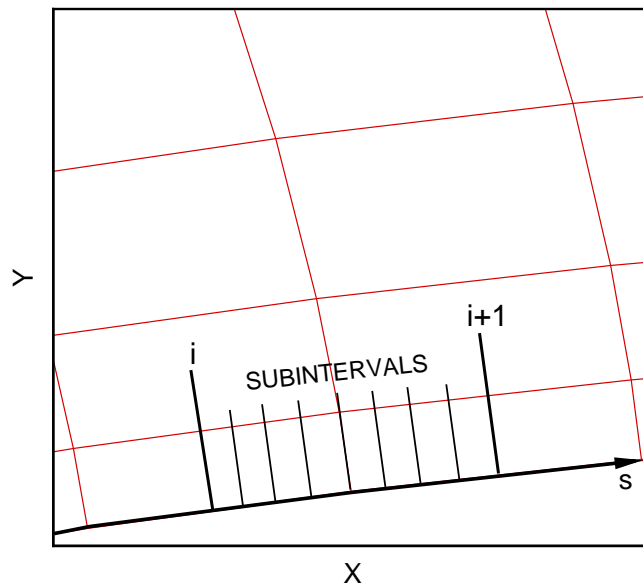


Figure 4.1: Boundary layer main stations and subintervals

spatial stations in the boundary layer. The algorithm starts with the known values for θ , H , C_τ at the starting station. Also, the values from the inviscid solver for both stations are known, namely values at the boundary layer edge Ma_e , u_e , ρ_e and du_e/ds . In the second and the subsequent steps of Runge-Kutta method the variable H^* is known value instead of H . This is because the derivative dH^*/ds is known, by which the increment of H^* at the interval midpoint (2. and 3. RK step) and the interval end (4. RK step) is obtained. As for the other closure relationships the value of H_k is required, that variable have to be calculated from the relationships (4.18) and (4.25) for laminar and turbulent flow respectively. As the variable H_k can not be explicitly expressed, the iterative procedure for the determination of H_k from (4.18) and (4.25) is employed, namely the bisection method. After one cycle of Runge-Kutta method, the values of boundary layer variables at the subsequent station is obtained.

In the whole integration procedure the transition method e^n is implemented. The method determines the position of transition, and according to this corresponding relationships for laminar or turbulent flow are employed. The transition method is described in the section 4.5.

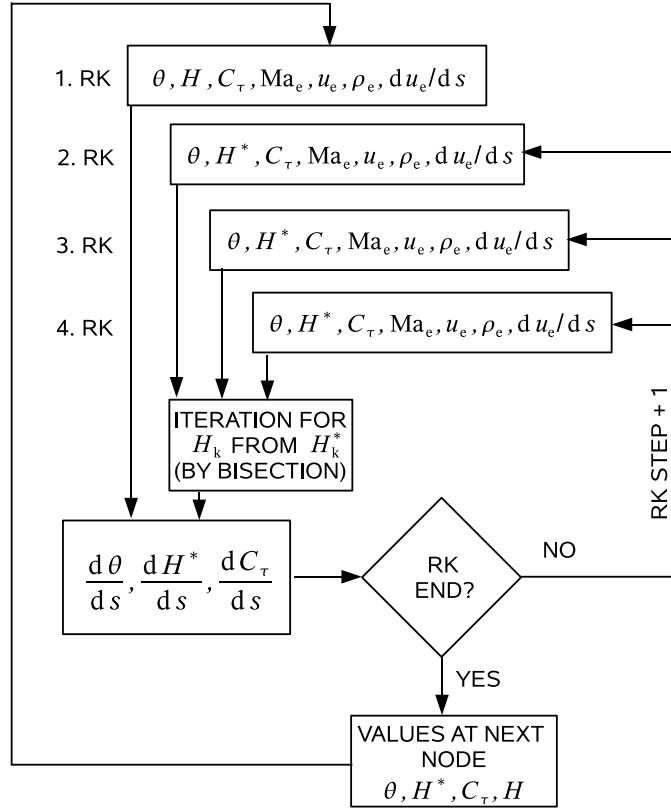


Figure 4.2: The algorithm for the integration of boundary layer equations

4.5. Transition

The method for determination of the onset of transition is derived from a spatial amplification theory based on Orr-Sommerfeld equation [35]. This method is also known as e^n method. The Orr-Sommerfeld equation describes the growth and breakdown of the disturbances in the shear layers. The growth of these disturbances is responsible for the onset of the transition in the boundary layers. The method determines the amplitude of the disturbances by the integration of disturbance growth rate, from the point of instability. The transition occurs when the amplitude grows by more than a factor $e^n = e^9$. The exponent n can be different from 9, actually it can vary between 7 and 11 depending mainly on free stream turbulence and surface roughness [14].

In [14] the equation for the amplification ratio n is derived:

$$\frac{dn}{ds}(H, \theta) = \frac{dn}{dRe_\theta}(H) \frac{m(H) + 1}{2} l(H) \frac{1}{\theta} \quad (4.37)$$

where

$$\frac{dn}{d\text{Re}_\theta} = 0.01\sqrt{\{2.4H - 3.7 + 2.5\tanh[1.5(H - 3.1)]\}^2 + 0.25} \quad (4.38)$$

$$m(H) = \frac{s}{u_e} \frac{du_e}{ds} = \left[0.058 \frac{(H - 4)^2}{H - 1} - 0.068 \right] \frac{1}{l(H)} \quad (4.39)$$

$$l(H) = \frac{\rho_e u_e \theta^2}{\mu_e s} = \frac{6.45H - 14.07}{H^2} \quad (4.40)$$

The amplification ratio n is a function of s , and the equation (4.37) can be integrated downstream from the point of instability s_{cr} :

$$n(s) = \int_{s_{\text{cr}}}^s \frac{dn}{ds} ds \quad (4.41)$$

At the position of instability s_{cr} the Reynolds number referenced by momentum thickness Re_θ is equal to its critical value $\text{Re}_\theta = \text{Re}_{\theta_0}$. This critical value can be calculated from the following expression:

$$\log_{10} \text{Re}_{\theta_0} = \left(\frac{1.415}{H - 1} - 0.489 \right) \tanh \left(\frac{20}{H - 1} - 12.9 \right) + \frac{3.295}{H - 1} + 0.440 \quad (4.42)$$

The integration of the equation (4.37) is finished when the amplification ration reaches the value $n = 9$, and then turbulent formulation of boundary layer equations is active. The changeover to the turbulent flow is made suddenly without gradual transition. The changeover from laminar to turbulent correlations has a little effect on the overall development of the boundary layer [14].

5 Results

In this chapter numerical method results will be presented. The main goal of presented test cases is to demonstrate that contour pressure determination by incorporation of transpiration velocity into momentum equation works and gives comparable results. Also, here will be shown that unsteady viscous-inviscid coupling gives results that are comparable with RANS solution and experimental data. All test cases calculations were performed on computer with two processors each at 2.4 GHz and 4 GB RAM. Complete source code is made in Fortran 95. First, computational grid will be presented and also grid convergence for NACA0012 airfoil will be performed. It is assumed that similar convergence results will be obtained for NLR7301 and NACA64A010 airfoils, which are also used for evaluation in this work.

The steady results were made for three types of airfoils, namely NACA0012, NACA64A010 and NLR7301. These airfoils have different character of pressure distribution and shock wave intensity, and this is a challenge to presented viscous-inviscid computational method. The steady test cases were selected from experimental datasets to cover transonic and subsonic compressible flow. The test cases without strong shock wave were used to show good performance of transition prediction algorithm. The unsteady results were made for two types of airfoils, NACA 0012 and NACA64A010. These unsteady test cases were selected from experimental datasets to cover appearance of strong shock wave.

5.1. Computational Grid

For all numerical calculations of inviscid flow model the structured grids of C-type are used. All grids are generated by the computational code developed in the Institute for aeroelasticity in Göttingen, which is part of DLR organization (Deutsches Zentrum für Luft- und Raumfahrt). The grid generation is performed by the solution of Poisson's equation according to Steger and Sorenson [36]. Details of this elliptic grid generator can be found in [37] and [38]. The grid is generated with the perpendicularity condition of coordinate lines on the airfoil contour and also on the outer domain boundary. This condition simplifies the application of boundary condition equation on airfoil, and facilitates the numerical calculations. Between many parameters used in the grid generation it has to be mentioned that the parameter for first and last control volume height in η direction is 0.5 and 70 percent respectively. Such setting is used for each generated grid.

An example of 2D C-type grid of NACA0012 airfoil, which is generated by elliptic grid generator, is presented in Fig. 5.1. The close view of the airfoil contour is shown in Fig. 5.2.

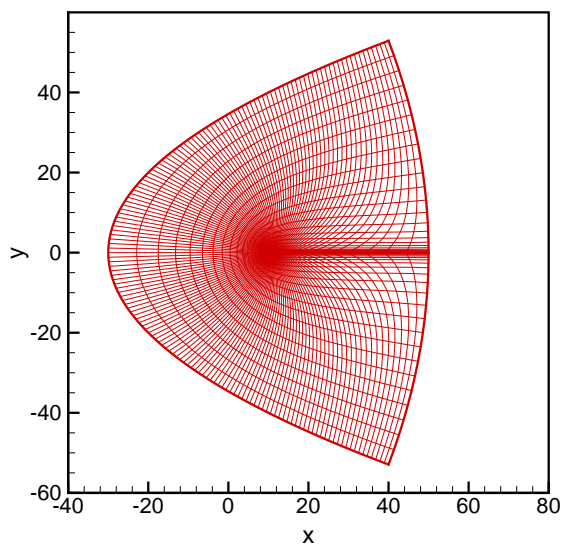


Figure 5.1: Computational grid around airfoil NACA0012 obtained by elliptic grid generator

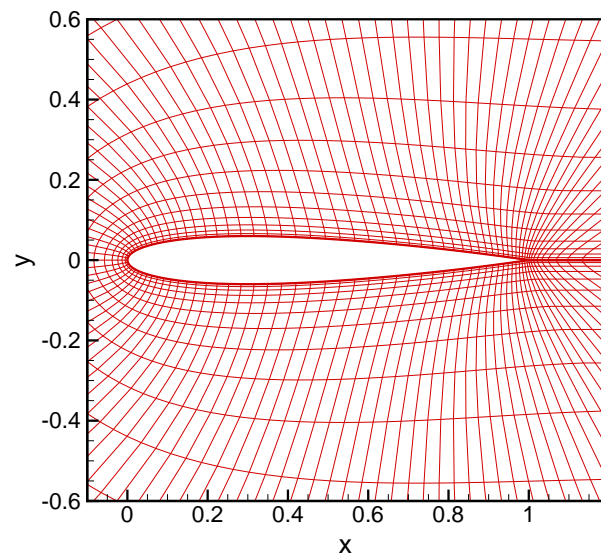


Figure 5.2: Close view of grid around airfoil NACA0012 contour

5.2. Grid Convergence

In this section a series of solution convergence tests for several different computational grids were made, for steady and also for unsteady cases. Convergence tests were made with inviscid solver for different grid densities and for different distances from airfoil to outer domain boundary. On the basis of these tests, appropriate grid density and distance of outer domain boundary from airfoil were chosen, in order to give grid independent solution taking into account required level of accuracy of the method. With such selected grid the subsequent numerical results were obtained. The test is conducted on five different grid densities and three distances between airfoil and outer domain boundary, according to table 5.1.

Table 5.1: Tested computational grids

NUMBER OF CONTROL VOLUMES	DISTANCE OF AIRFOIL TO OUTER DOMAIN BOUNDARY
GRID 100X30; 100 control volumes in ξ direction 30 control volumes in η direction	10 chord lengths
	40 chord lengths
	80 chord lengths
GRID 160X30; 160 control volumes in ξ direction 30 control volumes in η direction	10 chord lengths
	40 chord lengths
	80 chord lengths
GRID 160X60; 160 control volumes in ξ direction 60 control volumes in η direction	10 chord lengths
	40 chord lengths
	80 chord lengths
GRID 240X60; 240 control volumes in ξ direction 60 control volumes in η direction	10 chord lengths
	40 chord lengths
	80 chord lengths
GRID 320X60; 320 control volumes in ξ direction 60 control volumes in η direction	10 chord lengths
	40 chord lengths
	80 chord lengths

In Figs. 5.3, 5.5, 5.7, 5.9 and 5.11 the convergence tests of normal force coefficient are presented for steady flow solutions around airfoil NACA0012. Calculations were performed for Mach number $Ma = 0.77$ at angle of attack $\alpha = 1^\circ$, and for grid densities and distances between airfoil and outer domain boundary according to table 5.1. The steady solution is obtained by unsteady calculation of non-moving airfoil within time of nine unsteady periods. Normal force coefficient is obtained by integration of countour

pressure around airfoil, and represents pressure force perpendicular to airfoil chord. Normal force coefficient is calculated according to the following expression:

$$c_n = \int_0^1 (C_{pL} - C_{pU}) d\left(\frac{x}{c}\right) \quad (5.1)$$

where C_{pL} is pressure coefficient on lower side, C_{pU} is pressure coefficient on upper side of airfoil, c airfoil chord and x is local coordinate going from leading edge along airfoil chord.

In Figs. 5.4, 5.6, 5.8, 5.10 and 5.12 the solution relative error for grids with distances 10 and 40 chord lengths from airfoil to outer domain boundary is presented. The relative error is difference between solutions for the grids with 10 and 40 chord lengths and the grid with 80 chord lengths to outer boundary. Each figure represents different grid density according to table 5.1. In these figures the difference is represented as percent of the grid with 80 chord lengths to outer boundary.

In Figs. 5.3, 5.4, 5.5, 5.6, 5.7, 5.8, 5.9, 5.10, 5.11 and 5.12 the solutions and solution errors for the grid with 10 chord lengths show similar nature independent of the grid densities qualitatively and also quantitatively. The steady solution for normal force coefficient, for grids with outer boundary at distance 10 airfoil chords and all presented grid densities, has deviation about 10 percent relative to solutions for grids with outer boundary at distance 40 and 80 airfoil chords. The solution for distance 40 chord lengths show small deviation, smaller than 3 percent, for grid densities 100X30 and 160X30. For the grids 160X60, 240X60 and 320X60 and the same distance of 40 chord lengths, the solution show negligible difference, smaller than 1 percent. Variation of computational grid density gives approximately equal value of normal force coefficient in steady flow, for one distance of outer domain boundary. The bigger influence on the converged steady solution has the number of control volumes in direction of η coordinate.

From Figs. 5.3 to 5.12 it can be concluded that steady numerical calculations are grid independent for grids with distance of outer boundary from the airfoil greater than 40 airfoil chords. From the same figures it can be concluded that steady solution achieves its constant value with grids that have 60 and more control volumes in direction of η coordinate. Taking into account that the method developed in this work should give results that are comparable with high accuracy methods but should give it in the reasonable time, the selected grid for steady calculations is the grid with 160 control volumes in ξ direction, 60 control volumes in η direction and distance of 40 chord lengths

from airfoil to outer domain boundary.

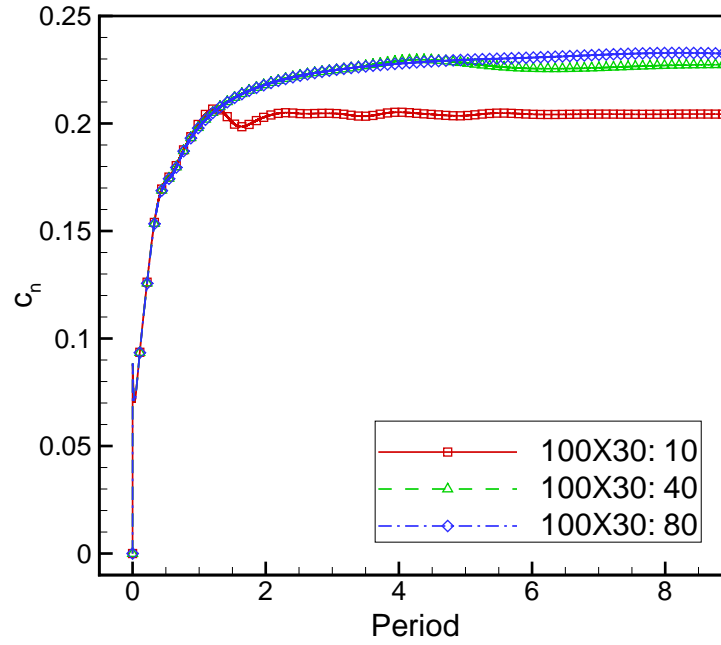


Figure 5.3: Grid 100X30; grid convergence test for steady solution for NACA0012 airfoil at $\alpha = 1^\circ$, $Ma = 0.77$; 10, 40, 80 are chord lengths from airfoil to outer boundary

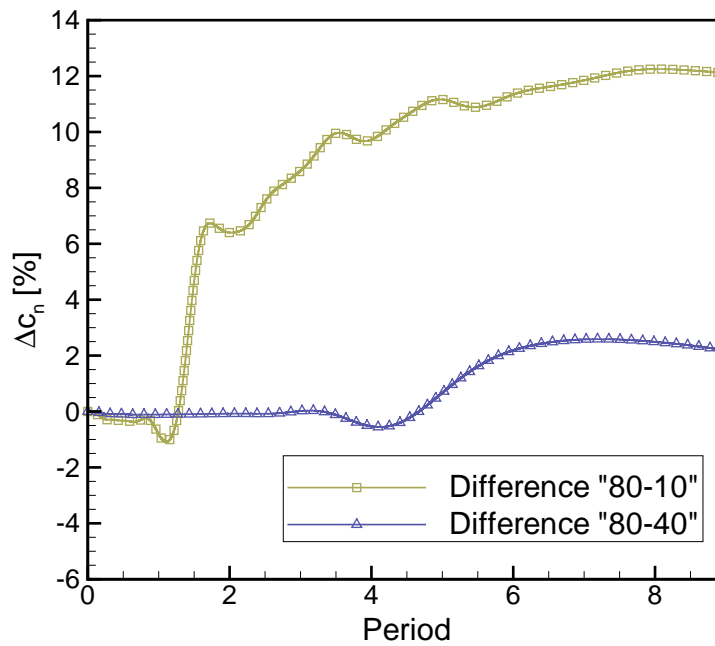


Figure 5.4: Grid 100X30; difference between solutions for distances 10 and 40 chord lengths and solution for distance 80 chord lengths, in percent of constant finest solution (80 chord lengths); NACA0012 airfoil at $\alpha = 1^\circ$, $Ma = 0.77$

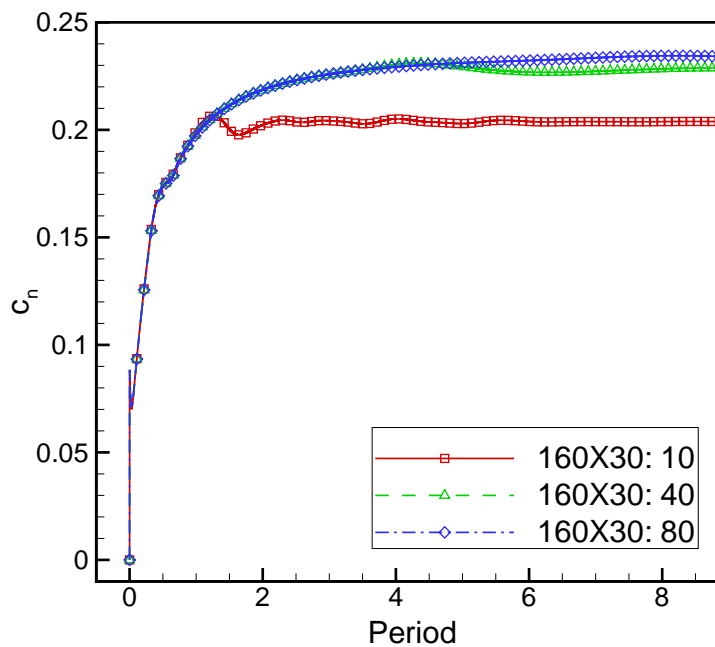


Figure 5.5: Grid 160X30; grid convergence test for steady solution for NACA0012 airfoil at $\alpha = 1^\circ$, $Ma = 0.77$; 10, 40, 80 are chord lengths from airfoil to outer boundary

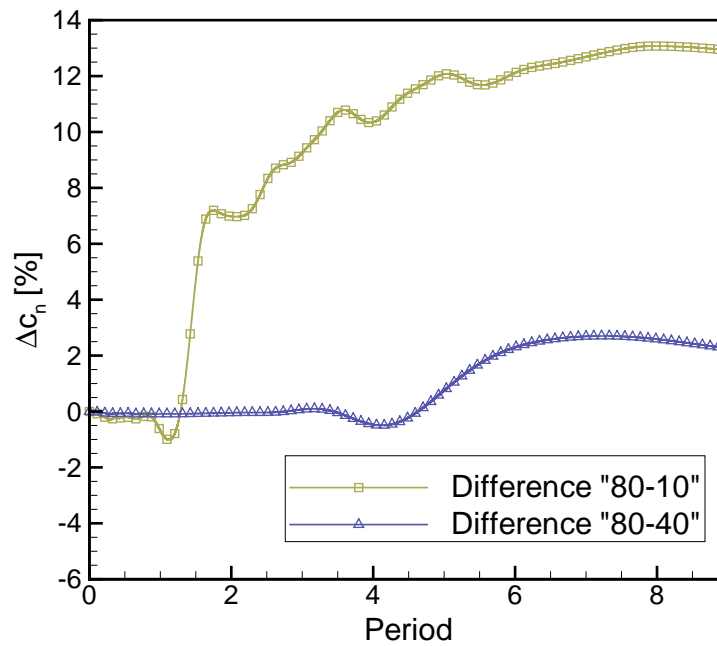


Figure 5.6: Grid 160X30; difference between solutions for distances 10 and 40 chord lengths and solution for distance 80 chord lengths, in percent of constant finest solution (80 chord lengths); NACA0012 airfoil at $\alpha = 1^\circ$, $Ma = 0.77$

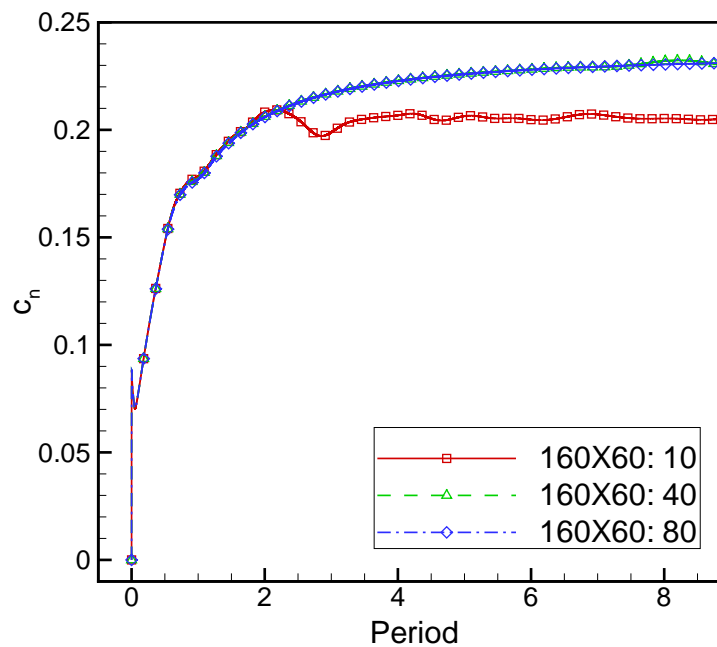


Figure 5.7: Grid 160X60; grid convergence test for steady solution for NACA0012 airfoil at $\alpha = 1^\circ$, $Ma = 0.77$; 10, 40, 80 are chord lengths from airfoil to outer boundary

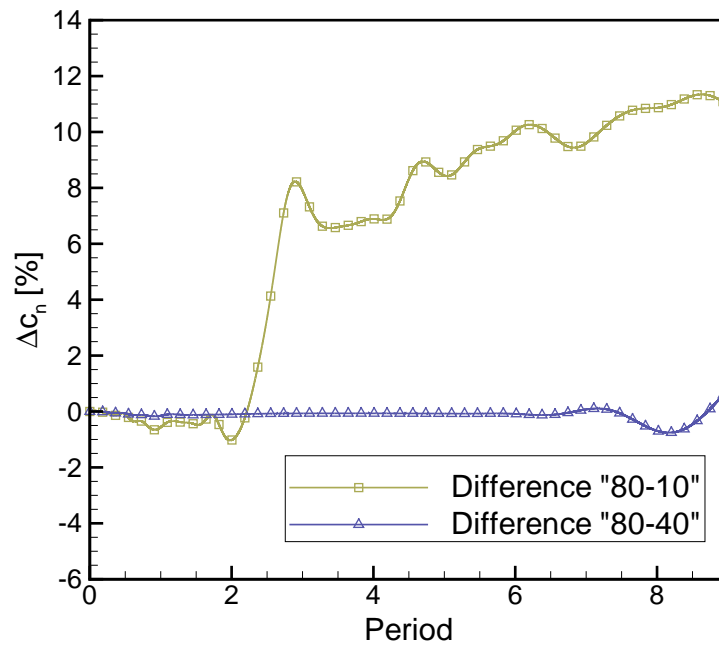


Figure 5.8: Grid 160X60; difference between solutions for distances 10 and 40 chord lengths and solution for distance 80 chord lengths, in percent of constant finest solution (80 chord lengths); NACA0012 airfoil at $\alpha = 1^\circ$, $Ma = 0.77$

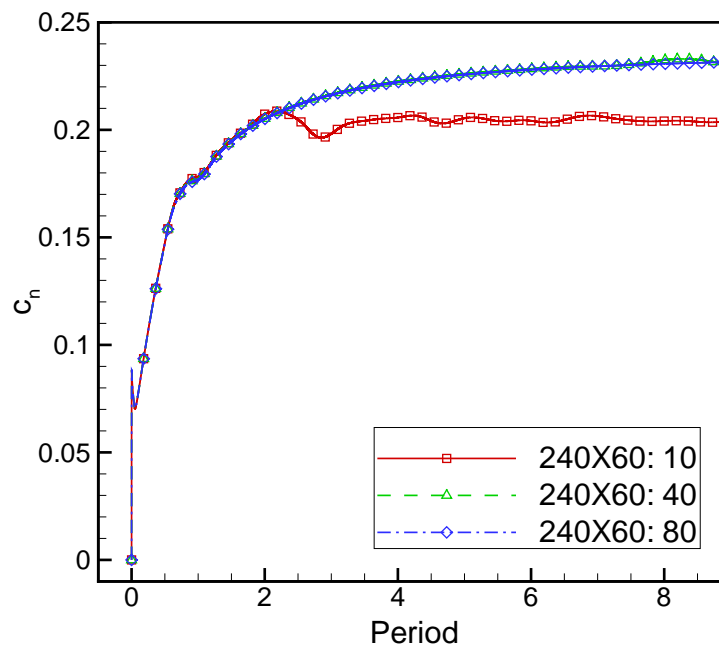


Figure 5.9: Grid 240X60; grid convergence test for steady solution for NACA0012 airfoil at $\alpha = 1^\circ$, $Ma = 0.77$; 10, 40, 80 are chord lengths from airfoil to outer boundary

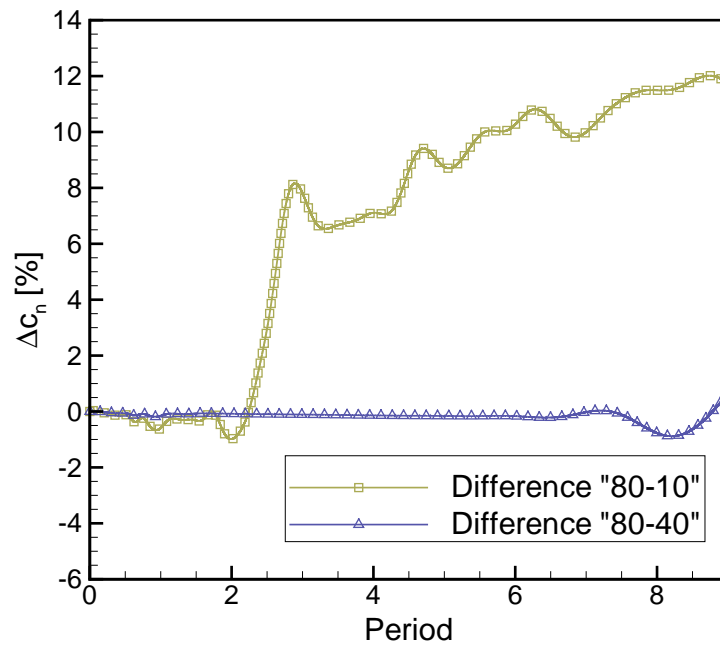


Figure 5.10: Grid 240X60; difference between solutions for distances 10 and 40 chord lengths and solution for distance 80 chord lengths, in percent of constant finest solution (80 chord lengths); NACA0012 airfoil at $\alpha = 1^\circ$, $Ma = 0.77$

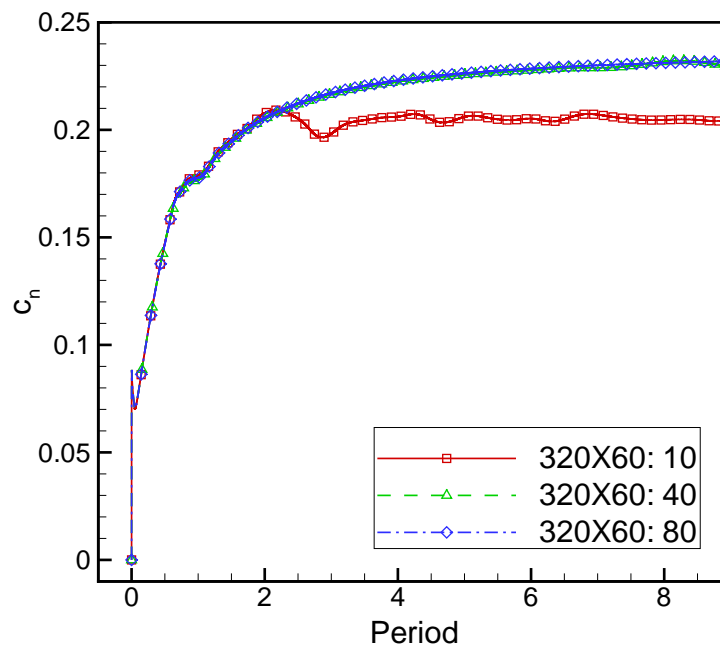


Figure 5.11: Grid 320X60; grid convergence test for steady solution for NACA0012 airfoil at $\alpha = 1^\circ$, $Ma = 0.77$; 10, 40, 80 are chord lengths from airfoil to outer boundary

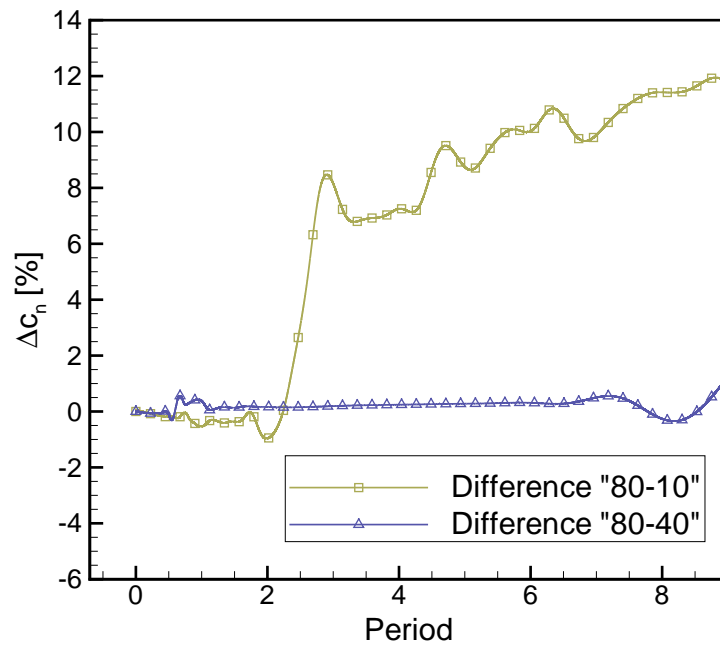


Figure 5.12: Grid 320X60; difference between solutions for distances 10 and 40 chord lengths and solution for distance 80 chord lengths, in percent of constant finest solution (80 chord lengths); NACA0012 airfoil at $\alpha = 1^\circ$, $Ma = 0.77$

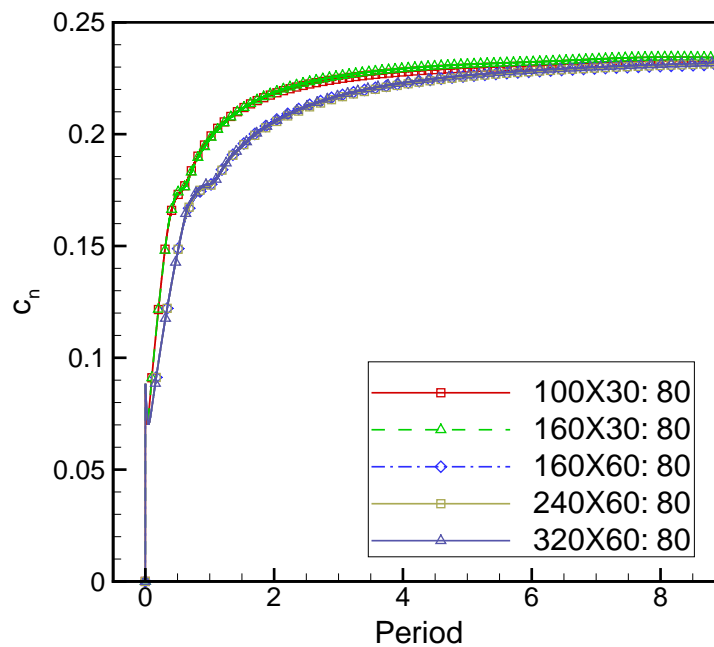


Figure 5.13: Grid convergence test for different grid densities for distance of 80 chord lengths from outer domain boundary to airfoil; NACA0012 airfoil at $\alpha = 1^\circ$, $Ma = 0.77$

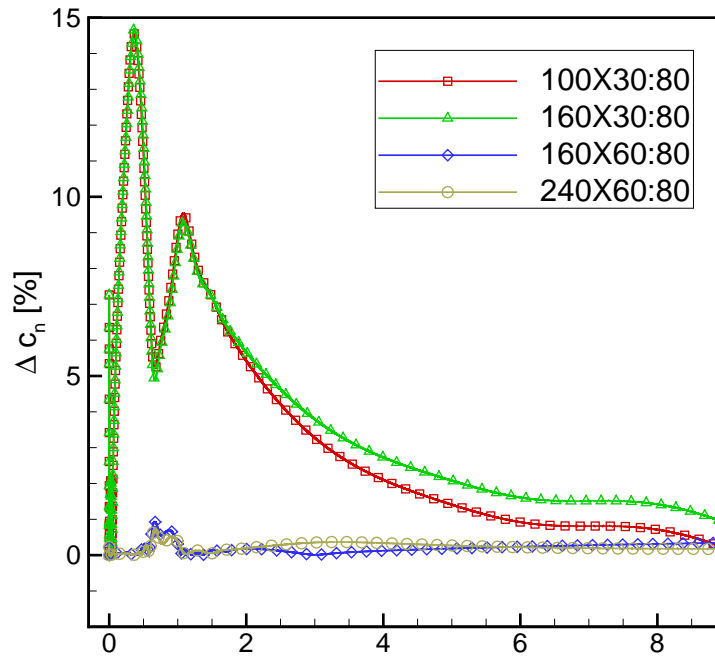


Figure 5.14: Differences between solutions obtained by grids stated in the figure's legend and grid 320X60 with 80 chord lengths from outer domain boundary to airfoil, for NACA0012 at $\alpha = 1^\circ$, $Ma = 0.77$

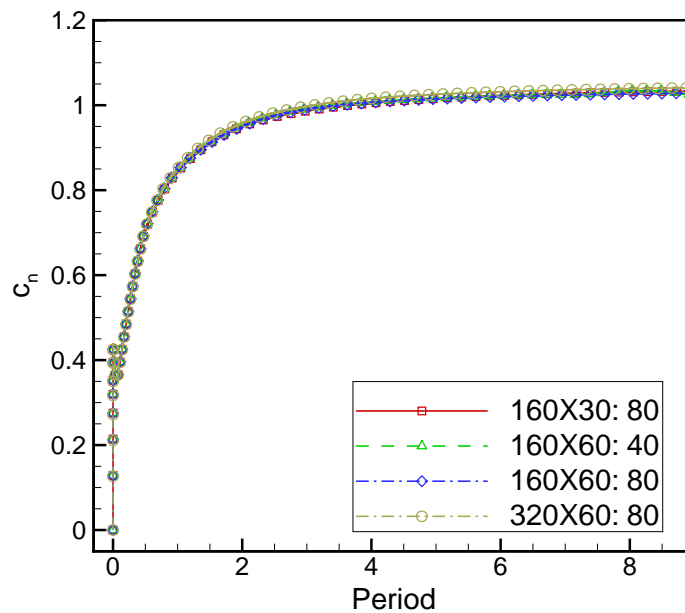


Figure 5.15: Grid convergence test for NACA0012 airfoil at $\alpha = 5^\circ$, $Ma = 0.77$

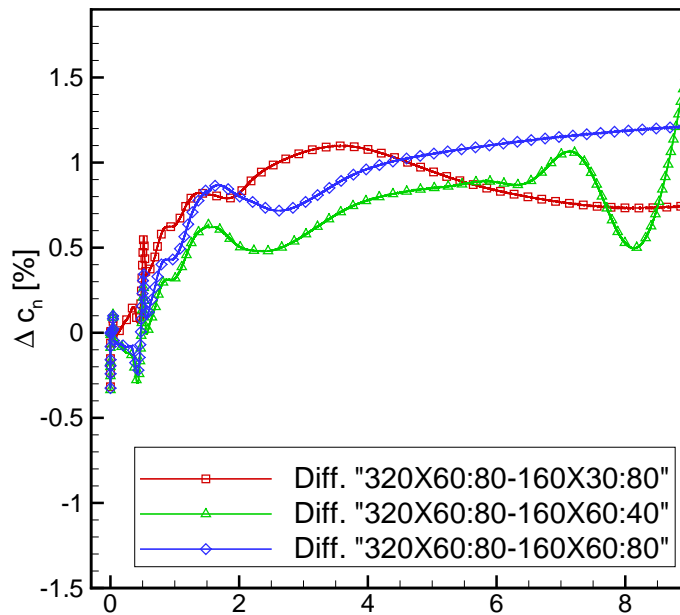


Figure 5.16: Differences between solutions obtained by grids stated in the figure's legend and grid 320X60 with 80 chord lengths from outer domain boundary to airfoil, for NACA0012 at $\alpha = 5^\circ$, $Ma = 0.77$

In table 5.2 the steady converged results from Figs. 5.3 - 5.12 are summarized. In the table the normal force coefficients are presented for grids with different number of control volumes and different distances from airfoil to outer boundary domain. The numerical values of normal force coefficients, for the same distance of outer domain boundary and for different grid densities, are approximately equal and their maximum relative difference is 1.7% (obtained for the grid with 40 chord lengths to outer domain boundary). Now for the sake of results comparison it can be assumed that the presented numerical values are the most accurate for the furthest outer domain boundary with the same grid density. Also, it is shown that the result accuracy does not significantly changes for switching between the presented grid densities, at the same distance to outer boundary. Therefore, the numerical values for normal force coefficients are compared with the grid with the furthest outer domain boundary. Relative difference, of normal force coefficient, between the grids with 40 and 80 airfoil chords to outer domain boundary equals 3.1%. The same relative difference between the grids with 10 and 80 airfoil chords to outer domain boundary equals 15.3%. Therefore, the conclusion can be drawn that, for the results of normal force coefficient in inviscid flow, the grid density does not

Table 5.2: Converged normal force coefficient results for steady cases

Grid size	Distance to outer domain boundary	c_n
100X30	10 chord lengths	0.204
	40 chord lengths	0.227
	80 chord lengths	0.232
160X30	10 chord lengths	0.203
	40 chord lengths	0.228
	80 chord lengths	0.234
160X60	10 chord lengths	0.205
	40 chord lengths	0.230
	80 chord lengths	0.231
240X60	10 chord lengths	0.204
	40 chord lengths	0.231
	80 chord lengths	0.232
320X60	10 chord lengths	0.204
	40 chord lengths	0.231
	80 chord lengths	0.232

play very important role but the distance to outer domain boundary does. The distance of 40 airfoil chords to outer domain boundary is sufficient for satisfactory solution. Although for the results of normal force coefficient in inviscid flow the grid density showed no important role, the grid density is important for accurate determination of shock position and intensity.

In Figs. from 5.17 to 5.26 unsteady flow solution for normal force coefficient are presented. All cases are calculated for inviscid flow at Mach number $Ma = 0.77$, mean angle of attack $\alpha_m = 0^\circ$, pitch amplitude $\alpha_o = 1^\circ$ and reduced frequency $\omega^* = 0.1$.

It can be noticed that unsteady flow solution for normal force coefficient adopt harmonic behavior already after two periods. Normal force coefficient value differs for

different distances of outer domain boundary from airfoil. Solution for the distance of 10 airfoil chords differs from the solution for 40 and 80 airfoil chords length in maximum value of normal force coefficient. Last two cases have practically equal values of normal force coefficient.

From the unsteady solutions for different grid densities in Figs. from 5.17 to 5.26, it can be noticed that there are no significant difference except smaller deviations at maximum values. The solution for smallest domain deviates from the solution for domains with distance of 40 and 80 airfoil chord lengths. Taking into account also grid convergence for steady cases, it can be concluded that the grid size 160X60 gives grid independent solution and is appropriate for further numerical calculations. Also, from the same figures of unsteady solution, it can be concluded that after second period of unsteady simulation the solution becomes periodic.

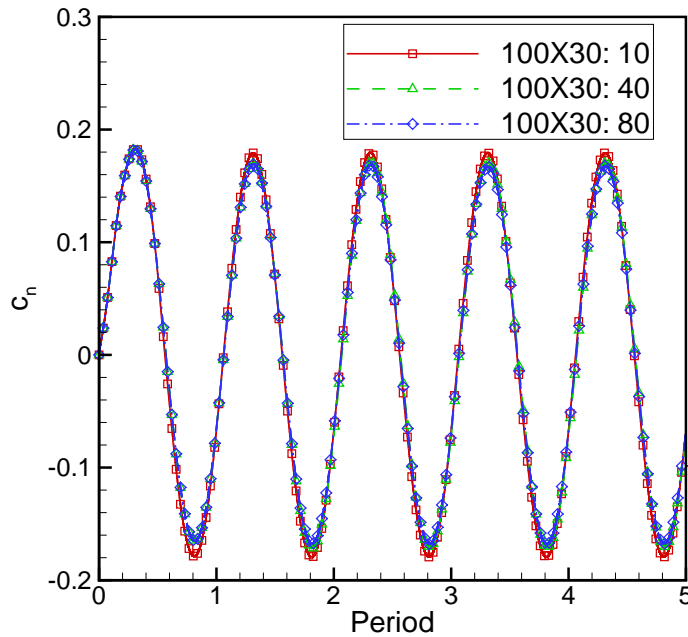


Figure 5.17: Grid 100X30; convergence test for unsteady solution; 10, 40 and 80 are chord lengths from airfoil to outer domain boundary; NACA0012 airfoil at $Ma = 0.77$, $\alpha_m = 0^\circ$, $\alpha_o = 1^\circ$

In table 5.3 the unsteady converged results from Figs. 5.17 - 5.26 are summarized. The unsteady normal force coefficient is presented in the form of complex number, namely as real and imaginary part according to the equation (5.5), which is equivalently applicable to the normal force coefficient. In this representation the real and imaginary parts

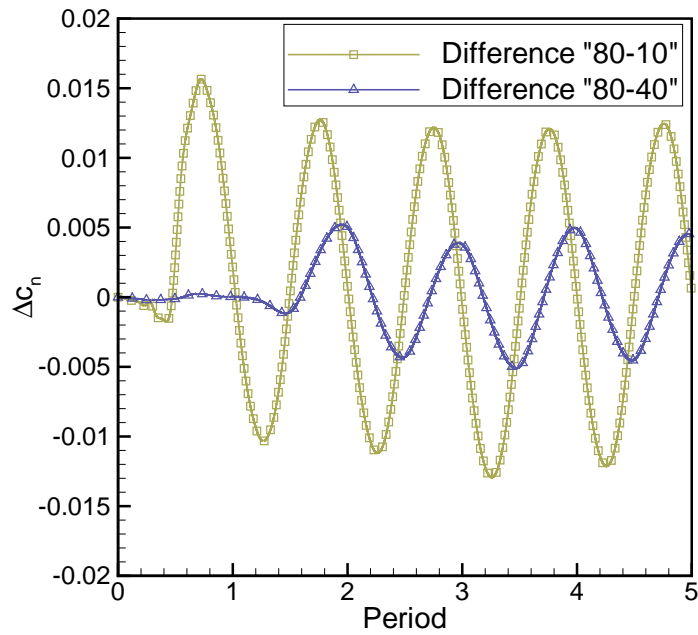


Figure 5.18: Grid 100X30; difference between solutions for distances 10 and 40 chord lengths and solution for distance 80 chord lengths; NACA0012 airfoil at $Ma = 0.77$, $\alpha_m = 0^\circ$, $\alpha_o = 1^\circ$

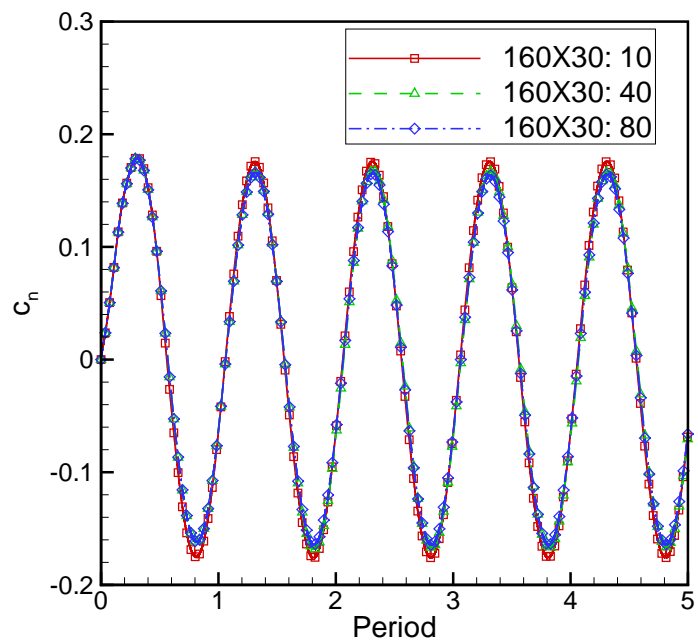


Figure 5.19: Grid 160X30; convergence test for unsteady solution; 10, 40 and 80 are chord lengths from airfoil to outer domain boundary; NACA0012 airfoil at $Ma = 0.77$, $\alpha_m = 0^\circ$, $\alpha_o = 1^\circ$

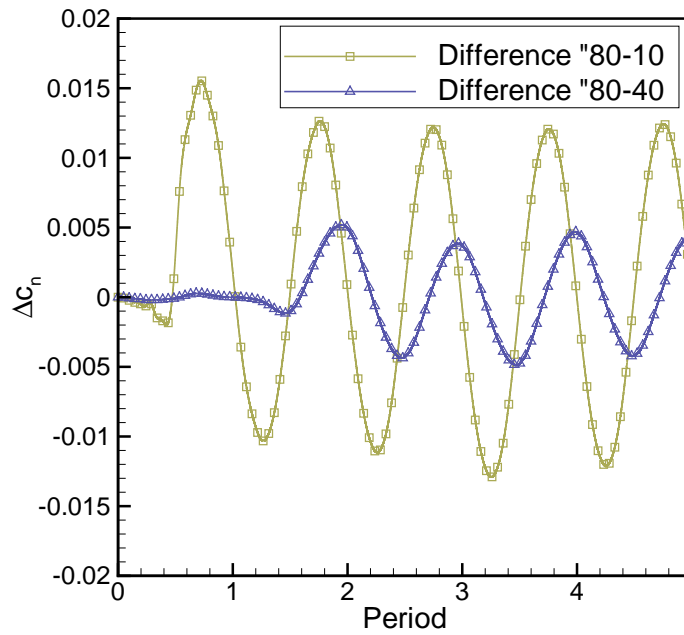


Figure 5.20: Grid 160X30; difference between solutions for distances 10 and 40 chord lengths and solution for distance 80 chord lengths; NACA0012 airfoil at $Ma = 0.77$, $\alpha_m = 0^\circ$, $\alpha_o = 1^\circ$

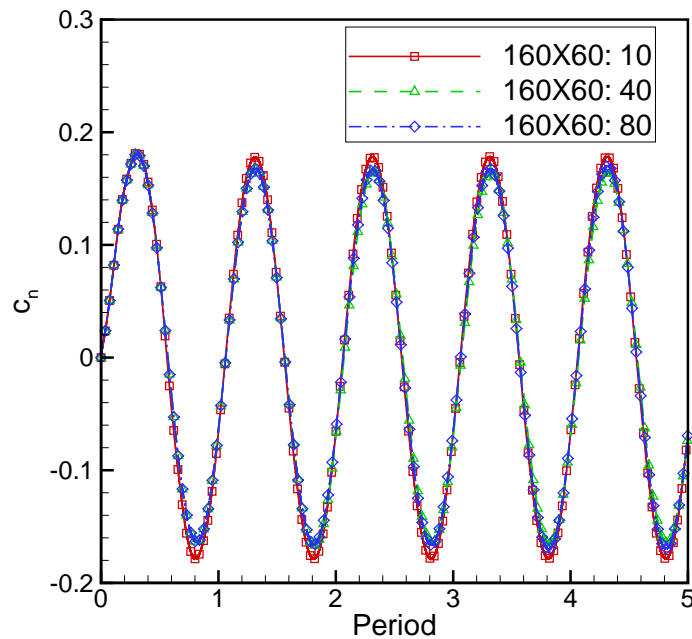


Figure 5.21: Grid 160X60; convergence test for unsteady solution; 10, 40 and 80 are chord lengths from airfoil to outer domain boundary; NACA0012 airfoil at $Ma = 0.77$, $\alpha_m = 0^\circ$, $\alpha_o = 1^\circ$

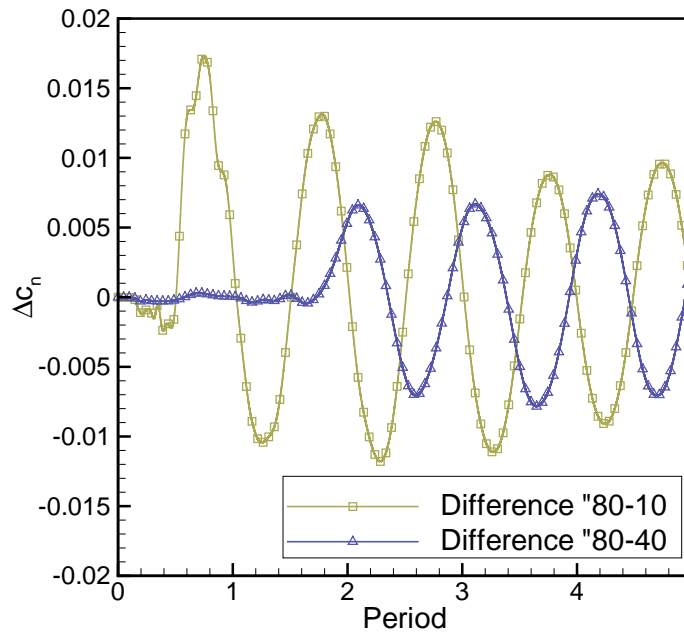


Figure 5.22: Grid 160X60; difference between solutions for distances 10 and 40 chord lengths and solution for distance 80 chord lengths; NACA0012 airfoil at $Ma = 0.77$, $\alpha_m = 0^\circ$, $\alpha_o = 1^\circ$

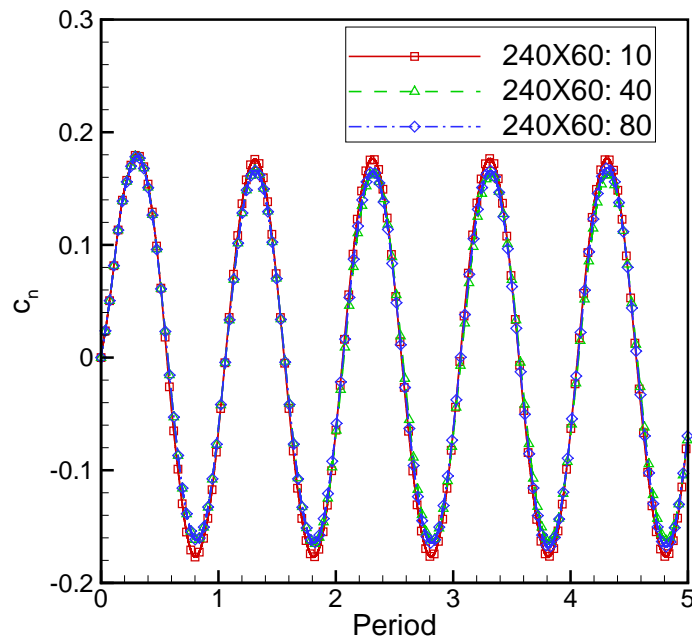


Figure 5.23: Grid 240X60; convergence test for unsteady solution; 10, 40 and 80 are chord lengths from airfoil to outer domain boundary; NACA0012 airfoil at $Ma = 0.77$, $\alpha_m = 0^\circ$, $\alpha_o = 1^\circ$

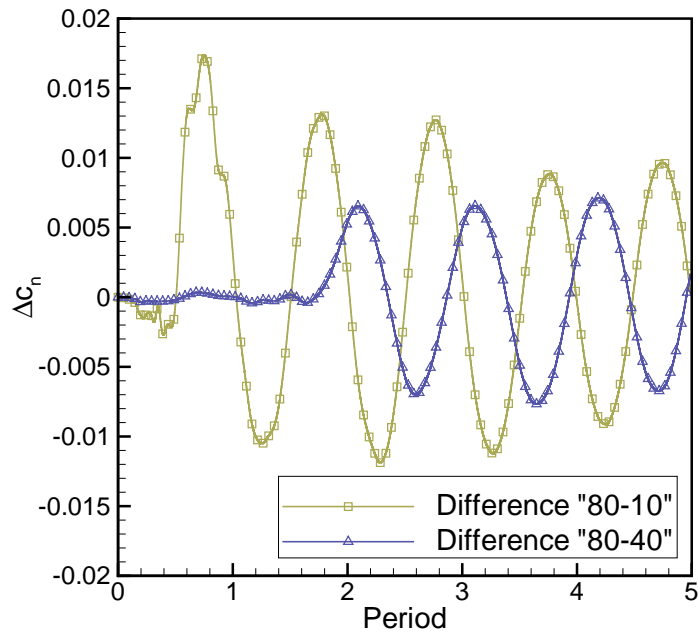


Figure 5.24: Grid 240X60; difference between solutions for distances 10 and 40 chord lengths and solution for distance 80 chord lengths; NACA0012 airfoil at $Ma = 0.77$, $\alpha_m = 0^\circ$, $\alpha_o = 1^\circ$

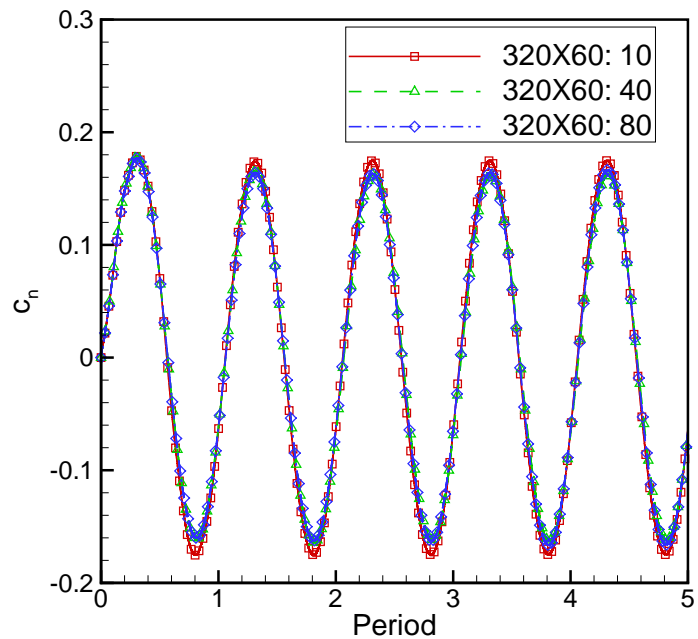


Figure 5.25: Grid 320X60; convergence test for unsteady solution; 10, 40 and 80 are chord lengths from airfoil to outer domain boundary; NACA0012 airfoil at $Ma = 0.77$, $\alpha_m = 0^\circ$, $\alpha_o = 1^\circ$

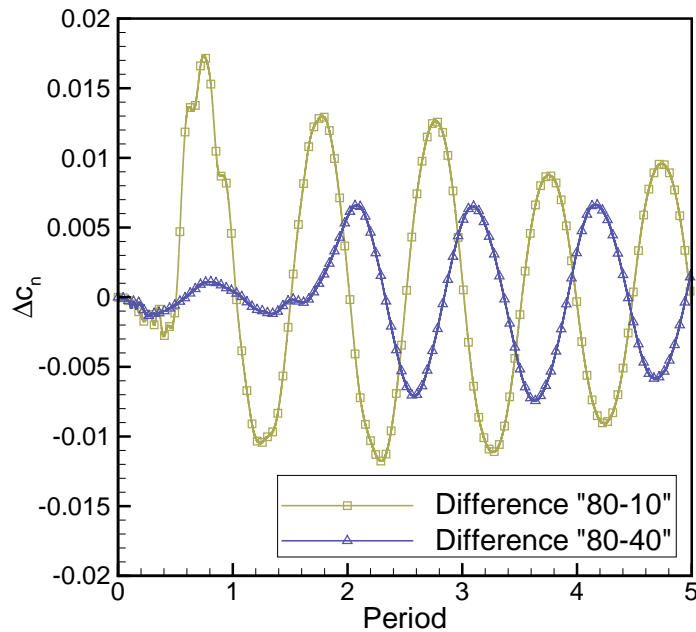


Figure 5.26: Grid 320X60; difference between solutions for distances 10 and 40 chord lengths and solution for distance 80 chord lengths; NACA0012 airfoil at $Ma = 0.77$, $\alpha_m = 0^\circ$, $\alpha_o = 1^\circ$

are not normed with amplitude of the angle of attack. The real parts of the unsteady normal force coefficient solution show the maximum relative difference of 6%, for all different grid densities and different distances from airfoil to outer domain boundary. The real part does not show some clear sign of ascending or descending values with respect to the increase or decrease of control volumes number or distance to outer domain. The imaginary parts of the unsteady normal force coefficients presented in table 5.3 show the maximum relative difference of 11% between all variations of grid densities and distances to outer domain boundary. The imaginary part for the same distance to outer boundary and for the different grid densities show smaller relative difference, maximum 5.7%. As the real part, the imaginary part also does not show some clear sign of ascending or descending values with respect to the increase or decrease of control volumes number or distance to outer domain.

Table 5.3: Converged normal force coefficient results for the unsteady cases

Grid size	Distance to outer domain boundary	Real (c_n)	Imag (c_n)
100X30	10 chord lengths	0.1668	-0.06602
	40 chord lengths	0.1547	-0.07123
	80 chord lengths	0.1541	-0.06652
160X30	10 chord lengths	0.1637	-0.06408
	40 chord lengths	0.1517	-0.06862
	80 chord lengths	0.1513	-0.06414
160X60	10 chord lengths	0.1657	-0.06606
	40 chord lengths	0.1491	-0.06943
	80 chord lengths	0.1563	-0.06648
240X60	10 chord lengths	0.1645	-0.06459
	40 chord lengths	0.1479	-0.06791
	80 chord lengths	0.1550	-0.06518
320X60	10 chord lengths	0.1612	-0.06779
	40 chord lengths	0.1474	-0.06738
	80 chord lengths	0.1535	-0.06419

5.3. Steady Results

Steady results are performed for three types of airfoils, namely NACA0012, NACA64A010 and NLR7301. These three airfoils have three different characteristic pressure distribution, and also there is available experimental data for these airfoils. The numerical results from viscous-inviscid method are compared with test cases from AGARD reports [39] and [40], and RANS code. The RANS code used throughout this work was Tau code [41] developed in DLR (Deutsches Zentrum fuer Luft- und Raumfahrt). The Tau code represents finite volume method solving Euler and Navier-Stokes equations on hybrid unstructured grid about complex geometries from low subsonic to the hypersonic flow. All calculations in Tau code were performed with the two-equation $k-\omega$ turbulence model. The flow in RANS calculations was solved as completely turbulent, without limiting the production of turbulence in the laminar part of boundary layer. The initial value of the ratio turbulent to laminar kinematic viscosity is prescribed for the whole flow region as also for the freestream, and was equal to the value much smaller than unity ($\nu_t/\nu \ll 1$). Test cases are chosen in such way to cover Mach numbers from lower limit of compressible flow to transonic flow region.

5.3.1. NACA0012 Airfoil

NACA0012 airfoil is symmetrical airfoil with 12% thickness (based on airfoil chord length). For this airfoil there are many experimental databases for steady and unsteady flow [39], and because of that it is very common in numerical codes testing. The other advantage of this airfoil is symmetrical property. Experimental data for symmetrical airfoil at zero angle of attack are not affected by wind tunnel walls interference due to lift.

In table 5.4 selected test cases for NACA0012 airfoil from experimental dataset in AGARD report [39] are presented. Three test cases at different Mach numbers are selected, which cover subsonic compressible flow with and without the appearance of shock waves.

Test case 1: NACA0012, $Ma = 0.504$, $Re = 2.93 \cdot 10^6$, $\alpha = 4.06^\circ$

In Fig. 5.27 steady results for NACA0012 airfoil are presented at Mach number $Ma = 0.504$, Reynolds number $Re = 2.93 \cdot 10^6$ and angle of attack $\alpha = 4.06^\circ$. This is compressible flow test case without shock wave occurrence. Experimental data are

Table 5.4: NACA0012 steady test cases

Test case	Ma	Re	α
1	0.504	$2.93 \cdot 10^6$	4.06°
2	0.756	$4.01 \cdot 10^6$	-0.01°
3	0.803	$4.09 \cdot 10^6$	0.05°

presented by triangles pointing up and down for upper and lower airfoil surface respectively. Viscous-inviscid method results are shown by full red line and RANS results are shown by dashed line. Transition region on upper and lower surface calculated by boundary layer method shows good agreement with experimental data. Slight pressure jump in transition region on upper surface follows the same occurrence in experimental data. This appearance is not seen in the RANS results because in the RANS solver the whole region is calculated as turbulent flow. Pressure coefficient distribution has good agreement with experimental data in the whole region except on the front part of airfoil where calculated pressure coefficient is underestimated, and this results in smaller normal force coefficient and lift coefficient. Complete pressure coefficient distribution shows slight shift which corresponds to experimental data for different angle of attack. This could be true because experimental data are not corrected for wind tunnel wall interference. Solution convergence criterion was that maximum pressure residual is reduced four orders of magnitude. Coupling method by transpiration velocity showed very unstable behavior, especially in presence of strong shock waves. Therefore under-relaxation method is used to reduce instability. The under-relaxation factor was set manually, and in majority test cases with non-monotonic convergence was set on values that are $0.1 \geq \beta \geq 0.001$. It was influenced mainly by the physics of the flow, namely separation bubble existence and great pressure jump at the trailing edge.

In Figs. 5.28 and 5.29 the results from boundary layer solver are presented for upper and lower side of airfoil, namely integral values: displacement thickness δ^* , momentum thickness θ and friction coefficient C_f . The displacement thickness and momentum thickness increase toward trailing edge, which represent boundary layer thickening and loss of momentum respectively. These curves show sudden jump at the position of boundary layer transition. These jumps correspond with jumps in the pressure coefficient distribution in Fig. 5.27. The growth of displacement thickness and momentum thickness

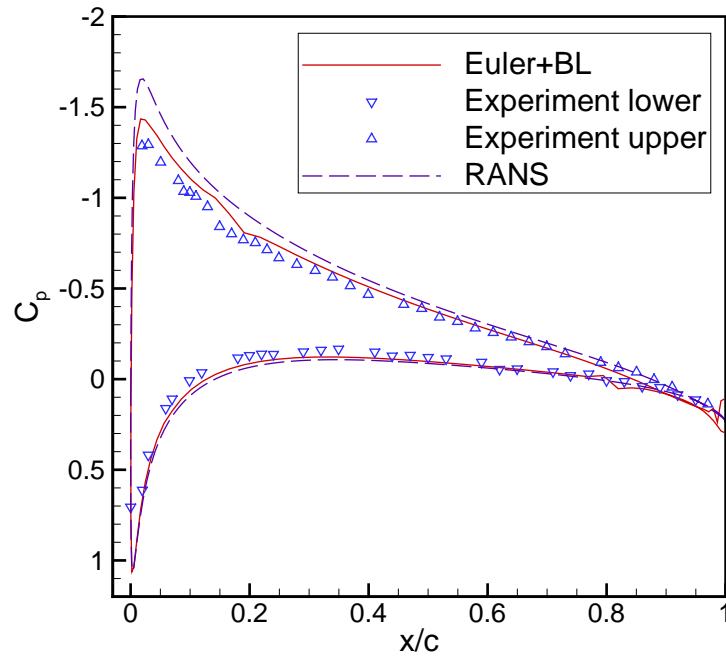


Figure 5.27: NACA0012 steady pressure coefficient distribution at $Ma = 0.504$, $Re = 2.93 \cdot 10^6$, $\alpha = 4.06^\circ$

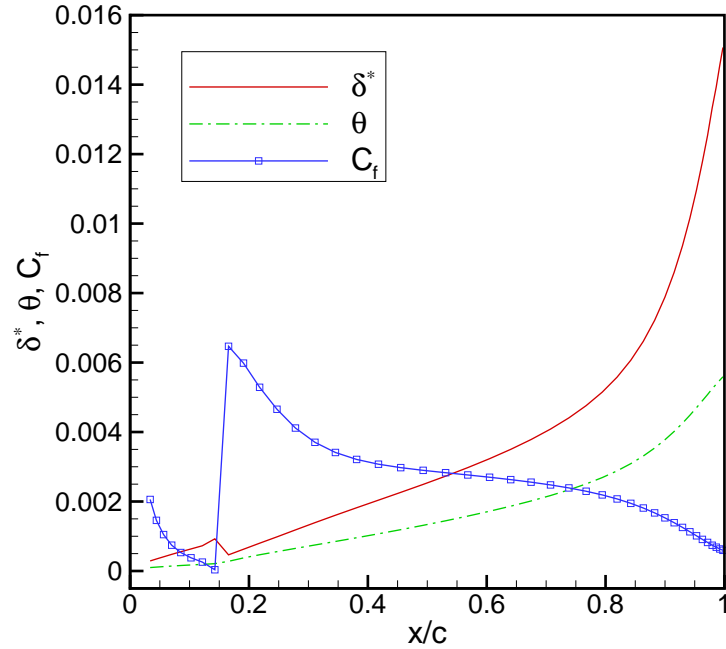


Figure 5.28: NACA0012 boundary layer integral values for upper surface at $Ma = 0.504$, $Re = 2.93 \cdot 10^6$, $\alpha = 4.06^\circ$

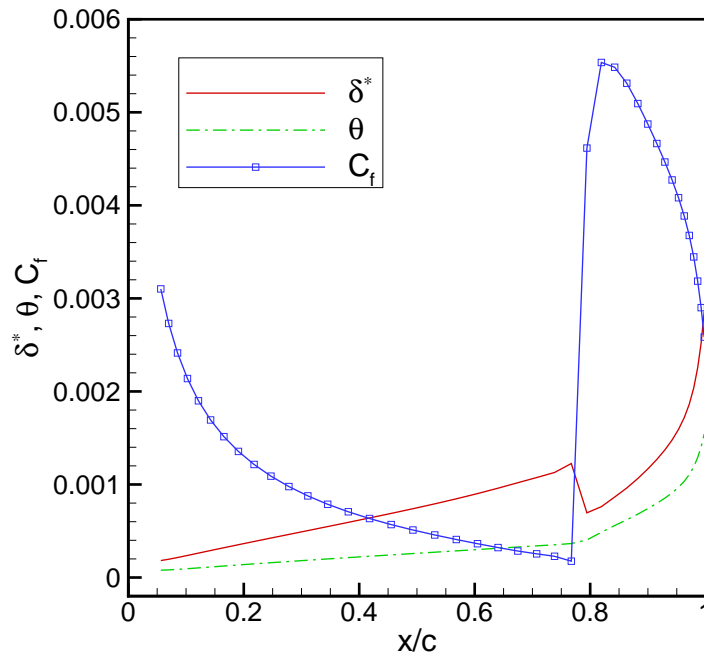


Figure 5.29: NACA0012 boundary layer integral values for lower surface at $Ma = 0.504$, $Re = 2.93 \cdot 10^6$, $\alpha = 4.06^\circ$

show higher rate of increase in turbulent flow region. The friction coefficient shows the same jump at the transition region with very small value before transition, which means very steep velocity profile in the boundary layer (close to separation).

Test case 2: NACA0012, $Ma = 0.756$, $Re = 4.01 \cdot 10^6$, $\alpha = -0.01^\circ$

In Figs. 5.30 and 5.31 calculated steady results and experimental data for NACA0012 airfoil are presented, for upper and lower surface respectively. These results are calculated at Mach number $Ma = 0.756$, Reynolds number $Re = 4.01 \cdot 10^6$ and angle of attack $\alpha = -0.01^\circ$. Practically this test case can be regarded as symmetrical test case. Results show good agreement with experimental data. Two little jumps of pressure coefficient on upper and lower side can be observed. First is because of weak shock wave, and second because of transition region existence in the boundary layer. Little deviations of RANS results from experimental data can be observed at weak shock wave position, while the viscous-inviscid method gives good results in this position. The viscous-inviscid method shows small deviations at the trailing edge of airfoil. It is shown that transition method (e^n method) accurately estimates transition region of boundary layer. In Figs. 5.30 and 5.31 RANS results are also presented for comparison, as results for higher order

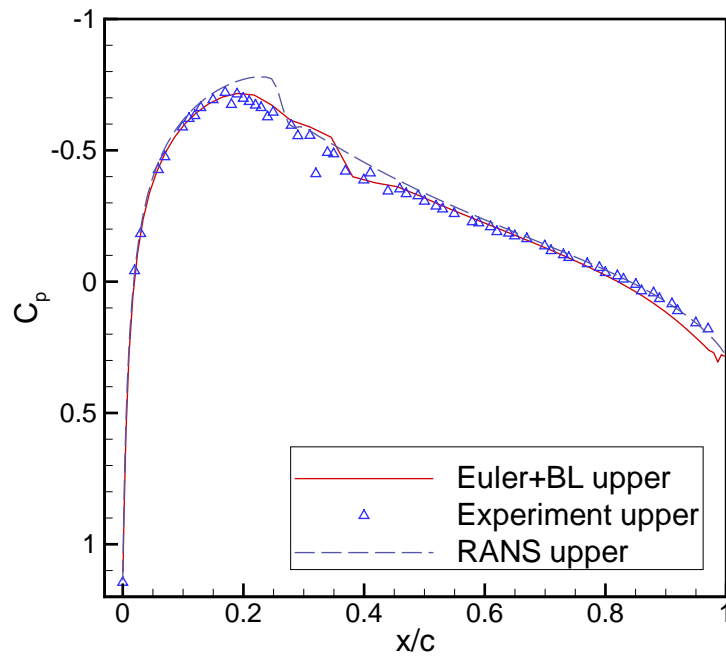


Figure 5.30: NACA0012 steady pressure coefficient distribution for upper surface at $Ma = 0.756$, $Re = 4.01 \cdot 10^6$, $\alpha = -0.01^\circ$

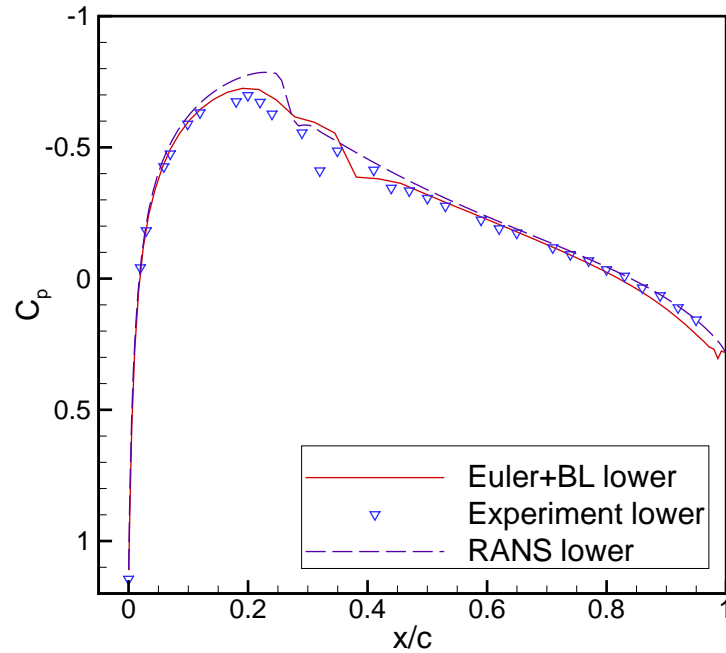


Figure 5.31: NACA0012 steady pressure coefficient distribution for lower surface at $Ma = 0.756$, $Re = 4.01 \cdot 10^6$, $\alpha = -0.01^\circ$

accuracy method. RANS results show stronger shock wave in a position of weak shock wave according to experimental data. It seems that RANS results calculated with the turbulent flow for whole region give too strong shock wave with respect to the experimental data. The reason for this can be in the steeper growth of displacement thickness in the turbulent boundary layer than in the laminar boundary layer. This leads to the compression in the outer inviscid flow which causes too soon shock wave appearance.

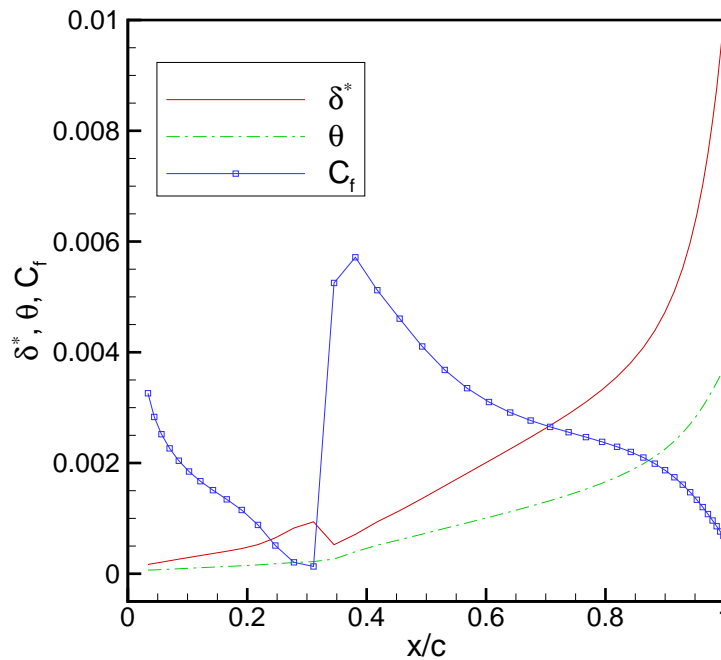


Figure 5.32: NACA0012 boundary layer integral values for lower surface at $Ma = 0.756$, $Re = 4.01 \cdot 10^6$, $\alpha = -0.01^\circ$

In Fig. 5.32 the values of displacement thickness δ^* , momentum thickness θ and friction coefficient C_f of boundary layer are shown, for the same NACA0012 test case at $Ma = 0.756$, $Re = 4.01 \cdot 10^6$ and $\alpha = -0.01^\circ$. These variables show jump at transition region at around 30% of airfoil chord for lower surface. The same is for upper surface which is not shown because of practically zero angle of attack and because the airfoil is symmetric one. Friction coefficient again shows the same behavior going toward zero (prior to separation) in laminar part of flow, and then experiencing positive jump in turbulent flow. The displacement thickness shows sudden drop in transition region, and then rapid growth in the turbulent region. The momentum thickness shows constant growth with higher rate of growth in turbulent flow.

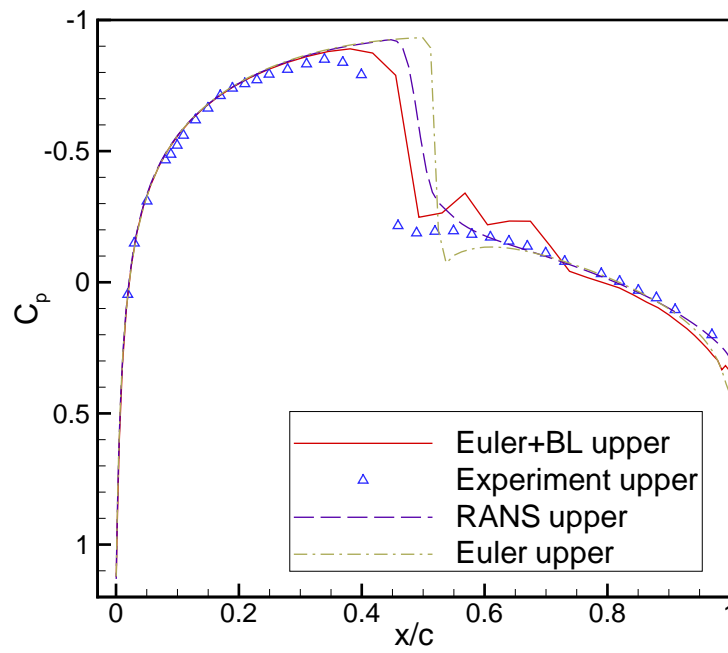


Figure 5.33: NACA0012 steady pressure coefficient distribution for upper surface at $Ma = 0.803$, $Re = 4.09 \cdot 10^6$ and $\alpha = 0.05^\circ$

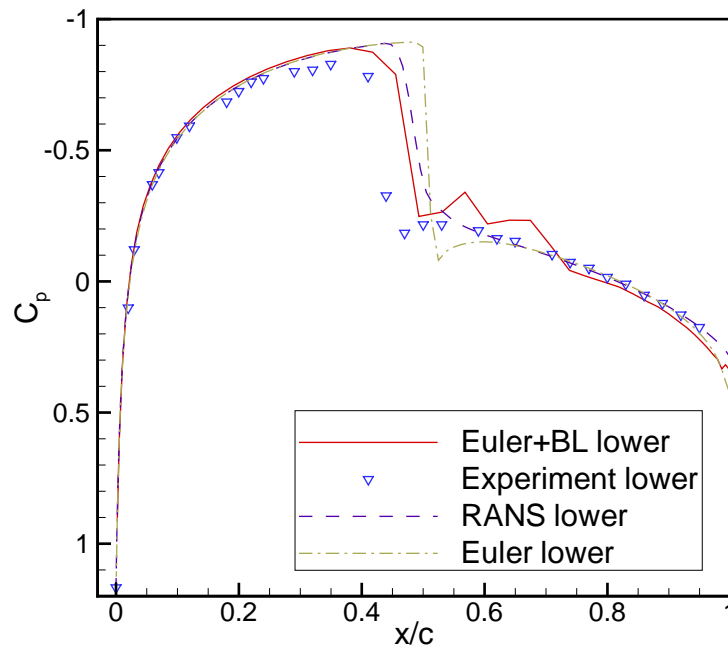


Figure 5.34: NACA0012 steady pressure coefficient distribution for lower surface at $Ma = 0.803$, $Re = 4.09 \cdot 10^6$ and $\alpha = 0.05^\circ$

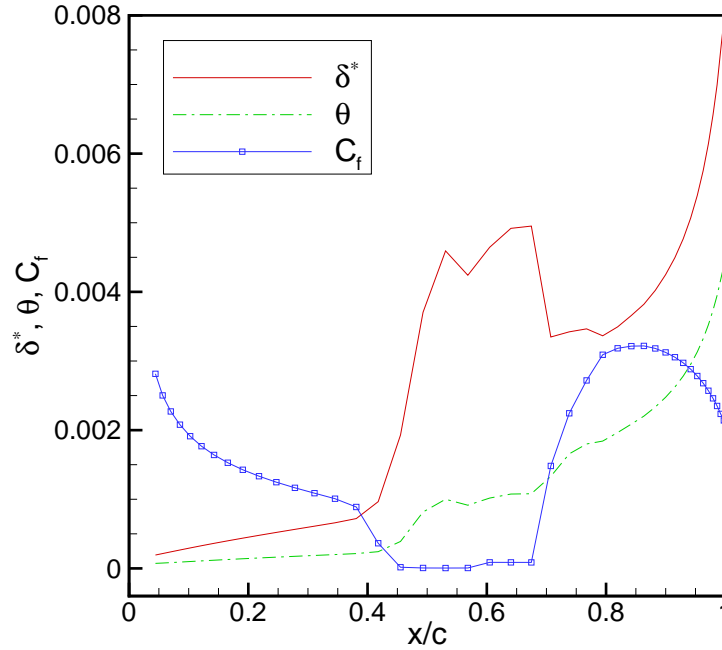


Figure 5.35: NACA0012 boundary layer integral values for lower side at $Ma = 0.803$, $Re = 4.09 \cdot 10^6$, $\alpha = 0.05^\circ$

Test case 3: NACA0012, $Ma = 0.803$, $Re = 4.09 \cdot 10^6$, $\alpha = 0.05^\circ$

In Figs. 5.33 and 5.34 NACA0012 airfoil steady results on upper and lower surface are presented. This test case is calculated for Mach number $Ma = 0.803$, Reynolds number $Re = 4.09 \cdot 10^6$ and angle of attack $\alpha = 0.05^\circ$. This case represents flow with strong shock wave and can practically be regarded as symmetrical. Results show the existence of strong shock wave at position 45% of the airfoil chord length from leading edge, which is in good agreement with experimental data. Viscous effects move the shock wave position toward leading edge of airfoil, while results for complete inviscid flow give shock wave position toward trailing edge relative to solution for viscous flow. This test case, shown in Figs. 5.33 and 5.34, and similar test cases with strong shock wave show difficulty for viscous-inviscid coupling method presented in this work. This difficulty appears as slow convergence rate and non-monotone convergence. To stabilize the convergence, in this test case the under-relaxation factor was set to $\beta = 0.001$. The number of iterations required to reach converged steady solution for the test case 3 was 6502. Converged solution is reached when greatest pressure residual at airfoil surface is less than $1 \cdot 10^{-3}$. In the pressure coefficient distribution this difficulty can be observed behind strong shock

wave as sawtooth distribution. Possible reason for instability is boundary layer coupling by transpiration velocity and direct solution method of boundary layer equations. Also, such case is close to separation bubble where direct solution of boundary layer equations is singular.

5.3.2. NACA64A010 Airfoil

In this subsection three NACA64A010 airfoil test cases will be investigated. NACA64A010 is symmetrical airfoil with maximum thickness 10% at around 40% of chord from leading edge, leading edge radius 0.0068 of chord and trailing edge angle 12.6° . Shape of the airfoil and used computational grid are shown in Fig. 5.36. This structured grid was used for calculations of all steady cases for NACA64A010 airfoil. The grid consists of 9600 control volumes, namely 160 volumes in ξ direction and 60 volumes in η direction.

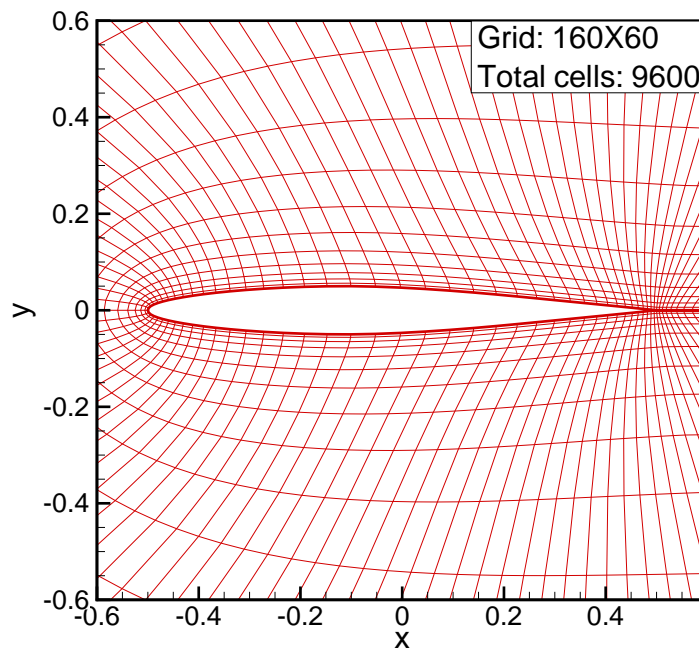


Figure 5.36: NACA64A010 computational grid; A far-field boundary is placed 40 chord lengths away from profile.

In table 5.5 selected test cases for NACA64A010 airfoil from experimental dataset in AGARD report [40] are presented. Three test cases at different Mach numbers are selected, which cover subsonic compressible flow with and without the appearance of

shock waves.

Table 5.5: NACA64A010 steady test cases

Test case	Mach number	Reynolds number	Angle of attack
4	0.49	$2.52 \cdot 10^6$	-0.01°
5	0.502	$1.00 \cdot 10^7$	-0.22°
6	0.796	$12.56 \cdot 10^6$	-0.21°

In Figs. 5.37, 5.38 and 5.41 steady cases are presented at three different Mach numbers $Ma = 0.49$, 0.502 and 0.796 . Only one side of airfoil is presented because of symmetrical airfoil, near zero angle of attack and less pronounced shockwave, except for test case 6. All cases are compared with experimental data obtained in AGARD report no. 702 [40].

Test case 4: NACA64A010, $Ma = 0.49$, $Re = 2.52 \cdot 10^6$, $\alpha = -0.01^\circ$

In Fig. 5.37 steady pressure coefficient distribution is shown on upper side of airfoil for test case 4 at $Ma = 0.49$, $Re = 2.52 \cdot 10^6$ and $\alpha = -0.01^\circ$. Numerical result shows perfect agreement with experimental data, except in transition region where numerical result shows exaggerated pressure drop compared with experimental data. This comes from the solution of boundary layer equations and transition prediction method. From Fig. 5.39, which shows boundary layer values for the same test case, it can be seen that boundary layer displacement thickness in laminar part has big predicted value because of smaller Reynolds number and then strong negative jump in turbulent region. This jump is also the reason for exaggerated pressure jump in the transition region in Fig. 5.37.

Test case 5: NACA64A010, $Ma = 0.502$, $Re = 1.0 \cdot 10^7$, $\alpha = -0.22^\circ$

In Fig. 5.38 steady pressure coefficient distribution is shown on upper side of airfoil for test case 5 at $Ma = 0.502$, $Re = 1.0 \cdot 10^7$ and $\alpha = -0.22^\circ$. Numerical result shows good agreement, but in this case shows good prediction at transition region. The pressure coefficient distribution on the leading part of airfoil before point of minimum pressure in Fig. 5.38, shows slight underprediction with respect to experimental data. This is not happening on the rear part of airfoil behind of the minimum pressure point. Boundary layer results for this case are shown in Fig. 5.40 and show similar behavior as in the test case 4, but because of greater Reynolds number boundary layer thickness and displacement thickness do not attain big values and consequently do not have stronger jump at the transition region. Weaker jump of displacement thickness has influence on

appropriate prediction of pressure jump in transition region in Fig. 5.38.

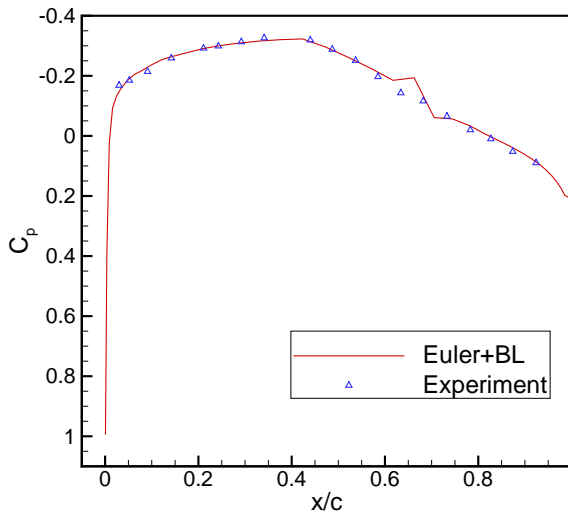


Figure 5.37: NACA64A010 steady pressure coefficient distribution for upper side at $Ma = 0.49$, $Re = 2.52 \cdot 10^6$, $\alpha = -0.01^\circ$

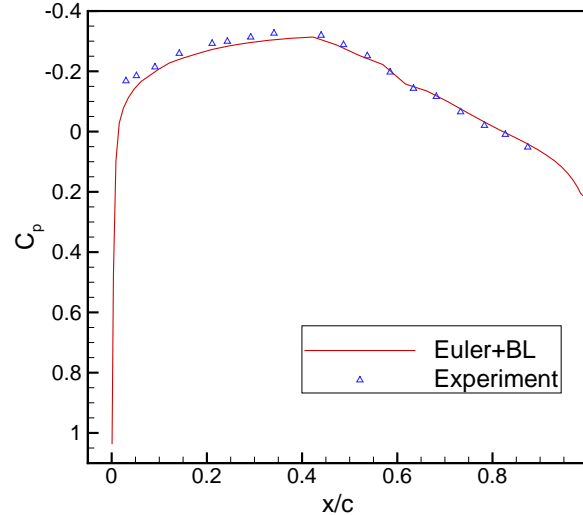


Figure 5.38: NACA64A010 steady pressure coefficient distribution for upper side at $Ma = 0.502$, $Re = 1.0 \cdot 10^7$, $\alpha = -0.22^\circ$

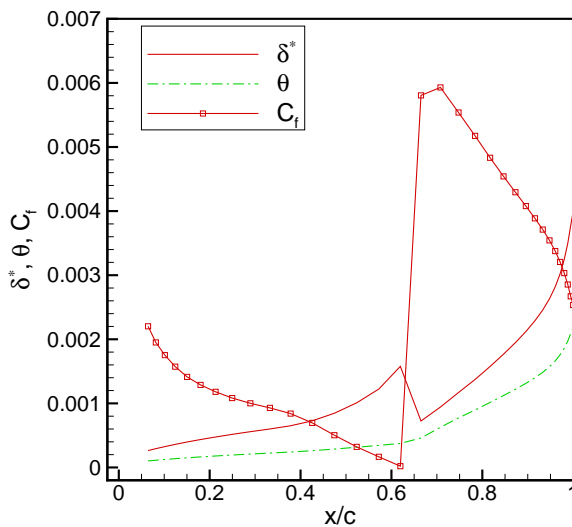


Figure 5.39: NACA64A010 boundary layer integral values for upper side at $Ma = 0.49$, $Re = 2.52 \cdot 10^6$, $\alpha = -0.01^\circ$

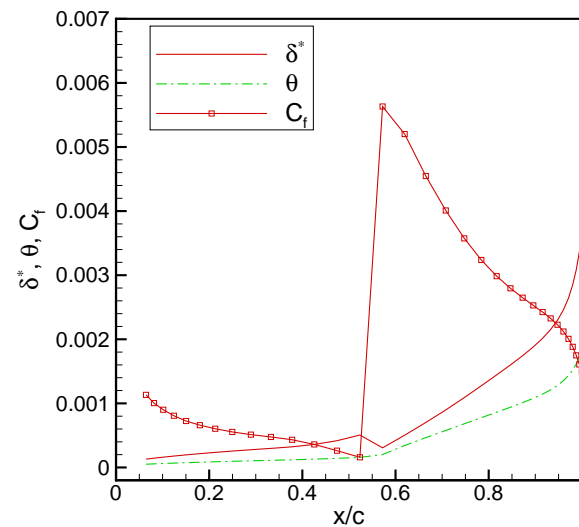


Figure 5.40: NACA64A010 boundary layer integral values for upper side at $Ma = 0.502$, $Re = 1.0 \cdot 10^7$, $\alpha = -0.22^\circ$

Test case 6: NACA64A010, $Ma = 0.796$, $Re = 12.56 \cdot 10^6$, $\alpha = -0.21^\circ$

In Fig. 5.41 numerical results and experimental data are shown for $Ma = 0.796$, $Re = 12.56 \cdot 10^6$ and $\alpha = -0.21^\circ$. At this Mach number flow field contains supersonic region

with weak shock wave. Numerical result for upper surface shows good agreement except at the position of shock wave where pressure peak is underpredicted. At this position of shock wave for upper and also for lower surface, numerical results show smoothing with respect to experimental data. This can indicate too strong impact of boundary layer on shock wave intensity. Due to the presence of thickening of boundary layer in the foot of shock wave, lambda shaped compression shock appears. As a consequence of this, shock wave intensity is smoothed and this can be seen in pressure coefficient distribution on airfoil surface [42, 43]. On the front part of lower surface, numerical solution shows a noticeable deviation from experimental data.

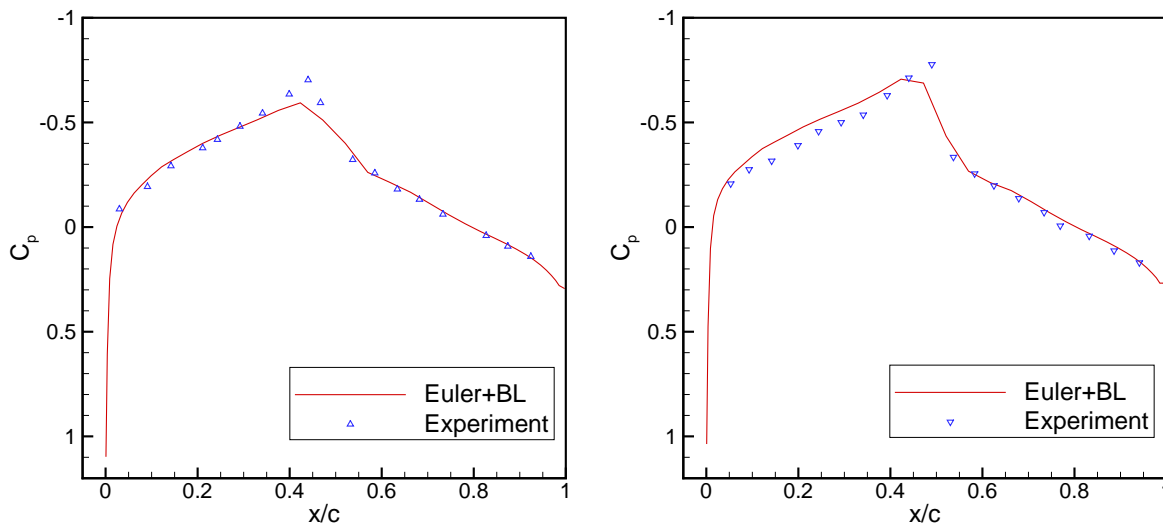


Figure 5.41: NACA64A010 pressure coefficient distribution for upper (left) and lower side (right) at $Ma = 0.796$, $Re = 12.56 \cdot 10^6$, $\alpha = -0.21^\circ$

In Figs. 5.42 and 5.43 results for displacement thickness, momentum thickness and friction coefficient for the test case 6 are shown. The displacement thickness and momentum thickness show growth with small jump in the transition region. Friction coefficient decreases to small positive values in transition region and then experiences positive jump. Afterwards it continually decreases to trailing edge.

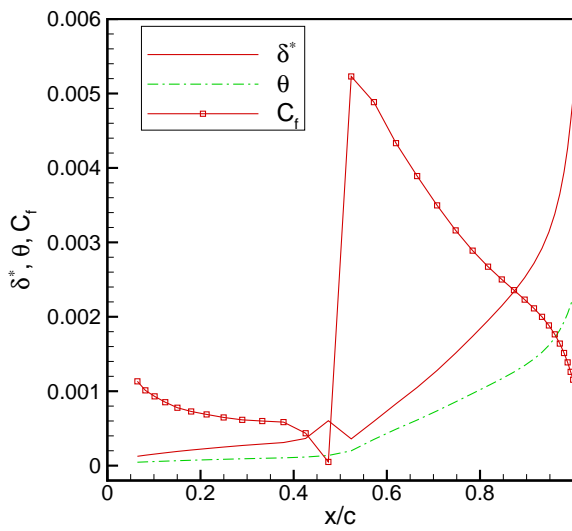


Figure 5.42: NACA64A010 boundary layer integral values for upper surface at $Ma = 0.796$, $Re = 12.56 \cdot 10^6$, $\alpha = -0.21^\circ$

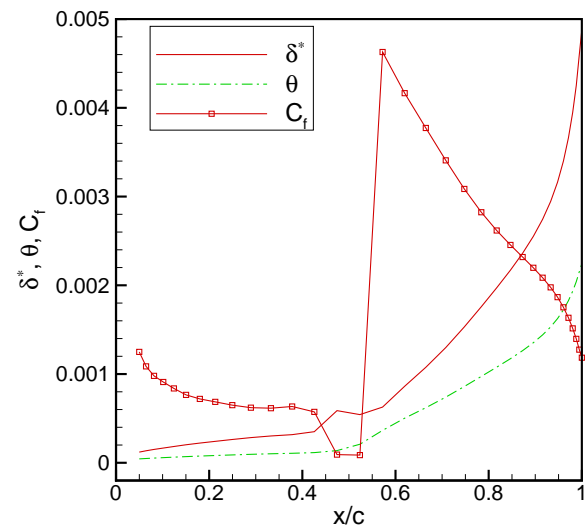


Figure 5.43: NACA64A010 boundary layer integral values for lower surface at $Ma = 0.796$, $Re = 12.56 \cdot 10^6$, $\alpha = -0.21^\circ$

5.3.3. NLR7301 Airfoil

The NLR7301 airfoil is the thickest supercritical airfoil, with value of thickness 16.5% (relative to chord length). The maximum thickness location is at approximately 35% (relative to chord length), camber is 1.66%, the leading edge radius 4.72% of chord length and trailing edge angle is 5.175° . Because of the rather extreme nose radius the airfoil represents probably a pretty hard test case for viscous-inviscid interaction methods. When compared to a conventional airfoil, a supercritical NLR7301 airfoil has reduced amount of camber, an increased leading edge radius, small surface curvature on the suction side, and a concavity in the rear part of the pressure side. At the design flow conditions this and similar supercritical airfoils typically develop larger supersonic regions, closed by a weak shock wave or, in ideal case, a shock-free re-compression, which leads to smaller drag coefficient and larger rear loading [44]. In practice, a shock-free recompression is very sensitive and unstable phenomenon which due to influence of boundary layer displacement or small surface imperfections, quickly degenerates into a more stable state characterized by a shock wave. Thus, flow conditions around supercritical airfoils are very sensitive and any deviation from the design flow condition is characterized by appearance of strong shock waves. Once in off-conditions, any further increase of Mach number or angle of attack leads to the increase of shock strength and subsequent thickening of the boundary layer. This can result in the shock induced boundary layer separation behind the shock and, ultimately, in the complete separation from the shock position to the trailing edge.

Shape and computational grid for the NLR7301 airfoil is shown in Fig. 5.44. Computational C-type grid consists of 9600 volume element and is generated by elliptical grid generator. A far-field boundary is 40 chord lengths away from profile. The grid has 160 volumes in ξ direction and 60 volumes in η direction. Test cases and corresponding parameters are listed in table 5.6.

Table 5.6: NLR7301 steady test cases

Test case	Mach number	Reynolds number	Angle of attack
7	0.299	$1.1 \cdot 10^6$	0.3966°
8	0.599	$1.9 \cdot 10^6$	0.3832°

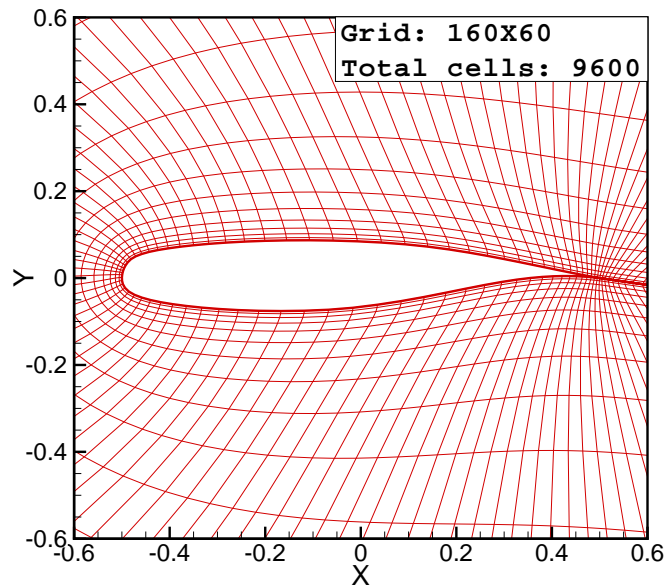


Figure 5.44: NLR7301; Computational grid. A far-field boundary is placed 40 chord lengths away from profile.

Figs. 5.45 and 5.46 show experimental data and numerical result for NLR7301 airfoil for test cases 7 and 8. Numerical result for the developed method shows moderate agreement with the experimental data in the whole region except at upper surface near trailing edge and at transition region, where bigger deviations are present. This could be explained by the shape of the leading edge radius, which violates the boundary layer flow assumptions, and greater pressure difference between upper and lower surface at the trailing edge. This kind of airfoil is very sensitive to any disturbance from wall boundary, that means also from boundary layer. Altogether, presented viscous-inviscid method gives results with moderate agreement on this kind of airfoils, and also shows very non-monotone convergence and long convergence history. The underrelaxation factor employed in the calculation of test cases 7 and 8 was equal $\beta = 0.001$. The number of iterations required to reach converged steady solution for test case 7 was equal 60 while for test case 8 was equal 2479. The viscous-inviscid calculation started after reaching steady inviscid solution of constant normal force coefficient. The convergence criterion was reached when pressure residual decreased to $1 \cdot 10^3$. At the trailing edge the method shows pressure oscillations on the upper surface where turbulent boundary layer is extremely thick. This could be explained by the separation of type B described in [45]. The reason for such separation lies in steep pressure gradient towards the trailing edge,

and this type of separation starts from the trailing edge (rear separation). The rear separation depends strongly on the thickness and the velocity profile of the boundary layer approaching the trailing edge and on the pressure gradient. Therefore, the B-type separation is very sensitive to the location of the point where transition takes place. Also, the reason for pressure oscillations at the trailing edge could be in violation of normal boundary layer assumption ($\partial p/\partial \eta = 0$) at the trailing edge, namely pressure gradient normal to boundary layer direction near trailing edge can be significant.

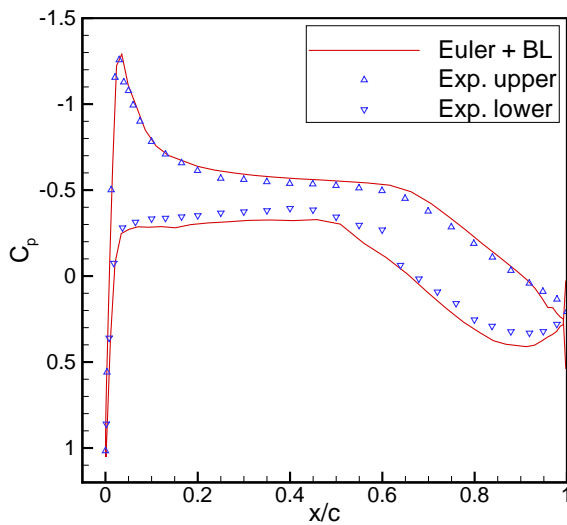


Figure 5.45: NLR7301 steady pressure coefficient distribution at $Ma = 0.299$, $Re = 1.1 \cdot 10^6$, $\alpha = 0.3966^\circ$

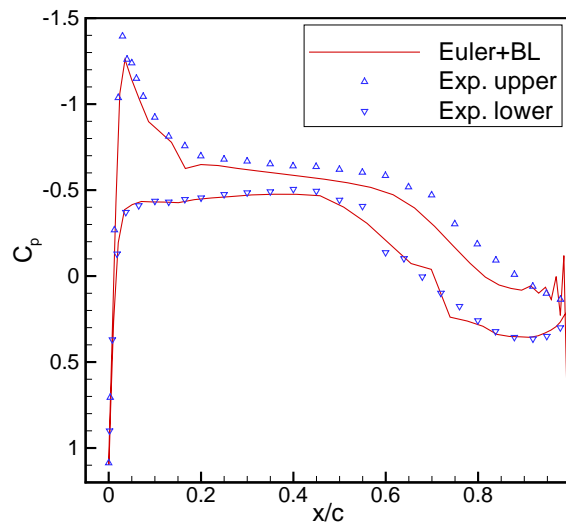


Figure 5.46: NLR7301 steady pressure coefficient distribution at $Ma = 0.599$, $Re = 1.9 \cdot 10^6$, $\alpha = 0.3832^\circ$

In the table 5.7 the results for all eight steady test cases are summarized. The results for underrelaxation factor β , number of iterations and CPU time for each test case are presented. It can be noticed that the number of iterations as also the CPU time grows as the Mach number is increased. The bigger time is required for the test cases with shock appearance. Also, it can be noticed that overall underrelaxation factor is very low because of probably very instable mechanism of coupling by transpiration velocity. Still smaller underrelaxation factor is required for the test case with shock appearance (test case 3). The test cases 7 and 8 (NLR7301) show also very small underrelaxation factor although the test cases are free of shocks. This is probably because such airfoil has big curvature near the leading edge which is not favorable with respect to the assumptions made in boundary layer equations.

Table 5.7: Summarized steady test cases

Airfoil	Test case	Ma	Re	α	β	num. of iter.	CPU time
NACA0012	1	0.504	$2.93 \cdot 10^6$	4.06°	0.01	683	38.2 s
	2	0.756	$4.01 \cdot 10^6$	-0.01°	0.01	840	46.4 s
	3	0.803	$4.09 \cdot 10^6$	0.05°	0.001	6502	321.3 s
NACA64A010	4	0.49	$2.52 \cdot 10^6$	-0.01°	0.01	71	3.8 s
	5	0.502	$1.00 \cdot 10^7$	-0.22°	0.01	54	2.7 s
	6	0.796	$12.56 \cdot 10^6$	-0.21°	0.01	336	19.5 s
NLR7301	7	0.299	$1.1 \cdot 10^6$	0.3966°	0.001	60	2.9 s
	8	0.599	$1.9 \cdot 10^6$	0.3832°	0.001	2479	122.5 s

5.4. Unsteady Results

When an airfoil performs sinusoidal oscillations around a given mean condition in the following way:

$$\alpha = \alpha_m + \alpha_o \cos(\omega t) \quad (5.2)$$

the local pressure distribution, hence the lift force and the moment show also periodical variations. The main parameter governing the unsteady flow is reduced frequency, ω^* , defined as:

$$\omega^* = \frac{\omega L}{U_\infty} \quad (5.3)$$

where ω is angular frequency, L reference length (airfoil chord) and U_∞ free stream velocity. This parameter is a measure for the unsteadiness of the flow.

To describe harmonic variations, two quantities are needed, namely magnitude and phase shift with respect to the motion of the airfoil (see fig. 5.47). An equivalent way of description is in terms of a complex number. In the latter notation, the real part of a pressure (or other variable) perturbation is in phase with the motion of the airfoil, and the imaginary part is in quadrature with it [45].

Description in terms of a *phase and magnitude* has following form:

$$\begin{aligned} p &= p_m + p_o \cos(\omega t + \varphi) \\ &= p_m + (p_o \cos \varphi) \cos(\omega t) - (p_o \sin \varphi) \sin(\omega t) \end{aligned} \quad (5.4)$$

where p_o is magnitude of pressure perturbation, and φ is phase shift. Description in terms of a *complex number* has following form:

$$\begin{aligned} p &= p_m + p_o \operatorname{Re} [e^{i(\omega t + \varphi)}] \\ &= p_m + \operatorname{Re} [(p' + ip'') e^{i\omega t}] \end{aligned} \quad (5.5)$$

where $p' = p_o \cos \varphi$ is real part, and $p'' = p_o \sin \varphi$ is imaginary part of pressure perturbation. The member multiplied with $\cos(\omega t)$ in equation (5.4) is also called *in-phase* component and the member multiplied with $\sin(\omega t)$ in the same equation is called *in-quadrature* component.

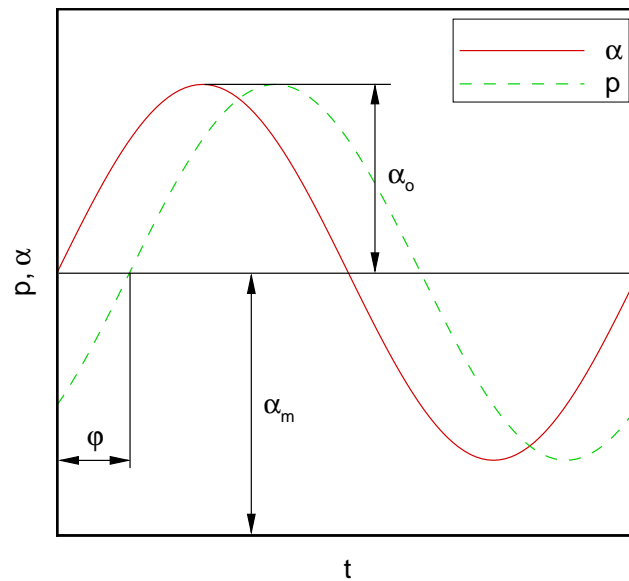


Figure 5.47: Example of unsteady variation of airfoil angle of attack and pressure

Such description of unsteady pressure or loads is only valid if the aerodynamic quantities vary sinusoidally in time, or, in other words, as long as linear relationship exists between the airfoil displacement and the unsteady airloads. This is, however, not always true, especially not in separated flows or in regions near oscillating shock waves.

When a system can be regarded as linear (p is varying linearly with α), steady pressure p_s for the steady mean condition is identical with p_m the mean pressure during the oscillation. Distribution of steady pressure characterizes the type of flow, which influences the oscillatory pressures. When non-linearities are present, higher harmonics are necessary to be incorporated in unsteady description. In general non-linear case pressure amplitudes are not proportional to the motion amplitude and the mean pressure p_m is not necessarily the same as the steady pressure p_s [40]. For attached flow serious non-linearities in pressure usually occur only at positions close to either a leading-edge, a flap hinge-line or a shock wave. The effect of non-linearities tend to disappear when the pressure is integrated to give forces and moments.

5.4.1. NACA0012 Airfoil

In this subsection unsteady results of viscous-inviscid interaction code for NACA0012 airfoil compared with experimental data [40] are presented. Airfoil performs rotational

harmonic motion about axis at quarter chord from leading edge. Results are calculated for subsonic compressible flow with strong shock wave appearance. Free stream and airfoil motion characteristics are given in table 5.8.

Table 5.8: NACA0012 unsteady test case

Mach number Ma	0.755
Reynolds number Re	$5.5 \cdot 10^6$
Mean angle of attack α_m	0.016°
Pitch amplitude α_o	2.51°
Reduced frequency ω^*	0.1628
Rotational axis position x_α/c	0.25

In Figs. 5.48 to 5.55 are unsteady results presented, for test case given in table 5.8. The computational grid had 160 volume elements in ξ direction and 60 volume elements in η direction (total 9600 volume elements). Numerical results of viscous-inviscid method are compared with experimental data at certain phase angle ϕ in the last period of simulation. Four periods were simulated to establish periodic lift variation. Unsteady pressure coefficient results show overall good agreement with experimental data. Bigger deviations from experimental data are present at smaller angles of attack unlike at greater ones. At some greater angles of attack in part of period where angle is increasing and strong shock waves appear, numerical results show shock wave position moved forward with respect to experimental data. This indicates that influence of boundary layer thickening on inviscid solver is too strong. On the other hand, in the part of period where angle of attack is decreasing and strong shock wave still exist, numerical results show good prediction of shock wave position and strength.

Also in Figs. 5.48 to 5.55 results from unsteady RANS code Tau are presented. Turbulence model used in RANS simulations was two equations $k-\omega$ turbulence model. Results from the viscous-inviscid interaction match mostly with the results from URANS, rather than with experimental data. The results from viscous-inviscid interaction code at the shock position show less pronounced pressure peak than URANS results and experimental data. The URANS results show also shock position moved toward the front of airfoil at some phase angles.

In Figs. 5.56 and 5.57 unsteady variation of normal force coefficient for NACA0012

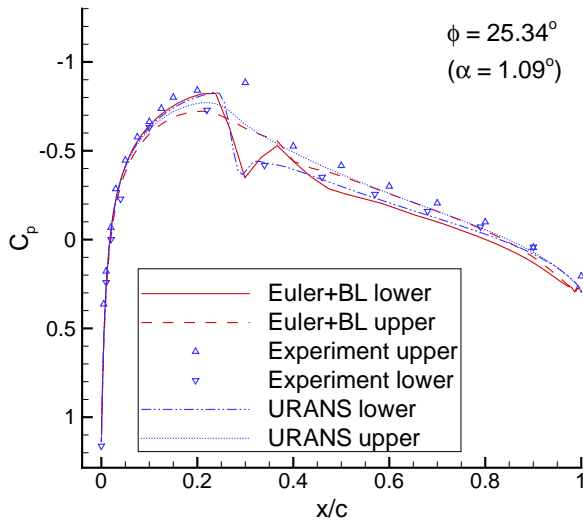


Figure 5.48: NACA0012 unsteady pressure coefficient distribution at phase angle $\phi = 25.34^\circ$ for $Ma = 0.755$, $Re = 5.5 \cdot 10^6$, $\alpha_m = 0.016^\circ$, $\alpha_o = 2.51^\circ$, $\omega^* = 0.1628$

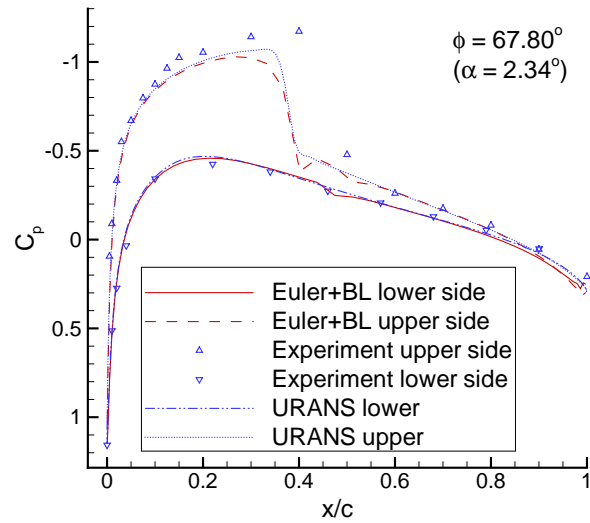


Figure 5.49: NACA0012 unsteady pressure coefficient distribution at phase angle $\phi = 67.80^\circ$ for $Ma = 0.755$, $Re = 5.5 \cdot 10^6$, $\alpha_m = 0.016^\circ$, $\alpha_o = 2.51^\circ$, $\omega^* = 0.1628$

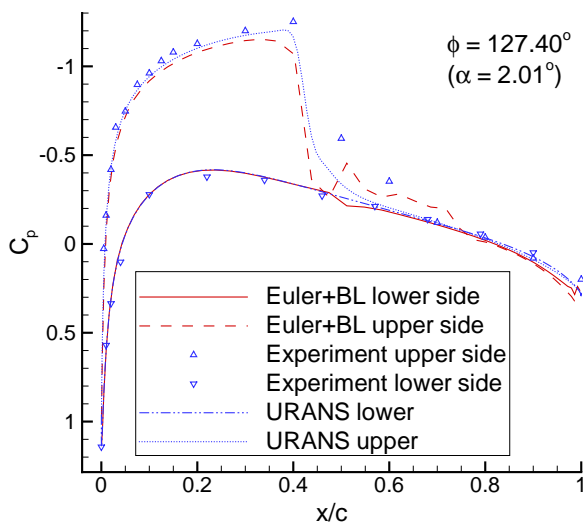


Figure 5.50: NACA0012 unsteady pressure coefficient distribution at phase angle $\phi = 127.40^\circ$ for $Ma = 0.755$, $Re = 5.5 \cdot 10^6$, $\alpha_m = 0.016^\circ$, $\alpha_o = 2.51^\circ$, $\omega^* = 0.1628$

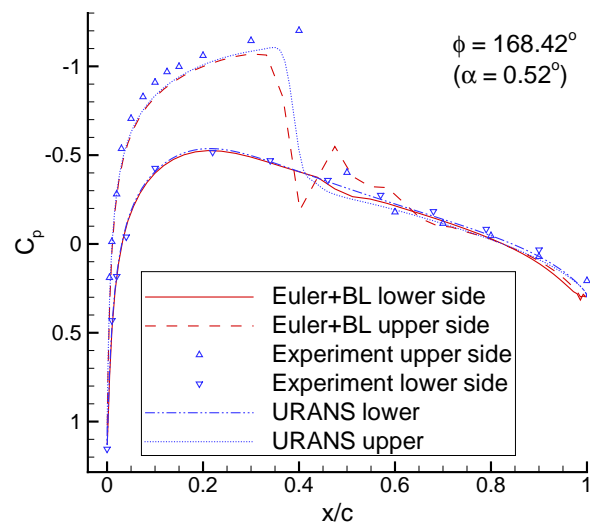


Figure 5.51: NACA0012 unsteady pressure coefficient distribution at phase angle $\phi = 168.42^\circ$ for $Ma = 0.755$, $Re = 5.5 \cdot 10^6$, $\alpha_m = 0.016^\circ$, $\alpha_o = 2.51^\circ$, $\omega^* = 0.1628$

test case at $Ma = 0.755$, $Re = 5.5 \cdot 10^6$, $\alpha_m = 0.016^\circ$, $\alpha_o = 2.51^\circ$, $\omega^* = 0.1628$ is presented. Force coefficient linearly follows angle of attack. In Fig. 5.56 the variation

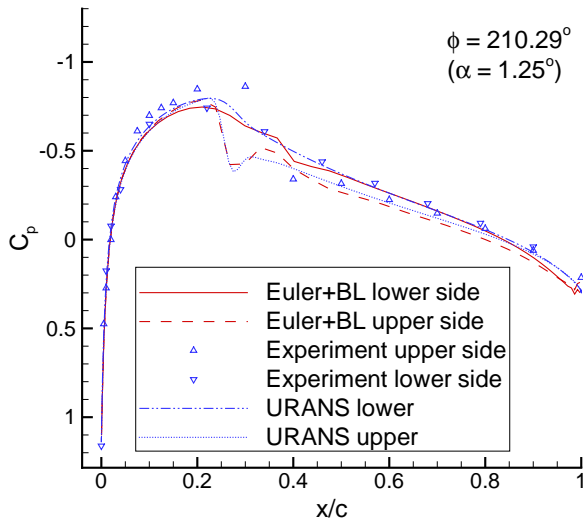


Figure 5.52: NACA0012 unsteady pressure coefficient distribution at phase angle $\phi = 210.29^\circ$ for $Ma = 0.755$, $Re = 5.5 \cdot 10^6$, $\alpha_m = 0.016^\circ$, $\alpha_o = 2.51^\circ$, $\omega^* = 0.1628$

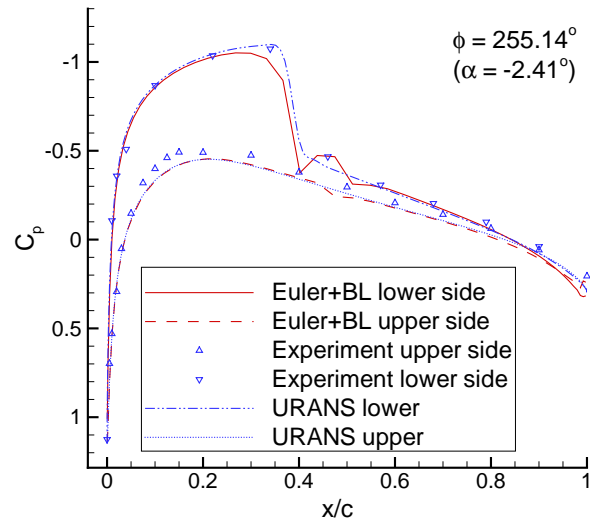


Figure 5.53: NACA0012 unsteady pressure coefficient distribution at phase angle $\phi = 255.14^\circ$ for $Ma = 0.755$, $Re = 5.5 \cdot 10^6$, $\alpha_m = 0.016^\circ$, $\alpha_o = 2.51^\circ$, $\omega^* = 0.1628$

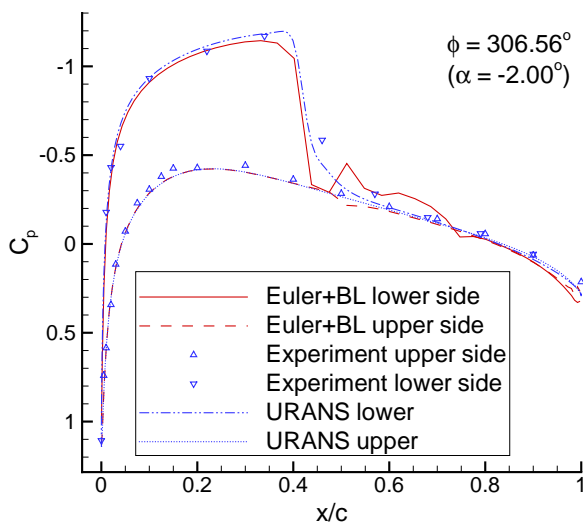


Figure 5.54: NACA0012 unsteady pressure coefficient distribution at phase angle $\phi = 306.56^\circ$ for $Ma = 0.755$, $Re = 5.5 \cdot 10^6$, $\alpha_m = 0.016^\circ$, $\alpha_o = 2.51^\circ$, $\omega^* = 0.1628$

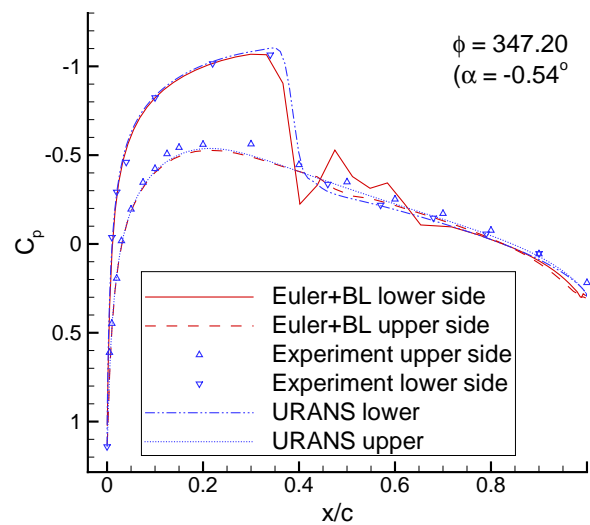


Figure 5.55: NACA0012 unsteady pressure coefficient distribution at phase angle $\phi = 347.20^\circ$ for $Ma = 0.755$, $Re = 5.5 \cdot 10^6$, $\alpha_m = 0.016^\circ$, $\alpha_o = 2.51^\circ$, $\omega^* = 0.1628$

of normal force coefficient is presented for the developed viscous-inviscid method, the Euler results and unsteady RANS results. Also instantaneous angle of attack in Fig. 5.56

is presented. A little phase lag between force coefficient and angle of attack (pitch motion) of airfoil can be noticed. Force coefficient lag behind the angle of attack, what can be seen at maximum points but also at the end and at the beginning of period. In Fig. 5.57 normal force coefficient as a function of instantaneous angle of attack is shown. Numerical results for viscous-inviscid method (Euler+BL) and unsteady RANS method are shown as also experimental data from AGARD report [40]. Overall, behavior of normal force coefficient for viscous-inviscid code matches URANS results, while in comparison with experimental data both codes are more shifted at smaller angles of attack. In Fig. 5.56 also the results of normal force coefficient for the pure Euler are presented. The difference in phase and magnitude between viscous-inviscid method (Euler+BL) and pure Euler can be observed. The results for the viscous-inviscid method have very good agreement, in phase and magnitude of normal force coefficient, with unsteady RANS results. Fig. 5.56 shows the influence of boundary layer coupling on the normal force coefficient with respect to the pure Euler results.

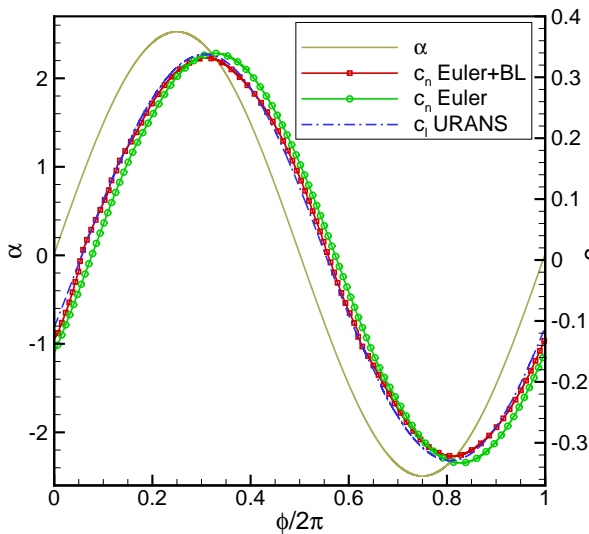


Figure 5.56: Normal force coefficient and instantaneous angle of attack as a function of phase angle in one period, for NACA0012 airfoil at $Ma = 0.755$, $Re = 5.5 \cdot 10^6$, $\alpha_m = 0.016^\circ$, $\alpha_o = 2.51^\circ$, $\omega^* = 0.1628$. The lag between normal force coefficient and pitch motion of airfoil (angle of attack) can be seen

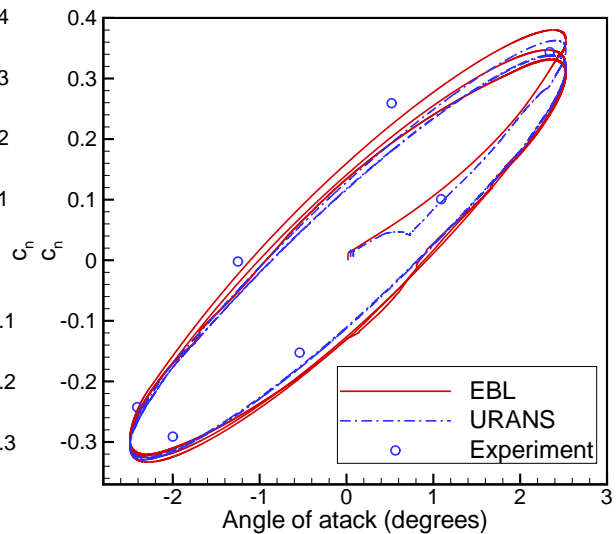


Figure 5.57: Normal force coefficient as a function of instantaneous angle of attack for NACA0012 airfoil at $Ma = 0.755$, $Re = 5.5 \cdot 10^6$, $\alpha_m = 0.016^\circ$, $\alpha_o = 2.51^\circ$, $\omega^* = 0.1628$

5.4.2. NACA64A010 Airfoil

In this subsection unsteady results for symmetric airfoil NACA64A010 will be presented. All results are compared with experimental data from AGARD report [40]. Airfoil performs rotational harmonic motion about axis at distance $x_\alpha/c = 0.239$ from leading edge. Results are calculated for subsonic compressible flow with strong shock wave appearance. Free stream and airfoil motion characteristics are given in table 5.9.

Table 5.9: NACA64A010 unsteady test case

Mach number Ma	0.797
Reynolds number Re	$12.4 \cdot 10^6$
Mean angle of attack α_m	-0.08°
Pitch amplitude α_o	2.00°
Reduced frequency ω^*	0.202
Rotational axis position x_α/c	0.239

The computational grid consists of 9600 volume elements, 160 in ξ direction and 60 in η direction. In Figs. 5.58 to 5.65 unsteady pressure coefficient results for pitching motion according to parameters in table 5.9 are presented. With dashed and full line numerical results of viscous-inviscid method for lower and upper airfoil surface are presented respectively. With triangles pointing up and pointing down, experimental data for upper and lower airfoil side are presented respectively. Results are presented for phase angles $\phi = 45^\circ, 90^\circ, 135^\circ, 180^\circ, 225^\circ, 270^\circ, 315^\circ, 360^\circ$, in the last period of simulation. Four unsteady periods are simulated prior these results are captured.

The developed method shows results which are in moderately good agreement with the experimental data in most of phase angles. At all phase angles, on front part of airfoil and in front of shock wave position, pressure coefficient distribution shows slight underprediction on both sides of airfoil. At the rear part of airfoil, behind the shock wave, calculated pressure coefficient is in good agreement with experimental data. Position of shock wave is mostly good predicted. At some phase angles, position for strong shock waves are better predicted than for weak shocks. The intensity of shock waves, namely peak pressures, are at several phase angles underpredicted. This underprediction happens at the airfoil side where smaller suction exist at the position of steep pressure coefficient distribution, as on upper side of airfoil in Fig. 5.62. In this situation the calculated and measured position, and intensity of shock wave are not in agreement.

The calculated pressure jump across the shock wave is rather smeared in comparison with the experimental data. It can be explained by the influence of boundary layer, as given in the analysis of steady state results. It is observed the nearly equal shift of pressure coefficient on upper and lower surface at the front part of airfoil which can be a consequence of unequal parameters of experimental and numerical calculations (non-corrected experimental data for the influence of wind tunnel walls).

Also, in Figs. 5.58 to 5.65 the calculated results by unsteady RANS method are shown. The results from the unsteady RANS method are calculated by two equation $k - \omega$ turbulence model. Results from the developed viscous-inviscid method are in practically perfect agreement with the unsteady RANS results. The calculated position and intensity of shock-wave is in majority of phase angles in perfect agreement with the unsteady RANS results. At some phase angles the shock-wave intensity of viscous-inviscid method is slightly smeared in comparison with unsteady RANS results.

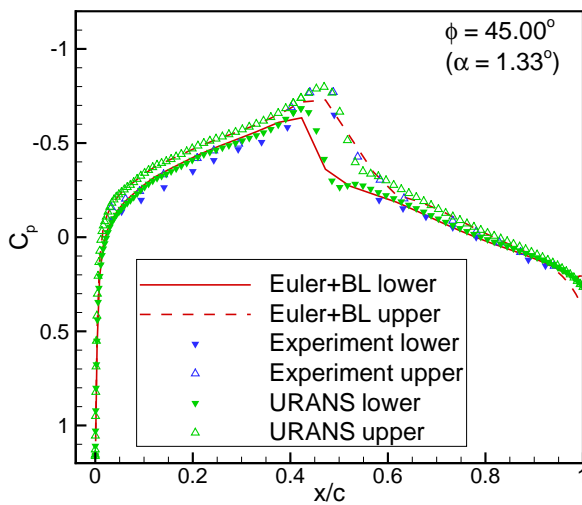


Figure 5.58: NACA64A010 unsteady pressure coefficient distribution at phase angle $\phi = 45.00^\circ$ for $Ma = 0.797$, $Re = 12.4 \cdot 10^6$, $\alpha_m = -0.08^\circ$, $\alpha_o = 2.00^\circ$, $\omega^* = 0.202$

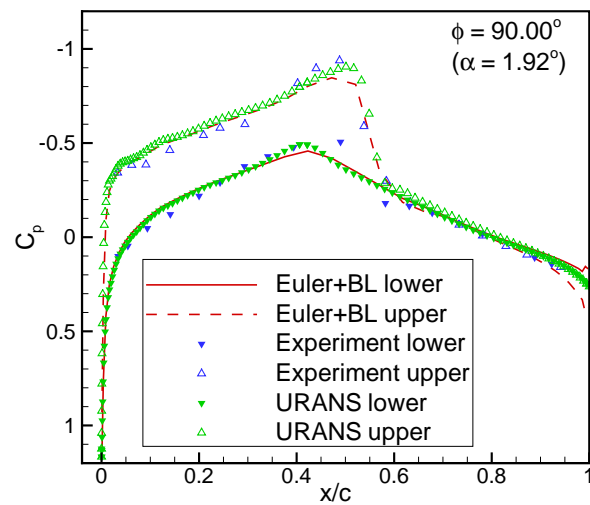


Figure 5.59: NACA64A010 unsteady pressure coefficient distribution at phase angle $\phi = 90.00^\circ$ for $Ma = 0.797$, $Re = 12.4 \cdot 10^6$, $\alpha_m = -0.08^\circ$, $\alpha_o = 2.00^\circ$, $\omega^* = 0.202$

In Fig. 5.66 the normal force coefficient results are shown in one period. The calculated viscous-inviscid results are compared with calculated inviscid results. Also, the angle of attack (pitch motion) is shown. The calculated results for the viscous-inviscid method show smaller magnitude and phase delay with respect to the inviscid calculated results.

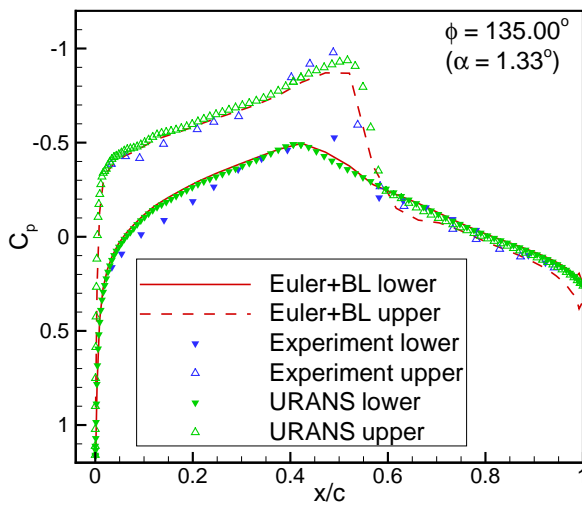


Figure 5.60: NACA64A010 unsteady pressure coefficient distribution at phase angle $\phi = 135.00^\circ$ for $Ma = 0.797$, $Re = 12.4 \cdot 10^6$, $\alpha_m = -0.08^\circ$, $\alpha_o = 2.00^\circ$, $\omega^* = 0.202$

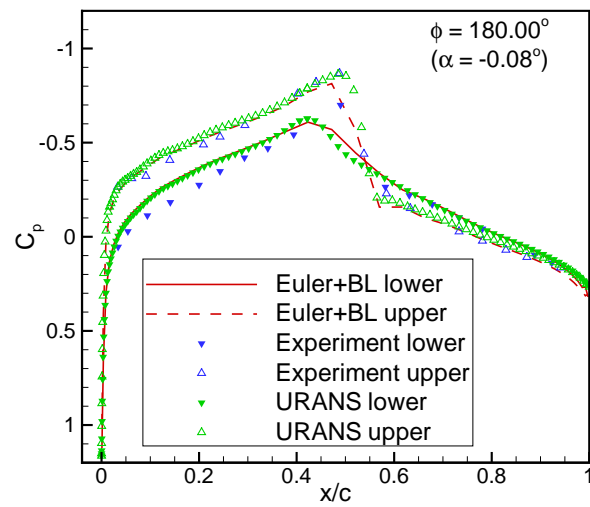


Figure 5.61: NACA64A010 unsteady pressure coefficient distribution at phase angle $\phi = 180.00^\circ$ for $Ma = 0.797$, $Re = 12.4 \cdot 10^6$, $\alpha_m = -0.08^\circ$, $\alpha_o = 2.00^\circ$, $\omega^* = 0.202$

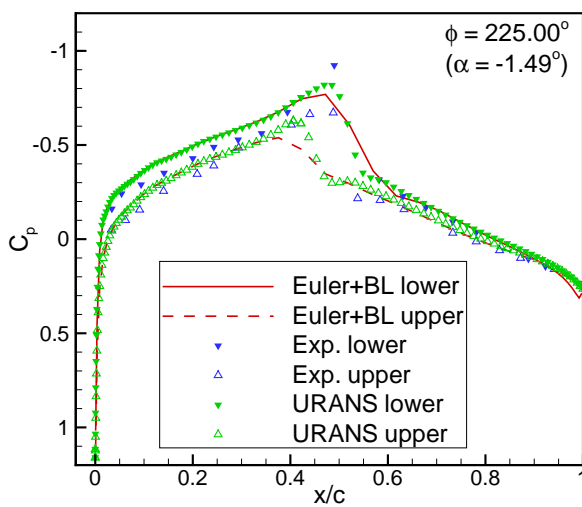


Figure 5.62: NACA64A010 unsteady pressure coefficient distribution at phase angle $\phi = 225.00^\circ$ for $Ma = 0.797$, $Re = 12.4 \cdot 10^6$, $\alpha_m = -0.08^\circ$, $\alpha_o = 2.00^\circ$, $\omega^* = 0.202$

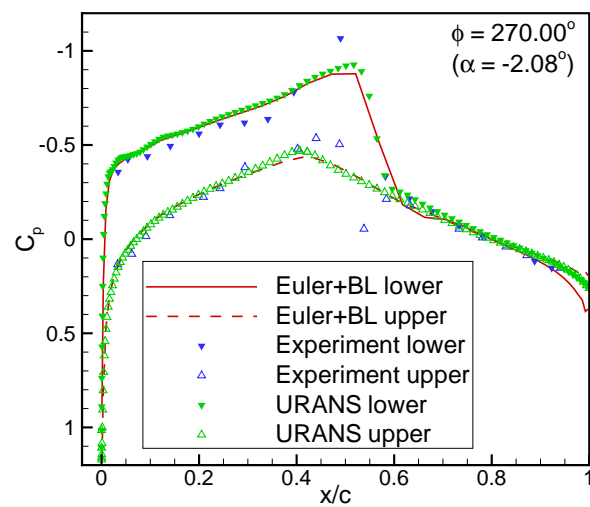


Figure 5.63: NACA64A010 unsteady pressure coefficient distribution at phase angle $\phi = 270.00^\circ$ for $Ma = 0.797$, $Re = 12.4 \cdot 10^6$, $\alpha_m = -0.08^\circ$, $\alpha_o = 2.00^\circ$, $\omega^* = 0.202$

In Fig. 5.67 unsteady normal force coefficient as a function of instantaneous angle of attack is presented. It can be seen that calculated force coefficient deviates from experi-

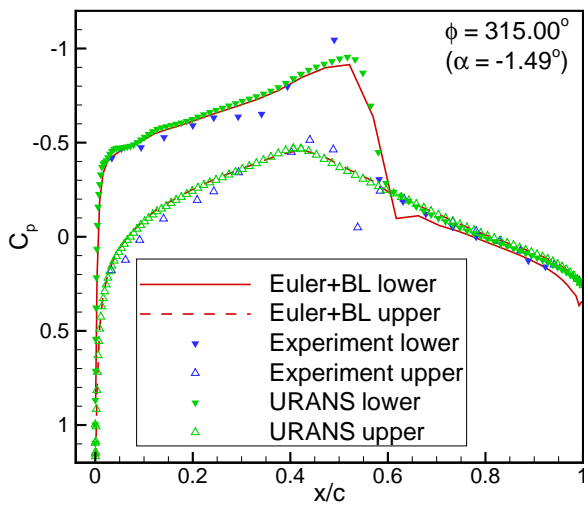


Figure 5.64: NACA64A010 unsteady pressure coefficient distribution at phase angle $\phi = 315.00^\circ$ for $Ma = 0.797$, $Re = 12.4 \cdot 10^6$, $\alpha_m = -0.08^\circ$, $\alpha_o = 2.00^\circ$, $\omega^* = 0.202$

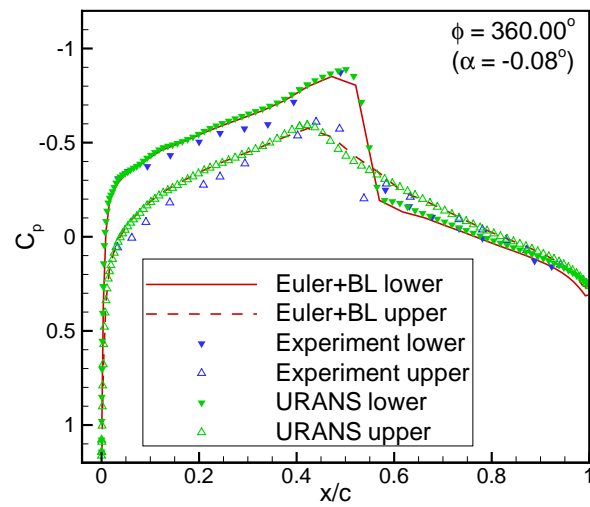


Figure 5.65: NACA64A010 unsteady pressure coefficient distribution at phase angle $\phi = 360.00^\circ$ for $Ma = 0.797$, $Re = 12.4 \cdot 10^6$, $\alpha_m = -0.08^\circ$, $\alpha_o = 2.00^\circ$, $\omega^* = 0.202$

mental data. This follows from differences in pressure coefficient distribution presented in previous figures.

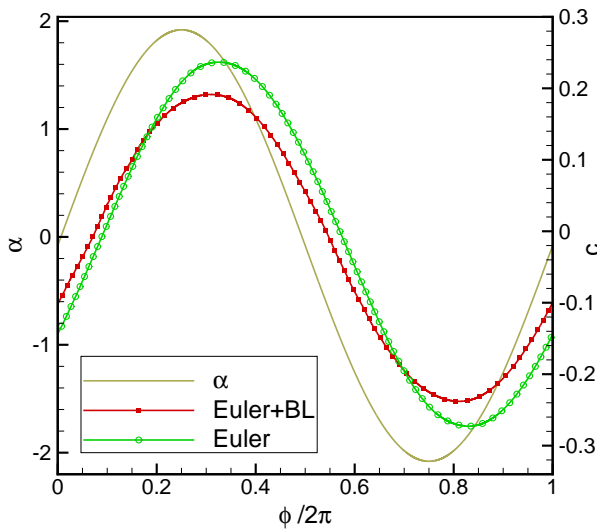


Figure 5.66: Normal force coefficient and instantaneous angle of attack as a function of phase angle in one period, for NACA64A010 airfoil at $Ma = 0.797$, $Re = 12.4 \cdot 10^6$, $\alpha_m = -0.08^\circ$, $\alpha_o = 2.00^\circ$, $\omega^* = 0.202$

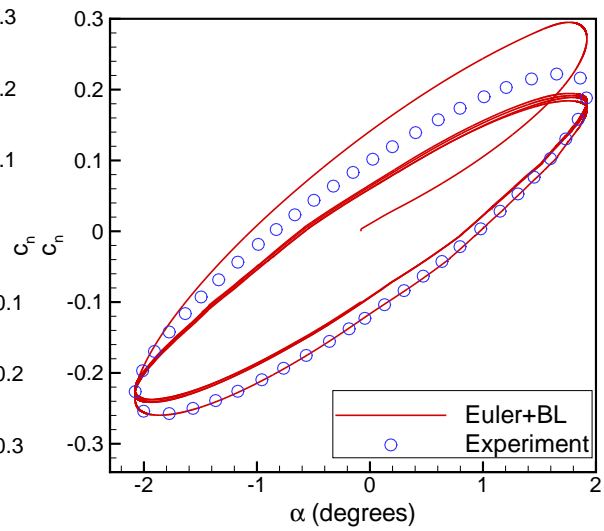


Figure 5.67: Normal force coefficient as a function of instantaneous angle of attack for NACA64A010 airfoil at $Ma = 0.797$, $Re = 12.4 \cdot 10^6$, $\alpha_m = -0.08^\circ$, $\alpha_o = 2.00^\circ$, $\omega^* = 0.202$

6 Conclusion

In this work the simple and accurate method for unsteady aerodynamic load prediction is developed. The method is based on viscous-inviscid decomposition of the calculation domain, where inviscid flow is governed by unsteady Euler equations and boundary layer is treated through the von Karman integral formulation. The Euler-boundary layer coupling is realized by transpiration velocity (the transpiration velocity calculated from the boundary layer equations is used as a boundary condition for the inviscid flow). The method is focused on subsonic and transonic flows, at high Reynolds number, with and without shock-wave appearance.

The unsteady Euler equations were solved in transformed body-fitted coordinates using conservative form of governing equations, by control volume method on the moving structured C-type rigid grid. Space discretization is performed by the Van Leer MUSCL scheme of second-order accuracy, while time integration was performed by explicit Euler method. The unsteady cases were performed only for airfoil pitch motion with the undeformed grid (in rigid body rotation). The grid generator is based on solving Poisson's equation and satisfies the grid orthogonality condition on airfoil contour.

Model of boundary layer equations consists of two integral momentum and kinetic energy equation closed by Drela's additional relationships. Transition was predicted by the e^n method. The model is integrated by the fourth order Runge-Kutta method.

Prior to the method validation in selected steady cases and application in unsteady problems, the grid convergence was analyzed in order to select grid size (in terms of distance of outer boundary from the airfoil and required number of control volumes) which provides a grid independent solution. Grid convergence was performed on NACA0012

airfoil at two angles of attack 1° and 5° , for steady and unsteady cases. It is concluded that grids with the distance of 40 chord lengths from the airfoil to outer domain boundary, with 160 control volumes along the airfoil contour and wake, and 60 volumes across provide the grid independent solution. From the unsteady results it follows that only two periods of numerical simulation are sufficient to achieve a periodical solution.

Steady test cases were performed for three characteristic airfoil configurations (NACA0012, NACA64A010 and NLR7301) at three different Mach numbers in the range of angle of attack in which no massively flow separation is expected, with and without shock wave appearance. The results obtained by the developed method are compared with experimental data from AGARD reports and RANS code results. Following is concluded:

- Steady results for NACA0012 and NACA64A010 show good agreement with experimental data at all Mach numbers.
- For these two airfoils the position of transition is accurately predicted. In the case without shock the transition is indicated as small jump in the distribution of the pressure coefficient, as in the experimental data. In the cases with shock wave transition occurs at the shock position, so it is not clearly evident.
- For the two airfoils the strength of shock wave is well predicted but its position is slightly moved toward trailing edge with respect to experimental data. The developed method predicts the shock wave position closer to the experimental one than the pure inviscid method which means that accounting for the boundary layer effects improves the result accuracy.
- The results for an airfoil NLR7301 (which represents a challenge, for viscous-inviscid methods because of extreme big nose radius) show strong sensitivity on the boundary layer thickening and position of transition point, what is also reported in literature. The developed method for this airfoil shows results with moderate agreement in pressure distribution prediction. Also, the predicted transition point on compression side of airfoil is not positioned in right place and the method shows pressure instabilities at the suction side of trailing edge.

Unsteady results are performed for NACA0012 and NACA64A010 airfoil test cases. The method is not suitable for the airfoil NLR7301 due to appearance of flow separation

at relatively small angle of attack (in the case of flow separation the boundary layer approach is not valid). The test cases are selected from AGARD reports for Mach numbers at which strong shock-waves appear. The obtained results are compared with experimental data and also with the results of unsteady RANS code. Following is concluded:

- Unsteady results for both airfoils showed moderate agreement with experimental data.
- Position of shock was at most phase angles accurately predicted. At several phase angles the shock position obtained by the developed method is moved toward leading edge of airfoil relative to position in experiment (as in the steady cases). These results are in very good agreement with the results of unsteady RANS method.
- Intensity is at several phase angles a little decreased relative to experimental data. The method showed at several phase angles, at smaller angles of attack, on airfoil side with weaker shockwave, smeared pressure distribution with respect to the distribution from experimental data.
- The pressure coefficient distribution on the both side shows a good agreement with experimental data. In front of the shock wave there is a slight shift of calculated pressure coefficient relative to experimental data. Since the shift is nearly equal at lower and upper surface it has no effect on normal force magnitude.
- The calculated normal force coefficient obtained by the developed method and by unsteady RANS method shows very close agreement. For the certain angle of attack, the both calculated results show uniform shift relative to experimental data.
- The calculated unsteady normal force coefficient obtained by the developed method shows decrease in magnitude and delay in phase angle with respect to the unsteady Euler results.

According to the experience in using the developed method, it can be concluded that the method shows oscillatory behavior of pressure coefficient in the vicinity of strong

shock or at the trailing edge. These oscillations may cause the method divergence, so certain underrelaxation and consequently a greater number of iterations are required. The underrelaxation factor for the most unstable test cases goes down to 0.001. In the future work a strong coupling of Euler and boundary layer equations should be considered. In such an approach all the equations are solved simultaneously (unlike the developed method in which the equations are solved sequentially). Such a method is more complex, but it can be expected that strong coupling will improve the robustness of the method.

7 Conclusion of the Doctoral Dissertation

In this work the simple and accurate method for unsteady aerodynamic load prediction is developed. The method is based on the unsteady Euler equations corrected for boundary layer effects.

- The inclusion of boundary layer into unsteady Euler method results in more accurate prediction method for unsteady aerodynamic loads.
- The hypothesis of the work is proved. The developed method is fast and gives results of nearly same accuracy as the higher mathematical model like RANS which are in good agreement with experimental data.
- There is a space to improve the robustness of the developed method by modifying the way of coupling between Euler and boundary layer equations.

A Derivation of Boundary Condition

Boundary condition on airfoil surface:

$$(\vec{v} - \vec{v}_k - \vec{v}_t) \cdot \vec{n} = 0 / \frac{D}{Dt} \quad (\text{A.1})$$

$$\frac{D(\vec{v} - \vec{v}_k - \vec{v}_t)}{Dt} \cdot \vec{n} + (\vec{v} - \vec{v}_k - \vec{v}_t) \cdot \frac{D\vec{n}}{Dt} = 0 \quad (\text{A.2})$$

$$\frac{D\vec{v}}{Dt} \cdot \vec{n} - \frac{D(\vec{v}_k + \vec{v}_t)}{Dt} \cdot \vec{n} + (\vec{v} - \vec{v}_k - \vec{v}_t) \cdot \frac{D\vec{n}}{Dt} = 0 / \cdot \rho \quad (\text{A.3})$$

$$\left| \frac{D\vec{v}}{Dt} = -\frac{1}{\rho} \text{grad}p \right| \quad (\text{A.4})$$

$$\rho \left\{ \frac{D\vec{n}}{Dt} \cdot (\vec{v} - \vec{v}_k - \vec{v}_t) - \frac{D(\vec{v}_k + \vec{v}_t)}{Dt} \cdot \vec{n} \right\} = \text{grad}p \cdot \vec{n} \quad (\text{A.5})$$

$$\text{I} = \frac{D\vec{n}}{Dt} \cdot (\vec{v} - \vec{v}_k - \vec{v}_t) \quad (\text{A.6})$$

$$\text{II} = -\frac{D(\vec{v}_k + \vec{v}_t)}{Dt} \cdot \vec{n} \quad (\text{A.7})$$

$$\vec{n} = \vec{k} \times \vec{e}_\xi \quad (\text{A.8})$$

$$\vec{n} = \begin{vmatrix} i & j & k \\ 0 & 0 & 1 \\ x_\xi & y_\xi & 0 \end{vmatrix} = (-y_\xi, x_\xi) \quad (\text{A.9})$$

$$\begin{aligned} \text{I} &= \left(\frac{\partial n_x}{\partial t} + v_x \frac{\partial n_x}{\partial x} + v_y \frac{\partial n_x}{\partial y} \right) \cdot (v_x - x_\tau - v_{tx}) \\ &\quad + \left(\frac{\partial n_y}{\partial t} + v_x \frac{\partial n_y}{\partial x} + v_y \frac{\partial n_y}{\partial y} \right) \cdot (v_y - y_\tau - v_{ty}) \end{aligned} \quad (\text{A.10})$$

$$\begin{aligned} \text{II} &= \left(\frac{\partial (\vec{v}_k + \vec{v}_t)}{\partial t} + v_x \frac{\partial (\vec{v}_k + \vec{v}_t)}{\partial x} + v_y \frac{\partial (\vec{v}_k + \vec{v}_t)}{\partial y} \right) \cdot \vec{n} \\ &= \left(\frac{\partial (x_\tau + v_{tx})}{\partial t} + v_x \frac{\partial (x_\tau + v_{tx})}{\partial x} + v_y \frac{\partial (x_\tau + v_{tx})}{\partial y} \right) n_x \\ &\quad + \left(\frac{\partial (y_\tau + v_{ty})}{\partial t} + v_x \frac{\partial (y_\tau + v_{ty})}{\partial x} + v_y \frac{\partial (y_\tau + v_{ty})}{\partial y} \right) n_y \end{aligned} \quad (\text{A.11})$$

$$\begin{aligned} \text{I} &= \left[-\frac{1}{J} (K_{31} y_{\xi\xi} + K_{32} y_{\xi\eta} + K_{33} y_{\xi\tau}) - \frac{v_x}{J} (y_\eta y_{\xi\xi} - y_\xi y_{\xi\eta}) \right. \\ &\quad \left. - \frac{v_y}{J} (-x_\eta y_{\xi\xi} + x_\xi y_{\xi\eta}) \right] (v_x - x_\tau - v_{tx}) \\ &\quad + \left[\frac{1}{J} (K_{31} x_{\xi\xi} + K_{32} x_{\xi\eta} + K_{33} x_{\xi\tau}) + \frac{v_x}{J} (y_\eta x_{\xi\xi} - y_\xi x_{\xi\eta}) \right. \\ &\quad \left. + \frac{v_y}{J} (-x_\eta x_{\xi\xi} + x_\xi x_{\xi\eta}) \right] (v_y - y_\tau - v_{ty}) \end{aligned} \quad (\text{A.12})$$

$$\begin{aligned} \text{II} &= y_\xi \left[\frac{1}{J} (K_{31} (x_{\tau\xi} + v_{tx\xi}) + K_{32} (x_{\tau\eta} + v_{tx\eta}) + K_{33} (x_{\tau\tau} + v_{tx\tau})) \right. \\ &\quad \left. + \frac{v_x}{J} (y_\eta (x_{\tau\xi} + v_{tx\xi}) - y_\xi (x_{\tau\eta} + v_{tx\eta})) \right. \\ &\quad \left. + \frac{v_y}{J} (-x_\eta (x_{\tau\xi} + v_{tx\xi}) + x_\xi (x_{\tau\eta} + v_{tx\eta})) \right] \\ &\quad - x_\xi \left[\frac{1}{J} (K_{31} (y_{\tau\xi} + v_{ty\xi}) + K_{32} (y_{\tau\eta} + v_{ty\eta}) + K_{33} (y_{\tau\tau} + v_{ty\tau})) \right. \\ &\quad \left. + \frac{v_x}{J} (y_\eta (y_{\tau\xi} + v_{ty\xi}) - y_\xi (y_{\tau\eta} + v_{ty\eta})) \right. \\ &\quad \left. + \frac{v_y}{J} (-x_\eta (y_{\tau\xi} + v_{ty\xi}) + x_\xi (y_{\tau\eta} + v_{ty\eta})) \right] \end{aligned} \quad (\text{A.13})$$

Wing surface correspond to surface $\eta = \text{konst.}$ and this is equal:

$$\frac{D\eta}{Dt} = 0 \quad (\text{A.14})$$

$$\frac{\partial \eta}{\partial t} + v_x \frac{\partial \eta}{\partial x} + v_y \frac{\partial \eta}{\partial y} = 0 \quad (\text{A.15})$$

$$\frac{1}{J}K_{32} - \frac{v_x}{J}y_\xi + \frac{v_y}{J}x_\xi = 0 \quad (\text{A.16})$$

$$\begin{aligned} \text{I} = & \left[-\frac{1}{J}(x_\eta y_\tau y_{\xi\xi} - y_\eta x_\tau y_{\xi\xi} + J y_{\xi\tau}) - \frac{v_x}{J}y_\eta y_{\xi\xi} + \frac{v_y}{J}x_\eta y_{\xi\xi} \right] (v_x - x_\tau - v_{tx}) \\ & + \left[\frac{1}{J}(x_\eta y_\tau x_{\xi\xi} - y_\eta x_\tau x_{\xi\xi} + J x_{\xi\tau}) + \frac{v_x}{J}y_\eta x_{\xi\xi} - \frac{v_y}{J}x_\eta x_{\xi\xi} \right] (v_y - y_\tau - v_{ty}) \end{aligned} \quad (\text{A.17})$$

$$\begin{aligned} \text{I} = & \left[-\frac{1}{J}y_\eta y_{\xi\xi} (v_x - x_\tau) + \frac{1}{J}x_\eta y_{\xi\xi} (v_y - y_\tau) - y_{\xi\tau} \right] [(v_x - x_\tau) - v_{tx}] \\ & + \left[\frac{1}{J}y_\eta x_{\xi\xi} (v_x - x_\tau) - \frac{1}{J}x_\eta x_{\xi\xi} (v_y - y_\tau) + x_{\xi\tau} \right] [(v_y - y_\tau) - v_{ty}] \end{aligned} \quad (\text{A.18})$$

$$\begin{aligned} \text{I} = & \left[-\frac{1}{J}y_\eta y_{\xi\xi} (v_x - x_\tau) + \frac{1}{J}x_\eta y_{\xi\xi} (v_y - y_\tau) - y_{\xi\tau} \right] [(v_x - x_\tau) - v_{tx}] \\ & + \left[\frac{1}{J}y_\eta x_{\xi\xi} (v_x - x_\tau) - \frac{1}{J}x_\eta x_{\xi\xi} (v_y - y_\tau) + x_{\xi\tau} \right] [(v_y - y_\tau) - v_{ty}] \end{aligned} \quad (\text{A.19})$$

$$\begin{aligned} \text{I} = & -\frac{1}{J}y_\eta y_{\xi\xi} (v_x - x_\tau)^2 + \frac{1}{J}x_\eta y_{\xi\xi} (v_y - y_\tau) (v_x - x_\tau) - y_{\xi\tau} (v_x - x_\tau) \\ & + \frac{1}{J}y_\eta y_{\xi\xi} (v_x - x_\tau) v_{tx} - \frac{1}{J}x_\eta y_{\xi\xi} (v_y - y_\tau) v_{tx} + y_{\xi\tau} v_{tx} \\ & + \frac{1}{J}y_\eta x_{\xi\xi} (v_x - x_\tau) (v_y - y_\tau) - \frac{1}{J}x_\eta x_{\xi\xi} (v_y - y_\tau)^2 + x_{\xi\tau} (v_y - y_\tau) \\ & - \frac{1}{J}y_\eta x_{\xi\xi} (v_x - x_\tau) v_{ty} + \frac{1}{J}x_\eta x_{\xi\xi} (v_y - y_\tau) v_{ty} - x_{\xi\tau} v_{ty} \end{aligned} \quad (\text{A.20})$$

$$\begin{aligned} \text{II} = & y_\xi \left[\frac{1}{J} (K_{31} (x_{\tau\xi} + v_{tx\xi}) + K_{33} (x_{\tau\tau} + v_{tx\tau})) \right. \\ & \left. + \frac{v_x}{J} y_\eta (x_{\tau\xi} + v_{tx\xi}) - \frac{v_y}{J} x_\eta (x_{\tau\xi} + v_{tx\xi}) \right] \\ & - x_\xi \left[\frac{1}{J} (K_{31} (y_{\tau\xi} + v_{ty\xi}) + K_{33} (y_{\tau\tau} + v_{ty\tau})) \right. \\ & \left. + \frac{v_x}{J} y_\eta (y_{\tau\xi} + v_{ty\xi}) - \frac{v_y}{J} x_\eta (y_{\tau\xi} + v_{ty\xi}) \right] \end{aligned} \quad (\text{A.21})$$

$$\begin{aligned}
\Pi &= y_\xi \left[\frac{1}{J} \left((x_\eta y_\tau - y_\eta x_\tau) (x_{\tau\xi} + v_{tx\xi}) + J (x_{\tau\tau} + v_{tx\tau}) \right) \right. \\
&\quad \left. + \frac{v_x}{J} y_\eta (x_{\tau\xi} + v_{tx\xi}) - \frac{v_y}{J} x_\eta (x_{\tau\xi} + v_{tx\xi}) \right] \\
&\quad - x_\xi \left[\frac{1}{J} \left((x_\eta y_\tau - y_\eta x_\tau) (y_{\tau\xi} + v_{ty\xi}) + J (y_{\tau\tau} + v_{ty\tau}) \right) \right. \\
&\quad \left. + \frac{v_x}{J} y_\eta (y_{\tau\xi} + v_{ty\xi}) - \frac{v_y}{J} x_\eta (y_{\tau\xi} + v_{ty\xi}) \right] \tag{A.22}
\end{aligned}$$

$$\begin{aligned}
\Pi &= y_\xi \left[\frac{1}{J} (x_\eta y_\tau x_{\tau\xi} + x_\eta y_\tau v_{tx\xi} - y_\eta x_\tau x_{\tau\xi} - y_\eta x_\tau v_{tx\xi} + J x_{\tau\tau} + J v_{tx\tau}) \right. \\
&\quad \left. + \frac{v_x}{J} y_\eta x_{\tau\xi} + \frac{v_x}{J} y_\eta v_{tx\xi} - \frac{v_y}{J} x_\eta x_{\tau\xi} - \frac{v_y}{J} x_\eta v_{tx\xi} \right] \\
&\quad - x_\xi \left[\frac{1}{J} (x_\eta y_\tau y_{\tau\xi} + x_\eta y_\tau v_{ty\xi} - y_\eta x_\tau y_{\tau\xi} - y_\eta x_\tau v_{ty\xi} + J y_{\tau\tau} + J v_{ty\tau}) \right. \\
&\quad \left. + \frac{v_x}{J} y_\eta y_{\tau\xi} + \frac{v_x}{J} y_\eta v_{ty\xi} - \frac{v_y}{J} x_\eta y_{\tau\xi} - \frac{v_y}{J} x_\eta v_{ty\xi} \right] \tag{A.23}
\end{aligned}$$

$$\begin{aligned}
\Pi &= y_\xi \left[\frac{1}{J} y_\eta x_{\tau\xi} (v_x - x_\tau) - \frac{1}{J} x_\eta x_{\tau\xi} (v_y - y_\tau) + \frac{1}{J} y_\eta v_{tx\xi} (v_x - x_\tau) \right. \\
&\quad \left. - \frac{1}{J} x_\eta v_{tx\xi} (v_y - y_\tau) + x_{\tau\tau} + v_{tx\tau} \right] \\
&\quad - x_\xi \left[\frac{1}{J} y_\eta y_{\tau\xi} (v_x - x_\tau) - \frac{1}{J} x_\eta y_{\tau\xi} (v_y - y_\tau) + \frac{1}{J} y_\eta v_{ty\xi} (v_x - x_\tau) \right. \\
&\quad \left. - \frac{1}{J} x_\eta v_{ty\xi} (v_y - y_\tau) + y_{\tau\tau} + v_{ty\tau} \right] \tag{A.24}
\end{aligned}$$

$$\begin{aligned}
\Pi &= \frac{1}{J} \left[y_\xi y_\eta x_{\tau\xi} (v_x - x_\tau) - y_\xi x_\eta x_{\tau\xi} (v_y - y_\tau) + y_\xi y_\eta v_{tx\xi} (v_x - x_\tau) \right. \\
&\quad \left. - y_\xi x_\eta v_{tx\xi} (v_y - y_\tau) + J x_{\tau\tau} y_\xi + J v_{tx\tau} y_\xi \right] \\
&\quad - \frac{1}{J} \left[x_\xi y_\eta y_{\tau\xi} (v_x - x_\tau) - x_\xi x_\eta y_{\tau\xi} (v_y - y_\tau) + x_\xi y_\eta v_{ty\xi} (v_x - x_\tau) \right. \\
&\quad \left. - x_\xi x_\eta v_{ty\xi} (v_y - y_\tau) + J y_{\tau\tau} x_\xi + J v_{ty\tau} x_\xi \right] \tag{A.25}
\end{aligned}$$

I + II (parts with $x_{\xi\tau}$ i $y_{\xi\tau}$):

$$\begin{aligned}
(\text{I} + \text{II})_{x_{\xi\tau} y_{\xi\tau}} &= \frac{1}{J} \left[y_\xi y_\eta x_{\tau\xi} (v_x - x_\tau) - y_\xi x_\eta x_{\tau\xi} (v_y - y_\tau) - x_\xi y_\eta y_{\tau\xi} (v_x - x_\tau) \right. \\
&\quad \left. + x_\xi x_\eta y_{\tau\xi} (v_y - y_\tau) - y_{\xi\tau} (v_x - x_\tau) J + x_{\xi\tau} (v_y - y_\tau) J \right. \\
&\quad \left. + y_{\xi\tau} v_{tx} J - x_{\xi\tau} v_{ty} J \right] \tag{A.26}
\end{aligned}$$

$$\begin{aligned}
(\text{I} + \text{II})_{x_{\xi\tau}y_{\xi\tau}} &= \frac{1}{J} [y_{\xi}y_{\eta}x_{\tau\xi}(v_x - x_{\tau}) - y_{\xi}x_{\eta}x_{\tau\xi}(v_y - y_{\tau}) - x_{\xi}y_{\eta}y_{\tau\xi}(v_x - x_{\tau}) \\
&\quad + x_{\xi}x_{\eta}y_{\tau\xi}(v_y - y_{\tau}) - x_{\xi}y_{\eta}y_{\xi\tau}(v_x - x_{\tau}) + y_{\xi}x_{\eta}y_{\xi\tau}(v_x - x_{\tau}) \\
&\quad + x_{\xi}y_{\eta}x_{\xi\tau}(v_y - y_{\tau}) - y_{\xi}x_{\eta}x_{\xi\tau}(v_y - y_{\tau}) \\
&\quad + x_{\xi}y_{\eta}y_{\xi\tau}v_{tx} - y_{\xi}x_{\eta}y_{\xi\tau}v_{tx} - x_{\xi}y_{\eta}x_{\xi\tau}v_{ty} + y_{\xi}x_{\eta}x_{\xi\tau}v_{ty}] \quad (\text{A.27})
\end{aligned}$$

$$\begin{aligned}
(\text{I} + \text{II})_{x_{\xi\tau}y_{\xi\tau}} &= \frac{1}{J} [y_{\xi}x_{\tau\xi}(y_{\eta}(v_x - x_{\tau}) - x_{\eta}(v_y - y_{\tau}) - x_{\eta}(v_y - y_{\tau})) \\
&\quad - x_{\xi}y_{\tau\xi}(y_{\eta}(v_x - x_{\tau}) - x_{\eta}(v_y - y_{\tau}) + y_{\eta}(v_x - x_{\tau})) \\
&\quad + y_{\xi}x_{\eta}y_{\xi\tau}(v_x - x_{\tau}) + x_{\xi}y_{\eta}x_{\xi\tau}(v_y - y_{\tau}) \\
&\quad + x_{\xi}y_{\eta}y_{\xi\tau}v_{tx} - y_{\xi}x_{\eta}y_{\xi\tau}v_{tx} - x_{\xi}y_{\eta}x_{\xi\tau}v_{ty} + y_{\xi}x_{\eta}x_{\xi\tau}v_{ty}] \quad (\text{A.28})
\end{aligned}$$

$$\begin{aligned}
(\text{I} + \text{II})_{x_{\xi\tau}y_{\xi\tau}} &= \frac{1}{J} [y_{\xi}x_{\tau\xi} \left(\sqrt{x_{\eta}^2 + y_{\eta}^2} \bar{u} - x_{\eta}(v_y - y_{\tau}) \right) \\
&\quad - x_{\xi}y_{\tau\xi} \left(\sqrt{x_{\eta}^2 + y_{\eta}^2} \bar{u} + y_{\eta}(v_x - x_{\tau}) \right) \\
&\quad + y_{\xi}x_{\eta}y_{\xi\tau}(v_x - x_{\tau}) + x_{\xi}y_{\eta}x_{\xi\tau}(v_y - y_{\tau}) \\
&\quad + x_{\xi}y_{\eta}y_{\xi\tau}v_{tx} - y_{\xi}x_{\eta}y_{\xi\tau}v_{tx} - x_{\xi}y_{\eta}x_{\xi\tau}v_{ty} + y_{\xi}x_{\eta}x_{\xi\tau}v_{ty}] \quad (\text{A.29})
\end{aligned}$$

$$\begin{aligned}
&(\text{I} + \text{II})_{x_{\xi\tau}y_{\xi\tau}} = \\
\frac{1}{J} & [y_{\xi}x_{\tau\xi} \left(\sqrt{x_{\eta}^2 + y_{\eta}^2} \bar{u} + y_{\eta}(v_x - x_{\tau}) - x_{\eta}(v_y - y_{\tau}) - y_{\eta}(v_x - x_{\tau}) \right) \\
& - x_{\xi}y_{\tau\xi} \left(\sqrt{x_{\eta}^2 + y_{\eta}^2} \bar{u} + y_{\eta}(v_x - x_{\tau}) - x_{\eta}(v_y - y_{\tau}) + x_{\eta}(v_y - y_{\tau}) \right) \\
& + y_{\xi}x_{\eta}y_{\xi\tau}(v_x - x_{\tau}) + x_{\xi}y_{\eta}x_{\xi\tau}(v_y - y_{\tau}) \\
& + x_{\xi}y_{\eta}y_{\xi\tau}v_{tx} - y_{\xi}x_{\eta}y_{\xi\tau}v_{tx} - x_{\xi}y_{\eta}x_{\xi\tau}v_{ty} + y_{\xi}x_{\eta}x_{\xi\tau}v_{ty}] \quad (\text{A.30})
\end{aligned}$$

$$\begin{aligned}
(\text{I} + \text{II})_{x_{\xi\tau}y_{\xi\tau}} &= \frac{1}{J} [y_{\xi}x_{\tau\xi} \left(2\sqrt{x_{\eta}^2 + y_{\eta}^2} \bar{u} - y_{\eta}(v_x - x_{\tau}) \right) \\
&\quad - x_{\xi}y_{\tau\xi} \left(2\sqrt{x_{\eta}^2 + y_{\eta}^2} \bar{u} + x_{\eta}(v_y - y_{\tau}) \right) \\
&\quad + y_{\xi}x_{\eta}y_{\xi\tau}(v_x - x_{\tau}) + x_{\xi}y_{\eta}x_{\xi\tau}(v_y - y_{\tau}) \\
&\quad + x_{\xi}y_{\eta}y_{\xi\tau}v_{tx} - y_{\xi}x_{\eta}y_{\xi\tau}v_{tx} - x_{\xi}y_{\eta}x_{\xi\tau}v_{ty} + y_{\xi}x_{\eta}x_{\xi\tau}v_{ty}] \quad (\text{A.31})
\end{aligned}$$

$$\begin{aligned}
(I + II)_{x_{\xi\tau}y_{\xi\tau}} &= \frac{1}{J} [2\sqrt{x_{\eta}^2 + y_{\eta}^2} \bar{u} (y_{\xi}x_{\tau\xi} - x_{\xi}y_{\tau\xi}) \\
&\quad - y_{\xi}x_{\tau\xi}y_{\eta} (v_x - x_{\tau}) - x_{\xi}y_{\tau\xi}x_{\eta} (v_y - y_{\tau}) \\
&\quad + y_{\xi}x_{\eta}y_{\xi\tau} (v_x - x_{\tau}) + x_{\xi}y_{\eta}x_{\xi\tau} (v_y - y_{\tau}) \\
&\quad + x_{\xi}y_{\eta}y_{\xi\tau}v_{tx} - y_{\xi}x_{\eta}y_{\xi\tau}v_{tx} - x_{\xi}y_{\eta}x_{\xi\tau}v_{ty} + y_{\xi}x_{\eta}x_{\xi\tau}v_{ty} \\
&\quad + y_{\xi}y_{\eta}x_{\xi\tau}v_{tx} - y_{\xi}y_{\eta}x_{\xi\tau}v_{tx} \\
&\quad + x_{\xi}x_{\eta}y_{\xi\tau}v_{ty} - x_{\xi}x_{\eta}y_{\xi\tau}v_{ty}] \tag{A.32}
\end{aligned}$$

$$\begin{aligned}
(I + II)_{x_{\xi\tau}y_{\xi\tau}} &= \frac{1}{J} [2\sqrt{x_{\eta}^2 + y_{\eta}^2} \bar{u} (y_{\xi}x_{\tau\xi} - x_{\xi}y_{\tau\xi}) \\
&\quad + x_{\tau\xi}y_{\eta} (-y_{\xi} (v_x - x_{\tau} - v_{tx}) + x_{\xi} (v_y - y_{\tau} - v_{ty})) \\
&\quad - y_{\xi\tau}x_{\eta} (-y_{\xi} (v_x - x_{\tau} - v_{tx}) + x_{\xi} (v_y - y_{\tau} - v_{ty})) \\
&\quad + x_{\xi}y_{\eta}y_{\xi\tau}v_{tx} + y_{\xi}x_{\eta}x_{\xi\tau}v_{ty} \\
&\quad - y_{\xi}y_{\eta}x_{\xi\tau}v_{tx} \\
&\quad - x_{\xi}x_{\eta}y_{\xi\tau}v_{ty}] \tag{A.33}
\end{aligned}$$

On wing surface, velocity v from G flux which is perpendicular to $\eta = konst.$ is equal zero and correspond to following expression in equation (A.33):

$$v = -y_{\xi} (v_x - x_{\tau} - v_{tx}) + x_{\xi} (v_y - y_{\tau} - v_{ty}) = 0. \tag{A.34}$$

From this follows

$$\begin{aligned}
(I + II)_{x_{\xi\tau}y_{\xi\tau}} &= \frac{1}{J} [2\sqrt{x_{\eta}^2 + y_{\eta}^2} \bar{u} (y_{\xi}x_{\tau\xi} - x_{\xi}y_{\tau\xi}) \\
&\quad + x_{\xi}y_{\eta}y_{\xi\tau}v_{tx} + y_{\xi}x_{\eta}x_{\xi\tau}v_{ty} - y_{\xi}y_{\eta}x_{\xi\tau}v_{tx} - x_{\xi}x_{\eta}y_{\xi\tau}v_{ty}] \tag{A.35}
\end{aligned}$$

I + II (parts with $x_{\xi\xi}$ i $y_{\xi\xi}$):

$$\begin{aligned}
(I + II)_{x_{\xi\xi}y_{\xi\xi}} &= \frac{1}{J}[-y_{\eta}y_{\xi\xi}(v_x - x_{\tau})^2 + x_{\eta}y_{\xi\xi}(v_y - y_{\tau})(v_x - x_{\tau}) \\
&\quad + y_{\eta}y_{\xi\xi}(v_x - x_{\tau})v_{tx} - x_{\eta}y_{\xi\xi}(v_y - y_{\tau})v_{tx} \\
&\quad + y_{\eta}x_{\xi\xi}(v_x - x_{\tau})(v_y - y_{\tau}) - x_{\eta}x_{\xi\xi}(v_y - y_{\tau})^2 \\
&\quad - y_{\eta}x_{\xi\xi}(v_x - x_{\tau})v_{ty} + x_{\eta}x_{\xi\xi}(v_y - y_{\tau})v_{ty}] \cdot \frac{J}{J}
\end{aligned} \tag{A.36}$$

$$\begin{aligned}
(I + II)_{x_{\xi\xi}y_{\xi\xi}} &= \frac{1}{J^2}[-y_{\eta}^2x_{\xi}y_{\xi\xi}(v_x - x_{\tau})^2 + x_{\eta}y_{\eta}y_{\xi}y_{\xi\xi}(v_x - x_{\tau})^2 \\
&\quad + x_{\xi}x_{\eta}y_{\eta}y_{\xi\xi}(v_x - x_{\tau})(v_y - y_{\tau}) - y_{\xi}x_{\eta}^2y_{\xi\xi}(v_x - x_{\tau})(v_y - y_{\tau}) \\
&\quad + x_{\xi}y_{\eta}^2y_{\xi\xi}(v_x - x_{\tau})v_{tx} - y_{\xi}x_{\eta}y_{\eta}y_{\xi\xi}(v_x - x_{\tau})v_{tx} \\
&\quad - x_{\xi}x_{\eta}y_{\eta}y_{\xi\xi}(v_y - y_{\tau})v_{tx} + y_{\xi}x_{\eta}^2y_{\xi\xi}(v_y - y_{\tau})v_{tx} \\
&\quad + x_{\xi}y_{\eta}^2x_{\xi\xi}(v_x - x_{\tau})(v_y - y_{\tau}) - x_{\eta}y_{\eta}y_{\xi}x_{\xi\xi}(v_x - x_{\tau})(v_y - y_{\tau}) \\
&\quad - x_{\xi}x_{\eta}y_{\eta}x_{\xi\xi}(v_y - y_{\tau})^2 + y_{\xi}x_{\eta}^2x_{\xi\xi}(v_y - y_{\tau})^2 \\
&\quad - x_{\xi}y_{\eta}^2x_{\xi\xi}(v_x - x_{\tau})v_{ty} + y_{\xi}x_{\eta}y_{\eta}x_{\xi\xi}(v_x - x_{\tau})v_{ty} \\
&\quad + x_{\xi}x_{\eta}y_{\eta}x_{\xi\xi}(v_y - y_{\tau})v_{ty} - y_{\xi}x_{\eta}^2x_{\xi\xi}(v_y - y_{\tau})v_{ty} \\
&\quad + x_{\xi}y_{\xi\xi}x_{\eta}^2(v_y - y_{\tau})^2 - x_{\xi}y_{\xi\xi}x_{\eta}^2(v_y - y_{\tau})^2 \\
&\quad + x_{\xi}x_{\eta}y_{\eta}y_{\xi\xi}(v_x - x_{\tau})(v_y - y_{\tau}) - x_{\xi}x_{\eta}y_{\eta}y_{\xi\xi}(v_x - x_{\tau})(v_y - y_{\tau})]
\end{aligned} \tag{A.37}$$

$$\begin{aligned}
& (I + II)_{x_{\xi\xi}y_{\xi\xi}} = \\
& \frac{1}{J^2} [-x_{\xi}y_{\xi\xi} (y_{\eta}^2 (v_x - x_{\tau})^2 - 2x_{\eta}y_{\eta} (v_x - x_{\tau}) (v_y - y_{\tau}) + x_{\eta}^2 (v_y - y_{\tau})^2) \\
& \quad + x_{\eta}y_{\eta}y_{\xi}y_{\xi\xi} (v_x - x_{\tau})^2 \\
& \quad - y_{\xi}x_{\eta}^2y_{\xi\xi} (v_x - x_{\tau}) (v_y - y_{\tau}) \\
& \quad + x_{\xi}y_{\eta}^2y_{\xi\xi} (v_x - x_{\tau}) v_{tx} - y_{\xi}x_{\eta}y_{\eta}y_{\xi\xi} (v_x - x_{\tau}) v_{tx} \\
& \quad - x_{\xi}x_{\eta}y_{\eta}y_{\xi\xi} (v_y - y_{\tau}) v_{tx} + y_{\xi}x_{\eta}^2y_{\xi\xi} (v_y - y_{\tau}) v_{tx} \\
& \quad + x_{\xi}y_{\eta}^2x_{\xi\xi} (v_x - x_{\tau}) (v_y - y_{\tau}) - x_{\eta}y_{\eta}y_{\xi}x_{\xi\xi} (v_x - x_{\tau}) (v_y - y_{\tau}) \\
& \quad - x_{\xi}x_{\eta}y_{\eta}x_{\xi\xi} (v_y - y_{\tau})^2 + y_{\xi}x_{\eta}^2x_{\xi\xi} (v_y - y_{\tau})^2 \\
& \quad - x_{\xi}y_{\eta}^2x_{\xi\xi} (v_x - x_{\tau}) v_{ty} + y_{\xi}x_{\eta}y_{\eta}x_{\xi\xi} (v_x - x_{\tau}) v_{ty} \\
& \quad + x_{\xi}x_{\eta}y_{\eta}x_{\xi\xi} (v_y - y_{\tau}) v_{ty} - y_{\xi}x_{\eta}^2x_{\xi\xi} (v_y - y_{\tau}) v_{ty} \\
& \quad + x_{\xi}y_{\xi\xi}x_{\eta}^2 (v_y - y_{\tau})^2 \\
& \quad - x_{\xi}x_{\eta}y_{\eta}y_{\xi\xi} (v_x - x_{\tau}) (v_y - y_{\tau})] \quad (A.38)
\end{aligned}$$

$$\begin{aligned}
& (I + II)_{x_{\xi\xi}y_{\xi\xi}} = \frac{1}{J^2} [-x_{\xi}y_{\xi\xi} (x_{\eta}^2 + y_{\eta}^2) \bar{u}^2 \\
& \quad + x_{\eta}y_{\eta}y_{\xi}y_{\xi\xi} (v_x - x_{\tau})^2 \\
& \quad - y_{\xi}x_{\eta}^2y_{\xi\xi} (v_x - x_{\tau}) (v_y - y_{\tau}) \\
& \quad + x_{\xi}y_{\eta}^2y_{\xi\xi} (v_x - x_{\tau}) v_{tx} - y_{\xi}x_{\eta}y_{\eta}y_{\xi\xi} (v_x - x_{\tau}) v_{tx} \\
& \quad - x_{\xi}x_{\eta}y_{\eta}y_{\xi\xi} (v_y - y_{\tau}) v_{tx} + y_{\xi}x_{\eta}^2y_{\xi\xi} (v_y - y_{\tau}) v_{tx} \\
& \quad + x_{\xi}y_{\eta}^2x_{\xi\xi} (v_x - x_{\tau}) (v_y - y_{\tau}) - x_{\eta}y_{\eta}y_{\xi}x_{\xi\xi} (v_x - x_{\tau}) (v_y - y_{\tau}) \\
& \quad - x_{\xi}x_{\eta}y_{\eta}x_{\xi\xi} (v_y - y_{\tau})^2 + y_{\xi}x_{\eta}^2x_{\xi\xi} (v_y - y_{\tau})^2 \\
& \quad - x_{\xi}y_{\eta}^2x_{\xi\xi} (v_x - x_{\tau}) v_{ty} + y_{\xi}x_{\eta}y_{\eta}x_{\xi\xi} (v_x - x_{\tau}) v_{ty} \\
& \quad + x_{\xi}x_{\eta}y_{\eta}x_{\xi\xi} (v_y - y_{\tau}) v_{ty} - y_{\xi}x_{\eta}^2x_{\xi\xi} (v_y - y_{\tau}) v_{ty} \\
& \quad + x_{\xi}y_{\xi\xi}x_{\eta}^2 (v_y - y_{\tau})^2 \\
& \quad - x_{\xi}x_{\eta}y_{\eta}y_{\xi\xi} (v_x - x_{\tau}) (v_y - y_{\tau}) \\
& \quad + y_{\xi}x_{\xi\xi}y_{\eta}^2 (v_x - x_{\tau})^2 - y_{\xi}x_{\xi\xi}y_{\eta}^2 (v_x - x_{\tau})^2 \\
& \quad + x_{\eta}y_{\eta}y_{\xi}x_{\xi\xi} (v_x - x_{\tau}) (v_y - y_{\tau}) - x_{\eta}y_{\eta}y_{\xi}x_{\xi\xi} (v_x - x_{\tau}) (v_y - y_{\tau})] \quad (A.39)
\end{aligned}$$

$$\begin{aligned}
(I + II)_{x_{\xi\xi}y_{\xi\xi}} &= \frac{1}{J^2} [-x_{\xi}y_{\xi\xi} (x_{\eta}^2 + y_{\eta}^2) \bar{u}^2 \\
&+ y_{\xi}x_{\xi\xi} (y_{\eta}^2 (v_x - x_{\tau})^2 - 2x_{\eta}y_{\eta} (v_x - x_{\tau}) (v_y - y_{\tau}) + x_{\eta}^2 (v_y - y_{\tau})^2) \\
&\quad + x_{\eta}y_{\eta}y_{\xi}y_{\xi\xi} (v_x - x_{\tau})^2 \\
&\quad - y_{\xi}x_{\eta}^2y_{\xi\xi} (v_x - x_{\tau}) (v_y - y_{\tau}) \\
&+ x_{\xi}y_{\eta}^2y_{\xi\xi} (v_x - x_{\tau}) v_{tx} - y_{\xi}x_{\eta}y_{\eta}y_{\xi\xi} (v_x - x_{\tau}) v_{tx} \\
&- x_{\xi}x_{\eta}y_{\eta}y_{\xi\xi} (v_y - y_{\tau}) v_{tx} + y_{\xi}x_{\eta}^2y_{\xi\xi} (v_y - y_{\tau}) v_{tx} \\
&\quad + x_{\xi}y_{\eta}^2x_{\xi\xi} (v_x - x_{\tau}) (v_y - y_{\tau}) \\
&\quad - x_{\xi}x_{\eta}y_{\eta}x_{\xi\xi} (v_y - y_{\tau})^2 \\
&- x_{\xi}y_{\eta}^2x_{\xi\xi} (v_x - x_{\tau}) v_{ty} + y_{\xi}x_{\eta}y_{\eta}x_{\xi\xi} (v_x - x_{\tau}) v_{ty} \\
&+ x_{\xi}x_{\eta}y_{\eta}x_{\xi\xi} (v_y - y_{\tau}) v_{ty} - y_{\xi}x_{\eta}^2x_{\xi\xi} (v_y - y_{\tau}) v_{ty} \\
&\quad + x_{\xi}y_{\xi\xi}x_{\eta}^2 (v_y - y_{\tau})^2 \\
&\quad - x_{\xi}x_{\eta}y_{\eta}y_{\xi\xi} (v_x - x_{\tau}) (v_y - y_{\tau}) \\
&\quad - y_{\xi}x_{\xi\xi}y_{\eta}^2 (v_x - x_{\tau})^2 \\
&+ x_{\eta}y_{\eta}y_{\xi}x_{\xi\xi} (v_x - x_{\tau}) (v_y - y_{\tau})] \tag{A.40}
\end{aligned}$$

$$\begin{aligned}
(\text{I} + \text{II})_{x_\xi y_\xi} &= \frac{1}{J^2} [-x_\xi y_\xi (x_\eta^2 + y_\eta^2) \bar{u}^2 + y_\xi x_\xi (x_\eta^2 + y_\eta^2) \bar{u}^2 \\
&\quad + x_\eta y_\eta y_\xi y_\xi (v_x - x_\tau)^2 \\
&\quad - y_\xi x_\eta^2 y_\xi (v_x - x_\tau) (v_y - y_\tau) \\
&\quad + x_\xi y_\eta^2 y_\xi (v_x - x_\tau) v_{tx} - y_\xi x_\eta y_\eta y_\xi (v_x - x_\tau) v_{tx} \\
&\quad - x_\xi x_\eta y_\eta y_\xi (v_y - y_\tau) v_{tx} + y_\xi x_\eta^2 y_\xi (v_y - y_\tau) v_{tx} \\
&\quad + x_\xi y_\eta^2 x_\xi (v_x - x_\tau) (v_y - y_\tau) \\
&\quad - x_\xi x_\eta y_\eta x_\xi (v_y - y_\tau)^2 \\
&\quad - x_\xi y_\eta^2 x_\xi (v_x - x_\tau) v_{ty} + y_\xi x_\eta y_\eta x_\xi (v_x - x_\tau) v_{ty} \\
&\quad + x_\xi x_\eta y_\eta x_\xi (v_y - y_\tau) v_{ty} - y_\xi x_\eta^2 x_\xi (v_y - y_\tau) v_{ty} \\
&\quad + x_\xi y_\xi x_\eta^2 (v_y - y_\tau)^2 \\
&\quad - x_\xi x_\eta y_\eta y_\xi (v_x - x_\tau) (v_y - y_\tau) \\
&\quad - y_\xi x_\xi y_\eta^2 (v_x - x_\tau)^2 \\
&\quad + x_\eta y_\eta y_\xi x_\xi (v_x - x_\tau) (v_y - y_\tau) \\
&\quad + x_\xi x_\eta y_\eta y_\xi (v_x - x_\tau) v_{ty} - x_\xi x_\eta y_\eta y_\xi (v_x - x_\tau) v_{ty} \\
&\quad + x_\xi x_\eta^2 y_\xi (v_y - y_\tau) v_{ty} - x_\xi x_\eta^2 y_\xi (v_y - y_\tau) v_{ty}] \tag{A.41}
\end{aligned}$$

$$\begin{aligned}
(I + II)_{x_\xi y_\xi} &= \frac{1}{J^2} [(x_\eta^2 + y_\eta^2) \bar{u}^2 (y_\xi x_{\xi\xi} - x_\xi y_{\xi\xi}) \\
&+ x_\eta y_\eta y_{\xi\xi} (v_x - x_\tau) (y_\xi (v_x - x_\tau - v_{tx}) - x_\xi (v_y - y_\tau - v_{ty})) \\
&+ x_\eta^2 y_{\xi\xi} (v_y - y_\tau) (-y_\xi (v_x - x_\tau - v_{tx}) + x_\xi (v_y - y_\tau - v_{ty})) \\
&\quad + x_\xi y_\eta^2 y_{\xi\xi} (v_x - x_\tau) v_{tx} \\
&\quad - x_\xi x_\eta y_\eta y_{\xi\xi} (v_y - y_\tau) v_{tx} \\
&\quad + x_\xi y_\eta^2 x_{\xi\xi} (v_x - x_\tau) (v_y - y_\tau) \\
&\quad - x_\xi x_\eta y_\eta x_{\xi\xi} (v_y - y_\tau)^2 \\
&- x_\xi y_\eta^2 x_{\xi\xi} (v_x - x_\tau) v_{ty} + y_\xi x_\eta y_\eta x_{\xi\xi} (v_x - x_\tau) v_{ty} \\
&+ x_\xi x_\eta y_\eta x_{\xi\xi} (v_y - y_\tau) v_{ty} - y_\xi x_\eta^2 x_{\xi\xi} (v_y - y_\tau) v_{ty} \\
&\quad - y_\xi x_\xi y_\eta^2 (v_x - x_\tau)^2 \\
&\quad + x_\eta y_\eta y_\xi x_{\xi\xi} (v_x - x_\tau) (v_y - y_\tau) \\
&\quad - x_\xi x_\eta y_\eta y_{\xi\xi} (v_x - x_\tau) v_{ty} \\
&\quad + x_\xi x_\eta^2 y_{\xi\xi} (v_y - y_\tau) v_{ty}] \tag{A.42}
\end{aligned}$$

With condition in equation (A.34), it follows

$$\begin{aligned}
(I + II)_{x_\xi y_\xi} &= \frac{1}{J^2} [(x_\eta^2 + y_\eta^2) \bar{u}^2 (y_\xi x_{\xi\xi} - x_\xi y_{\xi\xi}) \\
&\quad + x_\xi y_\eta^2 y_{\xi\xi} (v_x - x_\tau) v_{tx} \\
&\quad - x_\xi x_\eta y_\eta y_{\xi\xi} (v_y - y_\tau) v_{tx} \\
&\quad + x_\xi y_\eta^2 x_{\xi\xi} (v_x - x_\tau) (v_y - y_\tau) \\
&\quad - x_\xi x_\eta y_\eta x_{\xi\xi} (v_y - y_\tau)^2 \\
&- x_\xi y_\eta^2 x_{\xi\xi} (v_x - x_\tau) v_{ty} + y_\xi x_\eta y_\eta x_{\xi\xi} (v_x - x_\tau) v_{ty} \\
&+ x_\xi x_\eta y_\eta x_{\xi\xi} (v_y - y_\tau) v_{ty} - y_\xi x_\eta^2 x_{\xi\xi} (v_y - y_\tau) v_{ty} \\
&\quad - y_\xi x_\xi y_\eta^2 (v_x - x_\tau)^2 \\
&\quad + x_\eta y_\eta y_\xi x_{\xi\xi} (v_x - x_\tau) (v_y - y_\tau) \\
&\quad - x_\xi x_\eta y_\eta y_{\xi\xi} (v_x - x_\tau) v_{ty} \\
&\quad + x_\xi x_\eta^2 y_{\xi\xi} (v_y - y_\tau) v_{ty}] \tag{A.43}
\end{aligned}$$

$$\begin{aligned}
(I + II)_{x_{\xi\xi}y_{\xi\xi}} &= \frac{1}{J^2} [(x_{\eta}^2 + y_{\eta}^2) \bar{u}^2 (y_{\xi}x_{\xi\xi} - x_{\xi}y_{\xi\xi}) \\
&\quad x_{\xi\xi}y_{\eta}^2 (v_x - x_{\tau}) (-y_{\xi} (v_x - x_{\tau} - v_{tx}) + x_{\xi} (v_y - y_{\tau} - v_{ty})) \\
&\quad + x_{\eta}y_{\eta}x_{\xi\xi} (v_y - y_{\tau}) (y_{\xi} (v_x - x_{\tau} - v_{tx}) - x_{\xi} (v_y - y_{\tau} - v_{ty})) \\
&\quad \quad + x_{\xi}y_{\eta}^2 y_{\xi\xi} (v_x - x_{\tau}) v_{tx} \\
&\quad \quad - x_{\xi}x_{\eta}y_{\eta}y_{\xi\xi} (v_y - y_{\tau}) v_{tx} \\
&\quad \quad + y_{\xi}x_{\eta}y_{\eta}x_{\xi\xi} (v_x - x_{\tau}) v_{ty} \\
&\quad \quad - y_{\xi}x_{\eta}^2 x_{\xi\xi} (v_y - y_{\tau}) v_{ty} \\
&\quad \quad - x_{\xi}x_{\eta}y_{\eta}y_{\xi\xi} (v_x - x_{\tau}) v_{ty} \\
&\quad \quad + x_{\xi}x_{\eta}^2 y_{\xi\xi} (v_y - y_{\tau}) v_{ty} \\
&\quad \quad - y_{\xi}y_{\eta}^2 x_{\xi\xi} (v_x - x_{\tau}) v_{tx} \\
&\quad \quad + y_{\xi}x_{\eta}y_{\eta}x_{\xi\xi} (v_y - y_{\tau}) v_{tx}] \tag{A.44}
\end{aligned}$$

With condition in equation (A.34), it follows

$$\begin{aligned}
(I + II)_{x_{\xi\xi}y_{\xi\xi}} &= \frac{1}{J^2} [(x_{\eta}^2 + y_{\eta}^2) \bar{u}^2 (y_{\xi}x_{\xi\xi} - x_{\xi}y_{\xi\xi}) \\
&\quad + x_{\xi}y_{\eta}^2 y_{\xi\xi} (v_x - x_{\tau}) v_{tx} \\
&\quad - x_{\xi}x_{\eta}y_{\eta}y_{\xi\xi} (v_y - y_{\tau}) v_{tx} \\
&\quad + y_{\xi}x_{\eta}y_{\eta}x_{\xi\xi} (v_x - x_{\tau}) v_{ty} \\
&\quad \quad - y_{\xi}x_{\eta}^2 x_{\xi\xi} (v_y - y_{\tau}) v_{ty} \\
&\quad \quad - x_{\xi}x_{\eta}y_{\eta}y_{\xi\xi} (v_x - x_{\tau}) v_{ty} \\
&\quad \quad + x_{\xi}x_{\eta}^2 y_{\xi\xi} (v_y - y_{\tau}) v_{ty} \\
&\quad \quad - y_{\xi}y_{\eta}^2 x_{\xi\xi} (v_x - x_{\tau}) v_{tx} \\
&\quad \quad + y_{\xi}x_{\eta}y_{\eta}x_{\xi\xi} (v_y - y_{\tau}) v_{tx}] \tag{A.45}
\end{aligned}$$

$$\underline{(I + II)_{x_{\xi\tau}y_{\xi\tau}} + (I + II)_{x_{\xi\xi}y_{\xi\xi}} + (I + II)_{\text{rest}}}$$

$$\begin{aligned}
I + II = & \frac{1}{J} [2\sqrt{x_{\eta}^2 + y_{\eta}^2} \bar{u} (y_{\xi}x_{\tau\xi} - x_{\xi}y_{\tau\xi}) \\
& + x_{\xi}y_{\eta}y_{\xi\tau}v_{tx} + y_{\xi}x_{\eta}x_{\xi\tau}v_{ty} - y_{\xi}y_{\eta}x_{\xi\tau}v_{tx} - x_{\xi}x_{\eta}y_{\xi\tau}v_{ty}] \\
& + \frac{1}{J^2} [(x_{\eta}^2 + y_{\eta}^2) \bar{u}^2 (y_{\xi}x_{\xi\xi} - x_{\xi}y_{\xi\xi}) \\
& \quad + x_{\xi}y_{\eta}^2y_{\xi\xi} (v_x - x_{\tau}) v_{tx} \\
& \quad - x_{\xi}x_{\eta}y_{\eta}y_{\xi\xi} (v_y - y_{\tau}) v_{tx} \\
& \quad + y_{\xi}x_{\eta}y_{\eta}x_{\xi\xi} (v_x - x_{\tau}) v_{ty} \\
& \quad - y_{\xi}x_{\eta}^2x_{\xi\xi} (v_y - y_{\tau}) v_{ty} \\
& \quad - x_{\xi}x_{\eta}y_{\eta}y_{\xi\xi} (v_x - x_{\tau}) v_{ty} \\
& \quad + x_{\xi}x_{\eta}^2y_{\xi\xi} (v_y - y_{\tau}) v_{ty} \\
& \quad - y_{\xi}y_{\eta}^2x_{\xi\xi} (v_x - x_{\tau}) v_{tx} \\
& \quad + y_{\xi}x_{\eta}y_{\eta}x_{\xi\xi} (v_y - y_{\tau}) v_{tx}] \\
& \quad + \frac{1}{J} [y_{\xi}y_{\eta}v_{tx\xi} (v_x - x_{\tau}) \\
& \quad - y_{\xi}x_{\eta}v_{tx\xi} (v_y - y_{\tau}) + Jx_{\tau\tau}y_{\xi} + Jv_{tx\tau}y_{\xi}] \\
& \quad - \frac{1}{J} [x_{\xi}y_{\eta}v_{ty\xi} (v_x - x_{\tau}) \\
& \quad - x_{\xi}x_{\eta}v_{ty\xi} (v_y - y_{\tau}) + Jy_{\tau\tau}x_{\xi} + Jv_{ty\tau}x_{\xi}]
\end{aligned} \tag{A.46}$$

grad $p \cdot \vec{n}$:

$$\begin{aligned}
\text{grad}p \cdot \vec{n} &= \frac{\partial p}{\partial x} n_x + \frac{\partial p}{\partial y} n_y \\
&= \left[\frac{1}{J} \left(y_\eta \frac{\partial p}{\partial \xi} - y_\xi \frac{\partial p}{\partial \eta} \right) \right] (-y_\xi) + \left[\frac{1}{J} \left(-x_\eta \frac{\partial p}{\partial \xi} + x_\xi \frac{\partial p}{\partial \eta} \right) \right] (x_\xi) \\
&= \frac{1}{J} \left(-y_\xi y_\eta \frac{\partial p}{\partial \xi} + y_\xi^2 \frac{\partial p}{\partial \eta} \right) + \frac{1}{J} \left(-x_\xi x_\eta \frac{\partial p}{\partial \xi} + x_\xi^2 \frac{\partial p}{\partial \eta} \right) \\
&= \frac{1}{J} \frac{\partial p}{\partial \eta} (x_\xi^2 + y_\xi^2) - \frac{1}{J} \frac{\partial p}{\partial \xi} (x_\xi x_\eta + y_\xi y_\eta) \tag{A.47}
\end{aligned}$$

According to equation (A.5) it follows:

$$\begin{aligned}
&\rho \left[\frac{1}{J} [2\sqrt{x_\eta^2 + y_\eta^2} \bar{u} (y_\xi x_{\tau\xi} - x_\xi y_{\tau\xi}) \right. \\
&+ x_\xi y_\eta y_{\xi\tau} v_{tx} + y_\xi x_\eta x_{\xi\tau} v_{ty} - y_\xi y_\eta x_{\xi\tau} v_{tx} - x_\xi x_\eta y_{\xi\tau} v_{ty}] \\
&+ \frac{1}{J^2} [(x_\eta^2 + y_\eta^2) \bar{u}^2 (y_\xi x_{\xi\xi} - x_\xi y_{\xi\xi}) \\
&\quad + x_\xi y_\eta^2 y_{\xi\xi} (v_x - x_\tau) v_{tx} \\
&\quad - x_\xi x_\eta y_\eta y_{\xi\xi} (v_y - y_\tau) v_{tx} \\
&\quad + y_\xi x_\eta y_\eta x_{\xi\xi} (v_x - x_\tau) v_{ty} \\
&\quad - y_\xi x_\eta^2 x_{\xi\xi} (v_y - y_\tau) v_{ty} \\
&\quad - x_\xi x_\eta y_\eta y_{\xi\xi} (v_x - x_\tau) v_{ty} \\
&\quad + x_\xi x_\eta^2 y_{\xi\xi} (v_y - y_\tau) v_{ty} \\
&\quad - y_\xi y_\eta^2 x_{\xi\xi} (v_x - x_\tau) v_{tx} \\
&\quad \left. + y_\xi x_\eta y_\eta x_{\xi\xi} (v_y - y_\tau) v_{tx} \right] \\
&\quad + \frac{1}{J} [y_\xi y_\eta v_{tx\xi} (v_x - x_\tau) \\
&\quad - y_\xi x_\eta v_{tx\xi} (v_y - y_\tau) + J x_{\tau\tau} y_\xi + J v_{tx\tau} y_\xi] \\
&\quad - \frac{1}{J} [x_\xi y_\eta v_{ty\xi} (v_x - x_\tau) \\
&\quad - x_\xi x_\eta v_{ty\xi} (v_y - y_\tau) + J y_{\tau\tau} x_\xi + J v_{ty\tau} x_\xi] = \\
&\quad \frac{1}{J} \frac{\partial p}{\partial \eta} (x_\xi^2 + y_\xi^2) - \frac{1}{J} \frac{\partial p}{\partial \xi} (x_\xi x_\eta + y_\xi y_\eta) \tag{A.48}
\end{aligned}$$

$$\begin{aligned}
& \frac{\partial p}{\partial \eta} (x_\xi^2 + y_\xi^2) = \frac{\partial p}{\partial \xi} (x_\xi x_\eta + y_\xi y_\eta) \\
& + \rho \{ 2\sqrt{x_\eta^2 + y_\eta^2} \bar{u} (y_\xi x_{\tau\xi} - x_\xi y_{\tau\xi}) \\
& + x_\xi y_\eta y_{\xi\tau} v_{tx} + y_\xi x_\eta x_{\xi\tau} v_{ty} - y_\xi y_\eta x_{\xi\tau} v_{tx} - x_\xi x_\eta y_{\xi\tau} v_{ty} \\
& + \frac{1}{J} [(x_\eta^2 + y_\eta^2) \bar{u}^2 (y_\xi x_{\xi\xi} - x_\xi y_{\xi\xi}) \\
& + x_\xi y_\eta^2 y_{\xi\xi} (v_x - x_\tau) v_{tx} - x_\xi x_\eta y_\eta y_{\xi\xi} (v_y - y_\tau) v_{tx} \\
& + y_\xi x_\eta y_\eta x_{\xi\xi} (v_x - x_\tau) v_{ty} - y_\xi x_\eta^2 x_{\xi\xi} (v_y - y_\tau) v_{ty} \\
& - x_\xi x_\eta y_\eta y_{\xi\xi} (v_x - x_\tau) v_{ty} + x_\xi x_\eta^2 y_{\xi\xi} (v_y - y_\tau) v_{ty} \\
& - y_\xi y_\eta^2 x_{\xi\xi} (v_x - x_\tau) v_{tx} + y_\xi x_\eta y_\eta x_{\xi\xi} (v_y - y_\tau) v_{tx}] \\
& + y_\xi y_\eta v_{tx\xi} (v_x - x_\tau) - y_\xi x_\eta v_{tx\xi} (v_y - y_\tau) + J x_{\tau\tau} y_\xi + J v_{tx\tau} y_\xi \\
& - x_\xi y_\eta v_{ty\xi} (v_x - x_\tau) + x_\xi x_\eta v_{ty\xi} (v_y - y_\tau) - J y_{\tau\tau} x_\xi - J v_{ty\tau} x_\xi \} \tag{A.49}
\end{aligned}$$

$$\begin{aligned}
& \frac{\partial p}{\partial \eta} (x_\xi^2 + y_\xi^2) = \frac{\partial p}{\partial \xi} (x_\xi x_\eta + y_\xi y_\eta) \\
& + \rho \{ J \left[\frac{\bar{u}^2}{(x_\xi^2 + y_\xi^2)} (y_\xi x_{\xi\xi} - x_\xi y_{\xi\xi}) + \frac{2\bar{u}}{\sqrt{x_\xi^2 + y_\xi^2}} (y_\xi x_{\tau\xi} - x_\xi y_{\tau\xi}) \right. \\
& \left. + x_{\tau\tau} y_\xi - y_{\tau\tau} x_\xi \right] \\
& + x_\xi y_\eta y_{\xi\tau} v_{tx} + y_\xi x_\eta x_{\xi\tau} v_{ty} - y_\xi y_\eta x_{\xi\tau} v_{tx} - x_\xi x_\eta y_{\xi\tau} v_{ty} \\
& + \frac{1}{J} [x_\xi y_\eta^2 y_{\xi\xi} (v_x - x_\tau) v_{tx} - x_\xi x_\eta y_\eta y_{\xi\xi} (v_y - y_\tau) v_{tx} \\
& + y_\xi x_\eta y_\eta x_{\xi\xi} (v_x - x_\tau) v_{ty} - y_\xi x_\eta^2 x_{\xi\xi} (v_y - y_\tau) v_{ty} \\
& - x_\xi x_\eta y_\eta y_{\xi\xi} (v_x - x_\tau) v_{ty} + x_\xi x_\eta^2 y_{\xi\xi} (v_y - y_\tau) v_{ty} \\
& - y_\xi y_\eta^2 x_{\xi\xi} (v_x - x_\tau) v_{tx} + y_\xi x_\eta y_\eta x_{\xi\xi} (v_y - y_\tau) v_{tx}] \\
& + y_\xi y_\eta v_{tx\xi} (v_x - x_\tau) - y_\xi x_\eta v_{tx\xi} (v_y - y_\tau) + J v_{tx\tau} y_\xi \\
& - x_\xi y_\eta v_{ty\xi} (v_x - x_\tau) + x_\xi x_\eta v_{ty\xi} (v_y - y_\tau) - J v_{ty\tau} x_\xi \} \tag{A.50}
\end{aligned}$$

$$\begin{aligned}
\frac{\partial p}{\partial \eta} (x_\xi^2 + y_\xi^2) &= \frac{\partial p}{\partial \xi} (x_\xi x_\eta + y_\xi y_\eta) + \rho \left\{ J \left[\frac{\bar{u}^2}{(x_\xi^2 + y_\xi^2)} (y_\xi x_{\xi\xi} - x_\xi y_{\xi\xi}) \right. \right. \\
&\quad \left. \left. + \frac{2\bar{u}}{\sqrt{x_\xi^2 + y_\xi^2}} (y_\xi x_{\tau\xi} - x_\xi y_{\tau\xi}) + x_{\tau\tau} y_\xi - y_{\tau\tau} x_\xi \right] \right. \\
&\quad \left. + v_{tx} y_\eta (x_\xi y_{\xi\tau} - y_\xi x_{\xi\tau}) - v_{ty} x_\eta (x_\xi y_{\xi\tau} - y_\xi x_{\xi\tau}) \right. \\
+ \frac{1}{J} &\left[y_\eta^2 (v_x - x_\tau) v_{tx} (x_\xi y_{\xi\xi} - y_\xi x_{\xi\xi}) - x_\eta y_\eta (v_y - y_\tau) v_{tx} (x_\xi y_{\xi\xi} - y_\xi x_{\xi\xi}) \right. \\
&\quad \left. + x_\eta y_\eta (v_x - x_\tau) v_{ty} (x_\xi y_{\xi\xi} - y_\xi x_{\xi\xi}) + x_\eta^2 (v_y - y_\tau) v_{ty} (x_\xi y_{\xi\xi} - y_\xi x_{\xi\xi}) \right] \\
&\quad + y_\eta (v_x - x_\tau) (y_\xi v_{tx\xi} - x_\xi v_{ty\xi}) - x_\eta (v_y - y_\tau) (y_\xi v_{tx\xi} - x_\xi v_{ty\xi}) \\
&\quad \left. + J (v_{tx\tau} y_\xi - v_{ty\tau} x_\xi) \right\} \tag{A.51}
\end{aligned}$$

$$\begin{aligned}
\frac{\partial p}{\partial \eta} (x_\xi^2 + y_\xi^2) &= \frac{\partial p}{\partial \xi} (x_\xi x_\eta + y_\xi y_\eta) + \rho \left\{ J \left[\frac{\bar{u}^2}{(x_\xi^2 + y_\xi^2)} (y_\xi x_{\xi\xi} - x_\xi y_{\xi\xi}) \right. \right. \\
&\quad \left. \left. + \frac{2\bar{u}}{\sqrt{x_\xi^2 + y_\xi^2}} (y_\xi x_{\tau\xi} - x_\xi y_{\tau\xi}) + x_{\tau\tau} y_\xi - y_{\tau\tau} x_\xi \right] \right. \\
&\quad \left. + (x_\xi y_{\xi\tau} - y_\xi x_{\xi\tau}) (v_{tx} y_\eta - v_{ty} x_\eta) \right. \\
+ \frac{1}{J} &\left[(x_\xi y_{\xi\xi} - y_\xi x_{\xi\xi}) (y_\eta^2 (v_x - x_\tau) v_{tx} - x_\eta y_\eta (v_y - y_\tau) v_{tx}) \right. \\
&\quad \left. + x_\eta y_\eta (v_x - x_\tau) v_{ty} + x_\eta^2 (v_y - y_\tau) v_{ty} \right] \\
&\quad + (y_\xi v_{tx\xi} - x_\xi v_{ty\xi}) (y_\eta (v_x - x_\tau) - x_\eta (v_y - y_\tau)) \\
&\quad \left. + J (v_{tx\tau} y_\xi - v_{ty\tau} x_\xi) \right\} \tag{A.52}
\end{aligned}$$

References

- [1] Wright J.R. *Introduction to Aircraft Aeroelasticity and Loads*. John Wiley & Sons Ltd, 2007.
- [2] Voss R. Ueber die ausbreitung akustischer stoerungen in transonischen stroemungsfeldern von tragfluegeln. Rept. DFVLR-FB 88-13, DFVLR, Institut fuer Aeroelastik, Goettingen, February 1988.
- [3] Hodges D. H., Pierce G. A. *Introduction to Structural Dynamics and Aeroelasticity*. Cambridge University Press, 2002.
- [4] Schuster D.M., Liu D.D., Huttzell L.J. Computational aeroelasticity: Success, progress, challenge. *Journal of Aircraft*, 40(5):843–856, 2003.
- [5] Theodorsen T., Garrick I.E. A theoretical and experimental investigation of the flutter problem. NACA TR-685, September 1940.
- [6] Albano E., Rodden W.P. A doublet-lattice method for calculating the lift distributions on oscillating surfaces in subsonic flows. *AIAA Journal*, 7(2):279–285, 1969.
- [7] Giesing J.P., Kalman T.P., Rodden W.P. Subsonic unsteady aerodynamics for general configurations, part I—direct application of the non-planar doublet-lattice method. Rept. AFFDL-TR-71-5, Pt. 1, Air Force Flight Dynamics Lab., Air Force Systems Command, April 1972.

- [8] Rodden W.P., Taylor P.F., McIntosh S.C. Further refinement of the non-planar aspects of the subsonic doublet-lattice lifting surface method. In *Proceedings of the 20th International Council of Aeronautical Sciences Congress*, Naples, Italy, Paper ICAS-96-2.8.2, September 1996.
- [9] Batina J.T. A finite-difference approximate-factorization algorithm for solution of the unsteady transonic small-disturbance equation. NASA TP 3129, January 1992.
- [10] Edwards J.W. Transonic Shock Oscillations and Wing Flutter Calculated with an Interactive Boundary Layer Coupling Method. Rept. NAS 1.15:110284, NASA, Langley Research Center, August 1996.
- [11] Cebeci T., Besnard E., Chen H.H. An interactive boundary-layer method for multielement airfoils. *Computers & Fluids*, 27(5–6):651–661, 1998.
- [12] T. Cebeci. *An engineering approach to the calculation of aerodynamic flows*. Springer, 1988.
- [13] Catherall D., Mangler K.W. The integration of the two-dimensional laminar boundary-layer equations past the point of vanishing skin friction. *Journal of Fluid Mechanics*, 26(1), September.
- [14] Drela M. *Two-Dimensional Transonic Aerodynamic Design and Analysis Using the Euler Equations*. PhD thesis, Massachusetts Institute of Technology, 1985.
- [15] Whitfield D.L., Swafford T.W., Jacocks J.L. Calculation of turbulent boundary layers with separation and viscous-inviscid interaction. *AIAA Journal*, 19(10):1315–1322, 1981.
- [16] Drela M., Giles M.B. Viscous-inviscid analysis of transonic and low reynolds number airfoils. *AIAA Journal*, 25(10):1347–1355, 1987.
- [17] Zhang Z., Liu F., Schuster D.M. An efficient euler method on non-moving cartesian grids with boundary-layer correction for wing flutter simulations. In *AIAA 2006-884*, January, 2006.
- [18] Kreiselmaier E., Laschka B. Small disturbance euler equations: Efficient and accurate tool for unsteady load prediction. *Journal of Aircraft*, 37(5):770–778, 2000.

- [19] Pechloff A., Laschka B. Small disturbance navier-stokes method: Efficient tool for predicting unsteady air loads. *Journal of Aircraft*, 43(1):17–29, 2006.
- [20] Filippone A., Sorensen J.N. Viscous-inviscid interaction using the navier-stokes equations. *AIAA Journal*, 35(9):1464–1471, 1997.
- [21] Stock H.W., Haase W. Navier-stokes airfoil computations with e^n transition prediction including transitional flow regions. *AIAA Journal*, 38(11):2059–2066, 2000.
- [22] Stock H.W. Infinite swept-wing navier-stokes computations with e^n transition prediction. *AIAA Journal*, 43(6):1221–1229, 2005.
- [23] Lighthill M.J. On displacement thickness. *Journal of Fluid Mechanics*, 4(4):383–392, 1958.
- [24] Prandtl L. Über Flüssigkeitsbewegung bei sehr kleiner Reibung. In *Proc. of III. Intern. Math. Congr.*, Heidelberg, 1904.
- [25] Goldstein S. On laminar boundary-layer flow near a position of separation. *Quarterly Journal of Mechanics and Applied Mathematics*, (1), 1948.
- [26] Steger J. L., Warming R. F. Flux vector splitting of the inviscid gasdynamic equations with application to finite difference methods. NASA-TM 78605, July 1979.
- [27] Bram Van Leer. Towards the ultimate conservative difference scheme v. a second-order sequel to godunov’s method. *J. Comput. Phys.*, 135(2):229–248, 1997.
- [28] Anderson W.K., Thomas J.L., Van Leer B. A comparison of finite volume flux vector splittings for the euler equations. In *23rd Aerospace Sciences Meeting*, page 16. American Institute of Aeronautics and Astronautics, Jan 14-17 1985.
- [29] Toro E.F. *Riemann Solvers and Numerical Methods for Fluid Dynamics*. Springer, 1999.
- [30] Virag Z. Lecture notes in fluid mechanics 2. URL: <http://www.fsb.hr/hydro>, 2008.
- [31] Schlichting H., Gersten K. *Grenzschicht Theorie*. Springer, 2006.

- [32] Ramm H.J. *Fluid Dynamics for the Study of Transonic Flow*. Oxford University Press, 1990.
- [33] Whitfield D.L. Analytical description of the complete turbulent boundary layer velocity profile. In *AIAA-78-1158*, July 1978.
- [34] Blasius H. Grenzsichten in Flüssigkeiten mit Kleiner Reibung. *Z. Math. Physik*, (56):1–37, 1908.
- [35] Obremski H.J., Morovkin M.V., Landahl M.T. A Portfolio of Stability Characteristics of Incompressible Boundary Layer. AGARD-ograph 134, NATO, Neuilly Sur Seine, France, 1969.
- [36] Steger J. L., Sorenson R. L. Automatic mesh-point clustering near a boundary in grid generation with elliptic partial differential equations. *Journal of Computational Physics*, 33(3):405–410, 1979.
- [37] Carstens V. Two-dimensional elliptic grid generator for airfoils and cascades. DLR-FB 88-52, 1988.
- [38] Thompson J.E., Warsi Z.U.A., Mastin C.W. *Numerical Grid Generation*. Elsevier Science Publishing Co., 1985.
- [39] Various authors. Experimental data base for computer program assessment - report of the fluid dynamics panel working group 04. AGARD-AR 138, May 1979.
- [40] Various authors. Compendium of unsteady aerodynamic measurement. AGARD-R 702, August 1982.
- [41] Deutsches Zentrum für Luft- und Raumfahrt. *Technical Documentation of the DLR TAU-Code*.
- [42] Magnus R., Yoshihara H. Inviscid transonic flow over airfoils. *AIAA Journal*, 8(12):2157–2161, 1970.
- [43] Anderson J.D., Jr. *Modern Compressible Flow*. McGraw-Hill Publishing Company, 1990.

- [44] Soda A. Numerical investigation of unsteady transonic shock/boundary-layer interaction for aeronautical applications. Forschungsbericht 2007-03, Deutsches Zentrum für Luft- und Raumfahrt, March 2007.
- [45] Tijdeman H. Investigation of the transonic flow around oscillating airfoils. NLR TR 77090 U, October 1977.

Curriculum vitae

Name and surname: Frane Majić
Date of birth: 28.12.1977
Place of birth: Varaždin, Croatia

Employment:

2003. - present Research assistant at the Faculty of Mechanical Engineering and Naval Architecture in Zagreb, University of Zagreb, Croatia

Education:

2003. - present Doctoral Study, Faculty of Mechanical Engineering and Naval Architecture, University of Zagreb, Croatia
1996. - 2002. Dipl. ing. of Aeronautical Engineering, Faculty of Mechanical Engineering and Naval Architecture in Zagreb, University of Zagreb, Croatia
1992. - 1996. Aviation technical school Rudolf Perešin, Velika Gorica, Croatia
1984. - 1992. Elementary school Ivan Kukuljević Sakcinski, Ivanec, Croatia

SVEUČILIŠTE U ZAGREBU
FAKULTET STROJARSTVA I BRODOGRADNJE

**Metoda graničnog sloja za određivanje
nestacionarnih aerodinamičkih opterećenja**

DOKTORSKI RAD

FRANE MAJIĆ

ZAGREB, 2010.



Sveučilište u Zagrebu
Fakultet strojarstva i brodogradnje

Metoda graničnog sloja za određivanje nestacionarnih aerodinamičkih opterećenja

DOKTORSKI RAD

Mentor:

Dr. sc. Ralph Voss

Frane Majić, dipl. ing.

ZAGREB, 2010.

Podaci za bibliografsku karticu

UDK: 532.511:532.517.2:532.517.3:532.517.4:
532.526:533.6.011.3:533.6.011.7:533.6.013.2:
533.6.013.04:533.6.013.13

Ključne riječi: viskozno-neviskozno sprezanje, viskozno strujanje, Eulerove jednadžbe, transpiracijska brzina, računalna dinamika fluida, Machov broj, aeroprofil, udarni val, raspodjela koeficijenta tlaka na aeroprofilu

Znanstveno područje: tehničke znanosti

Znanstveno polje: zrakoplovstvo, raketna i svemirska tehnika

Institucija u kojoj je rad izrađen: Fakultet strojarstva i brodogradnje

Mentor: Dr. sc. Ralph Voss

Broj stranica: 117

Broj slika: 70

Broj tablica: 8

Broj korištenih bibliografskih jedinica: 32

Datum obrane: 24. svibanj 2010.

Povjerenstvo: Prof. dr. sc. Zdravko Terze,
Dr. sc. Ralph Voss,
Prof. dr. sc. Zdravko Viag,
Prof. dr. sc. Zoran Milas,
Doc. dr. sc. Milan Vrdoljak

Institucija u kojoj je rad pohranjen: Fakultet strojarstva i brodogradnje,
Sveučilište u Zagrebu

Najprije, želio bih se zahvaliti mojim mentorima dr. sc. Ralphu Vossu i prof. dr. sc. Zdravku Viragu za vrijeme koje su proveli sa mnom dok su nesebično dijelili svoje ogromno znanje i iskustvo iz računalne mehanike fluida. Zahvaljujem se doc. dr. sc. Milanu Vrdoljaku za korisne komentare i za nesebičnu pomoć oko savladavanja LaTeX-a. Zahvaljujem se dr. sc. Anti Šodi koji nije nikad zaboravio podsjetiti me na rokove izrade mog doktorata. Također, zahvaljujem se dr. sc. Anti Šodi i Jensu Nitzscheu za pomoć oko korištenja Tau koda za vrijeme mog boravka u DLR-u, u Göttingenu, gdje je i napravljen veći dio ovog rada. Zahvaljujem se prijatelju Heiku Uhlemannu za dobro društvo i pomoć za vrijeme mog boravka u Göttingenu. Zahvaljujem se Heiku Uhlemannu, dr. sc. Anti Šodi, Jensu Nitzscheu i Claudiu Maniniu za vrijeme koje smo proveli u "6 Millionen Dollar Club" i ostalim ugodnim mjestima u Göttingenu diskutirajući o CFD-u i aerodinamici. Na kraju, zahvaljujem se mojim roditeljima, sestri, Heleni i Mislavu za njihovu potporu i strpljenje.

Sadržaj

Sadržaj	iv
Predgovor	vi
Sažetak	viii
Summary	ix
Popis oznaka	x
Popis slika	xii
Popis tablica	xviii
1. Uvod	1
1.1. Motivacija	1
1.2. Pregled dosadašnjih istraživanja	4
1.3. Cilj i hipoteza istraživanja	7
2. Model neviskoznog strujanja	8
2.1. Transformacija koordinata	8
2.2. Eulerove jednačbe	11
2.3. Dijeljenje vektora protoka	13
2.4. Metoda rješavanja Eulerovih jednačbi	16
2.5. Rubni uvjeti i određivanje tlaka na konturi aeroprofila	17

3. Granični sloj	20
3.1. Integralne jednačbe graničnog sloja za stlačivo strujanje	20
4. Rezultati	25
4.1. Računalna mreža	26
4.2. Konvergencija Mreže	27
4.3. Rezultati za stacionarno strujanje	44
4.3.1. NACA0012 aeroprofil	44
4.3.2. NACA64A010 aeroprofil	52
4.3.3. NLR7301 aeroprofil	56
4.4. Rezultati za nestacionarno strujanje	61
4.4.1. NACA0012 aeroprofil	62
4.4.2. NACA64A010 aeroprofil	68
5. Zaključak	73
6. Zaključak doktorskog rada	77
A. Izvod rubnog uvjeta	78
Literatura	95
Životopis	99

Predgovor

Ovaj rad je izrađen na Fakultetu strojarstva i brodogradnje u Zagrebu i na Institutu za aeroelastičnost koji je dio DLR-a (Deutsches Zentrum für Luft- und Raumfahrt) u Göttingen.

Fenomen treperenja aerodinamičkih površina zrakoplova, koji treba biti ispitan za svaku novu konstrukciju zrakoplova ili strukturnu modifikaciju postojećeg zrakoplova, još uvijek je jedan od trenutno važnih tema istraživanja u aeroelastičnosti, a posebno za zrakoplove koji lete kroz zvučnim brzinama.

Jedan od načina provjere aeroelastičnog ponašanja zrakoplova su računalne metode koje su u mogućnosti izvesti veliki broj proračuna prije provjera u letu, dok je drugi način pomoću pokusa u zračnom tunelu. Direktna simulacija interakcije fluida i strukture u vremenskoj domeni, koristeći se najpreciznijim metodama za proračun opterećenja, zahtijeva ekstremno velike računalne resurse.

Kako najzahtjevniji dio pripada određivanju nestacionarnih opterećenja, razvijene su efikasnije metode za određivanje granice treperenja. Određivanje opterećenja sastoji se od proračuna nestacionarnih opterećenja fluida na zrakoplov koji izvodi periodička gibanja s različitim elastičnim modovima i različitim frekvencijama.

Zbog malih zahtjeva za računalnim i vremenskim resursima pri analizi opterećenja, panelna metoda s dipolima nazvana metoda rešetki dipola (Doublet-lattice method - DLM) još uvijek se mnogo koristi. Jedan od nedostataka DLM metode je nemogućnost razlučivanja jakih udarnih valova u krozzvučnom području. S druge strane, simulacije Navier-Stokesovih jednadžbi osrednjenih po Reynoldsu (RANS) daju preciznije rezultate, ali zahtijevaju velike računalne i vremenske resurse, pa zbog toga nije prvi izbor za preliminarnu fazu konstruiranja.

Između te dvije krajnosti, metode viskozno-neviskozne interakcije, poput sprege Eulerovih jednadžbi i jednadžbi graničnog sloja, predstavljaju dobar kompromis. Rješavanjem Eulerovih jednadžbi moguće je razlučiti udarne valove, a sprezanje s jednadžbama graničnog sloja daje ravnotežu između modela strujanja i računalne efikasnosti. Metode viskozno-neviskozne interakcije daju rezultate koji su usporedivi s RANS rezultatima, dok je računalno vrijeme nekoliko puta manje i to im daje prednost kod analize treperenja.

Zagreb, travanj 2010.

Frane Majić, dipl. ing.

Sažetak

U ovome radu razvijena je jednostavna i precizna metoda za određivanje nestacionarnih aerodinamičkih opterećenja za dvodimenzionalno strujanje oko aeroprofila. Metoda koristi princip sprezanja viskoznog i neviskoznog dijela strujanja. Neviskozni dio strujanja je opisano nestacionarnim Eulerovim jednadžbama koje su riješene pomoću metode kontrolnih volumena na pomičnoj nedeformabilnoj mreži C-tipa. Viskozni dio strujanja je opisan integralnim jednadžbama graničnog sloja za stacionarno strujanje koje su riješene Runge-Kutta metodom četvrtog reda. Eulerove jednadžbe su riješene u konzervativnom obliku, u transformiranim prijanjajućim koordinatama. Sprezanje viskoznog i neviskoznog dijela strujanja je izvedeno pomoću transpiracijske brzine koje je uključena u rubni uvjet na aeroprofilu. Iz tog razloga metoda ne zahtijeva deformaciju mreže da bi se uključio utjecaj graničnog sloja. Položaj tranzicije graničnog sloja je predviđen pomoću metode e^n . Metoda viskozno-neviskoznog sprezanja je usmjerena na podzvučno i krozzvučno strujanje pri velikim Reynoldsovima brojevima, s pojavom udarnog vala. Izvršeni su proračuni za stacionarno i nestacionarno strujanje, za tri karakteristična aeroprofila NACA 0012, NACA64A010 i NLR 7301. Rezultati su uspoređeni s eksperimentalnim podacima i s nestacionarnim RANS proračunima. Metoda daje rezultate koji se dobro slažu s eksperimentalnim podacima i s proračunatim nestacionarnim RANS rezultatima. U slučajevima strujanja s odvajanjem, metoda pokazuje probleme s konvergencijom. Metoda je primjenjiva u procesima razvoja gdje se zahtijeva proračun nestacionarnih opterećenja unutar prihvatljivog vremena računanja i s preciznošću koja je usporediva s RANS metodama.

Ključne riječi: viskozno-neviskozno sprezanje, viskozno strujanje, Eulerove jednadžbe, transpiracijska brzina, računalna dinamika fluida, Machov broj, aeroprofil, udarni val, raspodjela koeficijenta tlaka na aeroprofilu

Summary

In this work a simple and accurate method for two-dimensional unsteady aerodynamic load determination is developed. The method employs viscous-inviscid coupling. The inviscid flow is governed by the unsteady Euler equations solved by finite volume method on moving C-type rigid grid, while viscous flow is governed by steady boundary layer integral equations. The Euler equations are solved in conservative form, in transformed body-fitted coordinates. The viscous-inviscid coupling is performed by transpiration velocity incorporated in the boundary condition. Therefore, the method requires no grid deformation for the boundary layer influence inclusion. The transition is predicted by the e^n method. The viscous-inviscid method is focused on subsonic and transonic flows, at high Reynolds number, with shock-wave appearance. The steady and unsteady test cases for three characteristic airfoils are performed, namely NACA 0012, NACA64A010, NLR 7301. The results are compared with experimental data and with unsteady RANS calculations. The method gives results which are in good agreement with experimental data and with calculated unsteady RANS results. Problems in convergence the method has in the test cases with separation. The method is applicable in the design processes where unsteady loads are required within reasonable time and with accuracy comparable with RANS methods.

Keywords: viscous-inviscid coupling, viscous flow, Euler equations, transpiration velocity, computational fluid dynamics, mach number, airfoil, shock-wave, airfoil pressure coefficient distribution

Popis oznaka

Latinične oznake

c	Duljina tetive aeroprofila, [m]	28
c_n	Koeficijent normalne sile	28
C_p	Koeficijent tlaka	28
e	ukupna energija po jedinici mase, [J/kg]	11
F, G	vektori tokova konzervativnih varijabli	11
H^*	Kinetic energy shape parameter	20
h	ukupna entalpija po jedinici mase, [J/kg]	12
J	determinanta Jakobijeve matrice transformacije koordinata, [1]	11
L	referentna duljina, [m]	61
M	Machov broj	63
p_m	srednji tlak za nestacionarne oscilacije tlaka, [Pa]	61
p_o	iznos oscilatornog tlaka u nestacionarnom strujanju, [Pa]	61
p_s	tlak za srednji položaj, u stacionarnom strujanju, [Pa]	62
Q	vektor konzervativnih varijabli	11
p	tlak, [Pa]	11
Re	Reynoldsov broj	63
s	Krivolinijska koordinata u jednadžbama graničnog sloja	20
t	vrijeme, [s]	61
u	x-komponenta brzine, [m/s]	11
U_∞	iznos brzine slobodne struje, [m/s]	61
v	y-komponenta brzine, [m/s]	11

(x, y, z)	koordinate Kartezijskog koordinatnog sustava, [m]	11
x_α	udaljenost osi rotacije aeroprofila od prednjeg brida, [m]	68
x_t	Koordinata uzduž tetive aeroprofila, [m]	28

Grčke oznake

α	napadni kut, [°]	37
α_m	srednji napadni kut, [°]	37
α_o	amplituda napadnog kuta, [°]	37
γ	izentropski koeficijent, [1]	11
θ	Momentum thickness, [m]	20
ν	kinematička viskoznost, [m ² /s]	44
ν_t	turbulentna kinematička viskoznost, [m ² /s]	44
ξ	Krivolinijska koordinata u Eulerovim jednadžbama, [m]	20
ω^*	reducirana frekvencija, [1]	37
ρ	gustoća, [kg/m ³]	11
φ	fazni pomak, [rad]	61
ω	kutna frekvencija, [rad/s]	61

Indeksi

∞	Vrijednost slobodne struje	63
----------	--------------------------------------	----

Kratice

BL	Granični sloj	20
CPU	Central processing unit	59
MUSCL	Monotone upstream-centered schemes for conservation laws	17
URANS	unsteady Reynolds averaged Navier-Stokes equations	64

Popis slika

1.1	Krozzvučno propadanje	3
2.1	Prianjajući krivolinijski koordinatni sustav oko konture aeroprofila	9
2.2	Preslikavanje krivolinijske mreže na kartezijsku mrežu	10
4.1	Računalna mreža oko aeroprofila NACA0012 dobivena eliptičkim generatorom	26
4.2	Bliži pogled na mrežu oko konture aeroprofila NACA0012	26
4.3	Mreža 100X30; test konvergencije mreže za stacionarno rješenje za aeroprofil NACA0012 pri $\alpha = 1^\circ$, $Ma = 0.77$; 10, 40, 80 su udaljenosti od aeroprofila do vanjskog ruba domene izražen u duljinama tetiva aeroprofila	29
4.4	Mreža 100X30; razlika rješenja za udaljenosti 10 i 40 duljina tetiva i rješenja za udaljenost 80 duljina tetiva; razlika je izražena u postocima u odnosu na mrežu s 80 duljina tetive; aeroprofil NACA0012 pri $\alpha = 1^\circ$, $Ma = 0.77$	30
4.5	Mreža 160X30; test konvergencije mreže za stacionarno rješenje za aeroprofil NACA0012 pri $\alpha = 1^\circ$, $Ma = 0.77$; 10, 40, 80 su udaljenosti od aeroprofila do vanjskog ruba domene izražen u duljinama tetiva aeroprofila	30
4.6	Mreža 160X30; razlika rješenja za udaljenosti 10 i 40 duljina tetiva i rješenja za udaljenost 80 duljina tetiva; razlika je izražena u postocima u odnosu na mrežu s 80 duljina tetive; aeroprofil NACA0012 pri $\alpha = 1^\circ$, $Ma = 0.77$	31
4.7	Mreža 160X60; test konvergencije mreže za stacionarno rješenje za aeroprofil NACA0012 pri $\alpha = 1^\circ$, $Ma = 0.77$; 10, 40, 80 su udaljenosti od aeroprofila do vanjskog ruba domene izražen u duljinama tetiva aeroprofila	31

4.8	Mreža 160X60; razlika rješenja za udaljenosti 10 i 40 duljina tetiva i rješenja za udaljenost 80 duljina tetiva; razlika je izražena u postocima u odnosu na mrežu s 80 duljina tetive; aeroprofil NACA0012 pri $\alpha = 1^\circ$, $Ma = 0.77$	32
4.9	Mreža 240X60; test konvergencije mreže za stacionarno rješenje za aeroprofil NACA0012 pri $\alpha = 1^\circ$, $Ma = 0.77$; 10, 40, 80 su udaljenosti od aeroprofila do vanjskog ruba domene izražen u duljinama tetiva aeroprofila	32
4.10	Mreža 240X60; razlika rješenja za udaljenosti 10 i 40 duljina tetiva i rješenja za udaljenost 80 duljina tetiva; razlika je izražena u postocima u odnosu na mrežu s 80 duljina tetive; aeroprofil NACA0012 pri $\alpha = 1^\circ$, $Ma = 0.77$	33
4.11	Mreža 320X60; test konvergencije mreže za stacionarno rješenje za aeroprofil NACA0012 pri $\alpha = 1^\circ$, $Ma = 0.77$; 10, 40, 80 su udaljenosti od aeroprofila do vanjskog ruba domene izražen u duljinama tetiva aeroprofila	33
4.12	Mreža 320X60; razlika rješenja za udaljenosti 10 i 40 duljina tetiva i rješenja za udaljenost 80 duljina tetiva; razlika je izražena u postocima u odnosu na mrežu s 80 duljina tetive; aeroprofil NACA0012 pri $\alpha = 1^\circ$, $Ma = 0.77$	34
4.13	Test konvergencije za udaljenost 80 duljina tetiva od aeroprofila do vanjskog ruba domene; aeroprofil NACA0012 pri $\alpha = 1^\circ$, $Ma = 0.77$	34
4.14	Razlika rješenja za mreže napisane u legendi slike i mreže 320X60 s 80 duljina tetive od aeroprofila do vanjskog ruba domene; aeroprofil NACA0012 pri $\alpha = 1^\circ$, $Ma = 0.77$	35
4.15	Test konvergencije za NACA0012 aeroprofil pri $\alpha = 5^\circ$, $Ma = 0.77$	35
4.16	Razlika između rješenja dobivenih pomoću mreža navedenih u legendi slike i mreže 320X60 s udaljenošću 80 duljina tetiva od aeroprofila do vanjskog ruba domene, za aeroprofil NACA0012 pri $\alpha = 5^\circ$, $Ma = 0.77$	36
4.17	Mreža 100X30; konvergencija nestacionarnog rješenja; 10, 40 i 80 predstavljaju udaljenosti aeroprofila od vanjskog ruba domene u duljinama tetiva aeroprofila; NACA0012 aeroprofil pri $Ma = 0.77$, $\alpha_m = 0^\circ$, $\alpha_o = 1^\circ$	37
4.18	Mreža 100X30; razlika rješenja za udaljenosti vanjskog ruba domene od aeroprofila 10 i 40 duljina tetiva i rješenja za udaljenost 80 duljina tetiva; NACA0012 aeroprofil pri $Ma = 0.77$, $\alpha_m = 0^\circ$, $\alpha_o = 1^\circ$	38
4.19	Mreža 160X30; konvergencija nestacionarnog rješenja; 10, 40 i 80 predstavljaju udaljenosti aeroprofila od vanjskog ruba domene u duljinama tetiva aeroprofila; NACA0012 aeroprofil pri $Ma = 0.77$, $\alpha_m = 0^\circ$, $\alpha_o = 1^\circ$	39

4.20	Mreža 160X30; razlika rješenja za udaljenosti vanjskog ruba domene od aeroprofila 10 i 40 duljina tetiva i rješenja za udaljenost 80 duljina tetiva; NACA0012 aeroprofil pri $Ma = 0.77$, $\alpha_m = 0^\circ$, $\alpha_o = 1^\circ$	39
4.21	Mreža 160X60; konvergencija nestacionarnog rješenja; 10, 40 i 80 predstavljaju udaljenosti aeroprofila od vanjskog ruba domene u duljinama tetiva aeroprofila; NACA0012 aeroprofil pri $Ma = 0.77$, $\alpha_m = 0^\circ$, $\alpha_o = 1^\circ$	40
4.22	Mreža 160X60; razlika rješenja za udaljenosti vanjskog ruba domene od aeroprofila 10 i 40 duljina tetiva i rješenja za udaljenost 80 duljina tetiva; NACA0012 aeroprofil pri $Ma = 0.77$, $\alpha_m = 0^\circ$, $\alpha_o = 1^\circ$	40
4.23	Mreža 240X60; konvergencija nestacionarnog rješenja; 10, 40 i 80 predstavljaju udaljenosti aeroprofila od vanjskog ruba domene u duljinama tetiva aeroprofila; NACA0012 aeroprofil pri $Ma = 0.77$, $\alpha_m = 0^\circ$, $\alpha_o = 1^\circ$	41
4.24	Mreža 240X60; razlika rješenja za udaljenosti vanjskog ruba domene od aeroprofila 10 i 40 duljina tetiva i rješenja za udaljenost 80 duljina tetiva; NACA0012 aeroprofil pri $Ma = 0.77$, $\alpha_m = 0^\circ$, $\alpha_o = 1^\circ$	41
4.25	Mreža 320X60; konvergencija nestacionarnog rješenja; 10, 40 i 80 predstavljaju udaljenosti aeroprofila od vanjskog ruba domene u duljinama tetiva aeroprofila; NACA0012 aeroprofil pri $Ma = 0.77$, $\alpha_m = 0^\circ$, $\alpha_o = 1^\circ$	42
4.26	Mreža 320X60; razlika rješenja za udaljenosti vanjskog ruba domene od aeroprofila 10 i 40 duljina tetiva i rješenja za udaljenost 80 duljina tetiva; NACA0012 aeroprofil pri $Ma = 0.77$, $\alpha_m = 0^\circ$, $\alpha_o = 1^\circ$	42
4.27	Raspodjela koeficijenta tlaka za aeroprofil NACA0012 pri $Ma = 0.504$, $Re = 2.93 \cdot 10^6$, $\alpha = 4.06^\circ$	46
4.28	Integralne vrijednosti graničnog sloja za gornju stranu NACA0012 aeroprofila pri $Ma = 0.504$, $Re = 2.93 \cdot 10^6$, $\alpha = 4.06^\circ$	46
4.29	Integralne vrijednosti graničnog sloja za donju stranu NACA0012 aeroprofila pri $Ma = 0.504$, $Re = 2.93 \cdot 10^6$, $\alpha = 4.06^\circ$	47
4.30	Raspodjela koeficijenta tlaka na gornjoj strani NACA0012 aeroprofila za stacionarno strujanje pri $Ma = 0.756$, $Re = 4.01 \cdot 10^6$, $\alpha = -0.01^\circ$	48
4.31	Raspodjela koeficijenta tlaka na donjoj strani NACA0012 aeroprofila za stacionarno strujanje pri $Ma = 0.756$, $Re = 4.01 \cdot 10^6$, $\alpha = -0.01^\circ$	48
4.32	Integralne vrijednosti graničnog sloja za donju stranu NACA0012 aeroprofila pri $Ma = 0.756$, $Re = 4.01 \cdot 10^6$, $\alpha = -0.01^\circ$	49

4.33	Raspodjela koeficijenta tlaka na gornjoj strani NACA0012 aeroprofila za stacionarno strujanje pri $Ma = 0.803$, $Re = 4.09 \cdot 10^6$ and $\alpha = 0.05^\circ$	50
4.34	Raspodjela koeficijenta tlaka na donjoj strani NACA0012 aeroprofila za stacionarno strujanje pri $Ma = 0.803$, $Re = 4.09 \cdot 10^6$ and $\alpha = 0.05^\circ$	51
4.35	Integralne vrijednosti graničnog sloja za donju stranu NACA0012 aeroprofila pri $Ma = 0.803$, $Re = 4.09 \cdot 10^6$, $\alpha = 0.05^\circ$	51
4.36	Računalna mreža za aeroprofil NACA64A010; granica na vanjskom rubu domene je udaljena 40 duljina tetiva aeroprofila od aeroprofila.	53
4.37	NACA64A010 steady pressure coefficient distribution for upper side at $Ma = 0.49$, $Re = 2.52 \cdot 10^6$, $\alpha = -0.01^\circ$	54
4.38	NACA64A010 steady pressure coefficient distribution for upper side at $Ma = 0.502$, $Re = 1.0 \cdot 10^7$, $\alpha = -0.22^\circ$	54
4.39	NACA64A010 boundary layer integral values for upper side at $Ma = 0.49$, $Re = 2.52 \cdot 10^6$, $\alpha = -0.01^\circ$	54
4.40	NACA64A010 boundary layer integral values for upper side at $Ma = 0.502$, $Re = 1.0 \cdot 10^7$, $\alpha = -0.22^\circ$	54
4.41	Raspodjela koeficijenta tlaka za aeroprofil NACA64A010 za gornju (lijevo) i donju (desno) stranu aeroprofila pri $Ma = 0.796$, $Re = 12.56 \cdot 10^6$, $\alpha = -0.21^\circ$	55
4.42	Integralne vrijednosti graničnog sloja za aeroprofil NACA64A010 na gornjoj strani aeroprofila pri $Ma = 0.796$, $Re = 12.56 \cdot 10^6$, $\alpha = -0.21^\circ$	56
4.43	Integralne vrijednosti graničnog sloja za aeroprofil NACA64A010 na donjoj strani aeroprofila pri $Ma = 0.796$, $Re = 12.56 \cdot 10^6$, $\alpha = -0.21^\circ$	56
4.44	Računalna mreža za aeroprofil NLR7301; vanjski rub mreže je udaljen 40 duljina tetiva od aeroprofila	57
4.45	Raspodjela koeficijenta tlaka za stacionarno strujanje oko aeroprofila NLR7301 pri $Ma = 0.299$, $Re = 1.1 \cdot 10^6$, $\alpha = 0.3966^\circ$	59
4.46	Raspodjela koeficijenta tlaka za stacionarno strujanje oko aeroprofila NLR7301 pri $Ma = 0.599$, $Re = 1.9 \cdot 10^6$, $\alpha = 0.3832^\circ$	59
4.47	Primjer nestacionarnih oscilacija napadnog kuta aeroprofila i tlaka	62
4.48	Raspodjela tlaka za nestacionarno strujanje za aeroprofil NACA0012 pri kutu unutar periode $\phi = 25.34^\circ$; $Ma = 0.755$, $Re = 5.5 \cdot 10^6$, $\alpha_m = 0.016^\circ$, $\alpha_o = 2.51^\circ$, $\omega^* = 0.1628$	64

- 4.49 Raspodjela tlaka za nestacionarno strujanje za aeroprofil NACA0012 pri kutu unutar periode $\phi = 67.80^\circ$; $Ma = 0.755$, $Re = 5.5 \cdot 10^6$, $\alpha_m = 0.016^\circ$, $\alpha_o = 2.51^\circ$, $\omega^* = 0.1628$ 64
- 4.50 Raspodjela tlaka za nestacionarno strujanje za aeroprofil NACA0012 pri kutu unutar periode $\phi = 127.40^\circ$; $Ma = 0.755$, $Re = 5.5 \cdot 10^6$, $\alpha_m = 0.016^\circ$, $\alpha_o = 2.51^\circ$, $\omega^* = 0.1628$ 65
- 4.51 Raspodjela tlaka za nestacionarno strujanje za aeroprofil NACA0012 pri kutu unutar periode $\phi = 168.42^\circ$; $Ma = 0.755$, $Re = 5.5 \cdot 10^6$, $\alpha_m = 0.016^\circ$, $\alpha_o = 2.51^\circ$, $\omega^* = 0.1628$ 65
- 4.52 Raspodjela tlaka za nestacionarno strujanje za aeroprofil NACA0012 pri kutu unutar periode $\phi = 210.29^\circ$; $Ma = 0.755$, $Re = 5.5 \cdot 10^6$, $\alpha_m = 0.016^\circ$, $\alpha_o = 2.51^\circ$, $\omega^* = 0.1628$ 65
- 4.53 Raspodjela tlaka za nestacionarno strujanje za aeroprofil NACA0012 pri kutu unutar periode $\phi = 255.14^\circ$; $Ma = 0.755$, $Re = 5.5 \cdot 10^6$, $\alpha_m = 0.016^\circ$, $\alpha_o = 2.51^\circ$, $\omega^* = 0.1628$ 65
- 4.54 Raspodjela tlaka za nestacionarno strujanje za aeroprofil NACA0012 pri kutu unutar periode $\phi = 306.56^\circ$; $Ma = 0.755$, $Re = 5.5 \cdot 10^6$, $\alpha_m = 0.016^\circ$, $\alpha_o = 2.51^\circ$, $\omega^* = 0.1628$ 66
- 4.55 Raspodjela tlaka za nestacionarno strujanje za aeroprofil NACA0012 pri kutu unutar periode $\phi = 347.20^\circ$; $Ma = 0.755$, $Re = 5.5 \cdot 10^6$, $\alpha_m = 0.016^\circ$, $\alpha_o = 2.51^\circ$, $\omega^* = 0.1628$ 66
- 4.56 Koeficijent normalne sile i trenutni napadni kut kao funkcija faznog kuta unutar periode, za aeroprofil NACA0012 pri $Ma = 0.755$, $Re = 5.5 \cdot 10^6$, $\alpha_m = 0.016^\circ$, $\alpha_o = 2.51^\circ$, $\omega^* = 0.1628$ 67
- 4.57 Koeficijent normalne sile kao funkcija trenutnog napadnog kuta za aeroprofil NACA0012 pri $Ma = 0.755$, $Re = 5.5 \cdot 10^6$, $\alpha_m = 0.016^\circ$, $\alpha_o = 2.51^\circ$, $\omega^* = 0.1628$ 67
- 4.58 Raspodjela koeficijenta tlaka za nestacionarno strujanje oko aeroprofila NACA64A010 na faznom kutu $\phi = 45.00^\circ$ pri $Ma = 0.797$, $Re = 12.4 \cdot 10^6$, $\alpha_m = -0.08^\circ$, $\alpha_o = 2.00^\circ$, $\omega^* = 0.202$ 70
- 4.59 Raspodjela koeficijenta tlaka za nestacionarno strujanje oko aeroprofila NACA64A010 na faznom kutu $\phi = 90.00^\circ$ pri $Ma = 0.797$, $Re = 12.4 \cdot 10^6$, $\alpha_m = -0.08^\circ$, $\alpha_o = 2.00^\circ$, $\omega^* = 0.202$ 70

4.60	Raspodjela koeficijenta tlaka za nestacionarno strujanje oko aeroprofila NACA64A010 na faznom kutu $\phi = 135.00^\circ$ pri $Ma = 0.797$, $Re = 12.4 \cdot 10^6$, $\alpha_m = -0.08^\circ$, $\alpha_o = 2.00^\circ$, $\omega^* = 0.202$	70
4.61	Raspodjela koeficijenta tlaka za nestacionarno strujanje oko aeroprofila NACA64A010 na faznom kutu $\phi = 180.00^\circ$ pri $Ma = 0.797$, $Re = 12.4 \cdot 10^6$, $\alpha_m = -0.08^\circ$, $\alpha_o = 2.00^\circ$, $\omega^* = 0.202$	70
4.62	Raspodjela koeficijenta tlaka za nestacionarno strujanje oko aeroprofila NACA64A010 na faznom kutu $\phi = 225.00^\circ$ pri $Ma = 0.797$, $Re = 12.4 \cdot 10^6$, $\alpha_m = -0.08^\circ$, $\alpha_o = 2.00^\circ$, $\omega^* = 0.202$	71
4.63	Raspodjela koeficijenta tlaka za nestacionarno strujanje oko aeroprofila NACA64A010 na faznom kutu $\phi = 270.00^\circ$ pri $Ma = 0.797$, $Re = 12.4 \cdot 10^6$, $\alpha_m = -0.08^\circ$, $\alpha_o = 2.00^\circ$, $\omega^* = 0.202$	71
4.64	Raspodjela koeficijenta tlaka za nestacionarno strujanje oko aeroprofila NACA64A010 na faznom kutu $\phi = 315.00^\circ$ pri $Ma = 0.797$, $Re = 12.4 \cdot 10^6$, $\alpha_m = -0.08^\circ$, $\alpha_o = 2.00^\circ$, $\omega^* = 0.202$	71
4.65	Raspodjela koeficijenta tlaka za nestacionarno strujanje oko aeroprofila NACA64A010 na faznom kutu $\phi = 360.00^\circ$ pri $Ma = 0.797$, $Re = 12.4 \cdot 10^6$, $\alpha_m = -0.08^\circ$, $\alpha_o = 2.00^\circ$, $\omega^* = 0.202$	71
4.66	Koeficijent normalne sile i trenutni napadni kut kao funkcija faznog kuta u jednom periodu za aeroprofil NACA64A010 pri $Ma = 0.797$, $Re = 12.4 \cdot 10^6$, $\alpha_m = -0.08^\circ$, $\alpha_o = 2.00^\circ$, $\omega^* = 0.202$	72
4.67	Koeficijent normalne sile kao funkcija trenutnog napadnog kuta za aeroprofil NACA64A010 pri $Ma = 0.797$, $Re = 12.4 \cdot 10^6$, $\alpha_m = -0.08^\circ$, $\alpha_o = 2.00^\circ$, $\omega^* = 0.202$	72

Popis tablica

4.1	Testirane računalne mreže	27
4.2	Rezultati koeficijenta normalne sile za nestacionarno strujanje	43
4.3	NACA0012 probni slučajevi za stacionarno strujanje	45
4.4	Stacionarni probni slučajevi za aeroprofil NACA64A010	52
4.5	Probni slučajevi za aeroprofil NLR7301, za stacionarno strujanje	58
4.6	Skupljeni probni slučajevi za stacionarno strujanje	60
4.7	Probni slučaj za nestacionarno strujanje oko NACA0012 aeroprofila	63
4.8	NACA64A010 unsteady test case	68

1 | Uvod

1.1. Motivacija

Fenomen treperenja (eng. *flutter*) aerodinamičkih površina zrakoplova, koji treba biti ispitan za svaku novu konstrukciju zrakoplova ili strukturnu modifikaciju postojećeg zrakoplova, još uvijek je jedan od trenutno važnih tema istraživanja u aeroelastičnosti, a posebno za zrakoplove koji lete kroz zvučnim brzinama. Taj fenomen spada u problem aeroelastičnosti, koji je određen interakcijom elastičnih, prigušnih i inercijskih sila strukture i nestacionarnih aerodinamičkih sila uzrokovanih periodičkim gibanjem same strukture. Takvo periodičko gibanje može dovesti do progresivnog povećanja amplitude vibracija završavajući lomom strukture. Za određenu strukturu zrakoplova nestacionarne aerodinamičke sile se brzo povećavaju s brzinom leta, dok elastične, prigušne i inercijske sile ostaju nepromijenjene. Iz tog razloga postoji kritična brzina leta (brzina treperenja) iznad koje se pojavljuje treperenje¹.

Zapravo, svaki zrakoplov s ljudskom posadom mora proći neku vrstu analize aeroelastičnosti prije leta, pošto se treperenje i ostali aeroelastični fenomeni unutar envelope leta zrakoplova moraju izbjeći bez izuzetaka. Tri načina su moguća za provjeru aeroelastičnog ponašanja zrakoplova: ispitivanje u letu, ispitivanje u zračnom tunelu, i analiza računalnim metodama. Ispitivanja u letu i u zračnom tunelu mogu se izvoditi najranije u kasnoj fazi procesa konstruiranja zrakoplova, jer su ta ispitivanja vrlo skupa. Osim toga, zbog potrebe ispitivanja više različitih konfiguracija zrakoplova ili samo aerodinamičkih površina, izrada različitih modela za ispitivanje u zračnom tunelu i različitih

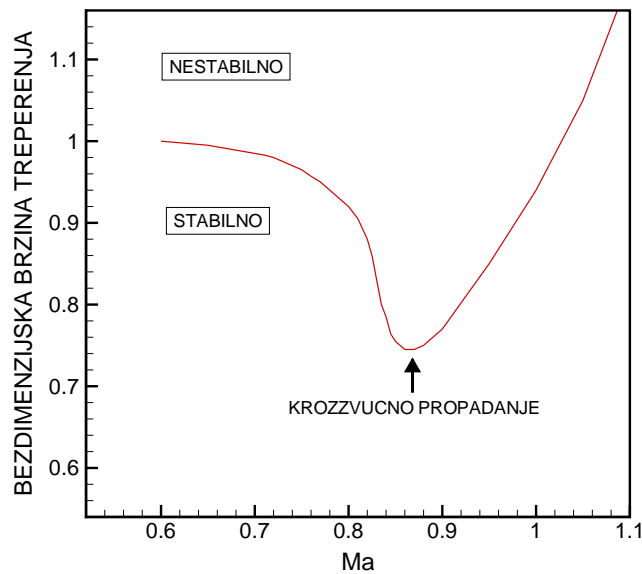
¹Samoinducirane oscilacije spregnutog aeroelastičnog sustava zbog međusobne interakcije između strukturnih sila (elastične, inercijske i prigušne sile) i nestacionarnih aerodinamičkih sila.

prototipova zrakoplova za ispitivanje u letu bila bi preveliki vremenski i financijski teret u ispitivanju zrakoplova. Stoga, mnogo jeftinije rješenje su računalne metode s kojima se mogu napraviti veliki broj ispitinih slučajeva prije ispitivanja u letu ili u zračnom tunelu.

Pri brzinama u krozzvučnom području, analiza aeroelastičnosti postaje značajno kompliciranija. Pri takvim uvjetima, udarni valovi se mogu pojavljivati i nestajati pod okolnostima kada zrakoplov vrši nestacionarno, fleksibilno gibanje strukture. Jačanjem i slabljenjem tih udarnih valova, također se mogu pojavljivati i nestajati područja odvojenog strujanja. To su vrlo nelinearni fenomeni koji mogu imati značajni utjecaj na aeroelastično ponašanje zrakoplova. Pojavljivanje udarnih valova na aerodinamičkim površinama zrakoplova može uzrokovati daljnje propadanje granice treperenja u području krozzvučnih brzina u odnosu na granicu treperenja zbog linearnih efekata u kompresibilnom strujanju. To propadanje granice treperenja naziva se krozzvučno propadanje (eng. *transonic dip*). Važna karakteristika krozzvučnog propadanja je dno krivulje treperenja u krozzvučnom području (slika 1.1), koje definira minimalnu brzinu pri kojoj se treperenje može pojaviti, u području envelope leta zrakoplova. Brzina treperenja predstavlja kritičnu brzinu pri kojoj struktura održava oscilacije uzrokovane nekim inicijalnim poremećajem. Ispod te brzine oscilacije su prigušene, dok iznad te brzine jedam od modova oscilacija postaje negativno prigušen i pojavljuju se nestabilne oscilacije osim ako neki oblik nelinearnosti ne ograniči takvo gibanje [1].

Linearna analiza obično adekvatno predviđa granicu treperenja pri podzvučnim i nadzvučnim brzinama, dok u području krozzvučnih brzina predviđa višu brzinu treperenja nego u eksperimentu [2]. Granica treperenja se može izračunati pomoću neviskozne nestacionarne aerodinamičke analize, npr. rješavajući nestacionarno krozzvučno potencijalno strujanje za male poremećaje, potpuno potencijalno strujanje, ili Eulerove jednadžbe. Iako su te metode u mogućnosti opisivati udarne valove i krozzvučno propadanje, one izračunavaju značajno nižu brzinu treperenja na mjestu krozzvučnog propadanja jer nemaju uključene viskozne efekte u proračunu. Viskozni efekti koji djeluju u obliku značajnijeg zadebljanja graničnog sloja i odvajanja strujanja zbog udarnog vala su odgovorni za bolje predviđnje dna krozzvučnog propadanja.

Pri analizi treperenja ne koristi se tako često neko proizvoljno gibanje aeroprofila, nego je veći interes da se zada harmonijsko gibanje za jednu frekvenciju oscilacija. Cilj takve analize je da se odrede uvjeti leta koji odgovaraju granici treperenja (granica



Slika 1.1: Krozzvučno propadanje

stabilnosti), za koju jedan od modova gibanja ima jednostavno vremenski harmonijsko ponašanje [3]. U linearnoj analizi treperenja je pretpostavljeno da rješenje uključuje jednostavno harmonijsko gibanje a također i pobudna sila i moment imaju harmonijsko ponašanje. S tom pretpostavkom jednadžbe gibanja su prevedene u problem vlastitih vrijednosti u frekvencijskoj domeni i riješene za kompleksne vlastite vrijednosti. Iz tih vlastitih vrijednosti može se zaključiti o stabilnim ili nestabilnim oscilacijama aeroprofila. Klasična analiza treperenja ne može dati neku konačnu mjeru o stabilnosti treperenja osim pozicije granice stabilnosti. Usprkos tom nedostatku metode, njezina primarna snaga je u tome što treba samo nestacionarna opterećenja za jednostavno harmonijsko gibanje aeroprofila.

Direktna simulacija interakcije fluid-struktura u vremenskoj domeni, koristeći najpreciznije modele za računanje aerodinamičkih opterećenja od fluida, zahtijeva ekstremno visoke računalne resurse. Kako je glavna proračuna potrebna za dio koji računa nestacionarna aerodinamička opterećenja, razvijene su efikasnije metode za predviđanje granice treperenja, koja je definirana kao stanje ravnoteže između dinamičkih sila strukture i aerodinamičkih sila na strukturu. Aerodinamički dio rješenja se stoga sastoji od proračuna nestacionarnog aerodinamičkog strujanja oko strukture zrakoplova koja izvodi oscilatorna gibanja u različitim zadanim elastičnim modovima i s različitim frek-

vencijama.

U tu svrhu, još i danas, za analizu konstrukcija prisutna je panelna metoda s dipolima (eng. *doublet-lattice method* - DLM) zbog malih zahtjeva za računalne i vremenske resurse, i jednostavne procedure za postavljanje računalnog problema. Jedan od nedostataka metode je nemogućnost detektiranja jakih udarnih valova u krozvučnom području. Simulacije Navier-Stokes-ovih jednadžbi osrednjenih po Reynolds-u (eng. *Reynolds averaged Navier-Stokes* - RANS) za analizu treperenja daju točnije rezultate, ali isto tako zahtijevaju velike računalne i vremenske resurse, i stoga nisu prvi izbor za preliminarnu fazu konstruiranja. K tome, RANS zahtijeva velike računalne mreže s visokom rezolucijom, a i postavljanje problema je mnogo zahtjevnije. RANS je također ograničen s nesigurnošću modeliranja turbulencije, poteškoćama s izradom mreža visoke kvalitete i poteškoćama s algoritmima za deformaciju mreže u nestacionarnim strujanjima [4].

U preliminarnom procesu konstruiranja, inženjeri koji se bave analizom aeroelastičnosti a nisu eksperti u računalnoj mehanici fluida (eng. *Computational fluid dynamics* - CFD) već u drugim područjima kao što je analiza čvrstoće konačnim elementima ili upravljanje i regulacija leta zrakoplova, trebaju biti također u mogućnosti koristiti CFD metode. To zahtijeva da računalne metode budu robusnije i automatiziranije nego što su trenutni RANS kodovi. Između tih ekstrema, metode viskozno-neviskozne interakcije kao što je Euler s graničnim slojem, su dobar kompromis. Metode koje rješavaju Eulerove jednadžbe su u mogućnosti razlučiti jake udarne valove, a spregnute zajedno s jednadžbama graničnog sloja predstavljaju dobru ravnotežu između opisa modela strujanja i računalne efikasnosti. Metode viskozno-neviskozne interakcije daju rezultate koji su usporedivi s RANS rezultatima ali je vrijeme računanja nekoliko puta manje i to im daje značajnu prednost za brzu analizu treperenja u procesu konstruiranja.

Ovaj rad je posvećen poboljšanju takve metode u kojoj je neviskozno područje opisano nestacionarnim Eulerovim jednadžbama a viskozni sloj jednadžbama graničnog sloja u integralnom obliku, s međusobnom interakcijom pomoću transpiracijske brzine.

1.2. Pregled dosadašnjih istraživanja

Najraniji radovi u području nestacionarne aerodinamike, povezano s analizom treperenja, su napravljeni tridesetih i četrdesetih godina prošlog stoljeća. Teorija isječaka (eng. *Strip theory*) je dugo vremena bila najviše korišten aerodinamički alat

za određivanje nestacionarnih aerodinamičkih opterećenja [5]. U toj aproksimacijskoj teoriji svaki segment po rasponu aerodinamičke površine razmatra se kao dio krila beskonačnog raspona s konstantnim karakteristikama.

Tijekom šezdesetih godina prošlog stoljeća razvijen je izvrstan alat za nestacionarnu aerodinamiku, metoda dipolnih panela (eng. *Doublet-lattice method* - DLM) [6]. Ta metoda razvijena je do razine da omogućava upotrebu zakrivljenih aerodinamičkih površina i trupa zrakoplova [7]. Ta metoda je stvorila važan doprinos analizi treperenja, aerodinamičke utjecajne koeficijente (eng. *Aerodynamic influence coefficients* - AIC). AIC koreliraju silu uzgona na svakom elementu aerodinamičkih površina prema pomacima (rotacija i translacija) i također dinamičkom tlaku. Nedavno, Rodden [8] je nastavio poboljšavati DLM metodu. Ta poboljšanja su bila zamjena aproksimacije brojnika inkrementalne jezgre (eng. *Incremental kernels*) i poboljšana aproksimacija integrala u jezgri. DLM metoda je u upotrebi već preko 30 godina i postala je standard za analizu treperenja u procesu proizvodnje. Postoje određene karakteristike koje su odgovorne za dugi život DLM metode. Prvo, metoda je dovoljno točna za rutinske analize treperenja u proizvodnji, osim u području krozvrućnih brzina leta i kada postoji odvajanje strujanja. Drugo, metoda zahtjeva malo vremena za računanje i kreira AIC-ove. Treće, metoda ima mogućnost modeliranja prilično kompleksnih geometrija i nema potrebu za generiranjem mreže. Metoda ima uzgonske površine koje su jednostavno diskretizirane serijom panela. Sve to daje konačnu važnu karakteristiku, a to je pristupačan kod za krajnjeg korisnika.

Među metodama zasnovanim na različitim oblicima jednadžbe potencijalnog strujanja s korekcijom graničnog sloja, koje su pokazale dobre rezultate za nestacionarne proračune, a ne zahtijevaju velike računalne resurse i mnogo radnih sati u postavljanju problema, CAP-TSD metoda (eng. *Computational Aeroelasticity Program - Transonic Small Disturbance*) je u širokoj upotrebi [9]. Taj kod ima mnogo prednosti pred RANS kodom: jednostavnost u generiranju mreže, nema potrebe za pomicanjem mreže i manji zahtjevi za računalnim resursima. Unatoč korištenju korekcija za vrtložnost i entropiju, pretpostavke u CAP-TSD metodi ograničavaju njegovu primjenjivost na nevrtložno strujanje s slabim udarnim valovima.

Pošto su metode koje rješavaju Eulerove jednadžbe u mogućnosti točno razlučiti jake udarne valove i transport vrtložnosti, mnogi istraživači su ispitivali metode interakcije graničnog sloja koristeći Eulerove jednadžbe za neviskozni dio strujanja [10, 11]. Mnogi

istraživači usredotočili su se na stacionarne proračune. Drela [12] je koristio Eulerove jednadžbe za neviskozno područje i integralne jednadžbe graničnog sloja za tanko viskozno područje u blizini aeroprofila. Određivanje tranzicije je temeljeno na formulaciji Orr-Sommerfeld-a (e^N metoda) i integrirano u dvojednadžbeni, integralni zapis graničnog sloja s mogućnošću laminarnog i turbulentnog strujanja. Viskozna formulacija je potpuno spregnuta s neviskoznom strujanjem koje je opisano Eulerovim jednadžbama na mreži oblika strujnica. Čitavi nelinearni spregnuti sustav jednadžbi je riješen Newton-ovom metodom.

Nedavno je Zhang [13] pokazao efikasnu Eulerovu metodu s korekcijom graničnog sloja pogodnu za anлізу treperenja krila. Debljina krila kao i njegovo gibanje s malim amplitudama je simulirano aproksimacijskim rubnim uvjetom primjenjenom na stacionarnoj ravnini tetive krila. Stoga je korištena stacionarna kartezijska mreža za nestacionarne simulacije krila zrakoplova.

U aeroelastičnim primjenama gdje je potrebno ispitati veliki broj parametara kao što su različiti prirodni načini gibanja, napadni kutevi, Machovi brojevi, frekvencija itd., pogodne su također metode koje rješavaju problem nestacionarne aerodinamike u frekventnoj domeni. Te metode su posebno prikladne za simulacije pri niskim reduciranim frekvencijama. Iste simulacije u vremenskoj domeni zahtijevaju mnogo vremena jer je potrebno postići periodički ustaljen slučaj koji se postiže tek nakon nekoliko ciklusa. Nedavno je demonstrirana jedna takva numerička metoda [14] koja je temeljena na takvom pristupu, Eulerovih jednadžbi uz pretpostavku malih poremećaja (eng. *Small disturbance Euler equations* - SDE). Pretpostavivši harmonijsko ponašanje nestacionarnih fizikalnih veličina, Eulerove jednadžbe daju skup linearnih jednadžbi s varijabilnim koeficijentima u kojima su nepoznate kompleksne vrijednosti fizikalnih veličina. Nestacionaran problem je sveden na stacionarni problem za nepoznati harmonijski oscilirajući dio. Fizika nelinearnog strujanja je sadržana u stacionarnom rješenju koje je potrebno za proračun lineariziranog rješenja. Takva nestacionarna rješenja se mogu direktno izračunati i koristiti unutar standardne modalne analize treperenja. Općenito metoda daje dobre rezultate, no u strujanjima s udarnim valom, raspodjela tlaka pokazuje značajne razlike u usporedbi s nelinearnim Eulerovim rješenjem. Pechloff [15] je napravio istu linearizaciju s Navier-Stokes jednadžbama. U tom radu također je napravljena linearizacija jednojednadžbenog Spalart-Almaras modela turbulencije.

Nedavno su izdani radovi koji analiziraju sprežanje RANS jednadžbi s graničnim

slojem [16, 17, 18]. U tim radovima je prikazano određivanje tranzicije graničnog sloja u svrhu konstruiranja laminarnih aeroprofila i smanjenja otpora.

1.3. Cilj i hipoteza istraživanja

Pristup efektivnog pomaka površine aeroprofila opisuje koncept viskozno-neviskozne interakcije. Taj pristup se može primjeniti u strujanjima s visokim Reynoldsovim brojem kod kojih su viskozni efekti smješteni unutar tankog graničnog sloja. Kako se u nestacionarnom strujanju mijenja debljina graničnog sloja, potrebno je poslije svake viskozno-neviskozne interakcije generirati novu mrežu za neviskozno rješenje. Metoda koja izbjegava tu poteškoću je metoda ekvivalentnih izvora (eng. *equivalent sources*) predložena od Lighthill-a [19]. Promjena debljine istisnuća graničnog sloja se koristi kao ekvivalent izvorima odnosno ponorima na površini aeroprofila. Efekt upuhavanja ili isisavanja strujanja oponaša zadebljanje graničnog sloja i djelovanje graničnog sloja na vanjsko neviskozno strujanje. U ovome radu napraviti će se ugradnja utjecaja količine gibanja upuhanog strujanja na interakciju s Eulerovim jednadžbama. Rješiti će se jednadžba količine gibanja u smjeru okomitom na površinu aeroprofila s ugrađenim utjecajem efekta upuhavanja graničnog sloja na neviskozno strujanje. Svi proračuni će se napraviti na krivolinijskoj mreži s uvjetom okomitosti na površini aeroprofila.

U ovome radu će se koristiti pristup u kojem se vanjsko neviskozno strujanje i strujanje u graničnom sloju povezuju tako da se u jednadžbi količine gibanja za vanjsko strujanje za rubni uvjet na površini aeroprofila uzima normalna komponenta količine gibanja dobivena iz jednadžbi graničnog sloja. Cilj i hipoteza ovog rada je pokazati da će takav pristup dati rezultate koji su usporedivi s danas raspoloživim kodovima temeljenim na višoj razini matematičkog modela. Metoda bi trebala biti dovoljno točna da bude korisna kao aerodinamički alat u rutinskim provjerama analize aeroelastičnosti, i također bi trebala dati dobre rezultate u području krozvučnih brzina leta gdje se pojavljuju udarni valovi.

2 Model neviskoznostrujanja

U ovome poglavlju prikazati će se jednadžbe koje opisuju dinamiku stlačivog fluida, što obuhvaća područje ovog rada. Biti će opisana metoda rješavanja tih jednadžbi i također transformacija krivolinijskih (fizičkih) koordinata u Kartezijske (računalne) koordinate mreže. Biti će pokazan rubni uvjet na vanjskom rubu domene kao i rubni uvjet na konturi aeroprofila. Također, u ovome poglavlju biti će pokazano uključivanje utjecaja graničnog sloja preko transpiracijske brzine u rubni uvjet na konturi aeroprofila.

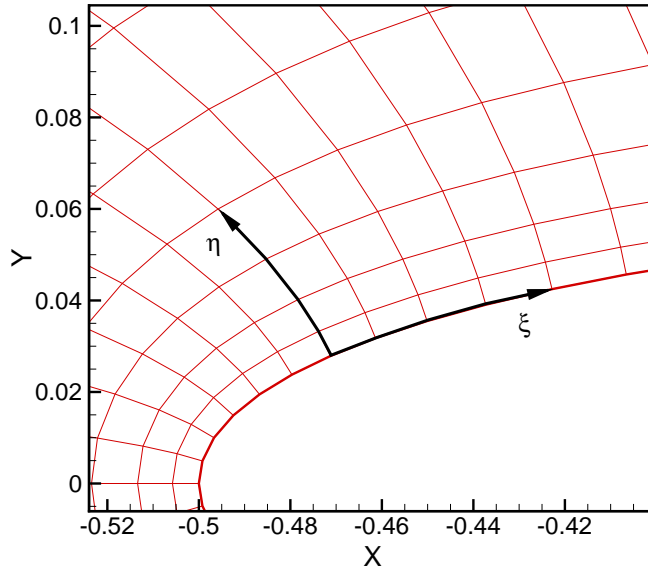
2.1. Transformacija koordinata

U strujanjima oko obliha tijela kao što je poprečni presjek krila odnosno aeroprofil, mogu se koristiti prijanjajući krivolinijski koordinatni sustavi (eng. *body-fitted coordinate system*). Na slici 2.1 prikazan je prijanjajući koordinatni sustav na dvodimenzionalnoj mreži oko aeroprofila s osima ξ i η .

Strukturirana mreža u takvom koordinatnom sustavu može se vrlo lako preslikati u kartezijski koordinatni sustav s kartezijskom mrežom koji olakšava numeričke proračune primjenom metode kontrolnih volumena. Funkcijski oblik preslikavanja iz kartezijskog sustava (x, y, t) u krivolinijski koordinatni sustav s prijanjajućim koordinatama (ξ, η, τ) može se izraziti u slijedećem obliku:

$$\begin{aligned}\xi &= \xi(x, y, t) \\ \eta &= \eta(x, y, t) \\ \tau &= t.\end{aligned}\tag{2.1}$$

Na slici 2.2 prikazane su karakteristične točke (od A do F) na krivolinijskoj struk-

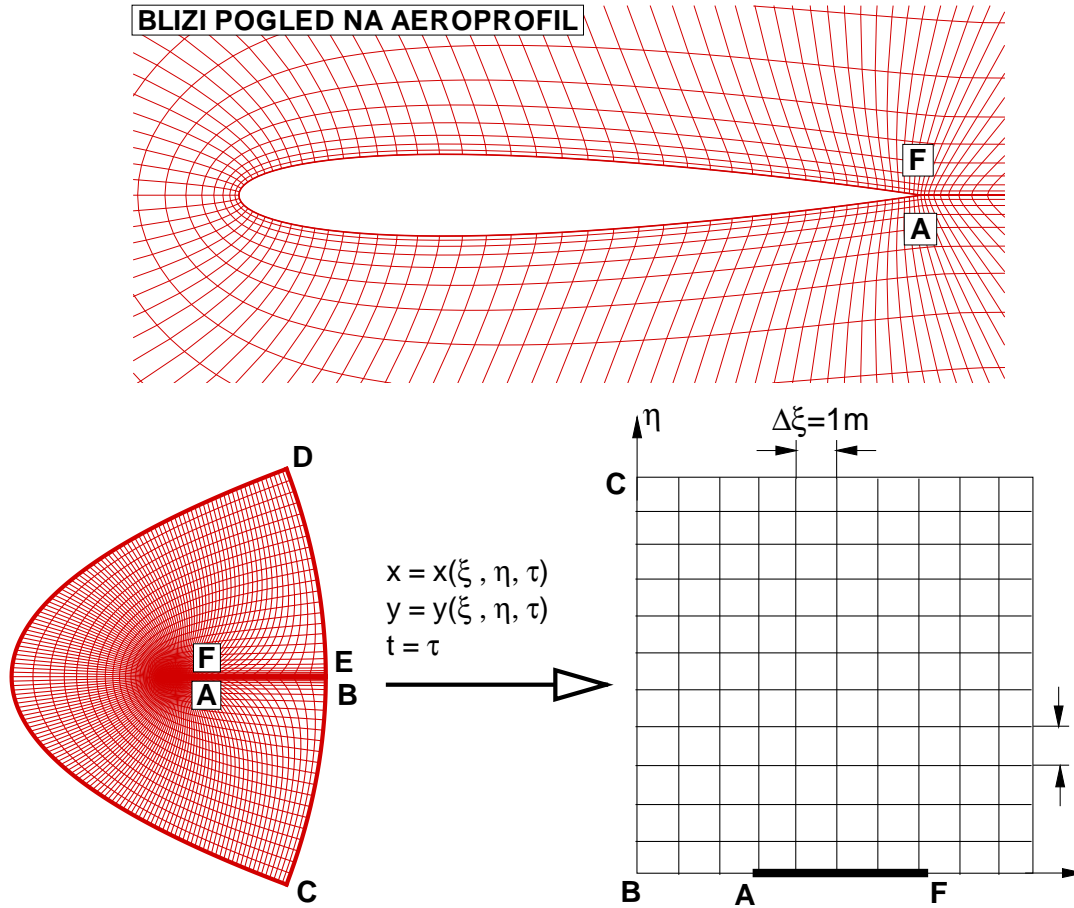


Slika 2.1: Prianjajući krivolinijski koordinatni sustav oko konture aeroprofila

turnoj mreži oko aeroprofila. Točka A se nalazi na izlaznom bridu na donjoj strani aeroprofila, a točka F se nalazi na izlaznom bridu na gornjoj strani aeroprofila. Na istoj slici te točke su prikazane u fizičkoj ravnini (dolje lijevo) i iste te točke u preslikanoj (računalnoj) ravnini (dolje desno). Gornjaka i donjaka aeroprofila je u preslikanoj ravnini prikazana linijom između točaka A i F, a u preslikanoj ravnini prikazana je punom podebljanom linijom između točaka A i F. Funkcije preslikavanja između tih dviju mreža dane su izrazima u jednadžbama (2.1).

Transformacijom Eulerovih jednadžbi iz Kartezijskog u krivolinijski koordinatni sustav potrebno je izračunati metričke koeficijente koji se pojavljuju u transformaciji mreže. Iz funkcijskih ovisnosti (2.1) mogu se izraziti derivacije u ovisnosti o Kartezijskih koordinata i vremena, koje se pojavljuju u jednadžbi (2.5), pomoću lančanog pravila na slijedeći način:

$$\begin{aligned}
 \frac{\partial}{\partial x} &= \xi_x \frac{\partial}{\partial \xi} + \eta_x \frac{\partial}{\partial \eta} + \tau_x \frac{\partial}{\partial \tau} \\
 \frac{\partial}{\partial y} &= \xi_y \frac{\partial}{\partial \xi} + \eta_y \frac{\partial}{\partial \eta} + \tau_y \frac{\partial}{\partial \tau} \\
 \frac{\partial}{\partial t} &= \xi_t \frac{\partial}{\partial \xi} + \eta_t \frac{\partial}{\partial \eta} + \tau_t \frac{\partial}{\partial \tau}
 \end{aligned} \tag{2.2}$$



Slika 2.2: Preslikavanje krivolinijske mreže na kartezijsku mrežu

Indeksi u izrazu (2.2) i narednim izrazima označavaju parcijalnu derivaciju po varijabli u indeksu. Metrika transformacije (preslikavanja) je dana slijedećim izrazima:

$$\begin{aligned}
 \xi_x &= J^{-1}y_\eta & \eta_x &= -J^{-1}y_\xi & \tau_x &= 0 \\
 \xi_y &= -J^{-1}x_\eta & \eta_y &= J^{-1}x_\xi & \tau_y &= 0 \\
 \xi_t &= 0 & \eta_t &= 0 & \tau_t &= 1
 \end{aligned} \tag{2.3}$$

gdje je J determinanta Jakobijeve matrice jednaka:

$$J = \left| \frac{\partial(x, y, t)}{\partial(\xi, \eta, \tau)} \right| = \begin{vmatrix} x_\xi & y_\xi & 0 \\ x_\eta & y_\eta & 0 \\ x_\tau & y_\tau & 1 \end{vmatrix} = x_\xi y_\eta - y_\xi x_\eta \quad (2.4)$$

2.2. Eulerove jednadžbe

Pri strujanjima oko aeroprofila s velikim Reynoldsovim brojevima, viskozni efekti su značajni samo u uskom području oko aeroprofila, u graničnom sloju. U takvim strujanjima, polje strujanja oko aeroprofila (osim tankog područja u blizini aeroprofila gdje viskozni efekti nisu zanemarivi) moguće je riješiti pomoću Eulerovih jednadžbi. Eulerove jednadžbe opisuju nestacionarno, neviskozno, stlačivo, neizentropsko i vrtložno strujanje. Takav oblik jednadžbi predstavlja nelinearni hiperbolički konzervativni oblik u kojima su efekti masenih sila, viskoznih naprezanja i tokova topline zanemareni. Za takav oblik jednadžbi, Riemannovi rješavači i uzvodne metode (eng. *upwind methods*) su direktno primjenjivi.

Postoje različiti zapisi Eulerovih jednadžbi. Eulerove jednadžbe mogu se napisati u konzervativnoj diferencijalnoj formi, u dvodimenzijском Kartezijском koordinatnom sustavu na slijedeći način:

$$\frac{\partial \mathbf{Q}}{\partial t} + \frac{\partial \mathbf{F}(\mathbf{Q})}{\partial x} + \frac{\partial \mathbf{G}(\mathbf{Q})}{\partial y} = 0 \quad (2.5)$$

gdje su vektori \mathbf{Q} , \mathbf{F} i \mathbf{G} jednaki

$$\mathbf{Q} = \begin{bmatrix} \rho \\ \rho u \\ \rho v \\ \rho e \end{bmatrix} \quad \mathbf{F} = \begin{bmatrix} \rho u \\ \rho u^2 + p \\ \rho uv \\ \rho uh \end{bmatrix} \quad \mathbf{G} = \begin{bmatrix} \rho v \\ \rho vu \\ \rho v^2 + p \\ \rho vh \end{bmatrix} \quad (2.6)$$

U vektorima (2.6), e je specifična ukupna energija (po jedinici mase)

$$e = \frac{1}{\gamma - 1} \frac{p}{\rho} + \frac{1}{2} (u^2 + v^2) \quad (2.7)$$

a h je specifična ukupna entalpija (po jedinici mase)

$$h = \frac{\gamma}{\gamma - 1} \frac{p}{\rho} + \frac{1}{2} (u^2 + v^2) \quad (2.8)$$

Sustav jednadžbi (2.5) može se napisati u matričnom obliku na slijedeći način:

$$\frac{\partial \mathbf{Q}}{\partial t} + \mathbf{A}(\mathbf{Q}) \frac{\partial \mathbf{Q}}{\partial x} + \mathbf{B}(\mathbf{Q}) \frac{\partial \mathbf{Q}}{\partial y} = 0 \quad (2.9)$$

gdje su

$$\mathbf{A}(\mathbf{Q}) = \frac{\partial \mathbf{F}}{\partial \mathbf{Q}} \quad \mathbf{B}(\mathbf{Q}) = \frac{\partial \mathbf{G}}{\partial \mathbf{Q}}. \quad (2.10)$$

Koeficijenti u matricama \mathbf{A} i \mathbf{B} su funkcije vektora \mathbf{Q} , pa je stoga sustav jednadžbi (2.9) nelinearan. Matrice \mathbf{A} i \mathbf{B} nazivaju se Jakobijeve matrice (Jakobijane) i imaju slijedeći oblik:

$$\mathbf{A}(\mathbf{Q}) = \frac{\partial \mathbf{F}}{\partial \mathbf{Q}} = \begin{bmatrix} \partial f_1 / \partial q_1 & \partial f_1 / \partial q_2 & \partial f_1 / \partial q_3 & \partial f_1 / \partial q_4 \\ \partial f_2 / \partial q_1 & \partial f_2 / \partial q_2 & \partial f_2 / \partial q_3 & \partial f_2 / \partial q_4 \\ \partial f_3 / \partial q_1 & \partial f_3 / \partial q_2 & \partial f_3 / \partial q_3 & \partial f_3 / \partial q_4 \\ \partial f_4 / \partial q_1 & \partial f_4 / \partial q_2 & \partial f_4 / \partial q_3 & \partial f_4 / \partial q_4 \end{bmatrix} \quad (2.11)$$

$$\mathbf{B}(\mathbf{Q}) = \frac{\partial \mathbf{G}}{\partial \mathbf{Q}} = \begin{bmatrix} \partial g_1 / \partial q_1 & \partial g_1 / \partial q_2 & \partial g_1 / \partial q_3 & \partial g_1 / \partial q_4 \\ \partial g_2 / \partial q_1 & \partial g_2 / \partial q_2 & \partial g_2 / \partial q_3 & \partial g_2 / \partial q_4 \\ \partial g_3 / \partial q_1 & \partial g_3 / \partial q_2 & \partial g_3 / \partial q_3 & \partial g_3 / \partial q_4 \\ \partial g_4 / \partial q_1 & \partial g_4 / \partial q_2 & \partial g_4 / \partial q_3 & \partial g_4 / \partial q_4 \end{bmatrix} \quad (2.12)$$

gdje su f_i , g_i i q_i komponente vektora \mathbf{F} , \mathbf{G} i \mathbf{Q} , za $i = 1, 2, 3, 4$.

Vlastite vrijednosti λ_i matrice \mathbf{A} su rješenja karakterističnog polinoma

$$|\mathbf{A} - \lambda \mathbf{I}| = \det(\mathbf{A} - \lambda \mathbf{I}) = 0 \quad (2.13)$$

gdje je \mathbf{I} jedinična matrica. Analogno vrijedi i za matricu \mathbf{B} . Fizikalno, vlastite vrijednosti predstavljaju brzine širenja poremećaja. Sustav jednadžbi hiperboličkog tipa ima sve realne vlastite vrijednosti.

2.3. Dijeljenje vektora protoka

U algoritmu dijeljenja protoka, vektori protoka se dijele na pozitivne i negativne doprinose $\mathbf{F} = \mathbf{F}^+ + \mathbf{F}^-$ i $\mathbf{G} = \mathbf{G}^+ + \mathbf{G}^-$ tako da matrice Jakobijane $\partial\mathbf{F}^+/\partial\mathbf{Q}$, $\partial\mathbf{G}^+/\partial\mathbf{Q}$ imaju samo pozitivne, a matrice Jakobijane $\partial\mathbf{F}^-/\partial\mathbf{Q}$, $\partial\mathbf{G}^-/\partial\mathbf{Q}$ samo negativne vlastite vrijednosti. Zbog takvog dijeljenja, računanje prostornih derivacija od \mathbf{F}^+ , \mathbf{G}^+ , odnosno \mathbf{F}^- , \mathbf{G}^- mora se provesti s diferenciranjem unazad odnosno unaprijed. Dijeljenje je napravljeno u odnosu na jednodimenzionalni Mach-ov broj $M_x = u/a$ i $M_y = v/a$. Za podzvučno strujanje, gdje su $|M_x| < 1$ za \mathbf{F} i $|M_y| < 1$ za \mathbf{G} , dijeljenje protoka \mathbf{F} i \mathbf{G} je napravljeno prema Van Leer-u [20] kako slijedi:

$$\mathbf{F}^\pm = \begin{bmatrix} \pm \frac{\rho a}{4} (1 \pm M_x)^2 \\ \frac{a}{\kappa} [(\kappa - 1) M_x \pm 2] f_1^\pm \\ v f_1^\pm \\ \frac{\kappa^2}{2(\kappa^2 - 1)} \frac{(f_2^\pm)^2}{f_1^\pm} + \frac{v^2}{2} f_1^\pm \end{bmatrix} \quad (2.14)$$

$$\mathbf{G}^\pm = \begin{bmatrix} \pm \frac{\rho a}{4} (1 \pm M_y)^2 \\ u g_1^\pm \\ \frac{a}{\kappa} [(\kappa - 1) M_y \pm 2] g_1^\pm \\ \frac{\kappa^2}{2(\kappa^2 - 1)} \frac{(g_3^\pm)^2}{g_1^\pm} + \frac{u^2}{2} g_1^\pm \end{bmatrix} \quad (2.15)$$

Za supersonično strujanje, gdje su $|M_x| > 1$ za \mathbf{F} i $|M_y| > 1$ za \mathbf{G} , slijedi:

$$\begin{aligned} \mathbf{F}^+ = \mathbf{F}, \quad \mathbf{F}^- = 0 & \quad \text{za} \quad M_x \geq +1 \\ \mathbf{F}^+ = 0, \quad \mathbf{F}^- = \mathbf{F} & \quad \text{za} \quad M_x \leq -1 \end{aligned} \quad (2.16)$$

$$\begin{aligned} \mathbf{G}^+ = \mathbf{G}, \quad \mathbf{G}^- = 0 & \quad \text{za} \quad M_y \geq +1 \\ \mathbf{G}^+ = 0, \quad \mathbf{G}^- = \mathbf{G} & \quad \text{za} \quad M_y \leq -1 \end{aligned} \quad (2.17)$$

Kad se Euler-ove jednačbe u kartezijskim koordinatama (x, y, t) transformiraju u pokretni prijanjajući koordinatni sustav (ξ, η, τ) , tada iste jednačbe u konzervativnom

obliku imaju sljedeći oblik:

$$\frac{\partial \hat{\mathbf{Q}}}{\partial \tau} + \frac{\partial \hat{\mathbf{F}}}{\partial \xi} + \frac{\partial \hat{\mathbf{G}}}{\partial \eta} = 0 \quad (2.18)$$

gdje su

$$\begin{aligned} \hat{\mathbf{Q}} &= J\mathbf{Q} \\ \hat{\mathbf{F}} &= (-y_\eta x_\tau + x_\eta y_\tau) \mathbf{Q} + y_\eta \mathbf{F} - x_\eta \mathbf{G} \\ \hat{\mathbf{G}} &= (-x_\xi y_\tau + y_\xi x_\tau) \mathbf{Q} + y_\xi \mathbf{F} - x_\xi \mathbf{G} \end{aligned} \quad (2.19)$$

U jednadžbama (2.19) i sljedećim jednadžbama u ovome radu, indeksi ξ, η, τ predstavljaju derivacije fizičkih koordinata prema krivolinijskim koordinatama (prijanjajuće koordinate). J je Jakobijana transformacije. Korektno dijeljenje transformiranih vektora protoka je napravljeno tako da se $\hat{\mathbf{F}}$ i $\hat{\mathbf{G}}$ napišu kao umnožak lokalne matrice rotacije i izmijenjenog vektora protoka, koji ima isti oblik kao kartezijski vektor protoka ali sadrži transformirane umjesto kartezijskih brzina. Vektori protoka napisani u tom obliku jednaki su:

$$\begin{aligned} \hat{\mathbf{F}}(\hat{\mathbf{Q}}) &= \sqrt{x_\eta^2 + y_\eta^2} T_F \bar{\mathbf{F}}(\bar{\mathbf{Q}}) \\ \hat{\mathbf{G}}(\hat{\mathbf{Q}}) &= \sqrt{x_\xi^2 + y_\xi^2} T_G \bar{\mathbf{G}}(\bar{\mathbf{Q}}) \end{aligned} \quad (2.20)$$

gdje sada tokovi imaju oblik kao i u kartezijskim koordinatama

$$\bar{\mathbf{Q}} = \rho \begin{bmatrix} 1 \\ \bar{u} \\ \bar{v} \\ \bar{E} \end{bmatrix} \quad (2.21)$$

$$\bar{\mathbf{F}} = \rho \begin{bmatrix} \bar{u} \\ \bar{u}^2 + \frac{a^2}{\gamma} \\ \bar{u}\bar{v} \\ \bar{u}\bar{H} \end{bmatrix} \quad (2.22)$$

$$\bar{\mathbf{G}} = \rho \begin{bmatrix} \bar{v} \\ \bar{u}\bar{v} \\ \bar{v}^2 + \frac{a^2}{\gamma} \\ \bar{v}\bar{H} \end{bmatrix} \quad (2.23)$$

Transformirane brzine u vektoru $\bar{\mathbf{F}}$ su jednake

$$\begin{aligned} \bar{u} &= \hat{y}_\eta(u - x_\tau) - \hat{x}_\eta(v - y_\tau) \\ \bar{v} &= \hat{x}_\eta(u - x_\tau) + \hat{y}_\eta(v - y_\tau) \end{aligned} \quad (2.24)$$

dok su u vektoru $\bar{\mathbf{G}}$ jednake

$$\begin{aligned} \bar{u} &= \hat{x}_\xi(u - x_\tau) + \hat{y}_\xi(v - y_\tau) \\ \bar{v} &= -\hat{y}_\xi(u - x_\tau) + \hat{x}_\xi(v - y_\tau) \end{aligned} \quad (2.25)$$

Izrazi $\hat{x}_\eta, \hat{y}_\eta, \hat{x}_\xi$ i \hat{y}_ξ su normalizirani na slijedeći način:

$$\begin{aligned} \hat{x}_\eta &= \frac{x_\eta}{\sqrt{x_\eta^2 + y_\eta^2}} \\ \hat{y}_\eta &= \frac{y_\eta}{\sqrt{x_\eta^2 + y_\eta^2}} \\ \hat{x}_\xi &= \frac{x_\xi}{\sqrt{x_\xi^2 + y_\xi^2}} \\ \hat{y}_\xi &= \frac{y_\xi}{\sqrt{x_\xi^2 + y_\xi^2}} \end{aligned} \quad (2.26)$$

Izmijenjena ukupna energija \bar{E} i ukupna entalpija \bar{H} su jednake

$$\bar{E} = \frac{a^2}{\gamma(\gamma - 1)} + \frac{1}{2}(\bar{u}^2 + \bar{v}^2) \quad (2.27)$$

$$\bar{H} = \frac{a^2}{\gamma - 1} + \frac{1}{2}(\bar{u}^2 + \bar{v}^2) \quad (2.28)$$

a matrice rotacije su jednake

$$T_F = \begin{bmatrix} 1 & 0 & 0 & 0 \\ x_\tau & \hat{y}_\eta & \hat{x}_\eta & 0 \\ y_\tau & -\hat{x}_\eta & \hat{y}_\eta & 0 \\ \frac{x_\tau^2 + y_\tau^2}{2} & \hat{y}_\eta x_\tau - \hat{x}_\eta y_\tau & \hat{x}_\eta x_\tau + \hat{y}_\eta y_\tau & 1 \end{bmatrix} \quad (2.29)$$

$$T_G = \begin{bmatrix} 1 & 0 & 0 & 0 \\ x_\tau & \hat{x}_\xi & -\hat{y}_\xi & 0 \\ y_\tau & \hat{y}_\xi & \hat{x}_\xi & 0 \\ \frac{x_\tau^2 + y_\tau^2}{2} & \hat{x}_\xi x_\tau + \hat{y}_\xi y_\tau & \hat{x}_\xi y_\tau - \hat{y}_\xi x_\tau & 1 \end{bmatrix} \quad (2.30)$$

Sada, dijeljenje izmijenjenih vektora tokova konzervativnih varijabli može se izvesti na slijedeći način:

$$\hat{\mathbf{F}}^\pm = \sqrt{x_\tau^2 + y_\tau^2} T_F \bar{\mathbf{F}}^\pm \quad (2.31)$$

$$\hat{\mathbf{G}}^\pm = \sqrt{x_\tau^2 + y_\tau^2} T_G \bar{\mathbf{G}}^\pm \quad (2.32)$$

gdje se vektori $\bar{\mathbf{F}}^\pm$ i $\bar{\mathbf{G}}^\pm$ računaju na isti način kao i podijeljeni vektori u kartezijskim koordinatama, ali s Mach-ovim brojevima $M_\xi = \bar{u}/a$ i $M_\eta = \bar{v}/a$

2.4. Metoda rješavanja Eulerovih jednadžbi

Euler-ove jednadžbe u pranjajućim koordinatama, s podijeljenim vektorima toka, sada imaju slijedeći oblik:

$$\frac{\partial \hat{\mathbf{Q}}}{\partial \tau} + \frac{\partial \hat{\mathbf{F}}^+}{\partial \xi} + \frac{\partial \hat{\mathbf{F}}^-}{\partial \xi} + \frac{\partial \hat{\mathbf{G}}^+}{\partial \eta} + \frac{\partial \hat{\mathbf{G}}^-}{\partial \eta} = 0 \quad (2.33)$$

Jednadžba (2.33) je diskretizirana i riješena u slijedećem obliku:

$$\begin{aligned} \hat{\mathbf{Q}}^{n+1}(i, j) = \hat{\mathbf{Q}}^n(i, j) - \Delta\tau [& \hat{\mathbf{F}}^+(i+1, j) - \hat{\mathbf{F}}^+(i, j) + \hat{\mathbf{F}}^-(i+1, j) - \hat{\mathbf{F}}^-(i, j) \\ & + \hat{\mathbf{G}}^+(i, j+1) - \hat{\mathbf{G}}^+(i, j) + \hat{\mathbf{G}}^-(i, j-1) - \hat{\mathbf{G}}^-(i, j)] \end{aligned} \quad (2.34)$$

Gornji indeksi $n+1$ odnosno n , predstavljaju stari odnosno novi vremenski trenutak. Razlika između dviju susjednih linija mreže u pranjajućim koordinatama ($\Delta\xi$, $\Delta\eta$)

je proizvoljno odabrana i jednaka jedinici. Prostorne derivacije su aproksimirane pomoću MUSCL sheme (MUSCL - *Monotone Upstream-centered Schemes for Conservation Laws*), gdje su tokovi računati neposredno ekstrapolacijom rješenja pomoću formule za naprijed odnosno unazad ovisno o tome o kojem toku se radi. Općenito, formula za računanje podijeljenih tokova slijedi:

$$\begin{aligned}\hat{\mathbf{F}}^\pm(i, j) &= \hat{\mathbf{F}}^\pm\left(\mathbf{Q}_{i-\frac{1}{2},j}^\mp, M_{i-\frac{1}{2},j}\right) \\ \hat{\mathbf{G}}^\pm(i, j) &= \hat{\mathbf{G}}^\pm\left(\mathbf{Q}_{i,j-\frac{1}{2}}^\mp, M_{i,j-\frac{1}{2}}\right)\end{aligned}\quad (2.35)$$

Član M predstavlja sve geometrijske članove uključene u transformaciju prijanjajućih koordinata. Ekstrapolirane vrijednosti vektora rješenja \mathbf{Q} su određene pomoću formula drugog reda točnosti:

$$\begin{aligned}\mathbf{Q}_{i+\frac{1}{2},j}^- &= \mathbf{Q}_{i,j} + 0.5(\mathbf{Q}_{i,j} - \mathbf{Q}_{i-1,j}) \\ \mathbf{Q}_{i+\frac{1}{2},j}^+ &= \mathbf{Q}_{i+1,j} + 0.5(\mathbf{Q}_{i+1,j} - \mathbf{Q}_{i+2,j})\end{aligned}\quad (2.36)$$

2.5. Rubni uvjeti i određivanje tlaka na konturi aeroprofila

Na površini aeroprofila, rubni uvjet je zadan nepostojanjem protoka kroz površinu aeroprofila, odnosno postojanjem samo tangენტne brzine na konturu:

$$(\vec{v} - \vec{v}_b - \vec{v}_t) \cdot \vec{n} = 0 \quad (2.37)$$

gdje su \vec{v} brzina fluida u kartezijskim koordinatama, \vec{v}_b propisana brzina gibanja granice (konture aeroprofila), i \vec{v}_t transpiracijska brzina proizašla iz postojanja graničnog sloja. Transpiracijska brzina predstavlja efekt zadebljanja graničnog sloja, i pomoću iste brzine je model graničnog sloja spregnut s neviskoznim modelom. Tlak je određen iz jednadžbe količine gibanja u smjeru normale na konturu aeroprofila, koja proizlazi iz jednadžbe (2.37) i jednaka je

$$\rho \left\{ \frac{D\vec{n}}{Dt} \cdot (\vec{\mathbf{V}} - \vec{\mathbf{V}}_b - \vec{\mathbf{V}}_t) - \frac{D(\vec{\mathbf{V}}_b + \vec{\mathbf{V}}_t)}{Dt} \cdot \vec{n} \right\} = \text{grad}p \cdot \vec{n} \quad (2.38)$$

Uz uvjet da se kontura aeroprofila poklapa s linijama mreže $\eta = \text{konst.}$, i da su linije $\xi = \text{konst.}$ okomite na konturu aeroprofila, transformacija izraza (2.38) u prijanjajući koordinatni sustav daje slijedeći izraz:

$$\begin{aligned} \frac{\partial p}{\partial \eta} (x_\xi^2 + y_\xi^2) &= \frac{\partial p}{\partial \xi} (x_\xi x_\eta + y_\xi y_\eta) + \\ \rho \left\{ J \left[\frac{\bar{u}^2}{(x_\xi^2 + y_\xi^2)} (y_\xi x_{\xi\xi} - x_\xi y_{\xi\xi}) + \frac{2\bar{u}}{\sqrt{x_\xi^2 + y_\xi^2}} (y_\xi x_{\tau\xi} - x_\xi y_{\tau\xi}) + x_{\tau\tau} y_\xi - y_{\tau\tau} x_\xi \right] + \right. & (2.39) \\ \left. + (y_\xi v_{tx\xi} - x_\xi v_{ty\xi}) (y_\eta (v_x - x_\tau) - x_\eta (v_y - y_\tau)) + J (v_{tx\tau} y_\xi - v_{ty\tau} x_\xi) \right\} \end{aligned}$$

U izrazu (2.39) brzina \bar{u} je definirana prema izrazu (2.25).

Na vanjskim rubovima domene, korišteni su karakteristični rubni uvjeti. Pri tome se problem promatra kao lokalno jednodimenzionalan, odnosno derivacije uzduž granice se mogu zanemariti ($\partial(\)/\partial\xi \rightarrow 0$). Iz generaliziranih Riemman-ovih invarijanti [21] za hiperbolički sustav jednadžbi, dolazi se do izraza koji vrijede uzduž smjera prostiranja poremećaja:

$$\begin{aligned} \frac{ds}{dt} = 0 \quad \text{uzduž} \quad C^0 : \frac{d\eta}{dt} = v_n & \\ \frac{dv_t}{dt} = 0 \quad \text{uzduž} \quad C^0 : \frac{d\eta}{dt} = v_n & \end{aligned} \quad (2.40)$$

gdje su s entropija, a lokalna brzina zvuka, a v_n odnosno v_t lokalne brzine okomito odnosno uzduž vanjske granice domene. C^0 i C^\pm predstavljaju tri karakteristike na vanjskoj granici domene. Uz pretpostavku da je stujanje lokalno homentropsko, posljednje dvije jednadžbe prelaze u slijedeći oblik:

$$\frac{d}{dt}(R^\pm) = 0 \quad \text{uzduž} \quad \frac{dx}{dt} = v_n \pm a \quad (2.41)$$

gdje su

$$R^\pm = v_n \pm \frac{2a}{\gamma - 1} \quad (2.42)$$

Karakteristične jednadžbe se koriste za izračun varijabli na granici u novom vremenskom koraku. Za dvodimenzionalni slučaj broj varijabli iznosi četiri. Stoga je potrebno

imati i četiri nezavisne jednadžbe. Za podzvučno ustujavanje na vanjskom rubu domene, gdje je $v_n < 0$, vrijede slijedeći izrazi:

$$\begin{aligned}
 R^+ &= R^+(\infty) \\
 R^- &= R^-(F) \\
 v_t &= v_t(\infty) \\
 p_T &= p_T(\infty)
 \end{aligned}
 \tag{2.43}$$

Isto tako za podzvučno istujavanje na vanjskom rubu domene, gdje je $v_n > 0$, vrijede slijedeći izrazi:

$$\begin{aligned}
 R^+ &= R^+(F) \\
 R^- &= R^-(\infty) \\
 v_t &= v_t(F) \\
 p_T &= p_T(F)
 \end{aligned}
 \tag{2.44}$$

Oznaka F označava da su karakteristične varijable ekstrapolirane lokalno iz unutrašnjosti domene, a oznaka ∞ da su varijable izračunate iz vrijednosti slobodne struje.

3 Granični sloj

U ovome poglavlju, opisane su integralne jednadžbe za stlačivo strujanje u graničnom sloju, koje su korištene pri viskozno-neviskoznom sprezanju. Uz osnovne jednadžbe koje opisuju strujanje u graničnom sloju, prikazane su i jednadžbe koje predstavljaju dopunske relacije. Efekt graničnog sloja na neviskozno strujanje je napravljeno pomoću transpiracijske brzine. U ovome radu je primjenjen model graničnog sloja prema Drela i Giles [12].

3.1. Integralne jednadžbe graničnog sloja za stlačivo strujanje

Integralne jednadžbe graničnog sloja korištene u ovome radu su dobro znane Von Karman-ove integralne jednadžbe koje predstavljaju jednadžba količine gibanja:

$$\frac{s}{\theta} \frac{d\theta}{ds} = \frac{s}{\theta} \frac{C_f}{2} - (H + 2 - M_e^2) \frac{s}{u_e} \frac{du_e}{ds}, \quad (3.1)$$

i jednadžba kinetičke energije, također znana kao jednadžba parametra oblika

$$\frac{s}{H^*} \frac{dH^*}{ds} = \frac{s}{\theta} \frac{2C_D}{H^*} - \frac{s}{\theta} \frac{C_f}{2} - \left(\frac{2H^{**}}{H^*} + 1 - H \right) \frac{s}{u_e} \frac{du_e}{ds}. \quad (3.2)$$

Varijable u jednadžbama (3.1) i (3.2) su definirane slijedećim izrazima:

- debljina istisnuća

$$\delta^* = \int_0^{\infty} \left(1 - \frac{\rho u}{\rho u_e}\right) d\eta \quad (3.3)$$

- debljina količine gibanja

$$\theta = \int_0^{\infty} \left(1 - \frac{u}{u_e}\right) \frac{\rho u}{\rho u_e} d\eta \quad (3.4)$$

- koeficijent trenja

$$C_f = \frac{2\tau_w}{\rho_e u_e^2} \quad (3.5)$$

- debljina kinetičke energije

$$\theta^* = \int_0^{\infty} \left(1 - \left(\frac{u}{u_e}\right)^2\right) \frac{\rho u}{\rho u_e} d\eta \quad (3.6)$$

- debljina gustoće

$$\delta^{**} = \int_0^{\infty} \left(1 - \frac{\rho}{\rho_e}\right) \frac{u}{u_e} d\eta \quad (3.7)$$

- koeficijent disipacije

$$C_D = \frac{1}{\rho_e u_e^3} \int_0^{\infty} \tau \frac{\partial u}{\partial \eta} d\eta. \quad (3.8)$$

Parametri oblika definirani su na slijedeći način:

$$H = \frac{\delta^*}{\theta} \quad H^* = \frac{\theta^*}{\theta} \quad H^{**} = \frac{\delta^{**}}{\delta} \quad (3.9)$$

Jednadžba količine gibanja (3.1) i jednadžba parametra oblika (3.2) vrijede za laminarno i za turbulentno strujanje u graničnom sloju, kao i za strujanje u slobodnom tragu. Te jednadžbe sadrže više od dvije nezavisne varijable i stoga će biti potrebno napraviti neke pretpostavke zbog dodatnih nepoznanica. Dodatne nepoznate varijable su: C_f , C_D , H^* , H^{**} .

Sve dodatne jednadžbe su izražene, između ostalih varijabli, i preko kinematičkog parametra oblika H_k koji je definiran s konstantnom gustoćom kroz granični sloj. Profili

brzina za stlačivo i nestlačivo strujanje imaju približno iste oblike što sugerira da dodatne relacije u stlačivom strujanju trebaju biti temeljene na kinematičkom parametru oblika koji ovisi samo o profilu brzina. Whitfield [22] je razvio empirijski izraz za H_k u ovisnosti o konvencionalnom parametru oblika i Machovom broju na vanjskom rubu graničnog sloja:

$$H_k = \frac{H - 0.29M_e^2}{1 + 0.113M_e^2}. \quad (3.10)$$

Kinematički parametar oblika se koristi i za laminarna i za turbulentna strujanja. Za laminarna strujanja, dodatne jednadžbe su definirane kao u [10]:

- Parametar oblika kinetičke energije

$$H^* = \frac{H_k^* + 0.028M_e^2}{1 + 0.014M_e^2} \quad (3.11)$$

gdje je

$$H_k^* = \begin{cases} 1.515 + 0.076 \frac{(H_k - 4)^2}{H_k}, & H_k < 4 \\ 1.515 + 0.04 \frac{(H_k - 4)^2}{H_k}, & H_k > 4 \end{cases} \quad (3.12)$$

- Koeficijent trenja (Koeficijent smicanja na zidu)

$$\text{Re}_\theta \frac{C_f}{2} = \begin{cases} -0.067 + 0.01977 \frac{(7.4 - H_k)^2}{H_k - 1}, & H_k < 7.4 \\ -0.067 + 0.022 \left(1 - \frac{1.4}{H_k - 6}\right)^2, & H_k > 7.4 \end{cases} \quad (3.13)$$

- Koeficijent disipacije

$$\text{Re}_\theta \frac{2C_D}{H^*} = \begin{cases} 0.207 + 0.00205 (4 - H_k)^{5.5}, & H_k < 4 \\ 0.207 - 0.003 (H_k - 4)^2, & H_k > 4 \end{cases} \quad (3.14)$$

- Parametar oblika debljine gustoće

$$H^{**} = \left(\frac{0.064}{H_k - 0.8} + 0.251 \right) M_e^2 \quad (3.15)$$

Izraz (3.15), za parametar oblika debljine gustoće, će se u proračunima koristiti za laminarna i turbulentna strujanja.

Za turbulentno strujanje, dodatne jednadžbe su izvedene na činjenici postojanja dvoslojne strukture turbulentnog graničnog sloja. Dodatne jednadžbe za turbulentno strujanje su definirane kao u [10]:

- Koeficijent trenja (Koeficijent smicanja na zidu)

$$F_c C_f = \frac{0.3e^{-1.33H_k}}{\left[\log_{10} \left(\frac{\text{Re}_\theta}{F_c} \right) \right]^{1.74+0.31H_k}} + 0.00011 \left[\tanh \left(4 - \frac{H_k}{0.875} \right) - 1 \right] \quad (3.16)$$

gdje je

$$F_c = (1 + 0.2M_e^2)^{1/2} \quad (3.17)$$

- Parametar oblika kinetičke energije

$$H^* = \frac{H_k^* + 0.028M_e^2}{1 + 0.014M_e^2} \quad (3.18)$$

gdje su

$$H_k^* = \begin{cases} 1.505 + \frac{4}{\text{Re}_\theta} + \left(0.165 - \frac{1.6}{\sqrt{\text{Re}_\theta}} \right) \frac{(H_0 - H_k)^{1.6}}{H_k}, & H_k < H_0 \\ 1.505 + \frac{4}{\text{Re}_\theta} + (H_k - H_0)^2 \left[\frac{0.04}{H_k} + 0.007 \frac{\ln(\text{Re}_\theta)}{\left(H_k - H_0 + \frac{4}{\ln(\text{Re}_\theta)} \right)^2} \right], & H_k > H_0 \end{cases} \quad (3.19)$$

i

$$H_0 = 3 + \frac{400}{\text{Re}_\theta}. \quad (3.20)$$

- Koeficijent disipacije (neravnoteža)

$$\frac{2C_D}{H^*} = \frac{C_f}{2} \left(\frac{4}{H_k} - 1 \right) \frac{1}{3} + \frac{2}{H^*} C_\tau (1 - U_s) \quad (3.21)$$

gdje je koeficijent smicanja izračunat iz jednadžbe zaostajanja (eng. *lag equation*):

$$\frac{\delta}{C_\tau} \frac{dC_\tau}{d\xi} = 4.2 \left(C_{\tau_{eq}}^{0.5} - C_\tau^{0.5} \right) \quad (3.22)$$

and expression for δ is equal

$$\delta = \theta \left(3.15 + \frac{1.72}{H_k - 1} \right) + \delta^*. \quad (3.23)$$

Bezdimenzijska smična brzina U_s i ravnoteža koeficijenta smičnog naprezanja $C_{\tau_{eq}}$ u jednadžbi 3.18 su definirani pomoću

$$U_s = \frac{H^*}{6} \left(\frac{4}{H_k} - 1 \right) \quad (3.24)$$

i

$$C_{\tau_{eq}} = \frac{H^*}{2} \frac{0.03}{1 - U_s} \left(\frac{H_k - 1}{H_k} \right)^3. \quad (3.25)$$

4 Rezultati

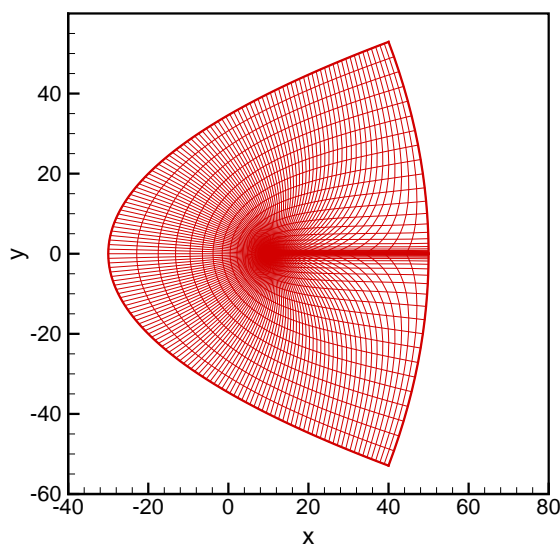
U ovome poglavlju će biti prikazani rezultati razvijene numeričke metode. Glavni cilj prikazanih slučajeva je pokazati da određivanje tlaka po konturi aeroprofila pomoću uključivanja transpiracijske brzine u jednadžbu količine gibanja radi i daje rezultate koji su usporedivi s eksperimentalnim podacima i proračunatim RANS rezultatima. Razvijena metoda viskozno-neviskozno sprežanja daje rezultate za stacionarno i za nestacionarno strujanje. Svi proračunati slučajevi su izvedeni na računalu s dva procesora, svaki je na taktu od 2.4 GHz, i veličinom radne memorije od 4 GB. Cijeli računalni kod je napisan u programskom jeziku Fortran 95. Najprije će biti opisana računalna mreža, a također će biti pokazana konvergencija računalne mreže za slučaj aeroprofila NACA0012. Pretpostavka je da će se postići slični rezultati konvergencije za aeroprofile NLR7301 i NACA64A010, koji su također korišteni za evaluaciju razvijene metode u ovome radu.

Stacionarni rezultati su proračunati za tri vrste aeroprofila, i to NACA0012, NACA64A010 and NLR7301. Ti aeroprofilu imaju različiti karakter raspodjele tlaka i intenziteta udarnog vala, i to predstavlja izazov za razvijenu numeričku metodu viskozno-neviskozno sprežanja. Stacionarni probni slučajevi su izabrani iz baze eksperimentalnih podataka tako da pokrivaju krozvučno i podzvučno stlačivo strujanje. Probni slučajevi bez pojave jakog udarnog vala su korišteni da pokažu dobro računanje položaja tranzicije pomoću metode za predviđanje tranzicije. Nestacionarni rezultati su proračunati za dva tipa aeroprofila, NACA0012 i NACA64A010. Nestacionarni probni slučajevi su izabrani iz baze eksperimentalnih podataka tako da imaju pojavu jakog udarnog vala.

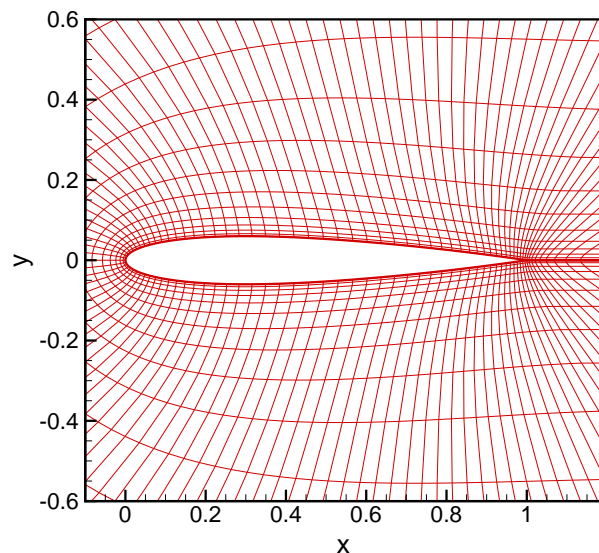
4.1. Računalna mreža

Za sve numeričke proračune neviskoznog modela korištene su strukturirane mreže C-tipa. Sve mreže su generirane pomoću računalnog koda koji je razvijen u Institutu za aeroelastičnost u Göttingenu, koji je dio DLR-a (Deutsches Zentrum für Luft- und Raumfahrt). Generiranje mreže postiže se rješavanjem Poissonove jednadžbe prema metodi Stegera i Sorensona [23]. Pojednostavljenosti funkcioniranja ovog eliptičkog generatora mreže može se naći u [24] i [25]. Mreža je generirana uz uvjet okomitosti na konturu aeroprofila kao i na vanjski rub domene. Taj uvjet u izvodu jednadžbi rubnog uvjeta na aeroprofilu pojednostavljuje te izraze i olakšava numerički proračun. Među mnogim parametrima koji su korišteni za generaciju računalne mreže, veličina visine prvog kontrolnog voluma u smjeru η osi jednaka 0.5% duljine tetive, a visina zadnjeg kontrolnog volumena u smjeru η osi je jednaka 70% duljine tetive aeroprofila. Takve postavke su korištene za sve korištene računalne mreže.

Primjer 2D mreže C-tipa za aeroprofil NACA0012, koja je generirana eliptičkim generatorom mreže, prikazan je na slici 4.1, dok je bliži pogled oko konture aeroprofila prikazan na slici 4.2.



Slika 4.1: Računalna mreža oko aeroprofila NACA0012 dobivena eliptičkim generatorom



Slika 4.2: Bliži pogled na mrežu oko konture aeroprofila NACA0012

4.2. Konvergencija Mreže

U ovome poglavlju učinjeno je se niz testova konvergencije računalne mreže za stacionarne i nestacionarne slučajeve. Probe konvergencije mreže su napravljene na neviskoznom rješavaču za različite gustoće mreže i za različite udaljenosti vanjskog ruba domene od aeroprofila. Na osnovu tih testova odabrana je gustoća mreže kao i udaljenost vanjskog ruba domene od aeroprofila tako da se dobije rješenje koje je praktično neovisno o daljnjem povećanju kvalitete mreže uzimajući pri tome u obzir potrebnu razinu točnosti metode. Tako odabrana kvaliteta mreže korištena je za računanje ostalih probnih slučajeva. Test konvergencije mreže je proveden na pet razina gustoća mreže i tri razine udaljenosti vanjskog ruba domene od aeroprofila, prema slijedećoj tablici:

Tablica 4.1: Testirane računalne mreže

BROJ KONTROLNIH VOLUMENA	UDALJENOST AEROPROFILA DO VANJSKOG RUBA DOMENE
MREŽA 100X30; 100 kontrolnih volumena u ξ smjeru 30 kontrolnih volumena u η smjeru	10 tetiva aeroprofila
	40 tetiva aeroprofila
	80 tetiva aeroprofila
MREŽA 160X30; 160 kontrolnih volumena u ξ smjeru 30 kontrolnih volumena u η smjeru	10 tetiva aeroprofila
	40 tetiva aeroprofila
	80 tetiva aeroprofila
MREŽA 160X60; 160 kontrolnih volumena u ξ smjeru 60 kontrolnih volumena u η smjeru	10 tetiva aeroprofila
	40 tetiva aeroprofila
	80 tetiva aeroprofila
MREŽA 240X60; 240 kontrolnih volumena u ξ smjeru 60 kontrolnih volumena u η smjeru	10 tetiva aeroprofila
	40 tetiva aeroprofila
	80 tetiva aeroprofila
MREŽA 320X60; 320 kontrolnih volumena u ξ smjeru 60 kontrolnih volumena u η smjeru	10 tetiva aeroprofila
	40 tetiva aeroprofila
	80 tetiva aeroprofila

Na slikama 4.3, 4.5, 4.7, 4.9 i 4.11 prikazane su probe konvergencije koeficijenta normalne sile za stacionarno rješenje strujanja oko aeroprofila NACA0012. Proračuni su napravljeni za Machov broj $Ma = 0.77$ pri napadnom kutu $\alpha = 1^\circ$, za mreže i udaljenosti vanjskog ruba domene prema tablici 4.1. Stacionarno rješenje je dobiveno pomoću nestacionarnog proračuna na mirujućem aeroprofilu s vremenom simulacije od devet

perioda. Koeficijent normalne sile je dobiven integracijom tlaka po konturi aeroprofila, i predstavlja silu od tlaka okomitu na tetivu aeroprofila. Koeficijent normalne sile izračunat je prema slijedećem izrazu:

$$c_n = \int_0^1 (C_{pL} - C_{pU}) d\left(\frac{x}{c}\right) \quad (4.1)$$

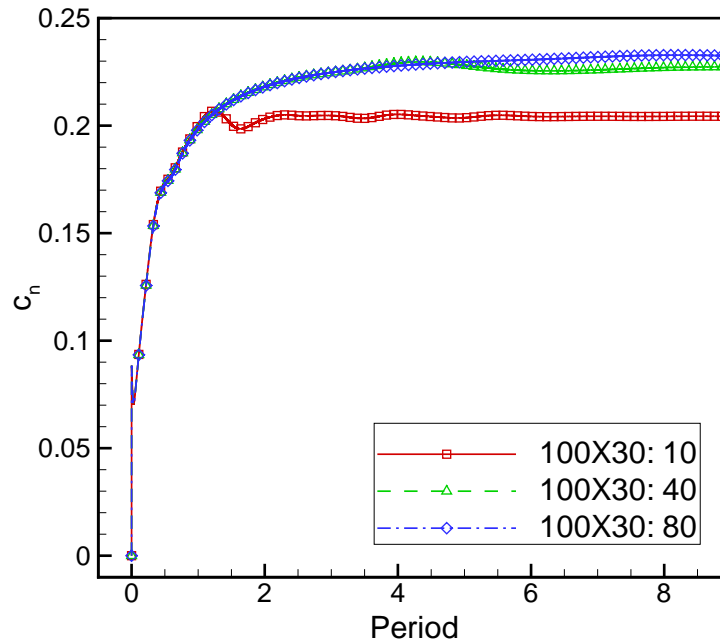
gdje su C_{pL} koeficijent tlaka na donjaci, C_{pU} koeficijent tlaka na gornjaci aeroprofila, c tetiva aeroprofila i x je lokalna koordinata koja ide od prednjeg brida uzduž tetive aeroprofila.

Na slikama 4.4, 4.6, 4.8, 4.10 i 4.12 prikazana je relativna greška rješenja, za mreže s udaljenošću 10 i 40 duljina tetiva od aeroprofila do vanjske granice domene. Ta relativna greška je razlika između rješenja za mreže veličine 10 i 40 duljina tetiva od aeroprofila do vanjske granice domene, i mreže s udaljenošću 80 duljina tetiva od aeroprofila do vanjske granice domene. Svaka slika predstavlja različite gustoće mreže prema tablici 4.1. Na tim slikama razlika je predstavljena kao postotak u odnosu na mrežu s udaljenošću 80 duljina tetive od aeroprofila do vanjskog ruba domene.

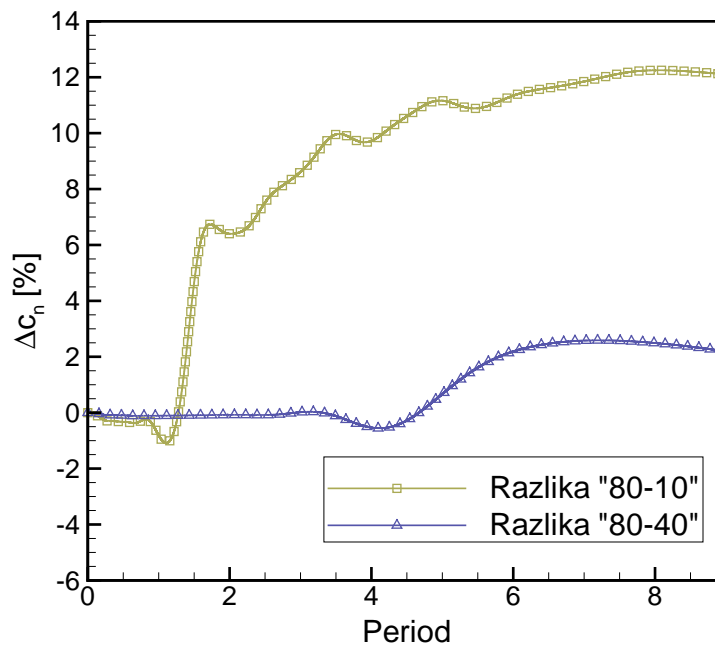
Na slikama 4.3, 4.4, 4.5, 4.6, 4.7, 4.8, 4.9, 4.10, 4.11 i 4.12 se vidi da rješenje i greška rješenja za mrežu s udaljenošću 10 duljina tetive pokazuje slično ponašanje neovisno od gustoće mreže, kako kvalitativno tako i kvantitativno. Stacionarno rješenje koeficijenta normalne sile, za mreže koje imaju vanjski rub domene na 10 duljina tetiva od aeroprofila i sve gustoće mreže, ima odstupanje od oko 10% u odnosu na rješenja za mreže koje imaju udaljeniji vanjski rub domene (na 40 odnosno 80 duljina tetive). Rješenje za udaljenost 40 duljina tetive pokazuje malo odstupanje (manje od 3 %) za gustoće mreže 100X30 i 160X30. Za mreže gustoće 160X60, 240X60 i 320X60 i iste udaljenosti od 40 duljina tetive, rješenje pokazuje zanemarivu razliku manju od 1 %. Promjena gustoće računalne mreže daje približno jednaku vrijednost koeficijenta normalne sile u stacionarnom strujanju, za jednaku udaljenost vanjskog ruba domene. Veći utjecaj na stacionarno rješenje ima broj kontrolnih volumena u smjeru koordinatne osi η .

Iz slika 4.3 do 4.12 može se zaključiti da su stacionarni numerički proračuni neovisni o daljnjem poboljšanju kvalitete mreže za mreže koje imaju vanjski rub na udaljenosti 40 duljina tetiva od aeroprofila i više. Iz istih slika može se zaključiti da stacionarno rješenje postiže svoju konstantnu vrijednost s mrežama koje imaju 60 i više kontrolnih volumena u smjeru koordinatne osi η . Uzimajući u obzir da razvijena metoda treba dati rješenja koja su usporediva s metodama visoke točnosti i istovremeno dati to rješenje u

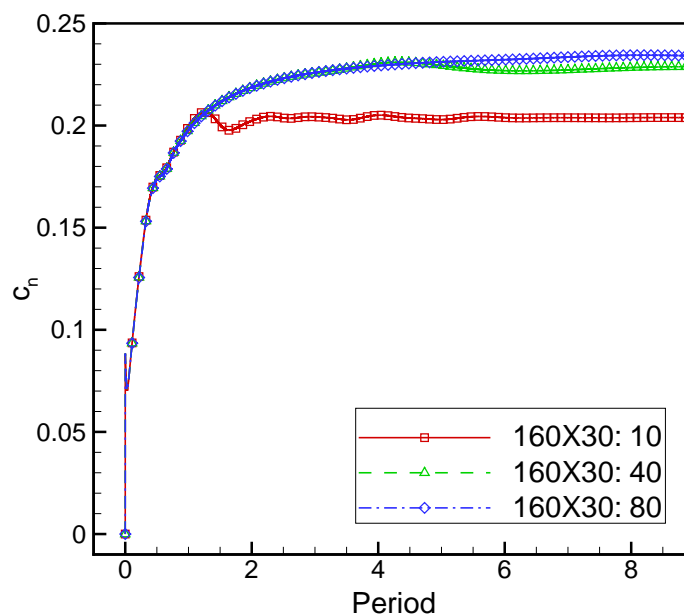
razumnom vremenu, izabrana mreža za stacionarne proračune ima 160 kontrolnih volumena u smjeru ξ koordinate, 60 kontrolnih volumena u smjeru η koordinate i udaljenost od 40 duljina tetiva od aeroprofila do vanjskog ruba domene.



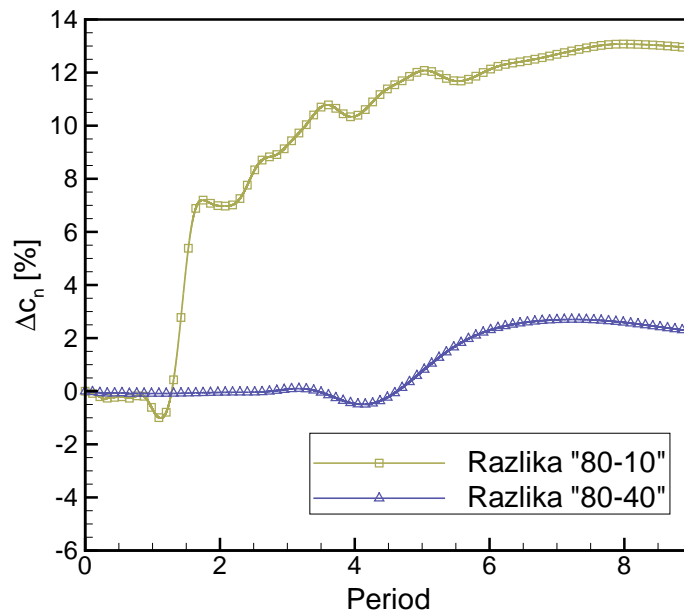
Slika 4.3: Mreža 100X30; test konvergencije mreže za stacionarno rješenje za aeroprofil NACA0012 pri $\alpha = 1^\circ$, $Ma = 0.77$; 10, 40, 80 su udaljenosti od aeroprofila do vanjskog ruba domene izražen u duljinama tetiva aeroprofila



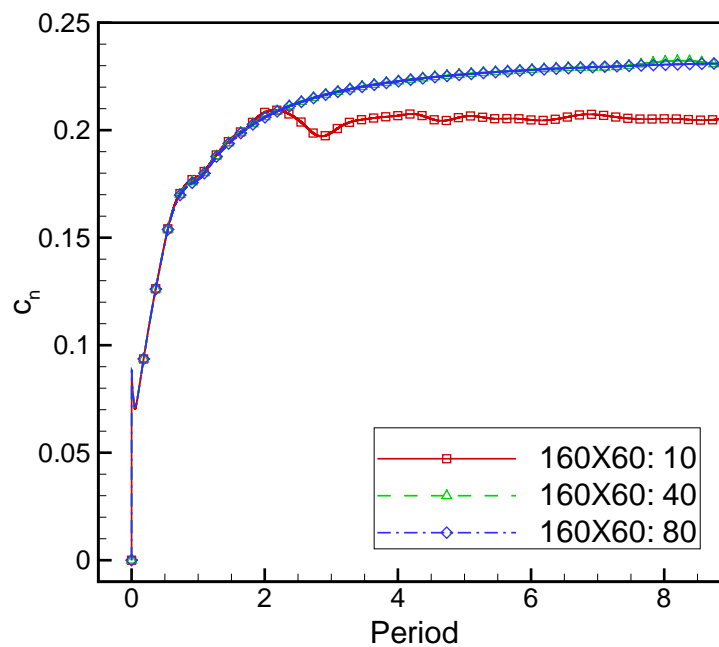
Slika 4.4: Mreža 100X30; razlika rješenja za udaljenosti 10 i 40 duljina tetiva i rješenja za udaljenost 80 duljina tetiva; razlika je izražena u postocima u odnosu na mrežu s 80 duljina tetive; aeroprofil NACA0012 pri $\alpha = 1^\circ$, $Ma = 0.77$



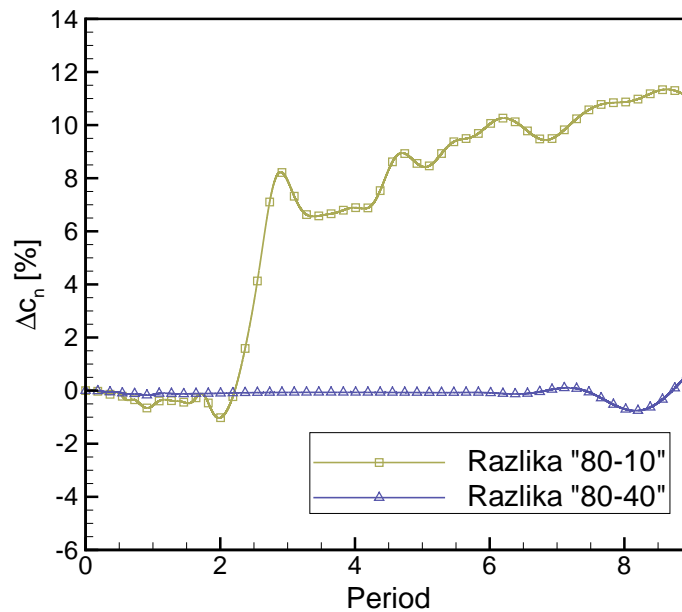
Slika 4.5: Mreža 160X30; test konvergencije mreže za stacionarno rješenje za aeroprofil NACA0012 pri $\alpha = 1^\circ$, $Ma = 0.77$; 10, 40, 80 su udaljenosti od aeroprofila do vanjskog ruba domene izražen u duljinama tetiva aeroprofila



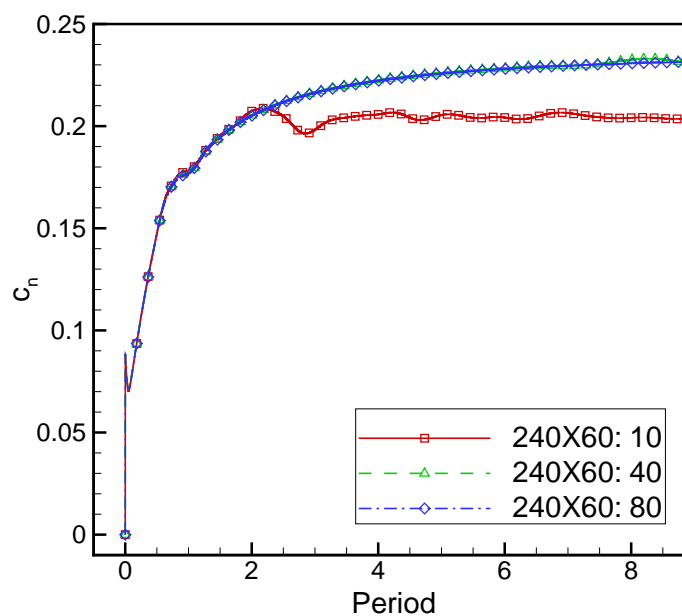
Slika 4.6: Mreža 160X30; razlika rješenja za udaljenosti 10 i 40 duljina tetiva i rješenja za udaljenost 80 duljina tetiva; razlika je izražena u postocima u odnosu na mrežu s 80 duljina tetive; aeroprofil NACA0012 pri $\alpha = 1^\circ$, $Ma = 0.77$



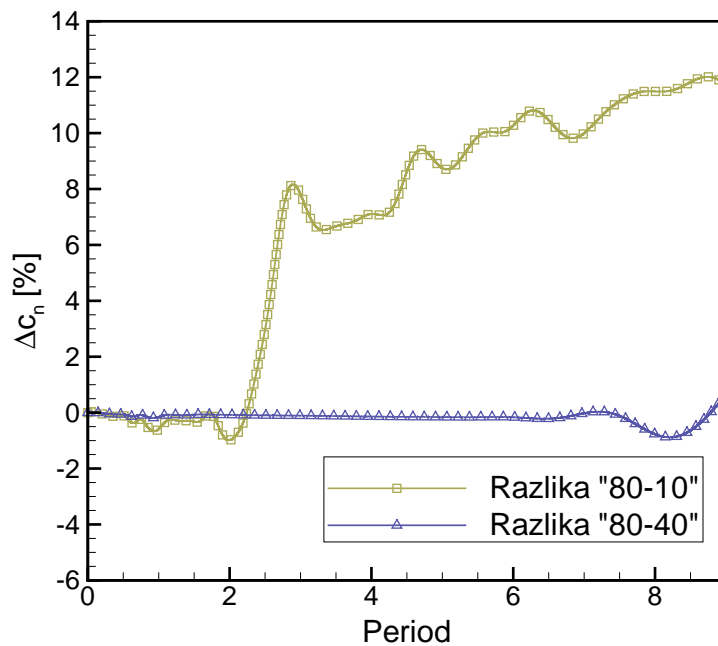
Slika 4.7: Mreža 160X60; test konvergencije mreže za stacionarno rješenje za aeroprofil NACA0012 pri $\alpha = 1^\circ$, $Ma = 0.77$; 10, 40, 80 su udaljenosti od aeroprofila do vanjskog ruba domene izražen u duljinama tetiva aeroprofila



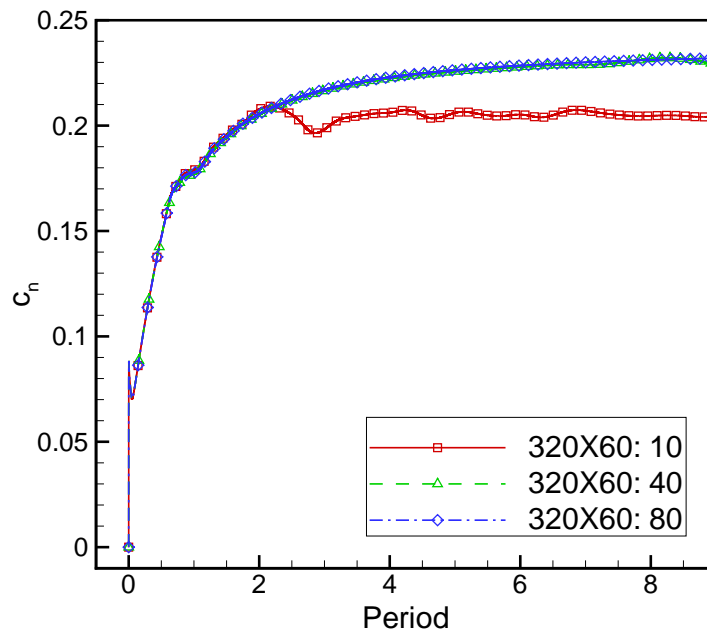
Slika 4.8: Mreža 160X60; razlika rješenja za udaljenosti 10 i 40 duljina tetiva i rješenja za udaljenost 80 duljina tetiva; razlika je izražena u postocima u odnosu na mrežu s 80 duljina tetive; aeroprofil NACA0012 pri $\alpha = 1^\circ$, $Ma = 0.77$



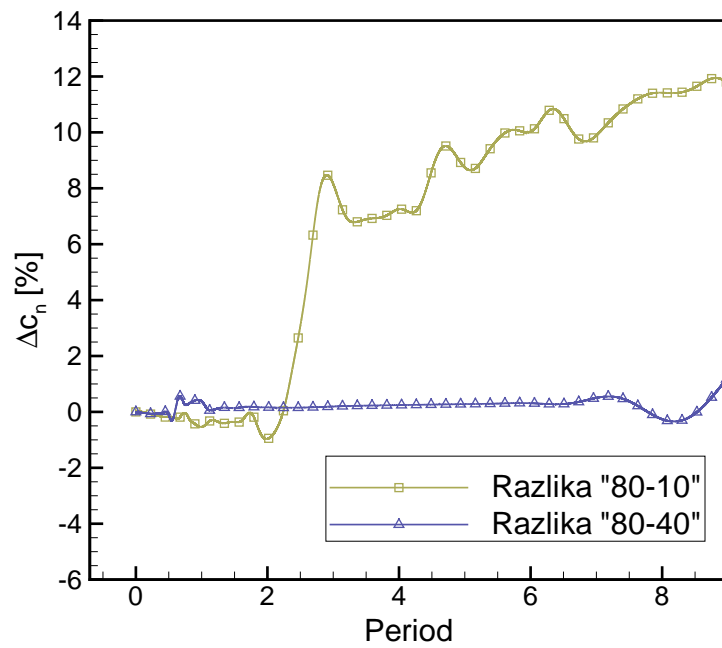
Slika 4.9: Mreža 240X60; test konvergencije mreže za stacionarno rješenje za aeroprofil NACA0012 pri $\alpha = 1^\circ$, $Ma = 0.77$; 10, 40, 80 su udaljenosti od aeroprofila do vanjskog ruba domene izražen u duljinama tetiva aeroprofila



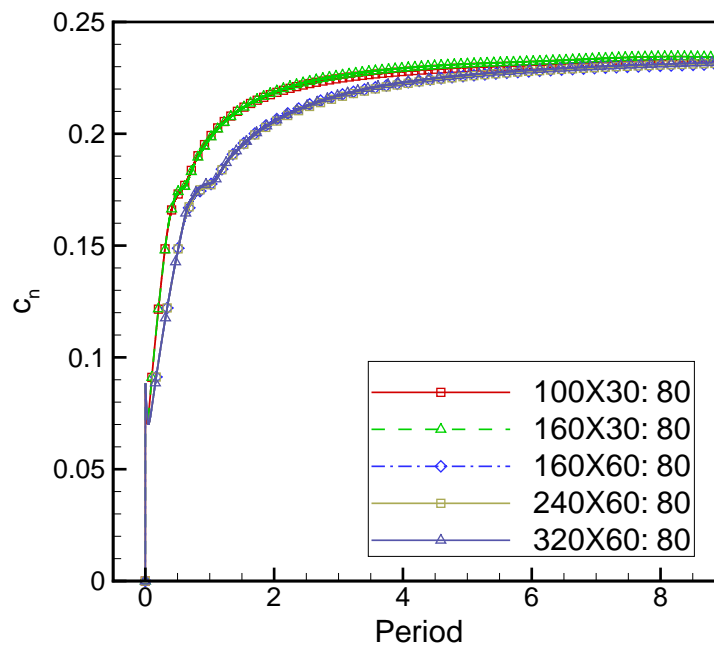
Slika 4.10: Mreža 240X60; razlika rješenja za udaljenosti 10 i 40 duljina tetiva i rješenja za udaljenost 80 duljina tetiva; razlika je izražena u postocima u odnosu na mrežu s 80 duljina tetive; aeroprofil NACA0012 pri $\alpha = 1^\circ$, $Ma = 0.77$



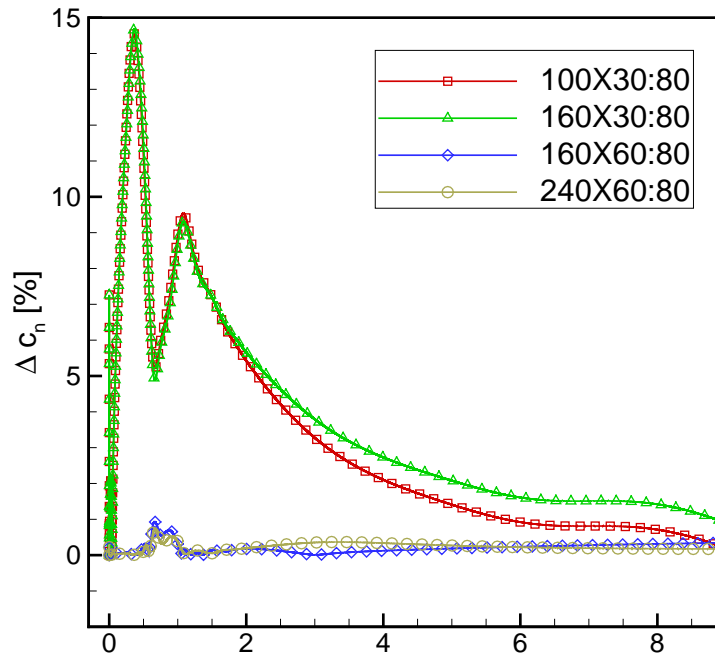
Slika 4.11: Mreža 320X60; test konvergencije mreže za stacionarno rješenje za aeroprofil NACA0012 pri $\alpha = 1^\circ$, $Ma = 0.77$; 10, 40, 80 su udaljenosti od aeroprofila do vanjskog ruba domene izražen u duljinama tetiva aeroprofila



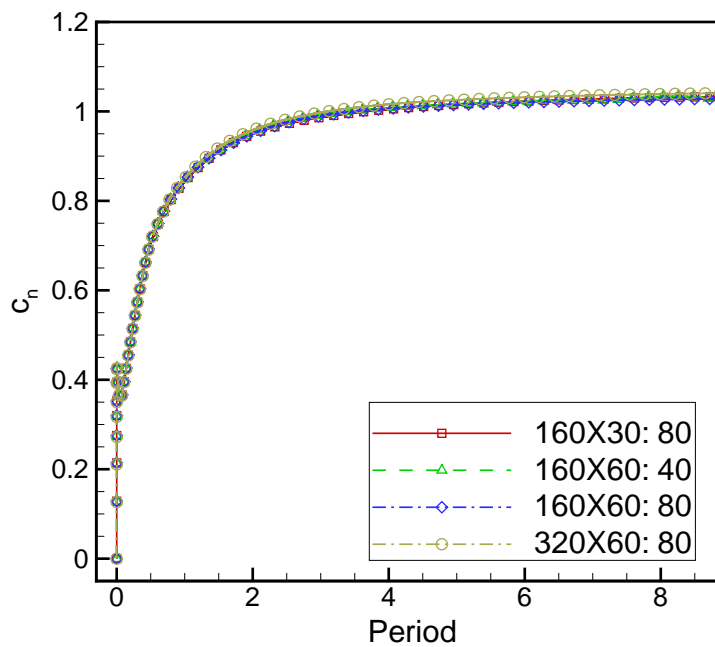
Slika 4.12: Mreža 320X60; razlika rješenja za udaljenosti 10 i 40 duljina tetiva i rješenja za udaljenost 80 duljina tetiva; razlika je izražena u postocima u odnosu na mrežu s 80 duljina tetive; aeroprofil NACA0012 pri $\alpha = 1^\circ$, $Ma = 0.77$



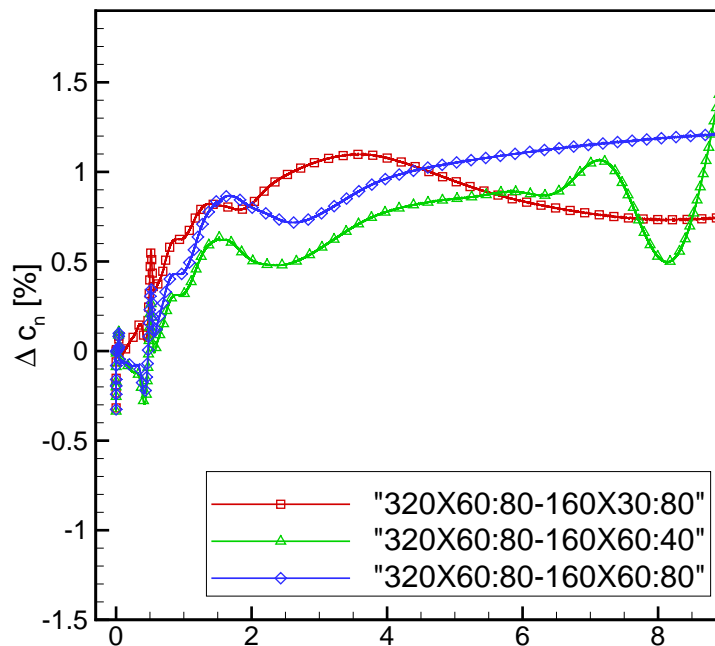
Slika 4.13: Test konvergencije za udaljenost 80 duljina tetiva od aeroprofila do vanjskog ruba domene; aeroprofil NACA0012 pri $\alpha = 1^\circ$, $Ma = 0.77$



Slika 4.14: Razlika rješenja za mreže napisane u legendi slike i mreže 320X60 s 80 duljina tetive od aeroprofila do vanjskog ruba domene; aeroprofil NACA0012 pri $\alpha = 1^\circ$, $Ma = 0.77$



Slika 4.15: Test konvergencije za NACA0012 aeroprofil pri $\alpha = 5^\circ$, $Ma = 0.77$

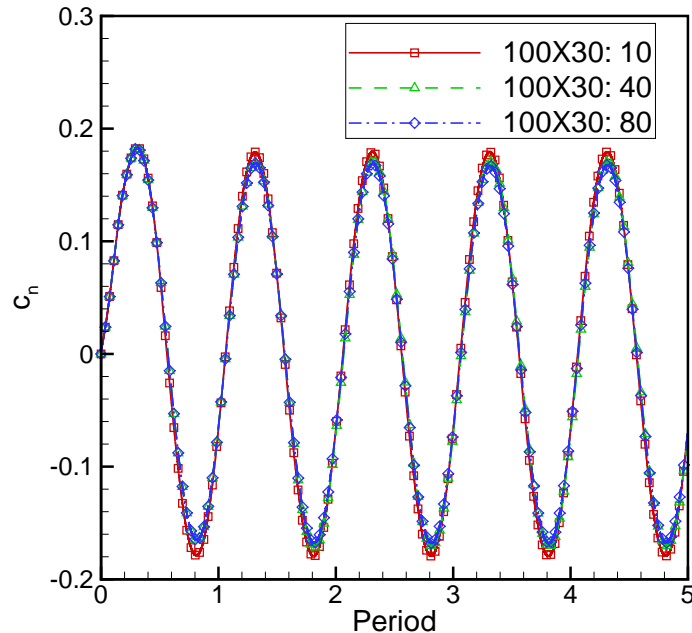


Slika 4.16: Razlika između rješenja dobivenih pomoću mreža navedenih u legendi slike i mreže 320X60 s udaljenošću 80 duljina tetiva od aeroprofila do vanjskog ruba domene, za aeroprofil NACA0012 pri $\alpha = 5^\circ$, $Ma = 0.77$

Na slikama od 4.17 do 4.26 prikazana su rješenja za nestacionarno strujanje za koeficijent normalne sile. Svi slučajevi su računati za neviskozno strujanje pri Machovom broju $Ma = 0.77$, srednjem napadnom kutu $\alpha_m = 0^\circ$, amplitudi napadnog kuta $\alpha_o = 1^\circ$ i reduciranoj frekvenciji $\omega^* = 0.1$.

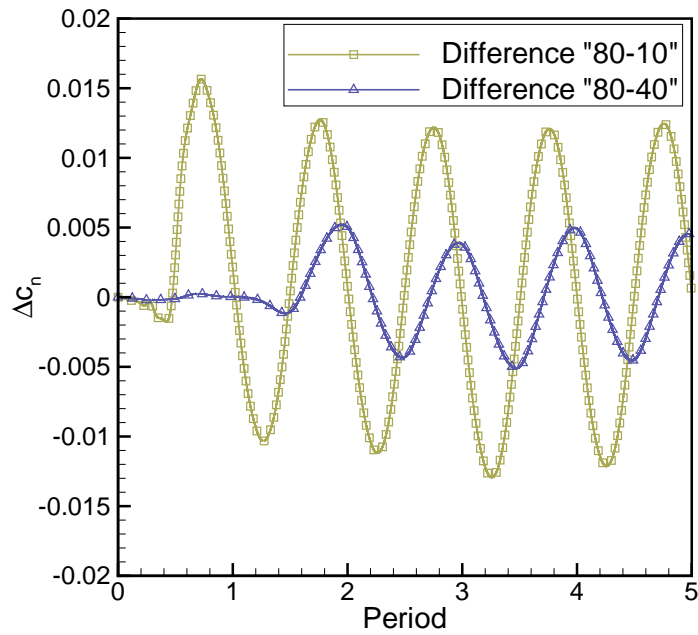
Može se primjetiti da rješenje koeficijenta normalne sile za nestacionarno strujanje poprima harmonijski tijek već nakon druge periode. Vrijednost koeficijenta normalne sile se razlikuje za različite udaljenosti vanjskog ruba domene. Rješenje za udaljenost 10 duljina tetive od aeroprofila do vanjskog ruba domene razlikuje se od rješenja za 40 i 80 duljina tetive u maksimalnoj vrijednosti, dok posljednja dva slučaja imaju jednake vrijednosti koeficijenta normalne sile. Promatrajući nestacionarni tijek koeficijenta normalne sile za različite gustoće mreže na slikama 4.17 do 4.26, može se primjetiti da nema značajnije razlike osim manjeg odstupanja u maksimalnoj vrijednosti. Rješenje za najmanju domenu odstupa od rješenja za domene s udaljenostima 40 i 80 duljina tetiva aeroprofila. Uzimajući u obzir konvergenciju stacionarnih rezultata, može se zaključiti da mreža veličine 160X60 daje zadovoljavajuće rezultate i prikladna je za daljnje pro-

račune. Također se može zaključiti da rješenje simulacije u nestacionarnom strujanju postaje periodično nakon druge periode.



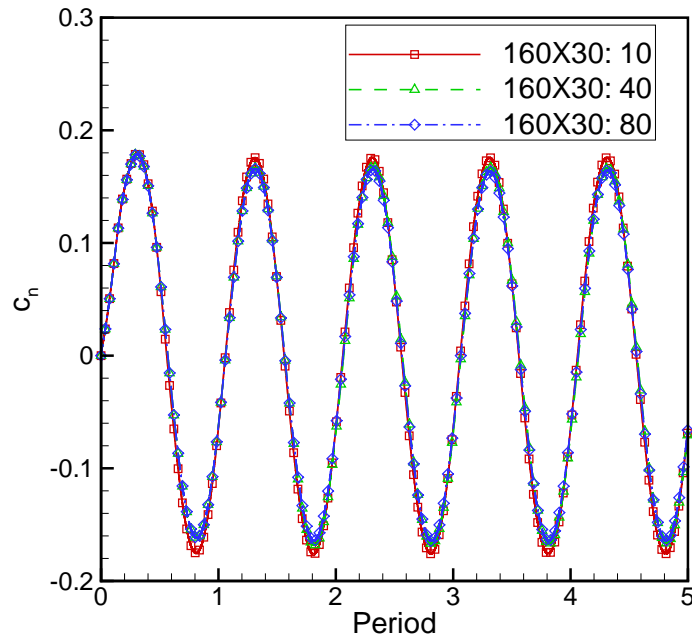
Slika 4.17: Mreža 100X30; konvergencija nestacionarnog rješenja; 10, 40 i 80 predstavljaju udaljenosti aeroprofila od vanjskog ruba domene u duljinama tetiva aeroprofila; NACA0012 aeroprofil pri $Ma = 0.77$, $\alpha_m = 0^\circ$, $\alpha_o = 1^\circ$

U tablici 4.2 dana su rješenja za nestacionarno strujanje prikazana na slikama 4.17 do 4.26. Koeficijent normalne sile za nestacionarno strujanje je prikazan u obliku kompleksnog broja, realnog i imaginarnog dijela prema jednadžbi (4.5), koja je ekvivalentno primjenjiva za koeficijent normalne sile. u tom obliku opisa realni i imaginarni dijelovi nisu normirani s amplitudom napadnog kuta. Realni dio koeficijenta normalne sile za nestacionarno strujanje pokazuje maksimalnu relativnu razliku od 6%, za sve različite gustoće mreže i različite udaljenosti od aeroprofila do vanjskog ruba domene. Realni dio nema jasni trend rasta ili pada vrijednosti u odnosu na povećanje ili smanjenje broja kontrolnih volumena ili udaljenosti aeroprofila do vanjskog ruba domene. Imaginarni dio koeficijenta normalne sile za nestacionarno strujanje pokazuje maksimalnu relativnu razliku od 11% između svih promjena gustoće mreže i udaljenosti od aeroprofila do vanjskog ruba domene. Imaginarni dio za istu udaljenost do vanjskog ruba domene i za različite gustoće mreže pokazuje manju relativnu razliku, čiji maksimalni iznos je 5.7%. Kai i realni dio, imaginarni dio također ne pokazuje jasan trend rasta i pada vrijed-

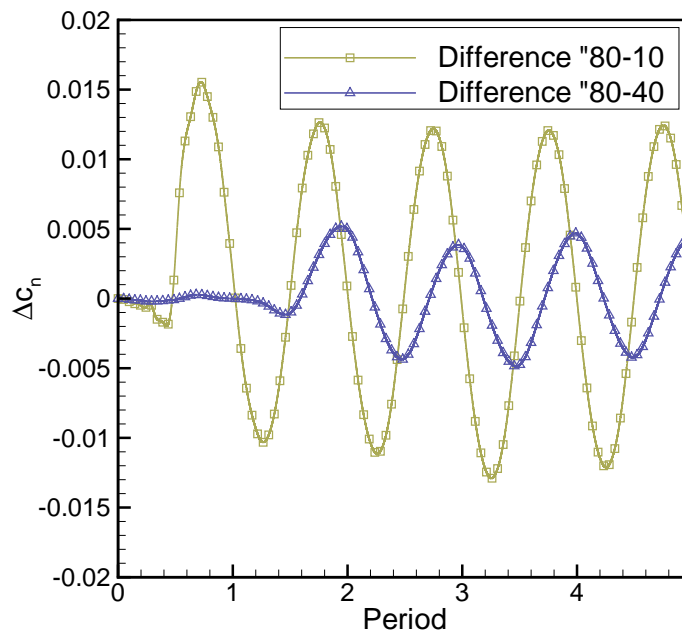


Slika 4.18: Mreža 100X30; razlika rješenja za udaljenosti vanjskog ruba domene od aeroprofila 10 i 40 duljina tetiva i rješenja za udaljenost 80 duljina tetiva; NACA0012 aeroprofil pri $Ma = 0.77$, $\alpha_m = 0^\circ$, $\alpha_o = 1^\circ$

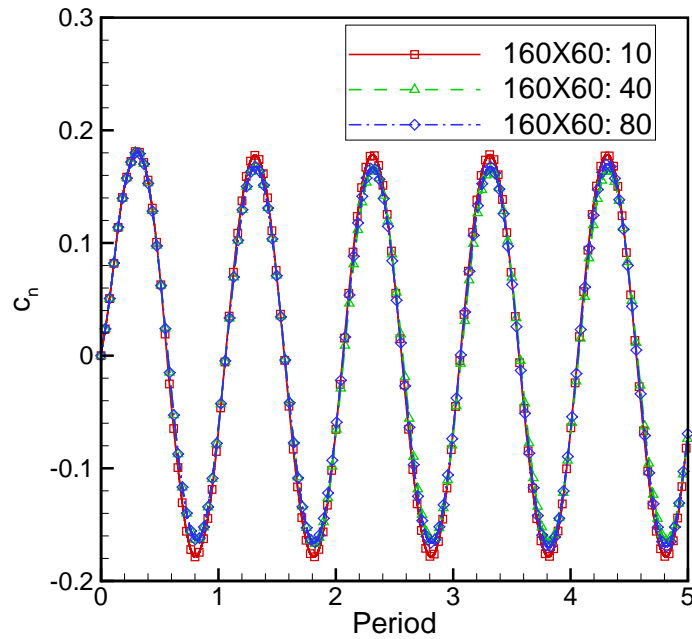
nosti u odnosu na povećanje ili smanjenje broja kontrolnih volumena ili udaljenosti do vanjskog ruba domene.



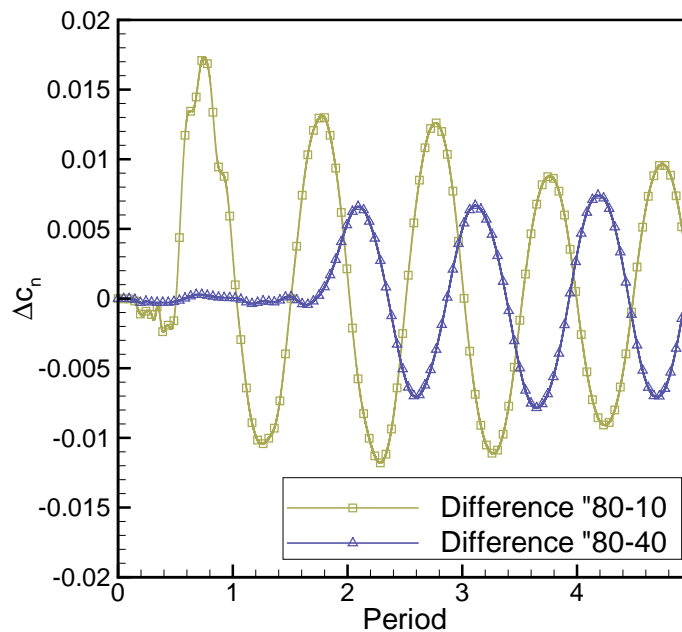
Slika 4.19: Mreža 160X30; konvergencija nestacionarnog rješenja; 10, 40 i 80 predstavljaju udaljenosti aeroprofila od vanjskog ruba domene u duljinama tetiva aeroprofila; NACA0012 aeroprofil pri $Ma = 0.77$, $\alpha_m = 0^\circ$, $\alpha_o = 1^\circ$



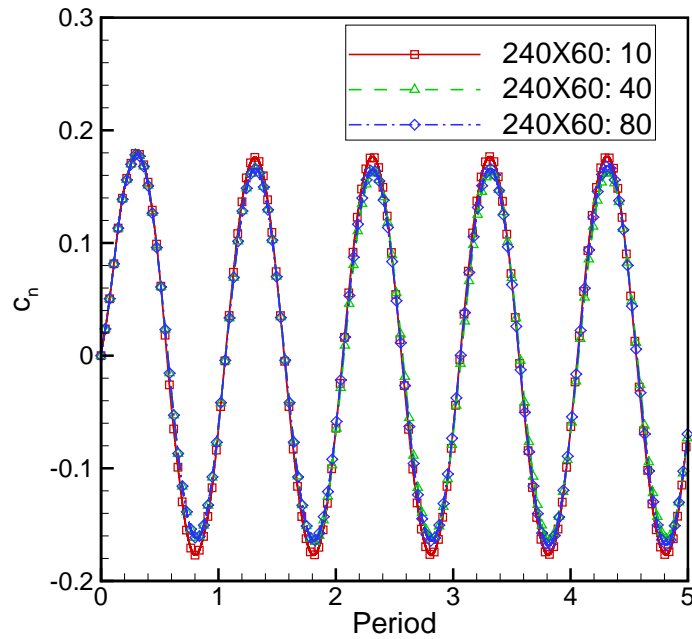
Slika 4.20: Mreža 160X30; razlika rješenja za udaljenosti vanjskog ruba domene od aeroprofila 10 i 40 duljina tetiva i rješenja za udaljenost 80 duljina tetiva; NACA0012 aeroprofil pri $Ma = 0.77$, $\alpha_m = 0^\circ$, $\alpha_o = 1^\circ$



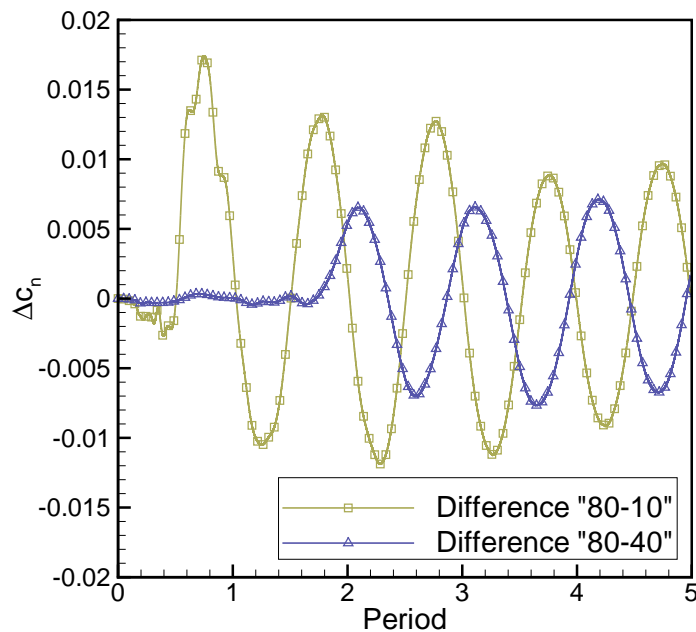
Slika 4.21: Mreža 160X60; konvergencija nestacionarnog rješenja; 10, 40 i 80 predstavljaju udaljenosti aeroprofila od vanjskog ruba domene u duljinama tetiva aeroprofila; NACA0012 aeroprofil pri $Ma = 0.77$, $\alpha_m = 0^\circ$, $\alpha_o = 1^\circ$



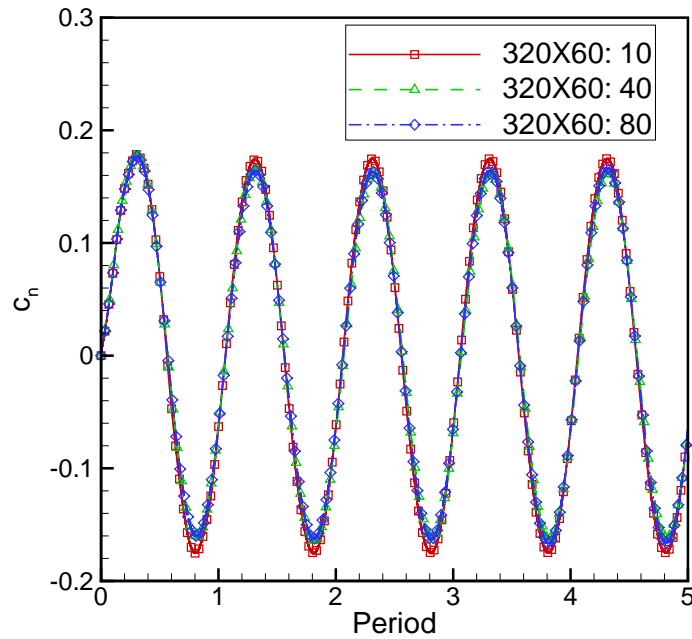
Slika 4.22: Mreža 160X60; razlika rješenja za udaljenosti vanjskog ruba domene od aeroprofila 10 i 40 duljina tetiva i rješenja za udaljenost 80 duljina tetiva; NACA0012 aeroprofil pri $Ma = 0.77$, $\alpha_m = 0^\circ$, $\alpha_o = 1^\circ$



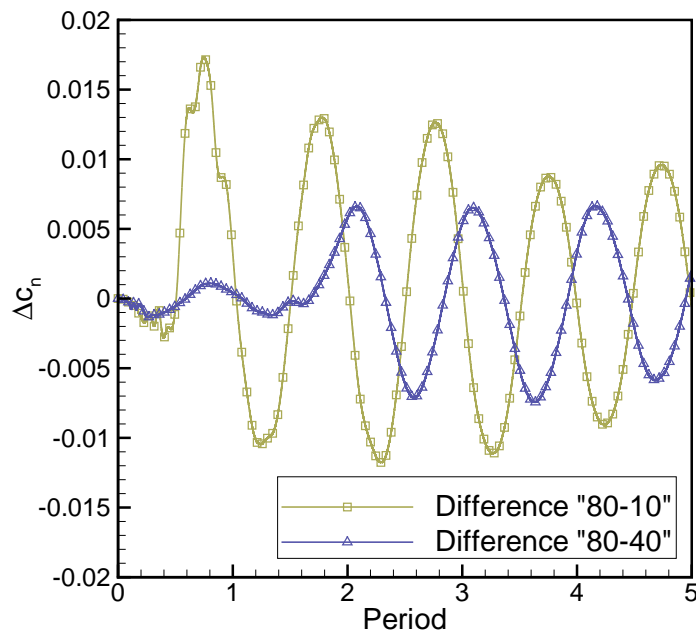
Slika 4.23: Mreža 240X60; konvergencija nestacionarnog rješenja; 10, 40 i 80 predstavljaju udaljenosti aeroprofila od vanjskog ruba domene u duljinama tetiva aeroprofila; NACA0012 aeroprofil pri $Ma = 0.77$, $\alpha_m = 0^\circ$, $\alpha_o = 1^\circ$



Slika 4.24: Mreža 240X60; razlika rješenja za udaljenosti vanjskog ruba domene od aeroprofila 10 i 40 duljina tetiva i rješenja za udaljenost 80 duljina tetiva; NACA0012 aeroprofil pri $Ma = 0.77$, $\alpha_m = 0^\circ$, $\alpha_o = 1^\circ$



Slika 4.25: Mreža 320X60; konvergencija nestacionarnog rješenja; 10, 40 i 80 predstavljaju udaljenosti aeroprofila od vanjskog ruba domene u duljinama tetiva aeroprofila; NACA0012 aeroprofil pri $Ma = 0.77$, $\alpha_m = 0^\circ$, $\alpha_o = 1^\circ$



Slika 4.26: Mreža 320X60; razlika rješenja za udaljenosti vanjskog ruba domene od aeroprofila 10 i 40 duljina tetiva i rješenja za udaljenost 80 duljina tetiva; NACA0012 aeroprofil pri $Ma = 0.77$, $\alpha_m = 0^\circ$, $\alpha_o = 1^\circ$

Tablica 4.2: Rezultati koeficijenta normalne sile za nestacionarno strujanje

Veličina mreže	Udaljenost do vanjskog ruba domene	Real (c_n)	Imag (c_n)
100X30	10 duljina tetiva	0.1668	-0.06602
	40 duljina tetiva	0.1547	-0.07123
	80 duljina tetiva	0.1541	-0.06652
160X30	10 duljina tetiva	0.1637	-0.06408
	40 duljina tetiva	0.1517	-0.06862
	80 duljina tetiva	0.1513	-0.06414
160X60	10 duljina tetiva	0.1657	-0.06606
	40 duljina tetiva	0.1491	-0.06943
	80 duljina tetiva	0.1563	-0.06648
240X60	10 duljina tetiva	0.1645	-0.06459
	40 duljina tetiva	0.1479	-0.06791
	80 duljina tetiva	0.1550	-0.06518
320X60	10 duljina tetiva	0.1612	-0.06779
	40 duljina tetiva	0.1474	-0.06738
	80 duljina tetiva	0.1535	-0.06419

4.3. Rezultati za stacionarno strujanje

Stacionarni rezultati su izvedeni za slijedeća tri tipa aeroprofila: NACA0012, NACA64A010 i NLR7301. Ta tri aeroprofila imaju tri različite i karakteristične raspodjele tlaka, a također postoje i dostupni su eksperimentalni podaci za te aeroprofile. Numerički rezultati viskozno-neviskozne metode su uspoređeni s probnim slučajevima iz AGARD izvještaja [26] i [27], a također i s rezultatima RANS koda. RANS kod koji je korišten u ovome radu je Tau kod [28] razvijen u DLR-u (Deutsches Zentrum fuer Luft- und Raumfahrt). Tau kod koristi metodu kontrolnih volumena rješavajući Eulerove i Navier-Stokesove jednadžbe, na hibridnoj nestrukturiranoj mreži oko složenih geometrija, za strujanja od niskog podzvučnog do hiperzvučnog strujanja. Svi proračuni u Tau kodu su izvedeni s dvojednadžbenim $k-\omega$ modelom turbulencije. U RANS kodu je svako strujanje računato kao potpuno turbulentno, bez ograničavanja produkcije turbulencije u laminarnom djelu graničnog sloja. Početna vrijednost odnosa turbulentne i laminarne kinematičke viskoznosti je propisana za cijelo polje strujanja kao i za rub domene i bila je jednaka vrijednosti koja je mnogo manja od jedinice ($\nu_t/\nu \ll 1$). Probni slučajevi su izabrani na način da pokriju Machove brojeve od donje granice kompresibilnog strujanja do krozzvučnog područja.

4.3.1. NACA0012 aeroprofil

NACA0012 je simetričan aeroprofil s 12% debljine (u odnosu na duljinu tetive aeroprofila). Za taj aeroprofil postoje mnoge baze eksperimentalnih podataka za stacionarno i za nestacionarno strujanje [26] i zbog toga je vrlo čest u provjerama numeričkih kodova. Druga prednost tog aeroprofila je svojstvo simetričnosti. Eksperimentalni podaci uzgona za simetrični aeroprofil pod nultim napadnim kutom nisu pod utjecajem zidova zračnog tunela.

U tablici 4.3 prikazani su izabrani probni slučajevi za NACA0012 aeroprofil iz eksperimentalnih podataka u AGARD izvještaju [26]. Izabrana su tri probna slučaja pri različitim Machovim brojevima koji pokrivaju podzvučno kompresibilno strujanje s i bez pojave udarnih valova.

Probni slučaj 1: NACA0012, $Ma = 0.504$, $Re = 2.93 \cdot 10^6$, $\alpha = 4.06^\circ$

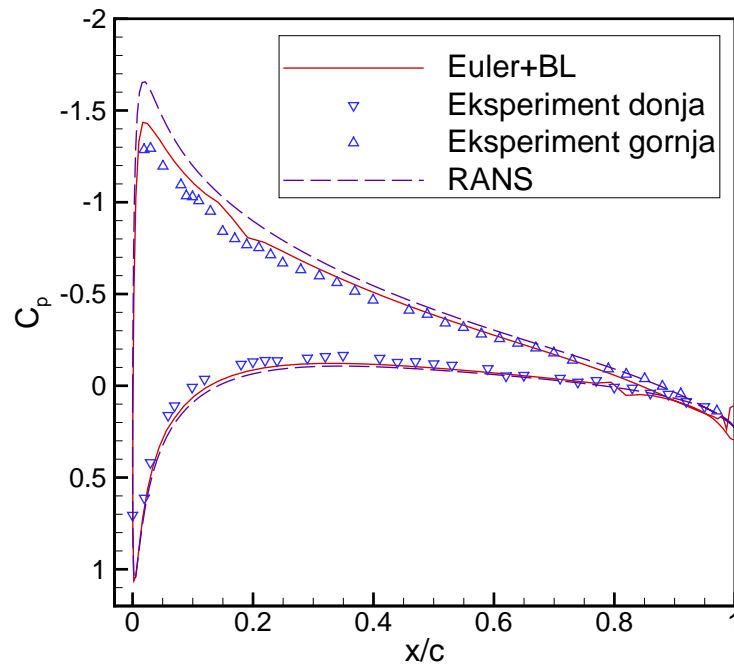
Na slici 4.27 prikazani su stacionarni rezultati za aeroprofil NACA0012, pri Machovom broju $Ma = 0.504$, Reynoldsovom broju $Re = 2.93 \cdot 10^6$ i napadnim kutem

Tablica 4.3: NACA0012 probni slučajevi za stacionarno strujanje

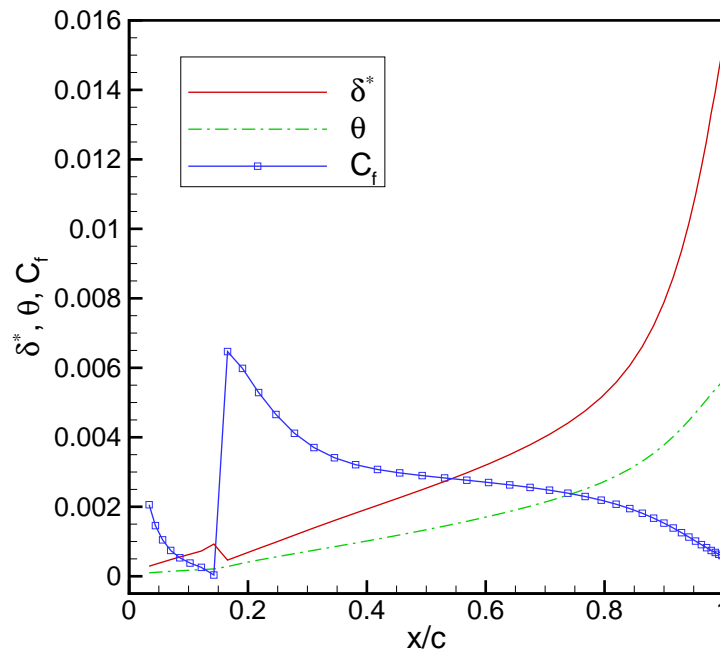
Probni slučaj	Ma	Re	α
1	0.504	$2.93 \cdot 10^6$	4.06°
2	0.756	$4.01 \cdot 10^6$	-0.01°
3	0.803	$4.09 \cdot 10^6$	0.05°

$\alpha = 4.06^\circ$. Taj probni slučaj spada u kompresibilno strujanje bez pojave udarnog vala. Eksperimentalni podaci su prikazani pomoću trokuta okrenutih prema gore za gornju stranu i trokutima okrenutih prema dolje za donju stranu aeroprofila. Rezultati metode viskozno-neviskozne interakcije su pokazani punom crvenom linijom, dok su RANS rezultati pokazani crtkanom linijom. Područje tranzicije na gornjoj i donjoj strani aeroprofila, izračunato pomoću metode graničnog sloja, pokazuje dobro slaganje s eksperimentalnim podacima. Lagani skok tlaka u području tranzicije na gornjoj strani aeroprofila slijedi istu pojavu u eksperimentalnim podacima. Ta pojava se ne može vidjeti u RANS rezultatima iz razloga što u RANS rješavaču je cijelo područje strujanja računato kao turbulentno. Raspodjela koeficijenta tlaka sveukupno ima dobro slaganje s eksperimentom, osim na prednjem dijelu aeroprofila gdje koeficijent tlaka ima podbačaj a to rezultira u manjem koeficijentu normalne sile i koeficijentu uzgona. Ukupna raspodjela izračunatog koeficijenta tlaka pokazuje lagani pomak koji odgovara eksperimentalnim podacima za malo smanjen napadni kut. To bi mogao biti razlog laganog neslaganja, jer eksperimentalni podaci nisu korigirani za utjecaj zidova. Kriterij konvergencije rješenja je da maksimalni iznos reziduala tlaka, u svakoj točki aeroprofila, bude smanjen više od četiri reda veličine. Metoda sprežanja pomoću transpiracijske brzine pokazala je vrlo nestabilno ponašanje, posebno u pisustvu jakih udarnih valova. Iz tog razloga je korištena metoda podrelaksacije rješenja, kako bi se smanjila nestabilnost rješenja. Faktor podrelaksacije je podešavan ručno, i u većini slučajeva s nemonotonom konvergencijom je namješten na vrijednosti $0.1 \geq \beta \geq 0.001$. To je uglavnom uzrokovano fizikom strujanja, postojanjem mjehura separacije i velikim skokom tlaka na izlaznom bridu.

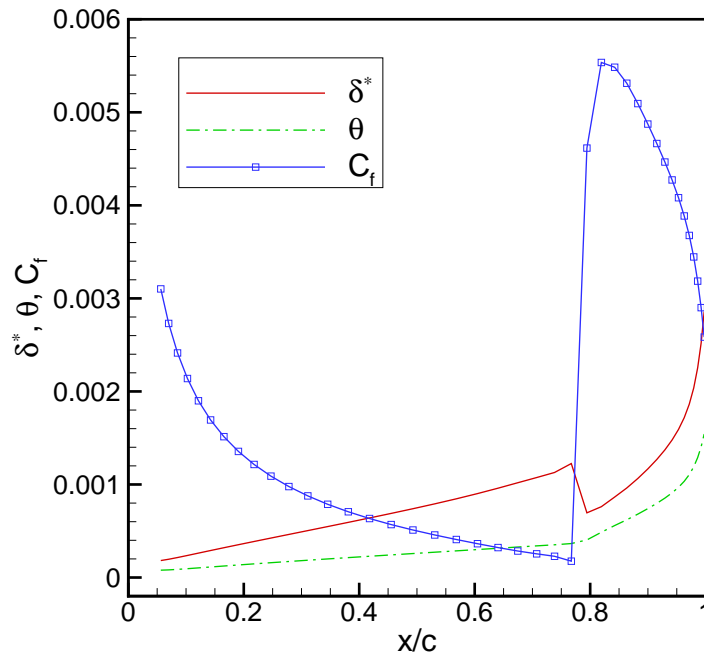
Na slikama 4.28 i 4.29 prikazana su rješenja jednadžbi graničnog sloja za gornju i donju stranu aeroprofila, integralne veličine debljina istisnuća δ^* , debljina količine gibanja θ i koeficijent trenja C_f . Debljina istisnuća i debljina količine gibanja rastu prema



Slika 4.27: Raspodjela koeficijenta tlaka za aeroprofil NACA0012 pri $Ma = 0.504$, $Re = 2.93 \cdot 10^6$, $\alpha = 4.06^\circ$



Slika 4.28: Integralne vrijednosti graničnog sloja za gornju stranu NACA0012 aeroprofila pri $Ma = 0.504$, $Re = 2.93 \cdot 10^6$, $\alpha = 4.06^\circ$

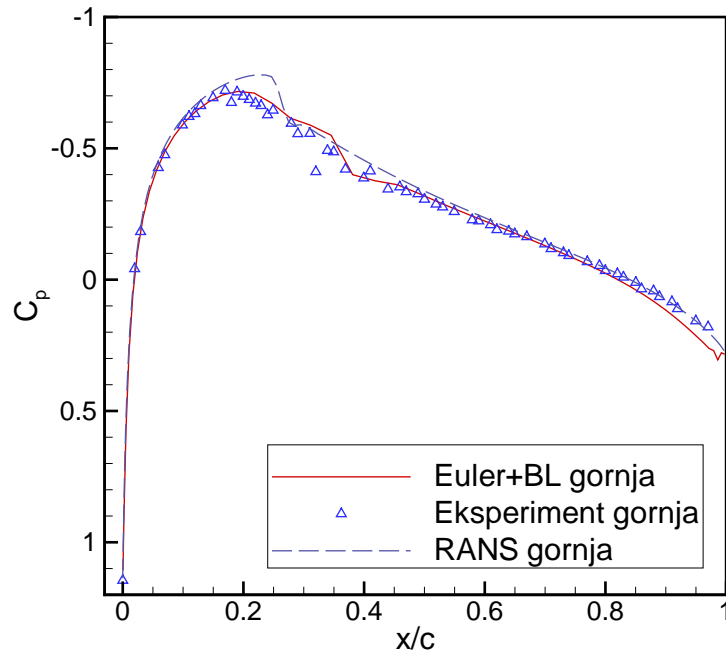


Slika 4.29: Integralne vrijednosti graničnog sloja za donju stranu NACA0012 aeroprofila pri $Ma = 0.504$, $Re = 2.93 \cdot 10^6$, $\alpha = 4.06^\circ$

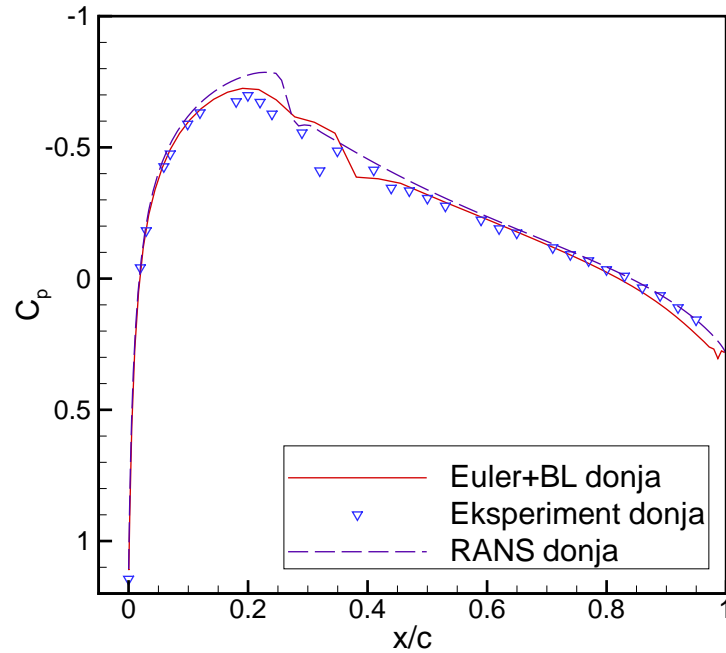
izlaznom bridu što predstavlja zadebljanje graničnog sloja i gubitak količine gibanja. Obje krivulje pokazuju nagli skok na poziciji tranzicije udarnog vala. Ti skokovi odgovaraju skoku u raspodjeli koeficijenta tlaka na slici 4.27. Rast debljine istisnuća i debljine količine gibanja je viši u području turbulentnog graničnog sloja. Koeficijent trenja pokazuje isti skok u području tranzicije s vrlo malom vrijednosti prije tranzicije, što odgovara vrlo strmom profilu brzine u graničnom sloju (blizu separacije).

Probni slučaj 2: NACA0012, $Ma = 0.756$, $Re = 4.01 \cdot 10^6$, $\alpha = -0.01^\circ$

Na slikama 4.30 i 4.31 prikazani su izračunati i eksperimentalni podaci za stacionarno strujanje oko aeroprofila NACA0012 za gornjaku i donjaku. Prikazani rezultati su dani za Machov broj $Ma = 0.756$, Reynoldsov broj $Re = 4.01 \cdot 10^6$ i napadni kut $\alpha = -0.01^\circ$. Praktično, taj slučaj se može promatrati kao simetričan. Rezultati pokazuju dobro slaganje s podacima iz eksperimenta. Mogu se primjetiti dva mala skoka koeficijenta tlaka na gornjaci i na donjaci. Prvi je zbog slabog udarnog vala, a drugi je zbog postojanja područja tranzicije graničnog sloja. Mala odstupanja RANS rezultata od eksperimentalnih podataka mogu se primjetiti na poziciji slabog udarnog vala, dok metoda viskozno-neviskozne interakcije daje dobre rezultate na toj poziciji. Metoda

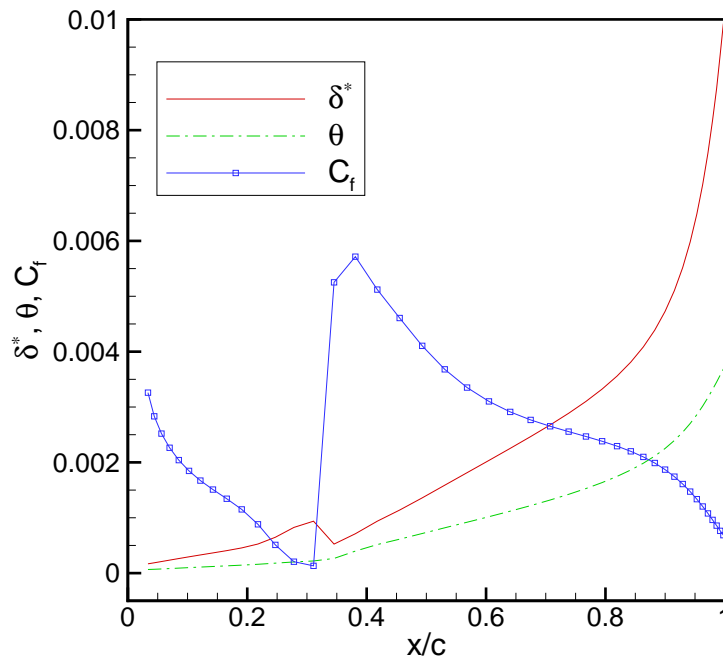


Slika 4.30: Raspodjela koeficijenta tlaka na gornjoj strani NACA0012 aeroprofila za stacionarno strujanje pri $Ma = 0.756$, $Re = 4.01 \cdot 10^6$, $\alpha = -0.01^\circ$



Slika 4.31: Raspodjela koeficijenta tlaka na donjoj strani NACA0012 aeroprofila za stacionarno strujanje pri $Ma = 0.756$, $Re = 4.01 \cdot 10^6$, $\alpha = -0.01^\circ$

viskozno-neviskozne interakcije pokazuje malo odstupanje na izlaznom bridu aeroprofila. Pokazano je da metoda tranzicije (e^n metoda) točno procjenjuje položaj tranzicije graničnog sloja. Na slikama 4.30 and 4.31 prikazani su i RANS rezultati za usporedbu, kao metoda višeg reda točnosti. RANS rezultati pokazuju jači udarni val na mjestima slabog udarnog vala u odnosu na eksperimentalne podatke. Čini se i iz ostalih rezultata da RANS rezultati, izračunati s turbulentnim strujanjem za cijelo područje, daju previše jak udarni val u odnosu na eksperimentalne podatke. Razlog za to bi mogao biti u strmijem rastu debljine istisnuća u turbulentnom graničnom sloju nego što je to u laminarnom graničnom sloju. To dovodi do kompresije u vanjskom neviskoznom strujanju što uzrokuje raniju pojavu udarnog vala.

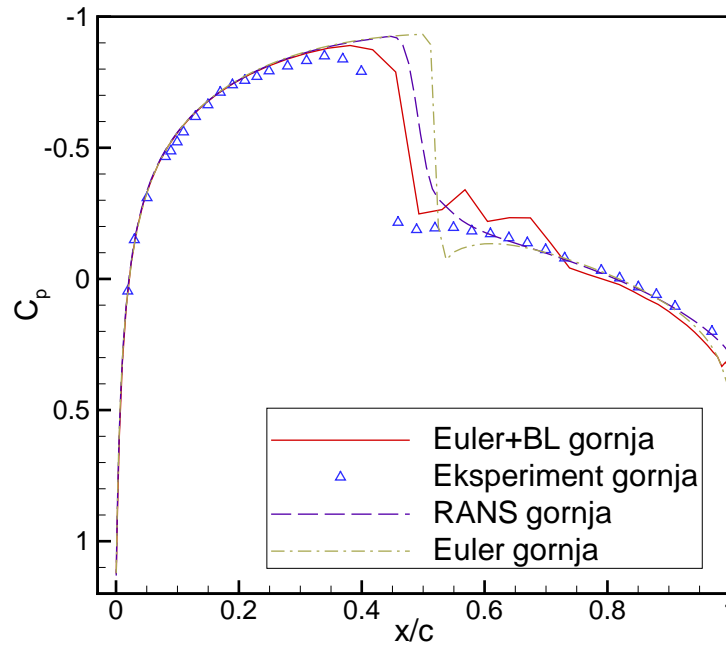


Slika 4.32: Integralne vrijednosti graničnog sloja za donju stranu NACA0012 aeroprofila pri $Ma = 0.756$, $Re = 4.01 \cdot 10^6$, $\alpha = -0.01^\circ$

Na slici 4.32 prikazana su rješenja debljine istisnuća δ^* , debljine količine gibanja θ i koeficijenta trenja C_f graničnog sloja, za slučaj NACA0012 aeroprofila pri $Ma = 0.756$, $Re = 4.01 \cdot 10^6$ i $\alpha = -0.01^\circ$. Te varijable pokazuju skok u području tranzicije na donjoj strani aeroprofila, na 30% duljine tetive od prednjeg brida. Isto vrijedi za gornju stranu aeroprofila koja nije pokazana zbog praktički nultog napadnog kuta i simetričnosti aeroprofila. Koeficijent trenja ponovo pokazuje isto ponašanje smanjujući se prema nuli

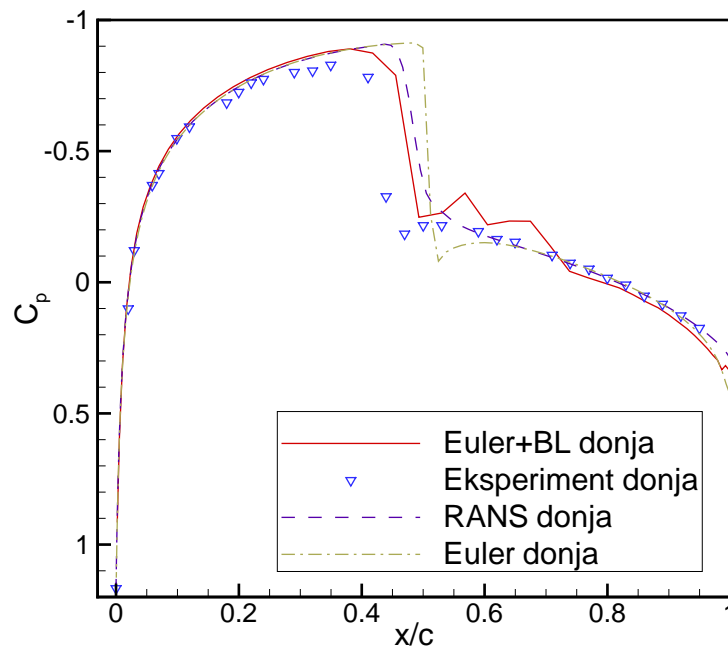
(prije separacije) u laminarnom dijelu strujanja, a potom doživljava pozitivni skok u turbulentnom strujanju. Debljina istisnuća pokazuje nagli pad u području tranzicije, a nakon tog područja naglo raste u turbulentnom strujanju. Debljina količine gibanja pokazuje stalan rast s višom brzinom rasta u turbulentnom strujanju.

Probni slučaj 3: NACA0012, $Ma = 0.803$, $Re = 4.09 \cdot 10^6$, $\alpha = 0.05^\circ$

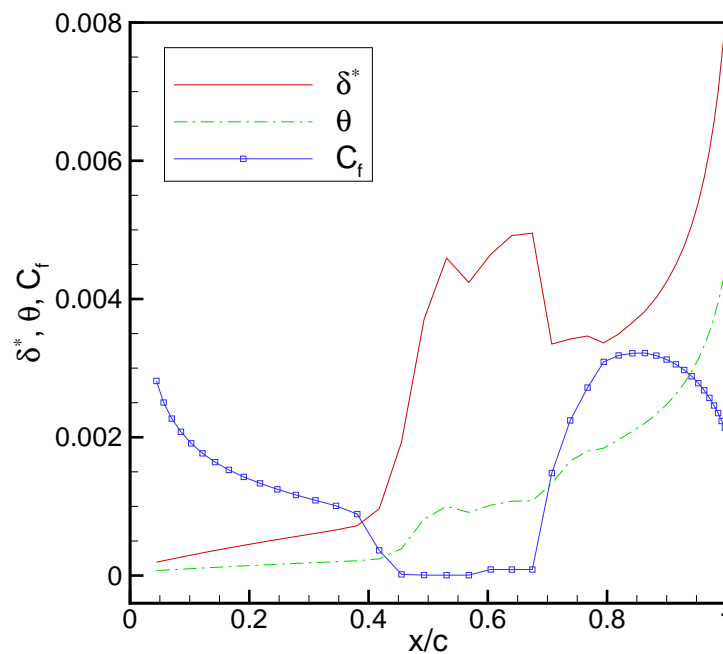


Slika 4.33: Raspodjela koeficijenta tlaka na gornjoj strani NACA0012 aeroprofila za stacionarno strujanje pri $Ma = 0.803$, $Re = 4.09 \cdot 10^6$ and $\alpha = 0.05^\circ$

Na slikama 4.33 i 4.34 prikazani su stacionarni rezultati za aeroprofil NACA0012 na gornjaci i donjaci. Rezultati su prikazani za Machov broj $Ma = 0.803$, Reynoldsov broj $Re = 4.09 \cdot 10^6$ i napadni kut $\alpha = 0.05^\circ$. Ovaj slučaj prikazuje strujanje s jakim udarnim valom i praktično se može promatrati kao simetrično optjecanje. Rezultati pokazuju postojanje jakog udarnog vala na udaljenosti 45% duljine tetive od prednjeg brida, što se dobro slaže s eksperimentalnim podacima. Efekti viskoznosti pomiču poziciju udarnog vala prema prednjem bridu aeroprofila, dok rezultati čisto neviskoznog strujanja daju položaj jakog udarnog vala prema zadnjem bridu aeroprofila u odnosu na viskozno strujanje. Taj slučaj, prikazan na slikama 4.33 i 4.34, i slični slučajevi s jakim udarnim valom pokazuju problem s nestabilnošću za metodu viskozno-neviskozne interakcije. Teškoća se pojavljuje kao spora brzina konvergencije i nemonotona konvergencija. Da



Slika 4.34: Raspodjela koeficijenta tlaka na donjoj strani NACA0012 aeroprofila za stacionarno strujanje pri $Ma = 0.803$, $Re = 4.09 \cdot 10^6$ and $\alpha = 0.05^\circ$



Slika 4.35: Integralne vrijednosti graničnog sloja za donju stranu NACA0012 aeroprofila pri $Ma = 0.803$, $Re = 4.09 \cdot 10^6$, $\alpha = 0.05^\circ$

bi se stabilizirala konvergencija, u probnom slučaju 3 je korišten faktor podrelaksacije $\beta = 0.001$. Broj iteracija potreban da se postigne konvergirano stacionarno rješenje je iznosio 6502. Uvjet konvergencije je postavljen na iznos tlaka na površini aeroprofila, i zadovoljen je kada je relativna promjena tlaka manja od $1 \cdot 10^{-3}$. U raspodjeli koeficijenti tlaka problem stabilnosti se može primjetiti iza udarnog vala, kao raspodjela u obliku zuba pile. Mogući razlog za tu nestabilnost je sprezanje graničnog sloja pomoću transpiracijske brzine i direktnog rješavanja jednadžbi graničnog sloja. Također, ovaj slučaj je blizu pojave balona separacije gdje rješenje jednadžbi postaje singularno.

4.3.2. NACA64A010 aeroprofil

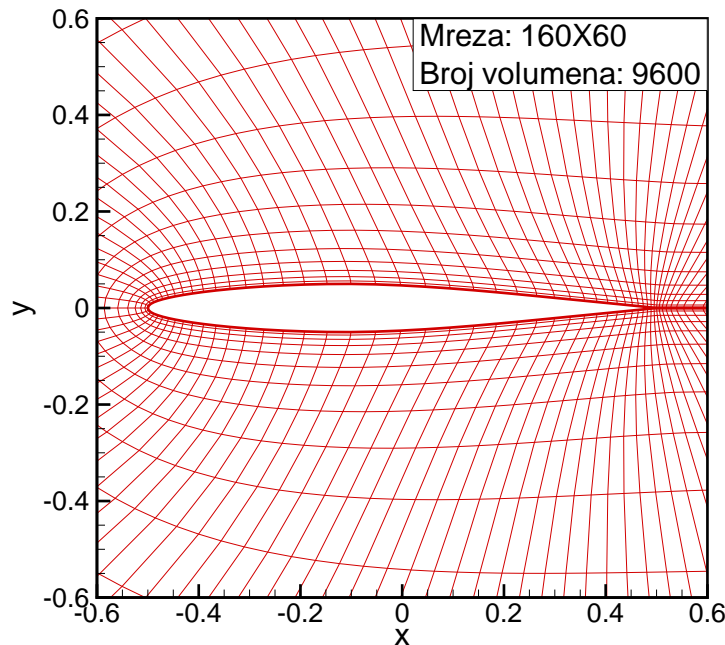
U ovome potpoglavlju biti će pokazani stacionarni rezultati za aeroprofil NACA64A010, za tri probna slučaja. NACA64A010 je simetričan aeroprofil s maksimalnom debljinom 10% na poziciji oko 40% duljine tetive aeroprofila od napadnog brida, s radijusom napadnog brida 0.68 % od duljine tetive i kutem izlaznog brida 12.6° . Oblik aeroprofila i korištena računalna mreža su pokazani na slici 4.36. Ta strukturirana mreža je korištena za proračune svih stacionarnih slučajeva NACA64A010 aeroprofila. Mreža se sastoji od 9600 kontrolnih volumena, i to 160 volumena u smjeru ξ koordinate i 60 volumena u smjeru η koordinate.

U tablici 4.4 su prikazani probni slučajevi za aeroprofil NACA64A010, izabrani iz baze eksperimentalnih podataka u AGARD izvještaju [27]. Izabrana su tri probna slučaja pri različitim Machovim brojevima, koji obuhvaćaju podzvučno stlačivo strujanje s i bez pojave udarnih valova.

Tablica 4.4: Stacionarni probni slučajevi za aeroprofil NACA64A010

Probni slučaj	Ma	Re	α
4	0.49	$2.52 \cdot 10^6$	-0.01°
5	0.502	$1.00 \cdot 10^7$	-0.22°
6	0.796	$12.56 \cdot 10^6$	-0.21°

Na slikama 4.37, 4.38 i 4.41 prikazani su stacionarni slučajevi pri tri različita Machova broja, $Ma = 0.49$, $Ma = 0.502$ i $Ma = 0.796$. Za prva dva slučaja je prikazana raspodjela koeficijenta tlaka samo za jednu stranu aeroprofila zbog simetričnosti, napadnog kuta bliskom nuli i neizraženog udarnog vala, osim za probni slučaj 6. Svi slučajevi su



Slika 4.36: Računalna mreža za aeroprofil NACA64A010; granica na vanjskom rubu domene je udaljena 40 duljina tetiva aeroprofila od aeroprofila.

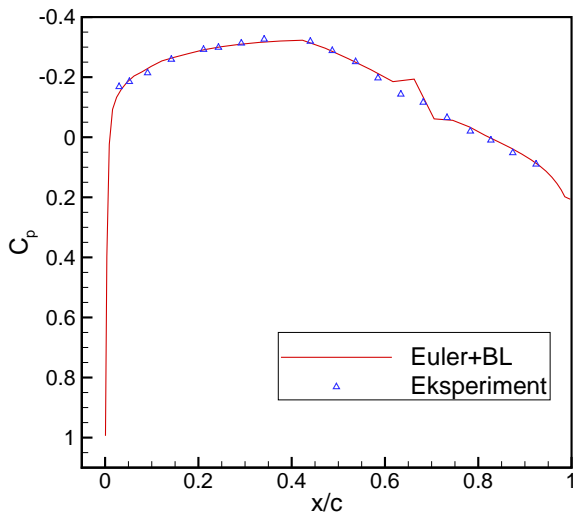
uspoređeni s eksperimentalnim podacima dobivenim u AGARD izvještaju broj 702 [27].

Probni slučaj 4: NACA64A010, $Ma = 0.49$, $Re = 2.52 \cdot 10^6$, $\alpha = -0.01^\circ$

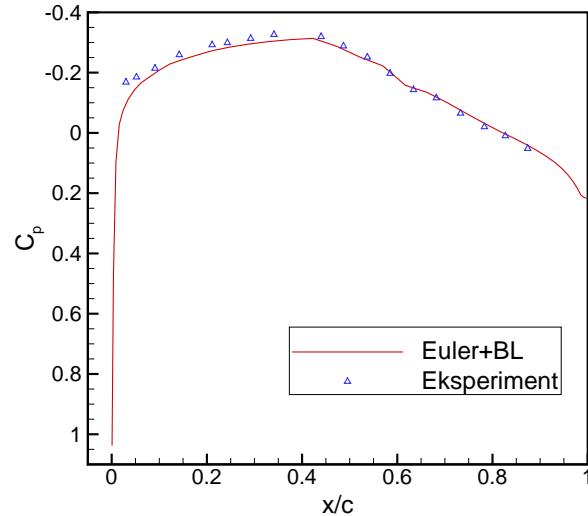
Na slici 4.37 prikazana je raspodjela koeficijenta tlaka za stacionarno strujanje na gornjoj strani aeroprofila za probni slučaj 4 pri $Ma = 0.49$, $Re = 2.52 \cdot 10^6$ i $\alpha = -0.01^\circ$. Numerički rezultat pokazuje odlično slaganje s eksperimentalnim podacima, osim u području tranzicije gdje rezultat pokazuje pretjerani pad koeficijenta tlaka u usporedbi s eksperimentalnim podacima. Ta pojava dolazi od rješenja jednadžbi graničnog sloja i metode za predviđanje tranzicije. Sa slike 4.39, koja pokazuje integralne vrijednosti graničnog sloja za isti probni slučaj, može se vidjeti da debljina istisnuća graničnog sloja u laminarnom strujanju ima veliku izračunatu vrijednost zbog malog Reynoldsovog broja a zatim ima jaki negativni skok ulaskom u turbulentno strujanje. Taj skok je također razlog za pretjerani skok koeficijenta tlaka u području tranzicije na slici 4.37.

Probni slučaj 5: NACA64A010, $Ma = 0.502$, $Re = 1.0 \cdot 10^7$, $\alpha = -0.22^\circ$

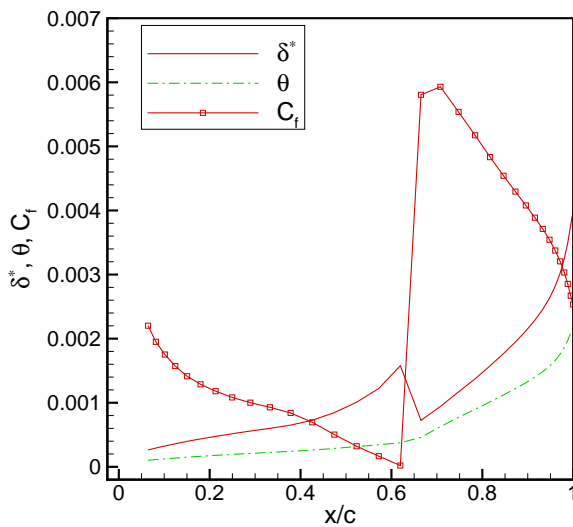
Na slici 4.38 pokazana je raspodjela koeficijenta tlaka za stacionarno strujanje na gornjoj strani aeroprofila za probni slučaj 5 pri $Ma = 0.502$, $Re = 1.0 \cdot 10^7$ i $\alpha =$



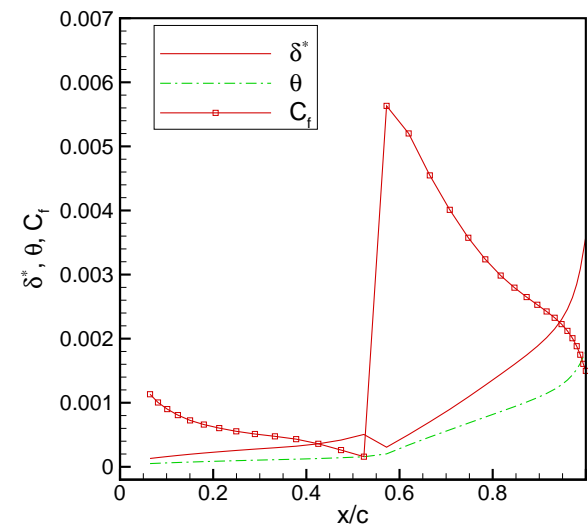
Slika 4.37: NACA64A010 steady pressure coefficient distribution for upper side at $Ma = 0.49$, $Re = 2.52 \cdot 10^6$, $\alpha = -0.01^\circ$



Slika 4.38: NACA64A010 steady pressure coefficient distribution for upper side at $Ma = 0.502$, $Re = 1.0 \cdot 10^7$, $\alpha = -0.22^\circ$



Slika 4.39: NACA64A010 boundary layer integral values for upper side at $Ma = 0.49$, $Re = 2.52 \cdot 10^6$, $\alpha = -0.01^\circ$



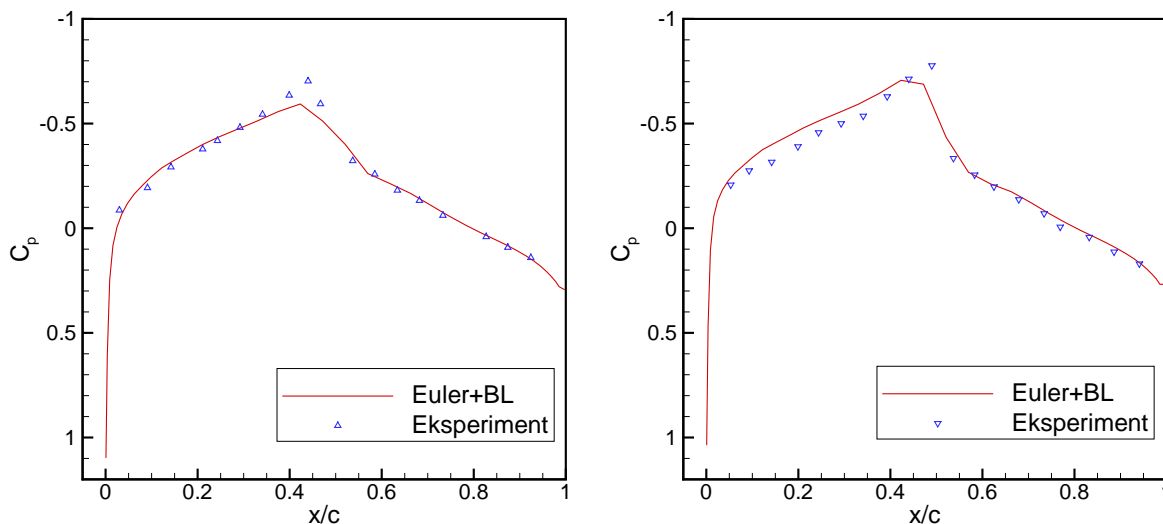
Slika 4.40: NACA64A010 boundary layer integral values for upper side at $Ma = 0.502$, $Re = 1.0 \cdot 10^7$, $\alpha = -0.22^\circ$

-0.22° . Izračunati rezultat pokazuje dobro slaganje, ali u ovome slučaju pokazuje i dobro predviđanje područja tranzicije. Raspodjela koeficijenta tlaka na prednjem dijelu aeroprofila prije točke minimalnog tlaka na slici 4.38, pokazuje malo podbacivanje u odnosu na eksperimentalne podatke. To se ne pojavljuje na stražnjem dijelu aeroprofila

iza točke minimalnog tlaka. Izračunati rezultati graničnog sloja za slučaj 5 su prikazani na slici 4.40 i pokazuju slično ponašanje kao i u probnom slučaju 4, no zbog većeg Reynoldsovog broja debljina istisnuća graničnog sloja ne postiže velike vrijednosti i stoga nema jači skok u području tranzicije. Slabiji skok debljine istisnuća ima utjecaj na odgovarajuće predviđanje skoka koeficijenta tlaka u području tranzicije na slici 4.38.

Probni slučaj 6: NACA64A010, $Ma = 0.796$, $Re = 12.56 \cdot 10^6$, $\alpha = -0.21^\circ$

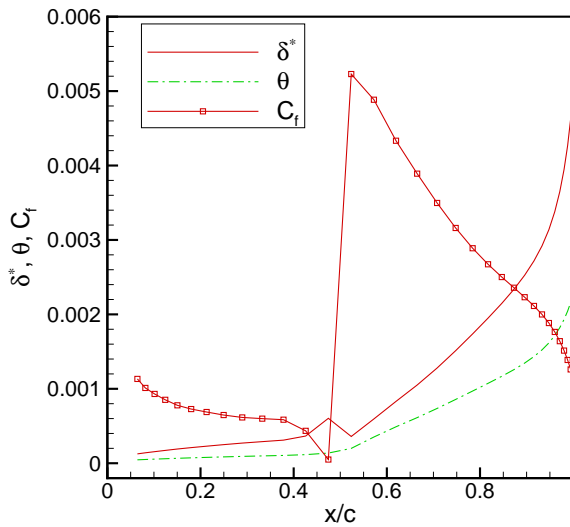
Na slici 4.41 pokazani su izračunati rezultati i eksperimentalni podaci za $Ma = 0.796$, $Re = 12.56 \cdot 10^6$ i $\alpha = -0.21^\circ$. Pri tom Machovom broju, polje strujanja sadrži nadzvučno područje s slabim udarnim valom. Izračunati rezultat za gornju stranu aeroprofila pokazuje dobro slaganje osim na poziciji udarnog vala gdje je vrh koeficijenta tlaka podbačen. Na poziciji udarnog vala za gornju i za donju stranu aeroprofila, izračunati rezultati pokazuju izgladivanje u odnosu na eksperimentalne podatke. To može ukazivati na prejak utjecaj graničnog sloja na intenzitet udarnog vala. Zbog prisustva zadebljanja graničnog sloja u dnu udarnog vala, pojavljuje se kompresijski udarni val lambda oblika. Kao posljedica toga, intenzitet udarnog vala je izgladen i to se može vidjeti u raspodjeli koeficijenta tlaka na aeroprofilu [29, 30]. Na prednjem dijelu donje strane aeroprofila izračunato rješenje pokazuje značajno odstupanje od eksperimentalnih podataka.



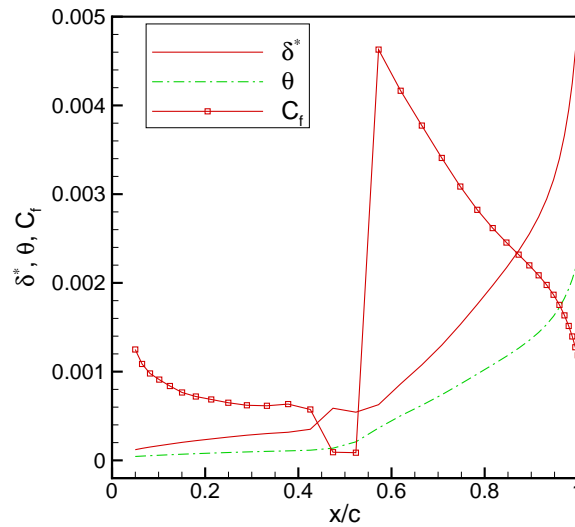
Slika 4.41: Raspodjela koeficijenta tlaka za aeroprofil NACA64A010 za gornju (lijevo) i donju (desno) stranu aeroprofila pri $Ma = 0.796$, $Re = 12.56 \cdot 10^6$, $\alpha = -0.21^\circ$

Na slikama 4.42 i 4.43 prikazani su rezultati za debljinu istisnuća, debljinu količine gibanja i koeficijent trenja gornje i donje strane aeroprofila za probni slučaj 6. Rezultati

debljine stisnuća i debljine količine gibanja pokazuju rast s malim skokom u području tranzicije. Koeficijent trenja smanjuje se do malih pozitivnih vrijednosti u području tranzicije, a zatim doživljava pozitivni skok. Nakon toga monotono se smanjuje vrijednost koeficijenta trenja do izlaznog brida aeroprofila.



Slika 4.42: Integralne vrijednosti graničnog sloja za aeroprofil NACA64A010 na gornjoj strani aeroprofila pri $Ma = 0.796$, $Re = 12.56 \cdot 10^6$, $\alpha = -0.21^\circ$



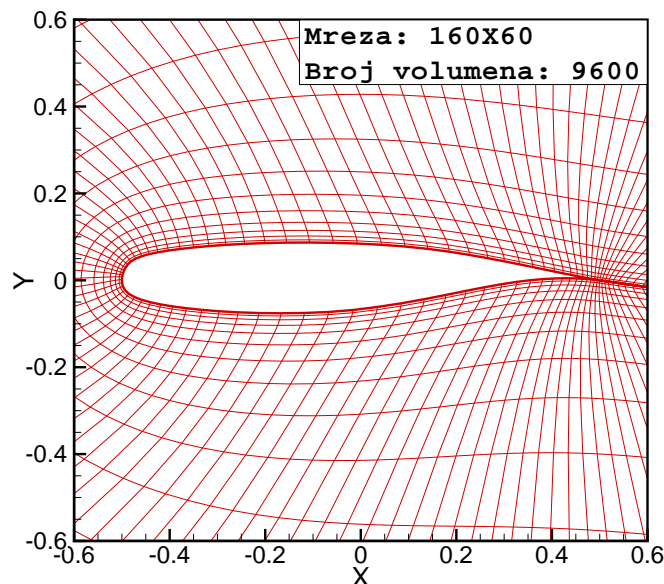
Slika 4.43: Integralne vrijednosti graničnog sloja za aeroprofil NACA64A010 na donjoj strani aeroprofila pri $Ma = 0.796$, $Re = 12.56 \cdot 10^6$, $\alpha = -0.21^\circ$

4.3.3. NLR7301 aeroprofil

Aeroprofil NLR7301 je najdeblji superkritični aeroprofil s debljinom 16.5% (u odnosu na duljinu tetive aeroprofila). Položaj maksimalne debljine je na udaljenosti oko 35% duljine tetive aeroprofila mjereno od napadnog brida, zakrivljenost iznosi 1.66% duljine tetive, radijus napadnog brida iznosi 4.72% duljine tetive, a kut izlaznog brida je jednak 5.175° . Zbog prilično velikog radijusa napadnog brida, ovaj aeroprofil predstavlja vjerojatno vrlo problematičan slučaj za metode interakcije viskoznog i neviskoznog strujanja. U odnosu na konvencionalne aeroprofile, superkritični aeroprofil NLR7301 ima smanjenu zakrivljenost, povećan radijus napadnog brida, malu zakrivljenost konture na podtllačnoj strani aeroprofila i konkavnost konture na zadnjem dijelu pretlačne strane aeroprofila. Pri konstrukcijskim uvjetima strujanja taj i slični superkritični aeroprofil uobičajeno razvijaju veće nadzvučno područje ubuhvaćeno slabim udarnim valom ili, u idealnom

slučaju, rekompresiju bez udarnog vala koja vodi manjem koeficijentu tlaka i većem opterećenju na stražnjem dijelu aeroprofila [31]. U praksi, rekompresija bez udarnog vala je vrlo osjetljiv i nestabilan fenomen koji zbog utjecaja debljine istisnuća graničnog sloja ili malih neravnina površine aeroprofila brzo prelazi u stabilnije stanje karakterizirano udarnim valom. Iz tog razloga su strujanja oko superkritičnih aeroprofila vrlo osjetljiva tako da je i najmanje odstupanje od konstrukcijskih uvjeta strujanja karakterizirano pojavom jakih udarnih valova. Kad se jedanput ode izvan konstrukcijskih uvjeta strujanja, daljnje povećanje Machovog broja ili napadnog kuta vodi povećanju intenziteta udarnog vala i daljnje povećanje debljine graničnog sloja. To može rezultirati separacijom graničnog sloja uzrokovanom udarnim valom koja se događa iza udarnog vala i na kraju potpunom separacijom od položaja udarnog vala do izlaznog brida aeroprofila.

Oblik i računalna mreža aeroprofila NLR7301 su pokazani na slici 4.44. Računalna mreža tipa C sastoji se od 9600 kontrolnih volumena i generirana je pomoću eliptičkog generatora mreže. Vanjski rub računalne domene je udaljen 40 duljina tetiva od aeroprofila. Mreža ima 160 kontrolnih volumena u smjeru ξ koordinate i 60 kontrolnih volumena u smjeru η koordinate. Probni slučajevi i pripadajući parametri strujanja su dani u tablici 4.5.



Slika 4.44: Računalna mreža za aeroprofil NLR7301; vanjski rub mreže je udaljen 40 duljina tetiva od aeroprofila

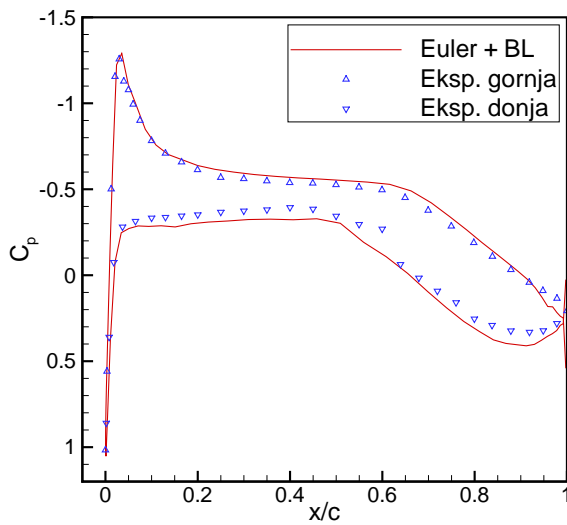
Slike 4.45 i 4.46 prikazuju eksperimentalne podatke i izračunate rezultate za aeropro-

Tablica 4.5: Probni slučajevi za aeroprofil NLR7301, za stacionarno strujanje

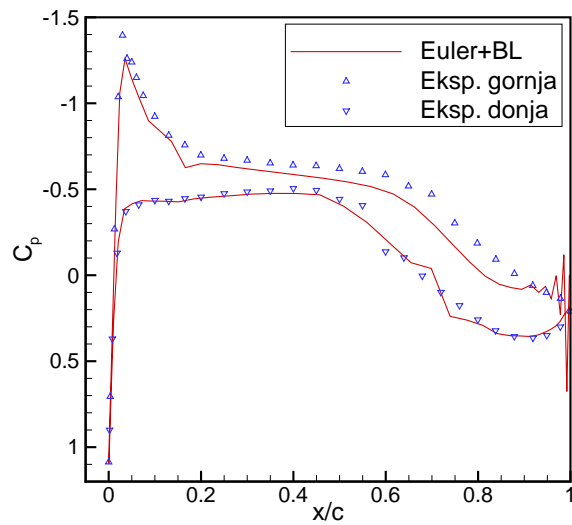
Probni slučaj	Ma	Re	α
7	0.299	$1.1 \cdot 10^6$	0.3966°
8	0.599	$1.9 \cdot 10^6$	0.3832°

fil NLR7301, za probne slučajeve 7 i 8. Izračunati rezultat za razvijenu metodu pokazuje umjereno slaganje s eksperimentalnim podacima u cijelom području duljine tetive osim na gornjoj strani aeroprofila u blizini izlaznog brida i mjestu područja tranzicije, gdje su prisutna veća odstupanja. To se može objasniti oblikom prednjeg brida koji krši pretpostavke strujanja u jednadžbama graničnog sloja, a također i većom razlikom tlaka između gornje i donje strane aeroprofila na izlaznom bridu. Ova vrsta aeroprofila je vrlo osjetljiva na bilo kakav poremećaj s konture aeroprofila, što znači i od graničnog sloja. Sveukupno, predstavljena metoda interakcije viskoznog i neviskoznog strujanja daje rezultate s umjerenim slaganjem na ovoj vrsti aeroprofila, a također pokazuje vrlo nemonotonu i dugotrajnu konvergenciju. Podrelaksacijski faktor koji se koristio u proračunima probnih slučajeva 7 i 8 je jednak $\beta = 0.001$. Broj iteracija potreban za postizanje konvergiranog stacionarnog rješenja za slučaj 7 iznosio je 60, dok je za slučaj 8 iznosio 2479. Proračun interakcije stacionarnog i nestacionarnog strujanja započet je nakon postizanja stacionarnog rješenja za neviskozno strujanje, s konstantnim koeficijentom normalne sile. Kriterij konvergencije je bio zadovoljen kad je rezidual tlaka u svakoj točki aeroprofil bio smanjen ispod vrijednosti $1 \cdot 10^3$. Na izlaznom bridu razvijena metoda pokazuje oscilacije tlaka na gornjoj strani aeroprofila gdje je turbulentni granični sloj ekstremno debeli. To se može objasniti separacijom tipa B opisanoj u [32]. Razlog takvoj separaciji leži u strmom gradijentu tlaka prema izlaznom bridu, i taj tip separacije započinje s izlaznog brida (stražnja separacija). Stražnja separacija ovisi snažno o debljini i profilu brzine graničnog sloja s približavanjem izlaznom bridu, a također i o gradijentu tlaka. Iz tog razloga je separacija tipa B vrlo osjetljiva na položaj tranzicije. Također, razlog za oscilacije tlaka na izlaznom bridu bi mogao biti u kršenju pretpostavke o gradijentu tlaka u smjeru normale na konturu ($\partial p / \partial \eta = 0$) oko izlaznog brida, tj. gradijent tlaka u okomitom smjeru na dominantni smjer strujanja u graničnom sloju, u blizini izlaznog brida, može biti značajan.

U tablici 4.6 skupljeni su rezultati za svih osam probnih slučajeva. Prikazani su



Slika 4.45: Raspodjela koeficijenta tlaka za stacionarno strujanje oko aeroprofila NLR7301 pri $Ma = 0.299$, $Re = 1.1 \cdot 10^6$, $\alpha = 0.3966^\circ$



Slika 4.46: Raspodjela koeficijenta tlaka za stacionarno strujanje oko aeroprofila NLR7301 pri $Ma = 0.599$, $Re = 1.9 \cdot 10^6$, $\alpha = 0.3832^\circ$

rezultati za faktor podrelaksacije β , broj iteracija i procesorsko (CPU) vrijeme za svaki probni slučaj. Može se primjetiti da broj iteracija kao i procesorsko vrijeme raste s povećanjem Machovog broja. Veće vrijeme je potrebno za slučajeve s pojavom udarnog vala. Također, može se primjetiti da je podrelaksacijski faktor vrlo nizak za sve slučajeve, najvjerojatnije iz razloga vrlo nestabilnog mehanizma sprežanja pomoću transpiracijske brzine. Još manji podrelaksacijski faktor je potreban za slučajeve s pojavom udarnog vala (slučaj 3). Probni slučajevi 7 i 8 (NLR7301) pokazuju također vrlo mali podrelaksacijski faktor iako su ti slučajevi bez pojave udarnog vala. To je vjerojatno zbog toga što taj aeroprofil ima veliku zakrivljenost u blizini napadnog brida što je nepovoljno obzirom na pretpostavke napravljene u jednadžbama graničnog sloja.

Tablica 4.6: Skupljeni probni slučajevi za stacionarno strujanje

Aeroprofil	Slučaj	Ma	Re	α	β	br. iter.	CPU vrijeme
NACA0012	1	0.504	$2.93 \cdot 10^6$	4.06°	0.01	683	38.2 s
	2	0.756	$4.01 \cdot 10^6$	-0.01°	0.01	840	46.4 s
	3	0.803	$4.09 \cdot 10^6$	0.05°	0.001	6502	321.3 s
NACA64A010	4	0.49	$2.52 \cdot 10^6$	-0.01°	0.01	71	3.8 s
	5	0.502	$1.00 \cdot 10^7$	-0.22°	0.01	54	2.7 s
	6	0.796	$12.56 \cdot 10^6$	-0.21°	0.01	336	19.5 s
NLR7301	7	0.299	$1.1 \cdot 10^6$	0.3966°	0.001	60	2.9 s
	8	0.599	$1.9 \cdot 10^6$	0.3832°	0.001	2479	122.5 s

4.4. Rezultati za nestacionarno strujanje

Kada aeroprofil izvodi oscilatorno gibanje po sinusoidi oko zadanog srednjeg položaja na slijedeći način:

$$\alpha = \alpha_m + \alpha_o \cos(\omega t), \quad (4.2)$$

koeficijent tlaka u nekoj točki na aeroprofilu, a stoga i sila uzgona i moment pokazuju također oscilatornu promjenu. Glavni parametar koji opisuje nestacionarno strujanje je reducirana frekvencija ω^* definirana kao:

$$\omega^* = \frac{\omega L}{U_\infty} \quad (4.3)$$

gdje je ω kutna frekvencija, L referentna duljina (obično tetiva aeroprofila) i U_∞ brzina slobodne struje. Ovaj parametar je mjera za nestacionarnost strujanja.

Kako bi se opisalo harmoničke oscilacije potrebne su dvije veličine, iznos i fazni pomak u odnosu na gibanje aeroprofila (vidjeti sliku 4.47). Ekvivalentan način opisa je pomoću kompleksnog broja. U posljednjem opisu realni dio poremećaja tlaka (ili neke druge varijable) je u fazi s gibanjem aeroprofila, dok je imaginarni dio pomaknut za 90° u odnosu na gibanje aeroprofila [32].

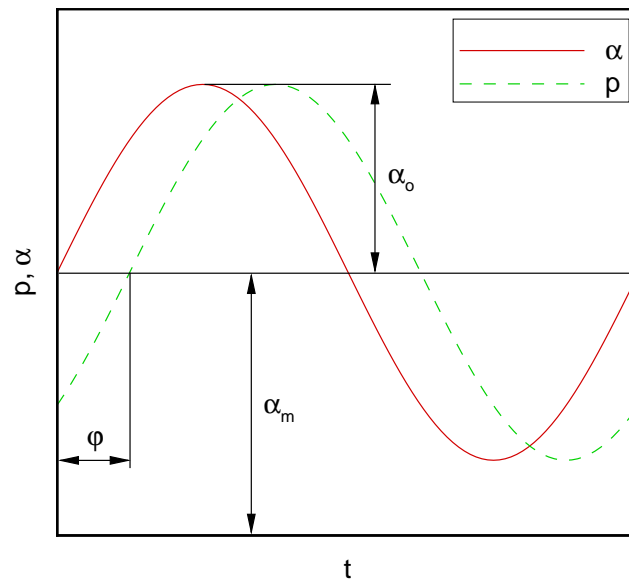
Opis u obliku *iznosa i faze* ima slijedeći zapis:

$$\begin{aligned} p &= p_m + p_o \cos(\omega t + \varphi) \\ &= p_m + (p_o \cos \varphi) \cos(\omega t) - (p_o \sin \varphi) \sin(\omega t) \end{aligned} \quad (4.4)$$

gdje je p_o iznos oscilatornog tlaka, a φ fazni pomak. Opis u obliku *kompleksnog broja* ima slijedeći zapis:

$$\begin{aligned} p &= p_m + p_o \operatorname{Re} [e^{i(\omega t + \varphi)}] \\ &= p_m + \operatorname{Re} [(p' + ip'') e^{i\omega t}] \end{aligned} \quad (4.5)$$

gdje je $p' = p_o \cos \varphi$ realni dio, a $p'' = p_o \sin \varphi$ je imaginarni dio oscilacija tlaka. Član pomnožen s $\cos(\omega t)$ u jednadžbi (4.4) se također naziva komponenta *u fazi* (eng. *in-phase*), a član pomnožen s $\sin(\omega t)$ u istoj jednadžbi se naziva komponenta *u kvadraturi* (eng. *in-quadrature*).



Slika 4.47: Primjer nestacionarnih oscilacija napadnog kuta aeroprofila i tlaka

Takav opis nestacionarnog tlaka ili opterećenja je valjan samo ako se aerodinamičke veličine mijenjaju po sinusoidi u vremenu, ili drugim riječima, sve dok postoji linearna ovisnost između pomaka aeroprofila i nestacionarnih opterećenja. Međutim, to nije uvijek istina, pogotovo ne u strujanjima sa separacijom ili u područjima u blizini oscilirajućih udarnih valova.

Kada se sustav može promatrati kao linearan (p se mijenja linearno s α), tlak p_s za srednji položaj za stacionarno strujanje je jednak kao p_m , srednji tlak tijekom oscilacija. Raspodjela stacionarnog tlaka karakterizira tip strujanja, koja utječe na oscilatorni tlak. Kada su prisutne nelinearnosti, potrebno je uključiti i više harmonike u opisu nestacionarnosti. U općem nelinearnom slučaju amplituda tlaka nije proporcionalna amplitudi gibanja, a srednji tlak p_m nije obavezno isti kao stacionarni tlak p_s [27]. Za strujanje bez separacije ozbiljne nelinearnosti tlaka obično se pojavljuju samo na položaju blizu napadnog brida, osi okretanja zakrilaca ili udarnog vala.

4.4.1. NACA0012 aeroprofil

U ovome poglavlju prikazani su nestacionarni rezultati računalnog koda viskozno-neviskozne interakcije za aeroprofil NACA0012 i uspoređeni s eksperimentalnim podacima [27] i RANS rezultatima. Aeroprofil izvodi harmonijsko gibanje rotacije oko točke na

čtvrtnini tetive od prednjeg brida. Rezultati su ispitani za podzvučno stlačivo strujanje uz pojavu jakih udarnih valova. Karakteristike slobodne struje i gibanja aeroprofila su dane u tablici 4.7.

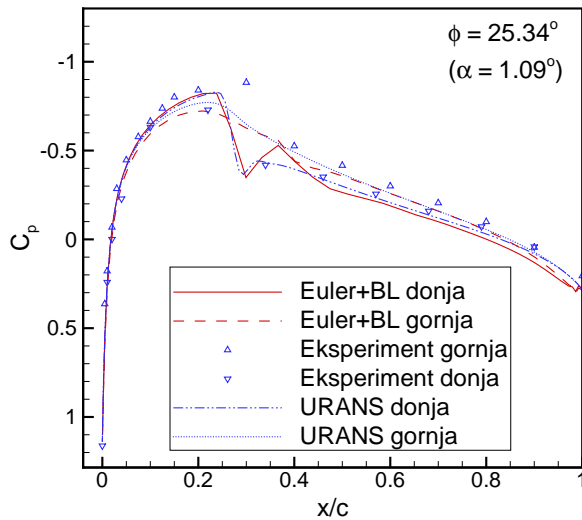
Tablica 4.7: Probni slučaj za nestacionarno strujanje oko NACA0012 aeroprofila

Mach number Ma	0.755
Reynolds number Re	$5.5 \cdot 10^6$
Mean angle of attack α_m	0.016°
Pitch amplitude α_o	2.51°
Reduced frequency ω^*	0.1628
Rotational axis position x_α/c	0.25

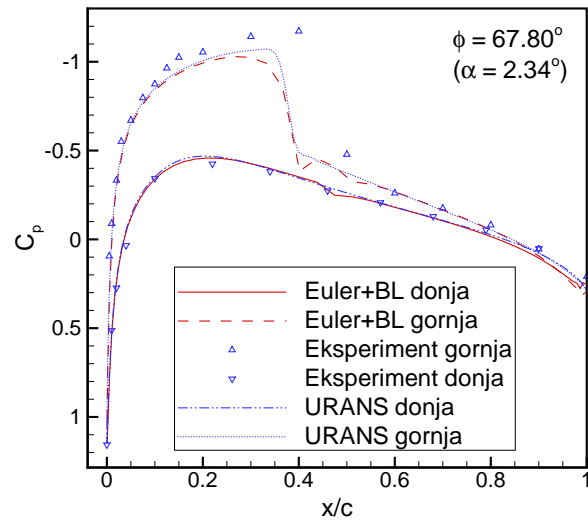
Na slikama od 4.48 do 4.55 prikazani su rezultati za nestacionarno strujanje, za probni slučaj dan u tablici 4.7. Računalna mreža imala je 160 kontrolnih volumena u smjeru ξ koordinate i 60 kontrolnih volumenau smjeru η koordinate (ukupno 9600 kontrolnih volumena). Izračunati rezultati metode interakcije viskoznog i neviskoznog strujanja su uspoređeni s eksperimentalnim podacima i nestacionarnim RANS rezultatima pri određenom faznom kutu ϕ u zadnjoj periodi simulacije. Simulirane su četiri periode da se postigne periodiča promjena uzgona. Rezultati nestacionarnog koeficijenta tlaka pokazuju sveukupno dobro slaganje s eksperimentalnim podacima. Veća odstupanja u odnosu na eksperimentalne podatke su prisutna pri manjim napadnim kutevima, dok su bolja slaganja pri većim napadnim kutevima. Pri pojedinim većim napadnim kutevima u dijelu periode gdje se napadni kut povećava i pojavljuje se udarni val, izračunati rezultati pokazuju položaj udarnog vala pomaknut prema naprijed u odnosu na eksperimentalne podatke. To pokazuje prejak utjecaj zadebljanja graničnog sloja na neviskozno strujanje. S druge strane, u dijelu periode gdje se napadni kut smanjuje i pojavljuje se jaki udarni val, izračunati rezultati pokazuju dobro predviđanje pozicije i intenziteta udarnog vala.

Također, na slikama od 4.48 do 4.55 prikazani su nestacionarni RANS rezultati iz Tau računalnog programa. U RANS simulacijama korišten je dvojednadžbeni model turbulencije $k-\omega$. Rezultati metode interakcije viskoznog i neviskoznog strujanja uglavnom se poklapaju s rezultatima nestacionarnog RANS-a, bolje nego s eksperimentalnim podacima. Rezultati interakcije viskoznog i neviskoznog strujanja na položaju udarnog

vala pokazuju slabije naglašen njegov vrh, nego što to pokazuju nestacionarni RANS rezultati i eksperimentalni podaci. Nestacionarni RANS rezultati također pokazuju položaj udarnog vala pomaknut prema prdnjem dijelu aeroprofila pri određenim faznim kutevima.

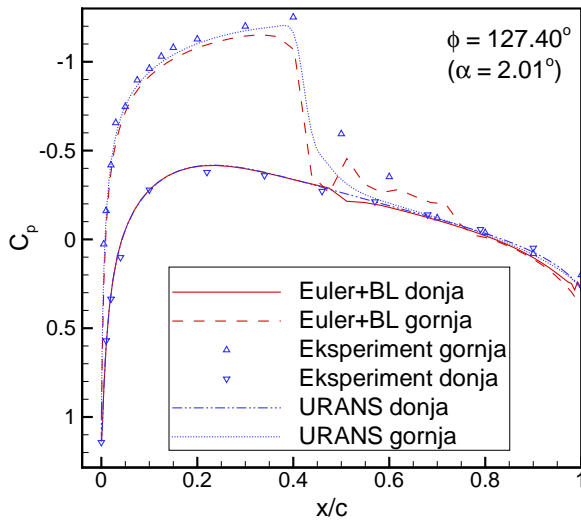


Slika 4.48: Raspodjela tlaka za nestacionarno strujanje za aeroprofil NACA0012 pri kutu unutar periode $\phi = 25.34^\circ$; $Ma = 0.755$, $Re = 5.5 \cdot 10^6$, $\alpha_m = 0.016^\circ$, $\alpha_o = 2.51^\circ$, $\omega^* = 0.1628$

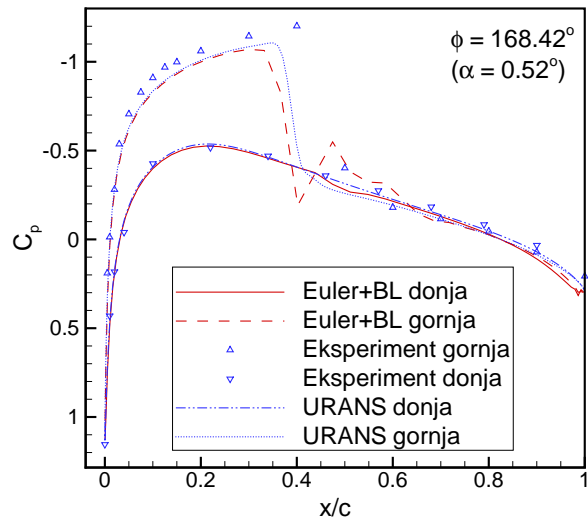


Slika 4.49: Raspodjela tlaka za nestacionarno strujanje za aeroprofil NACA0012 pri kutu unutar periode $\phi = 67.80^\circ$; $Ma = 0.755$, $Re = 5.5 \cdot 10^6$, $\alpha_m = 0.016^\circ$, $\alpha_o = 2.51^\circ$, $\omega^* = 0.1628$

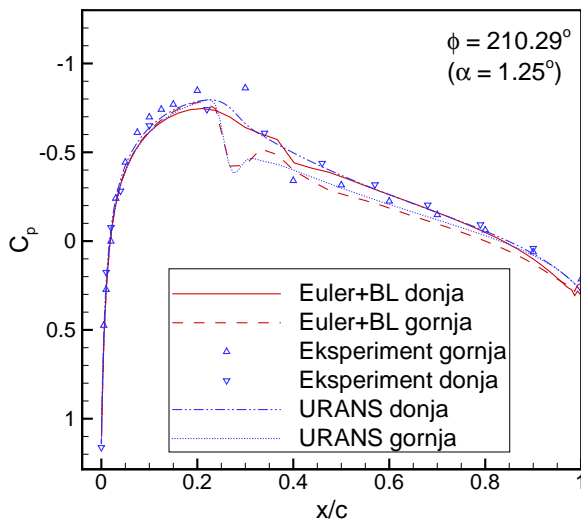
Na slikama 4.56 i 4.57 prikazani su rezultati koeficijenta normalne sile za nestacionarne oscilacije, za probni slučaj NACA0012 aeroprofila pri $Ma = 0.755$, $Re = 5.5 \cdot 10^6$, $\alpha_m = 0.016^\circ$, $\alpha_o = 2.51^\circ$, $\omega^* = 0.1628$. Koeficijent normalne sile linearno prati promjenu napadnog kuta. Na slici 4.56 prikazani su rezultati promjene koeficijenta normalne sile za razvijenu metodu interakcije viskoznog i neviskoznog strujanja, za rješavač nestacionarnog neviskoznog strujanja (Euler) i za rješavač nestacionarnog RANS strujanja. Na slici 4.56 također je prikazan trenutni napadni kut aeroprofila. Može se primjetiti mali fazni kut između koeficijenta normalne sile i napadnog kuta aeroprofila. Koeficijent normalne sile zaostaje iza napadnog kuta, što se može vidjeti u maksimumima, ali također i na krajevima i počecima perioda. Na slici 4.57 prikazan je koeficijent normalne sile kao funkcija trenutnog napadnog kuta. Prikazani su rezultati za metodu interakcije viskoznog i neviskoznog strujanja (Euler+BL) i metodu nestacionarnog RANS strujanja, kao i eksperimentalni podaci iz AGARD izvještaja [27]. Sveukupno, koeficijent normalne



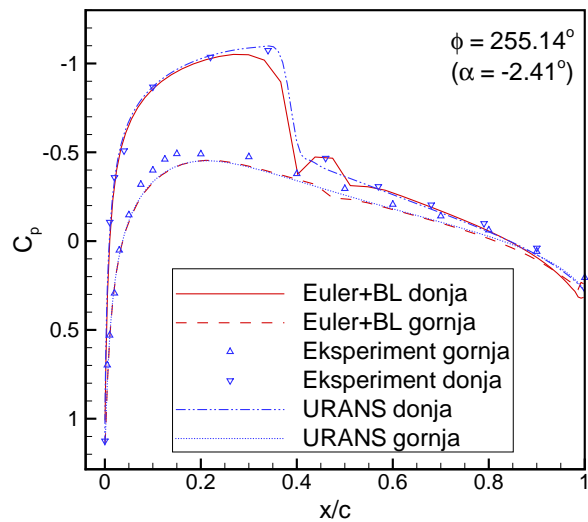
Slika 4.50: Raspodjela tlaka za nestacionarno strujanje za aeroprofil NACA0012 pri kutu unutar periode $\phi = 127.40^\circ$; $Ma = 0.755$, $Re = 5.5 \cdot 10^6$, $\alpha_m = 0.016^\circ$, $\alpha_o = 2.51^\circ$, $\omega^* = 0.1628$



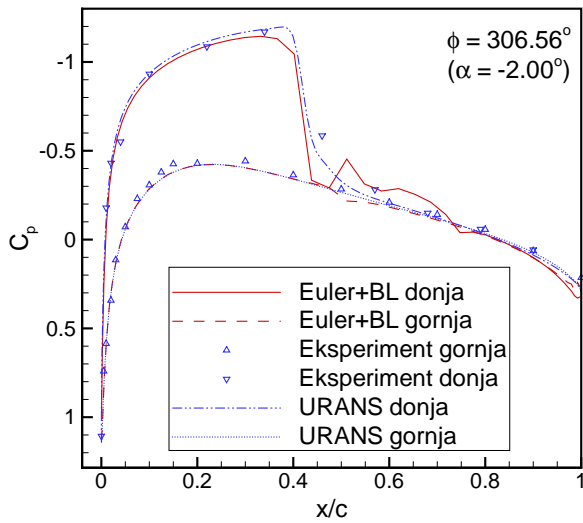
Slika 4.51: Raspodjela tlaka za nestacionarno strujanje za aeroprofil NACA0012 pri kutu unutar periode $\phi = 168.42^\circ$; $Ma = 0.755$, $Re = 5.5 \cdot 10^6$, $\alpha_m = 0.016^\circ$, $\alpha_o = 2.51^\circ$, $\omega^* = 0.1628$



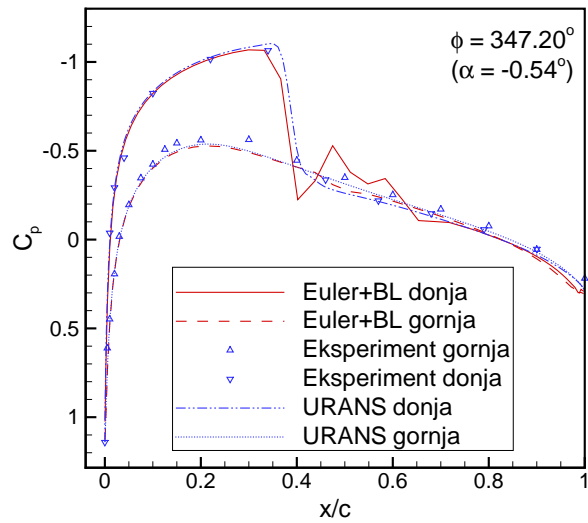
Slika 4.52: Raspodjela tlaka za nestacionarno strujanje za aeroprofil NACA0012 pri kutu unutar periode $\phi = 210.29^\circ$; $Ma = 0.755$, $Re = 5.5 \cdot 10^6$, $\alpha_m = 0.016^\circ$, $\alpha_o = 2.51^\circ$, $\omega^* = 0.1628$



Slika 4.53: Raspodjela tlaka za nestacionarno strujanje za aeroprofil NACA0012 pri kutu unutar periode $\phi = 255.14^\circ$; $Ma = 0.755$, $Re = 5.5 \cdot 10^6$, $\alpha_m = 0.016^\circ$, $\alpha_o = 2.51^\circ$, $\omega^* = 0.1628$

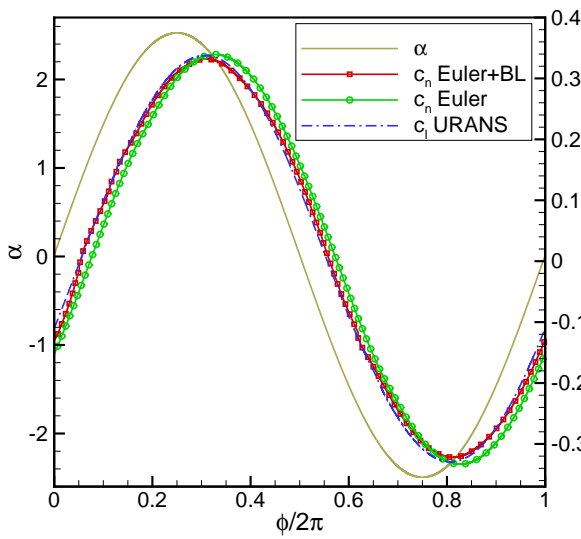


Slika 4.54: Raspodjela tlaka za nestacionarno strujanje za aeroprofil NACA0012 pri kutu unutar periode $\phi = 306.56^\circ$; $Ma = 0.755$, $Re = 5.5 \cdot 10^6$, $\alpha_m = 0.016^\circ$, $\alpha_o = 2.51^\circ$, $\omega^* = 0.1628$

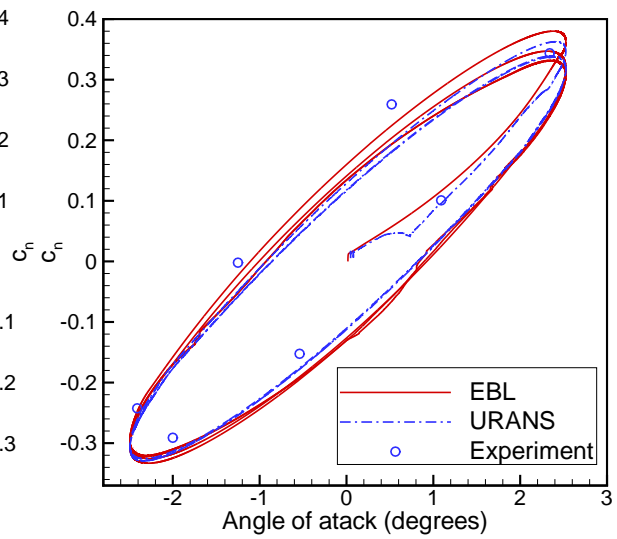


Slika 4.55: Raspodjela tlaka za nestacionarno strujanje za aeroprofil NACA0012 pri kutu unutar periode $\phi = 347.20^\circ$; $Ma = 0.755$, $Re = 5.5 \cdot 10^6$, $\alpha_m = 0.016^\circ$, $\alpha_o = 2.51^\circ$, $\omega^* = 0.1628$

sile za razvijenu metodu poklapa se s rezultatima nestacionarnog RANS-a, dok u usporedbi s eksperimentalnim podacima obje metode daju rješenje koje je više zamaknuto pri manjim napadnim kutevima. Na slici 4.56 također je pokazano rješenje za koeficijent normalne sile za rješavač neviskozno strujanja. Može se primjetiti razlika u fazi i iznosu rješenja između razvijene metode i metode za neviskozno strujanje. Rezultati za razvijenu metodu imaju vrlo dobro slaganje, u fazi i iznosu koeficijenta normalne sile, s rezultatima rješavača nestacionarnog RANS-a. Slika 4.56 pokazuje utjecaj sprezanja graničnog sloja na koeficijent normalne sile u odnosu na rezultate rješavača neviskozno strujanja.



Slika 4.56: Koeficijent normalne sile i trenutni napadni kut kao funkcija faznog kuta unutar periode, za aeroprofil NACA0012 pri $Ma = 0.755$, $Re = 5.5 \cdot 10^6$, $\alpha_m = 0.016^\circ$, $\alpha_o = 2.51^\circ$, $\omega^* = 0.1628$.



Slika 4.57: Koeficijent normalne sile kao funkcija trenutnog napadnog kuta za aeroprofil NACA0012 pri $Ma = 0.755$, $Re = 5.5 \cdot 10^6$, $\alpha_m = 0.016^\circ$, $\alpha_o = 2.51^\circ$, $\omega^* = 0.1628$.

4.4.2. NACA64A010 aeroprofil

U ovome potpoglavlju prikazani su rezultati za simetrični aeroprofil NACA64A010, za nestacionarno strujanje. Svi rezultati su uspoređeni s eksperimentalnim podacima iz AGARD izvještaja [27] i rezultatima rješavača nestacionarnog RANS (URANS) strujanja. Aeroprofil izvodi harmonijsko gibanje s rotacijom oko osi na udaljenosti $x_\alpha/c = 0.239$ od napadnog brida. Rezultati su izračunati za podzvučno stlačivo strujanje s pojavom jakog udarnog vala. Karakteristike slobodne struje i gibanja aeroprofila su dane u tablici 4.8.

Tablica 4.8: NACA64A010 unsteady test case

Machov broj Ma	0.797
Reynoldsov broj Re	$12.4 \cdot 10^6$
srednji napadni kut α_m	-0.08°
Amplituda napadnog kuta α_o	2.00°
Reducirana frekvencija ω^*	0.202
Položaj osi rotacije x_α/c	0.239

Računalna mreža sastoji se od 9600 kontrolnih volumena, 160 kontrolnih volumena u smjeru ξ koordinate i 60 kontrolnih volumena u smjeru η koordinate. Na slikama od 4.58 do 4.65 prikazani su rezultati koeficijenta tlaka za nestacionarno strujanje i gibanje aeroprofila prema parametrima u tablici 4.8. S crtkanim i punim linijama prikazani su izračunati rezultati s razvijenom metodom interakcije viskoznog i neviskoznog strujanja za gornju i donju stranu aeroprofila. S trokutima okrenutim prema gore i dolje prikazani su eksperimentalni podaci za gornju i donju stranu aeroprofila. Rezultati su dani za slijedeće fazne kuteve u zadnjem periodu simulacije: $\phi = 45^\circ, 90^\circ, 135^\circ, 180^\circ, 225^\circ, 270^\circ, 315^\circ, 360^\circ$. Simulirane su četiri periode nestacionarnog strujanja prije nego su zapisani rezultati za zadnji period.

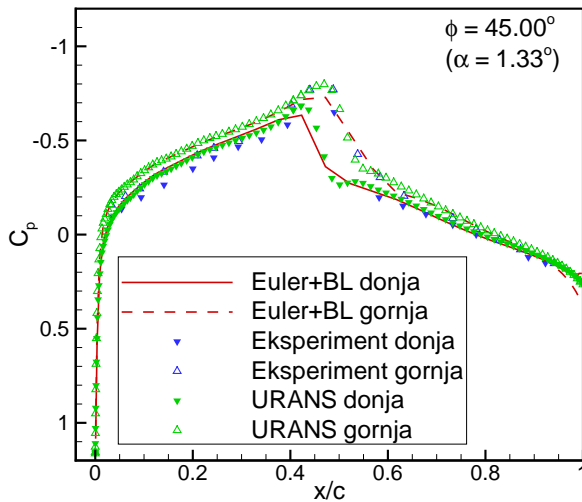
Razvijena metoda pokazuje rezultate koji se umjereno slažu s eksperimentalnim podacima u većini faznih kuteva zadnjeg perioda. Raspodjela koeficijenta tlaka pokazuje malo podbacivanje na obje strane aeroprofila, na dijelu ispred udarnog vala, pri svim faznim kutevima. Izračunati koeficijent tlaka se dobro slaže s eksperimentalnim podacima na stražnjem dijelu aeroprofila i iza udarnog vala. Položaj udarnog vala je u većini faznih kuteva dobro predviđen. Pri pojedinim faznim kutevima položaj jakog udarnog vala je bolje predviđen nego za slabi udarni val. Intenzitet udarnog vala, tj. vrh iznosa koefici-

jenta tlaka na udarnom valu, je na pojedinim faznim kutevima podbačen. Taj podbačaj se događa na strani aeroprofila gdje postoji manji podtlak, na položaju strme raspodjele koeficijenta tlaka, kao što je na gornjoj strani aeroprofila na slici 4.62. U takvom slučaju položaj i intenzitet udarnog vala dobiveni razvijenom metodom i eksperimentom se ne slažu. Izračunati skok koeficijenta tlaka kroz udarni val dobiven razvijenom metodom je prilično blaži u odnosu na eksperimentalne podatke. To se može objasniti prejakim utjecajem graničnog sloja na neviskozno strujanje, kao što je pokazano i u stacionarnom strujanju. Može se primjetiti gotovo jednaka razlika koeficijenta tlaka, koji je dobiven razvijenom metodom, u odnosu na eksperimentalne podatke na prednjem dijelu gornje i donje strane aeroprofila što može biti posljedica različitih parametara eksperimenta i računalne simulacije (zbog nekorrigiranih eksperimentalnih podataka za utjecaj zidova zračnog tunela).

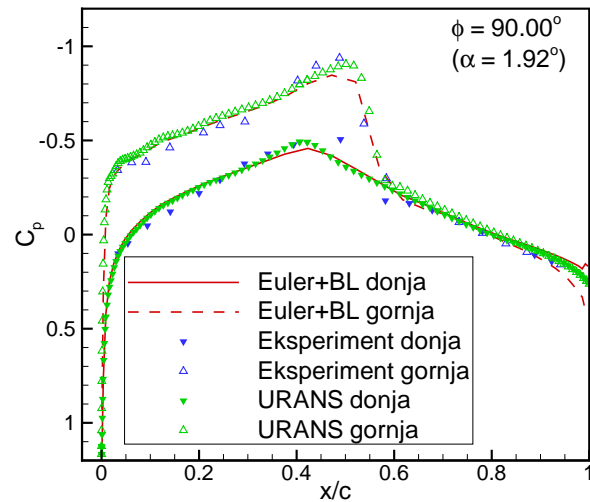
Na slikama od 4.58 do 4.65 su također prikazani rezultati izračunati RANS metodom za nestacionarno strujanje. Rezultati RANS metode su izračunati za dvojednadžbenim $k - \omega$ modelom turbulencije. Rezultati dobiveni metodom interakcije viskoznog i neviskoznog strujanja se gotovo odlično slažu s rezultatima izračunatim RANS metodom. Položaj i intenzitet udarnog vala dobiven razvijenom metodom u većini faznih kuteva jednog perioda se dobro slažu s rezultatima RANS metode. Pri pojedinim faznim kutevima intenzitet udarnog vala dobiven razvijenom metodom je malo položeniji u odnosu na RANS metodu za nestacionarno strujanje.

Na slici 4.66 prikazan je rezultat za koeficijent normalne sile u jednom periodu. Rezultati izračunati metodom interakcije viskoznog i neviskoznog strujanja uspoređeni su s rezultatima za neviskozno strujanje. Na istoj slici prikazana je i promjena napadnog kuta u jednom periodu. Rezultati izračunati razvijenom metodom pokazuju manji iznos i fazni pomak u odnosu na rezultate za neviskozno strujanje.

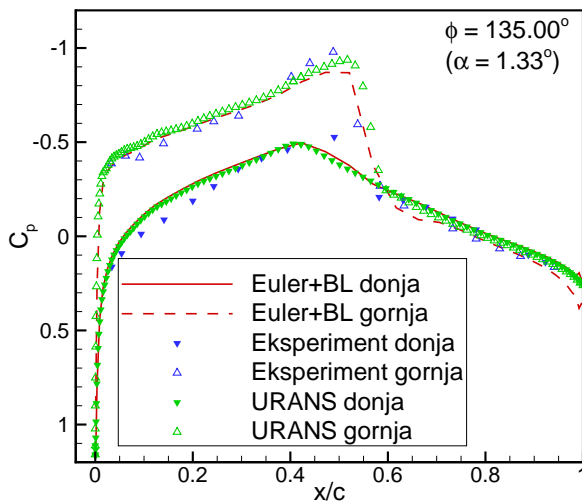
Na slici 4.67 prikazani su rezultati koeficijenta normalne sile u ovisnosti o trenutnom napadnom kutu za nestacionarno strujanje. Iz te slike se može vidjeti da izračunati koeficijent normalne sile odstupa od eksperimentalnih podataka. Uzrok tome leži u razlici raspodjele koeficijenta tlaka prikazan na prethodnim slikama.



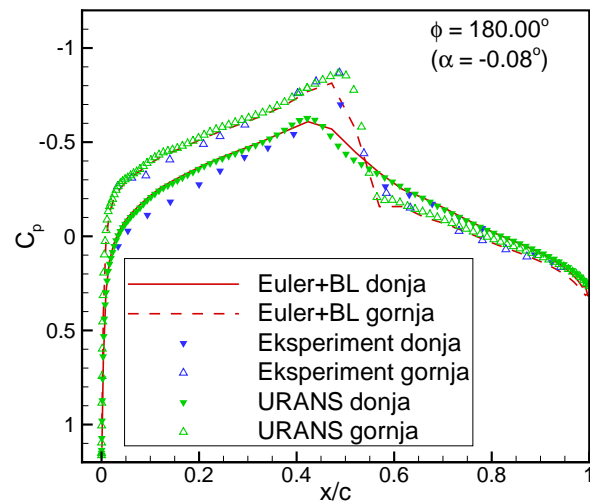
Slika 4.58: Raspodjela koeficijenta tlaka za nestacionarno strujanje oko aeroprofila NACA64A010 na faznom kutu $\phi = 45.00^\circ$ pri $Ma = 0.797$, $Re = 12.4 \cdot 10^6$, $\alpha_m = -0.08^\circ$, $\alpha_o = 2.00^\circ$, $\omega^* = 0.202$



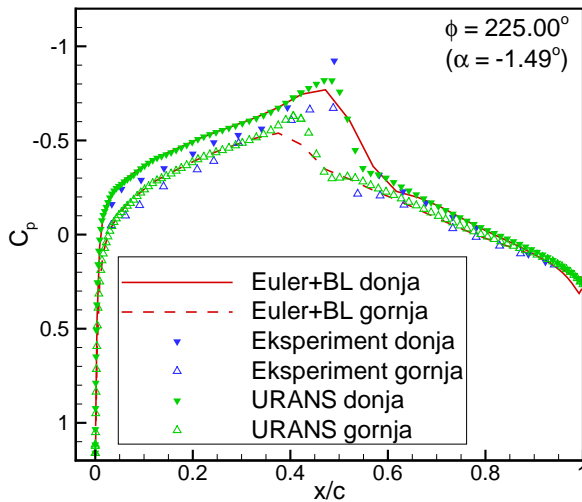
Slika 4.59: Raspodjela koeficijenta tlaka za nestacionarno strujanje oko aeroprofila NACA64A010 na faznom kutu $\phi = 90.00^\circ$ pri $Ma = 0.797$, $Re = 12.4 \cdot 10^6$, $\alpha_m = -0.08^\circ$, $\alpha_o = 2.00^\circ$, $\omega^* = 0.202$



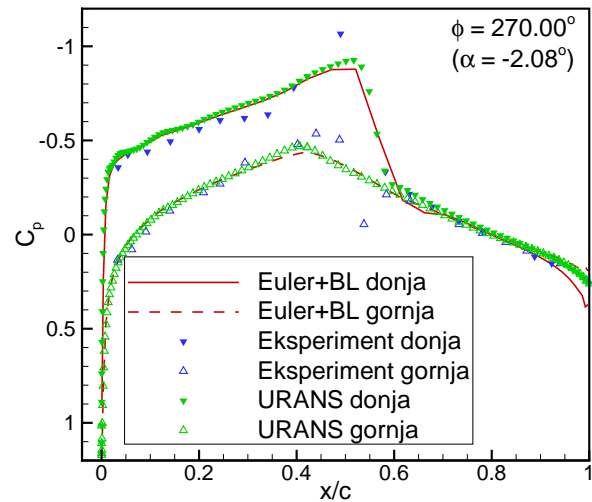
Slika 4.60: Raspodjela koeficijenta tlaka za nestacionarno strujanje oko aeroprofila NACA64A010 na faznom kutu $\phi = 135.00^\circ$ pri $Ma = 0.797$, $Re = 12.4 \cdot 10^6$, $\alpha_m = -0.08^\circ$, $\alpha_o = 2.00^\circ$, $\omega^* = 0.202$



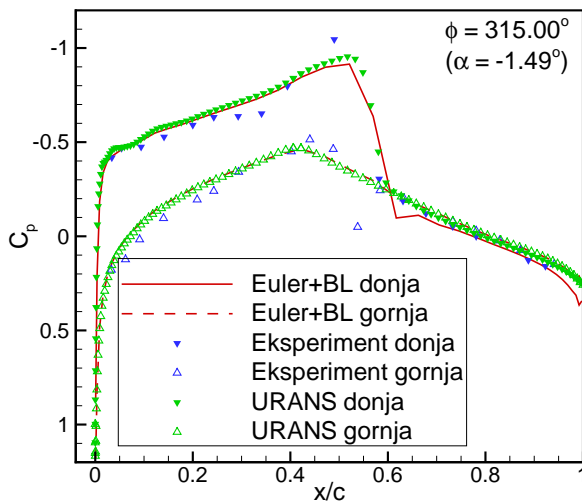
Slika 4.61: Raspodjela koeficijenta tlaka za nestacionarno strujanje oko aeroprofila NACA64A010 na faznom kutu $\phi = 180.00^\circ$ pri $Ma = 0.797$, $Re = 12.4 \cdot 10^6$, $\alpha_m = -0.08^\circ$, $\alpha_o = 2.00^\circ$, $\omega^* = 0.202$



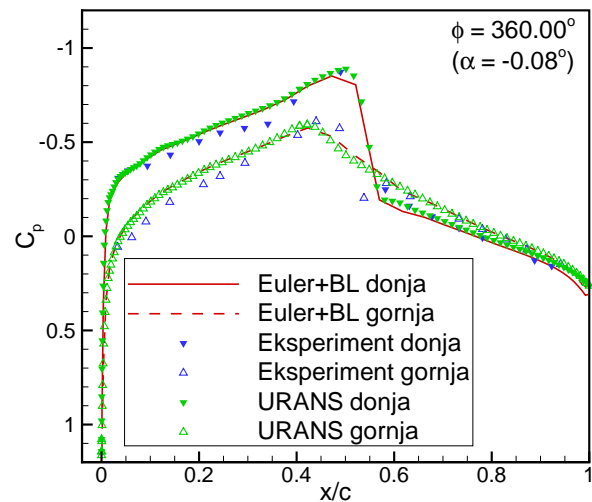
Slika 4.62: Raspodjela koeficijenta tlaka za nestacionarno strujanje oko aeroprofila NACA64A010 na faznom kutu $\phi = 225.00^\circ$ pri $Ma = 0.797$, $Re = 12.4 \cdot 10^6$, $\alpha_m = -0.08^\circ$, $\alpha_o = 2.00^\circ$, $\omega^* = 0.202$



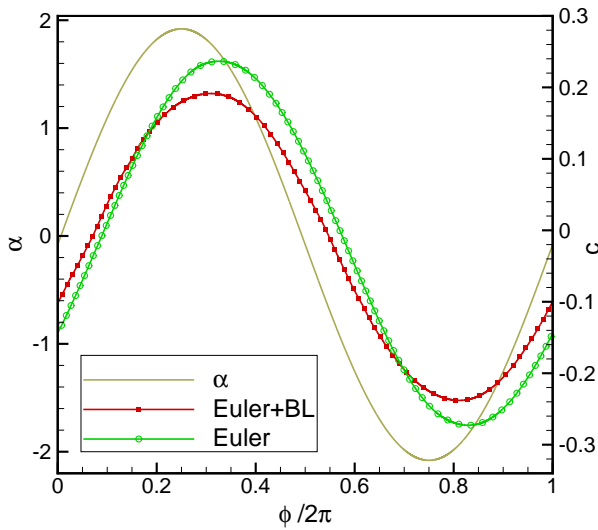
Slika 4.63: Raspodjela koeficijenta tlaka za nestacionarno strujanje oko aeroprofila NACA64A010 na faznom kutu $\phi = 270.00^\circ$ pri $Ma = 0.797$, $Re = 12.4 \cdot 10^6$, $\alpha_m = -0.08^\circ$, $\alpha_o = 2.00^\circ$, $\omega^* = 0.202$



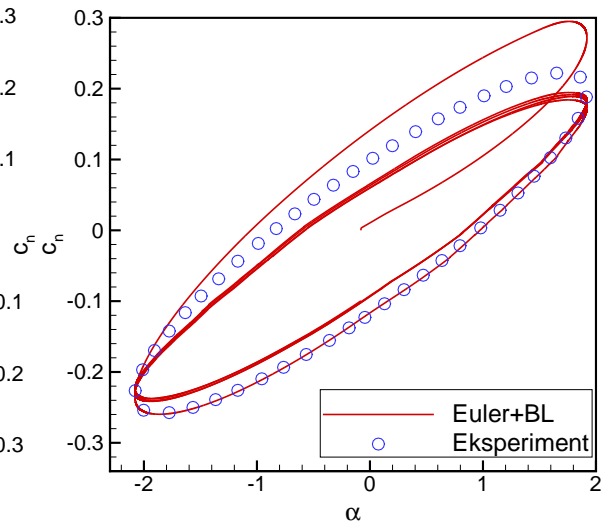
Slika 4.64: Raspodjela koeficijenta tlaka za nestacionarno strujanje oko aeroprofila NACA64A010 na faznom kutu $\phi = 315.00^\circ$ pri $Ma = 0.797$, $Re = 12.4 \cdot 10^6$, $\alpha_m = -0.08^\circ$, $\alpha_o = 2.00^\circ$, $\omega^* = 0.202$



Slika 4.65: Raspodjela koeficijenta tlaka za nestacionarno strujanje oko aeroprofila NACA64A010 na faznom kutu $\phi = 360.00^\circ$ pri $Ma = 0.797$, $Re = 12.4 \cdot 10^6$, $\alpha_m = -0.08^\circ$, $\alpha_o = 2.00^\circ$, $\omega^* = 0.202$



Slika 4.66: Koeficijent normalne sile i trenutni napadni kut kao funkcija faznog kuta u jednom periodu za aeroprofil NACA64A010 pri $Ma = 0.797$, $Re = 12.4 \cdot 10^6$, $\alpha_m = -0.08^\circ$, $\alpha_o = 2.00^\circ$, $\omega^* = 0.202$



Slika 4.67: Koeficijent normalne sile kao funkcija trenutnog napadnog kuta za aeroprofil NACA64A010 pri $Ma = 0.797$, $Re = 12.4 \cdot 10^6$, $\alpha_m = -0.08^\circ$, $\alpha_o = 2.00^\circ$, $\omega^* = 0.202$

5 Zaključak

U ovome radu razvijena je jednostavna i točna metoda za određivanje nestacionarnih aerodinamičkih opterećenja. Metoda je temeljena na viskozno-neviskoznoj dekompoziciji računalne domene, pri čemu je neviskozno strujanje opisano nestacionarnim Eulerovim jednadžbama dok je granični sloj opisan Von Karmanovim integralnim jednadžbama. Sprezanje Euler-granični sloj je ostvareno pomoću transpiracijske brzine (transpiracijska brzina, koja je izračunata iz jednadžbi graničnog sloja, korištena je u rubnom uvjetu neviskoznog rješavača). Metoda je usmjerena na podzvučno i krozzvučno strujanje pri velikim Reynoldsovima, s i bez pojave udarnog vala.

Nestacionarne Eulerove jednadžbe su riješene u transformiranim krivolinijskim koordinatama koristeći konzervativni oblik Eulerovih jednadžbi, pomoću metode kontrolnih volumena na pomičnoj strukturiranoj krutoj mreži C-tipa. Prostorna diskretizacija je izvedena pomoću Van Leerove MUSCL sheme drugog reda točnosti, dok je vremenska integracija izvršena pomoću eksplicitne Eulerove metode. Nestacionarni slučajevi su izvedeni za oscilatorno gibanje aeroprofila s promjenom napadnog kuta s nedeformiranom mrežom (kao rotacija krutog tijela). Generator mreže je temeljen na rješavanju Poissonove jednadžbe i zadovoljenjem ortogonalnosti mreže na konturi aeroprofila.

Model jednadžbi graničnog sloja sastoji se od dviju jednadžbi, integralne jednadžbe količine gibanja i jednadžbe kinetičke energije, zatvorene s dodatnim izrazima prema Dreli. Tranzicija je predviđena pomoću e^n metode. Model graničnog sloja je integriran pomoću Runge-Kutta metode četvrtog reda.

Prije validacije metode odabranim stacionarnim i nestacionarnim slučajevima, analizirana je konvergencija mreže kako bi se napravio odabir veličine mreže (u obliku uda-

ljenosti aeroprofila do vanjskog ruba domene i potrebnog broja kontrolnih volumena) koja omogućava rješenje neovisno o mreži. Konvergencija mreže je učinjena na aeroprofilu NACA0012 na dva napadna kuta 1° i 5° za stacionarne i nestacionarne slučajeve. Zaključeno je da mreže s udaljenošću aeroprofila do vanjskog ruba dome od 40 duljina tetiva, s 160 kontrolnih volumena uzduž konture traga aeroprofila i 60 kontrolnih volumena u smjeru okomito na konturu, omogućavaju rješenje koje je nezavisno o mreži. Iz nestacionarnih rezultata slijedi da su samo dva perioda numeričke simulacije dovoljna da se postigne periodičko rješenje.

Stacionarni rezultati su izvedeni za tri karakteristična aeroprofila (NACA0012, NACA64A010 i NLR7301) pri tri različita Machova broja u rasponu napadnih kuteva gdje se nije očekivalo masivno odvajanje strujanja, s i bez pojave udarnog vala. Rezultati dobiveni razvijenom metodom su uspoređeni s eksperimentalnim podacima iz AGARD izvještaja i s rezultatima RANS rješavača. Slijedeće je zaključeno:

- Stacionarni rezultati za aeroprofile NACA0012 i NACA64A010 pokazuju dobro slaganje s eksperimentalnim podacima pri svim Machovim brojevima.
- Za ta dva aeroprofila položaj tranzicije je točno predviđen. U slučaju bez udarnog vala, tranzicija je pokazana kao mali skok u distribuciji koeficijenta tlaka, kao i u eksperimentalnim podacima. U slučaju s udarnim valom tranzicija se pojavljuje na mjestu udarnog vala, tako da nije jasno vidljiva.
- Za ta dva aeroprofila intenzitet udarnog vala je dobro predviđen, no njegova pozicija je lagano pomaknuta prema izlaznom bridu aeroprofila u odnosu na eksperimentalne podatke. Razvijena metoda predviđa poziciju udarnog vala bliže poziciji prema podacima iz eksperimenta, nego što to daje rješenje čisto neviskozno rješavača, što znači da uzimanje u obzir efekte graničnog sloja poboljšava točnost rješenja.
- Rezultati za aeroprofil NLR7301 (koji predstavlja izazov za metode viskozno-neviskozne interakcije zbog ekstremno velikog radijusa nosa aeroprofila) pokazuju veliku osjetljivost na zadebljanje graničnog sloja i poziciju točke tranzicije, što je također pokazano i u literaturi. Razvijena metoda za taj aeroprofil pokazuje rezultate s umjerenim slaganjem u predviđanju raspodjele tlaka. Također, predviđena

točka tranzicije na kompresijskoj strani aeroprofila nije smještena na točnoj poziciji i metoda pokazuje nestabilnosti tlaka na izlaznom bridu podtlačne strane aeroprofila.

Nestacionarni rezultati su izvedeni za slučajeve aeroprofila NACA0012 i NACA64A010. Metoda nije prikladna za aeroprofil NLR7301 zbog pojave separacije strujanja pri relativno malom napadnom kutu (u slučaju separacije strujanja, model graničnog sloja više ne vrijedi). Probni slučajevi su izabrani iz AGARD izvještaja za Machove brojeve pri kojima se pojavljuju udarni valovi. Dobiveni rezultati su uspoređeni s eksperimentalnim podacima a također i s rezultatima nestacionarnog RANS rješavača. Slijedeće je zaključeno:

- Nestacionarni rezultati za oba aeroprofila su pokazali umjereno slaganje s eksperimentalnim podacima.
- Pozicija udarnog vala je u većini faznih kuteva točno predviđena. Na nekoliko faznih kuteva pozicija udarnog vala, dobivena pomoću razvijene metode, je pomaknuta prema napadnom bridu aeroprofila relativno na poziciju u eksperimentu (kao i u stacionarnom slučaju). Ti rezultati se vrlo dobro slažu s rezultatima nestacionarnog RANS rješavača.
- Intenzitet je na nekoliko faznih kuteva malo smanjen u odnosu na eksperimentalne podatke. Metoda je pokazala na nekoliko faznih kuteva, pri manjim napadnim kutovima, na strani aeroprofila s slabijim udarnim valom, izglađenu raspodjelu tlaka u odnosu na raspodjelu tlaka prema eksperimentalnim podacima.
- Raspodjela koeficijenta tlaka na obje strane aeroprofila pokazuje dobro slaganje s eksperimentalnim podacima. Na dijelu aeroprofila ispred udarnog vala postoji mali pomak izračunatog koeficijenta tlaka u odnosu na eksperimentalne podatke. Kako je taj pomak otprilike jednak na donjoj i gornjoj strani aeroprofila, to nema utjecaja na iznos normalne sile tlaka.
- Izračunati koeficijent normalne sile dobiven pomoću razvijene metode i pomoću nestacionarnog RANS rješavača pokazuje vrlo blisko slaganje. Za određeni napadni kut, izračunati rezultati koeficijenta normalne sile pokazuju jednolik pomak u odnosu na eksperimentalne podatke.

- Izračunati nestacionarni koeficijent normalne sile dobiven pomoću razvijene metode pokazuje smanjenje iznosa i zaostajanje u faznom kutu u odnosu na nestacionarne Eulerove rezultate.

Prema iskustvu u korištenju razvijene metode, može se zaključiti da metoda pokazuje oscilatorno ponašanje koeficijenta tlaka u blizini jakog udarnog vala i na izlaznom bridu aeroprofila. Te oscilacije mogu uzrokovati divergenciju metode, tako da je potrebna podrelaksacija pa stoga i veći broj iteracija. Podrelaksacijski faktor za većinu nestabilnih slučajeva pada i do vrijednosti 0.001. U budućem radu trebalo bi razmotriti čvrsti način sprežanja Eulerovih jednadžbi i jednadžbi graničnog sloja. U takvom pristupu sve jednadžbe su riješene simultano (za razliku od razvijene metode u kojoj su jednadžbe riješene sekvencijalno). Takva metoda je kompleksnija, ali se može očekivati da će čvrsto sprežanje poboljšati robusnost metode.

6 Zaključak doktorskog rada

U ovome radu razvijena je jednostavna i točna metoda za određivanje nestacionarnih aerodinamičkih opterećenja. Metoda je temeljena na nestacionarnim Eulerovim jednadžbama korigiranim za utjecaj graničnog sloja.

- Uključivanje graničnog sloja u metodu s nestacionarnim Eulerovim jednadžbama rezultira metodom s točnijim predviđanjem nestacionarnih aerodinamičkih opterećenja.
- Dokazana je hipoteza rada. Razvijena metoda je brza i daje rezultate približno iste točnosti kao i matematički model više točnosti poput RANS-a, i rezultati se dobro slažu s eksperimentalnim podacima.
- Postoji mogućnost da se poboljša robusnost razvijene metode modificirajući način sprezanja između Eulerovih jednadžbi i jednadžbi graničnog sloja.

A Izvod rubnog uvjeta

Rubni uvjet na površini aeroprofila jednak je:

$$(\vec{v} - \vec{v}_k - \vec{v}_t) \cdot \vec{n} = 0 / \frac{D}{Dt} \quad (\text{A.1})$$

$$\frac{D(\vec{v} - \vec{v}_k - \vec{v}_t)}{Dt} \cdot \vec{n} + (\vec{v} - \vec{v}_k - \vec{v}_t) \cdot \frac{D\vec{n}}{Dt} = 0 \quad (\text{A.2})$$

$$\frac{D\vec{v}}{Dt} \cdot \vec{n} - \frac{D(\vec{v}_k + \vec{v}_t)}{Dt} \cdot \vec{n} + (\vec{v} - \vec{v}_k - \vec{v}_t) \cdot \frac{D\vec{n}}{Dt} = 0 / \cdot \rho \quad (\text{A.3})$$

$$\left| \frac{D\vec{v}}{Dt} = -\frac{1}{\rho} \text{grad} p \right| \quad (\text{A.4})$$

$$\rho \left\{ \frac{D\vec{n}}{Dt} \cdot (\vec{v} - \vec{v}_k - \vec{v}_t) - \frac{D(\vec{v}_k + \vec{v}_t)}{Dt} \cdot \vec{n} \right\} = \text{grad} p \cdot \vec{n} \quad (\text{A.5})$$

$$\text{I} = \frac{D\vec{n}}{Dt} \cdot (\vec{v} - \vec{v}_k - \vec{v}_t) \quad (\text{A.6})$$

$$\text{II} = -\frac{D(\vec{v}_k + \vec{v}_t)}{Dt} \cdot \vec{n} \quad (\text{A.7})$$

$$\vec{n} = \vec{k} \times \vec{e}_\xi \quad (\text{A.8})$$

$$\vec{n} = \begin{vmatrix} i & j & k \\ 0 & 0 & 1 \\ x_\xi & y_\xi & 0 \end{vmatrix} = (-y_\xi, x_\xi) \quad (\text{A.9})$$

$$\begin{aligned} \text{I} &= \left(\frac{\partial n_x}{\partial t} + v_x \frac{\partial n_x}{\partial x} + v_y \frac{\partial n_x}{\partial y} \right) \cdot (v_x - x_\tau - v_{tx}) \\ &\quad + \left(\frac{\partial n_y}{\partial t} + v_x \frac{\partial n_y}{\partial x} + v_y \frac{\partial n_y}{\partial y} \right) \cdot (v_y - y_\tau - v_{ty}) \end{aligned} \quad (\text{A.10})$$

$$\begin{aligned} \text{II} &= \left(\frac{\partial (\vec{v}_k + \vec{v}_t)}{\partial t} + v_x \frac{\partial (\vec{v}_k + \vec{v}_t)}{\partial x} + v_y \frac{\partial (\vec{v}_k + \vec{v}_t)}{\partial y} \right) \cdot \vec{n} \\ &= \left(\frac{\partial (x_\tau + v_{tx})}{\partial t} + v_x \frac{\partial (x_\tau + v_{tx})}{\partial x} + v_y \frac{\partial (x_\tau + v_{tx})}{\partial y} \right) n_x \\ &\quad + \left(\frac{\partial (y_\tau + v_{ty})}{\partial t} + v_x \frac{\partial (y_\tau + v_{ty})}{\partial x} + v_y \frac{\partial (y_\tau + v_{ty})}{\partial y} \right) n_y \end{aligned} \quad (\text{A.11})$$

$$\begin{aligned} \text{I} &= \left[-\frac{1}{J} (K_{31} y_{\xi\xi} + K_{32} y_{\xi\eta} + K_{33} y_{\xi\tau}) - \frac{v_x}{J} (y_\eta y_{\xi\xi} - y_\xi y_{\xi\eta}) \right. \\ &\quad \left. - \frac{v_y}{J} (-x_\eta y_{\xi\xi} + x_\xi y_{\xi\eta}) \right] (v_x - x_\tau - v_{tx}) \\ &\quad + \left[\frac{1}{J} (K_{31} x_{\xi\xi} + K_{32} x_{\xi\eta} + K_{33} x_{\xi\tau}) + \frac{v_x}{J} (y_\eta x_{\xi\xi} - y_\xi x_{\xi\eta}) \right. \\ &\quad \left. + \frac{v_y}{J} (-x_\eta x_{\xi\xi} + x_\xi x_{\xi\eta}) \right] (v_y - y_\tau - v_{ty}) \end{aligned} \quad (\text{A.12})$$

$$\begin{aligned} \text{II} &= y_\xi \left[\frac{1}{J} (K_{31} (x_{\tau\xi} + v_{tx\xi}) + K_{32} (x_{\tau\eta} + v_{tx\eta}) + K_{33} (x_{\tau\tau} + v_{tx\tau})) \right. \\ &\quad \left. + \frac{v_x}{J} (y_\eta (x_{\tau\xi} + v_{tx\xi}) - y_\xi (x_{\tau\eta} + v_{tx\eta})) \right. \\ &\quad \left. + \frac{v_y}{J} (-x_\eta (x_{\tau\xi} + v_{tx\xi}) + x_\xi (x_{\tau\eta} + v_{tx\eta})) \right] \\ &\quad - x_\xi \left[\frac{1}{J} (K_{31} (y_{\tau\xi} + v_{ty\xi}) + K_{32} (y_{\tau\eta} + v_{ty\eta}) + K_{33} (y_{\tau\tau} + v_{ty\tau})) \right. \\ &\quad \left. + \frac{v_x}{J} (y_\eta (y_{\tau\xi} + v_{ty\xi}) - y_\xi (y_{\tau\eta} + v_{ty\eta})) \right. \\ &\quad \left. + \frac{v_y}{J} (-x_\eta (y_{\tau\xi} + v_{ty\xi}) + x_\xi (y_{\tau\eta} + v_{ty\eta})) \right] \end{aligned} \quad (\text{A.13})$$

Površina aeroprofila odgovara površini $\eta = \text{konst.}$ i odgovara slijedećem izrazu:

$$\frac{D\eta}{Dt} = 0 \quad (\text{A.14})$$

$$\frac{\partial \eta}{\partial t} + v_x \frac{\partial \eta}{\partial x} + v_y \frac{\partial \eta}{\partial y} = 0 \quad (\text{A.15})$$

$$\frac{1}{J}K_{32} - \frac{v_x}{J}y_\xi + \frac{v_y}{J}x_\xi = 0 \quad (\text{A.16})$$

$$\begin{aligned} \text{I} = & \left[-\frac{1}{J}(x_\eta y_\tau y_{\xi\xi} - y_\eta x_\tau y_{\xi\xi} + J y_{\xi\tau}) - \frac{v_x}{J}y_\eta y_{\xi\xi} + \frac{v_y}{J}x_\eta y_{\xi\xi} \right] (v_x - x_\tau - v_{tx}) \\ & + \left[\frac{1}{J}(x_\eta y_\tau x_{\xi\xi} - y_\eta x_\tau x_{\xi\xi} + J x_{\xi\tau}) + \frac{v_x}{J}y_\eta x_{\xi\xi} - \frac{v_y}{J}x_\eta x_{\xi\xi} \right] (v_y - y_\tau - v_{ty}) \end{aligned} \quad (\text{A.17})$$

$$\begin{aligned} \text{I} = & \left[-\frac{1}{J}y_\eta y_{\xi\xi} (v_x - x_\tau) + \frac{1}{J}x_\eta y_{\xi\xi} (v_y - y_\tau) - y_{\xi\tau} \right] [(v_x - x_\tau) - v_{tx}] \\ & + \left[\frac{1}{J}y_\eta x_{\xi\xi} (v_x - x_\tau) - \frac{1}{J}x_\eta x_{\xi\xi} (v_y - y_\tau) + x_{\xi\tau} \right] [(v_y - y_\tau) - v_{ty}] \end{aligned} \quad (\text{A.18})$$

$$\begin{aligned} \text{I} = & \left[-\frac{1}{J}y_\eta y_{\xi\xi} (v_x - x_\tau) + \frac{1}{J}x_\eta y_{\xi\xi} (v_y - y_\tau) - y_{\xi\tau} \right] [(v_x - x_\tau) - v_{tx}] \\ & + \left[\frac{1}{J}y_\eta x_{\xi\xi} (v_x - x_\tau) - \frac{1}{J}x_\eta x_{\xi\xi} (v_y - y_\tau) + x_{\xi\tau} \right] [(v_y - y_\tau) - v_{ty}] \end{aligned} \quad (\text{A.19})$$

$$\begin{aligned} \text{I} = & -\frac{1}{J}y_\eta y_{\xi\xi} (v_x - x_\tau)^2 + \frac{1}{J}x_\eta y_{\xi\xi} (v_y - y_\tau) (v_x - x_\tau) - y_{\xi\tau} (v_x - x_\tau) \\ & + \frac{1}{J}y_\eta y_{\xi\xi} (v_x - x_\tau) v_{tx} - \frac{1}{J}x_\eta y_{\xi\xi} (v_y - y_\tau) v_{tx} + y_{\xi\tau} v_{tx} \\ & + \frac{1}{J}y_\eta x_{\xi\xi} (v_x - x_\tau) (v_y - y_\tau) - \frac{1}{J}x_\eta x_{\xi\xi} (v_y - y_\tau)^2 + x_{\xi\tau} (v_y - y_\tau) \\ & - \frac{1}{J}y_\eta x_{\xi\xi} (v_x - x_\tau) v_{ty} + \frac{1}{J}x_\eta x_{\xi\xi} (v_y - y_\tau) v_{ty} - x_{\xi\tau} v_{ty} \end{aligned} \quad (\text{A.20})$$

$$\begin{aligned} \text{II} = & y_\xi \left[\frac{1}{J} (K_{31} (x_{\tau\xi} + v_{tx\xi}) + K_{33} (x_{\tau\tau} + v_{tx\tau})) \right. \\ & \left. + \frac{v_x}{J} y_\eta (x_{\tau\xi} + v_{tx\xi}) - \frac{v_y}{J} x_\eta (x_{\tau\xi} + v_{tx\xi}) \right] \\ & - x_\xi \left[\frac{1}{J} (K_{31} (y_{\tau\xi} + v_{ty\xi}) + K_{33} (y_{\tau\tau} + v_{ty\tau})) \right. \\ & \left. + \frac{v_x}{J} y_\eta (y_{\tau\xi} + v_{ty\xi}) - \frac{v_y}{J} x_\eta (y_{\tau\xi} + v_{ty\xi}) \right] \end{aligned} \quad (\text{A.21})$$

$$\begin{aligned}
 \text{II} = & y_\xi \left[\frac{1}{J} \left((x_\eta y_\tau - y_\eta x_\tau) (x_{\tau\xi} + v_{tx\xi}) + J (x_{\tau\tau} + v_{tx\tau}) \right) \right. \\
 & \left. + \frac{v_x}{J} y_\eta (x_{\tau\xi} + v_{tx\xi}) - \frac{v_y}{J} x_\eta (x_{\tau\xi} + v_{tx\xi}) \right] \\
 & - x_\xi \left[\frac{1}{J} \left((x_\eta y_\tau - y_\eta x_\tau) (y_{\tau\xi} + v_{ty\xi}) + J (y_{\tau\tau} + v_{ty\tau}) \right) \right. \\
 & \left. + \frac{v_x}{J} y_\eta (y_{\tau\xi} + v_{ty\xi}) - \frac{v_y}{J} x_\eta (y_{\tau\xi} + v_{ty\xi}) \right] \quad (\text{A.22})
 \end{aligned}$$

$$\begin{aligned}
 \text{II} = & y_\xi \left[\frac{1}{J} (x_\eta y_\tau x_{\tau\xi} + x_\eta y_\tau v_{tx\xi} - y_\eta x_\tau x_{\tau\xi} - y_\eta x_\tau v_{tx\xi} + J x_{\tau\tau} + J v_{tx\tau}) \right. \\
 & \left. + \frac{v_x}{J} y_\eta x_{\tau\xi} + \frac{v_x}{J} y_\eta v_{tx\xi} - \frac{v_y}{J} x_\eta x_{\tau\xi} - \frac{v_y}{J} x_\eta v_{tx\xi} \right] \\
 & - x_\xi \left[\frac{1}{J} (x_\eta y_\tau y_{\tau\xi} + x_\eta y_\tau v_{ty\xi} - y_\eta x_\tau y_{\tau\xi} - y_\eta x_\tau v_{ty\xi} + J y_{\tau\tau} + J v_{ty\tau}) \right. \\
 & \left. + \frac{v_x}{J} y_\eta y_{\tau\xi} + \frac{v_x}{J} y_\eta v_{ty\xi} - \frac{v_y}{J} x_\eta y_{\tau\xi} - \frac{v_y}{J} x_\eta v_{ty\xi} \right] \quad (\text{A.23})
 \end{aligned}$$

$$\begin{aligned}
 \text{II} = & y_\xi \left[\frac{1}{J} y_\eta x_{\tau\xi} (v_x - x_\tau) - \frac{1}{J} x_\eta x_{\tau\xi} (v_y - y_\tau) + \frac{1}{J} y_\eta v_{tx\xi} (v_x - x_\tau) \right. \\
 & \left. - \frac{1}{J} x_\eta v_{tx\xi} (v_y - y_\tau) + x_{\tau\tau} + v_{tx\tau} \right] \\
 & - x_\xi \left[\frac{1}{J} y_\eta y_{\tau\xi} (v_x - x_\tau) - \frac{1}{J} x_\eta y_{\tau\xi} (v_y - y_\tau) + \frac{1}{J} y_\eta v_{ty\xi} (v_x - x_\tau) \right. \\
 & \left. - \frac{1}{J} x_\eta v_{ty\xi} (v_y - y_\tau) + y_{\tau\tau} + v_{ty\tau} \right] \quad (\text{A.24})
 \end{aligned}$$

$$\begin{aligned}
 \text{II} = & \frac{1}{J} [y_\xi y_\eta x_{\tau\xi} (v_x - x_\tau) - y_\xi x_\eta x_{\tau\xi} (v_y - y_\tau) + y_\xi y_\eta v_{tx\xi} (v_x - x_\tau) \\
 & - y_\xi x_\eta v_{tx\xi} (v_y - y_\tau) + J x_{\tau\tau} y_\xi + J v_{tx\tau} y_\xi] \\
 & - \frac{1}{J} [x_\xi y_\eta y_{\tau\xi} (v_x - x_\tau) - x_\xi x_\eta y_{\tau\xi} (v_y - y_\tau) + x_\xi y_\eta v_{ty\xi} (v_x - x_\tau) \\
 & - x_\xi x_\eta v_{ty\xi} (v_y - y_\tau) + J y_{\tau\tau} x_\xi + J v_{ty\tau} x_\xi] \quad (\text{A.25})
 \end{aligned}$$

I + II (dijelovi s $x_{\xi\tau}$ i $y_{\xi\tau}$):

$$\begin{aligned}
 (\text{I} + \text{II})_{x_{\xi\tau} y_{\xi\tau}} = & \frac{1}{J} [y_\xi y_\eta x_{\tau\xi} (v_x - x_\tau) - y_\xi x_\eta x_{\tau\xi} (v_y - y_\tau) - x_\xi y_\eta y_{\tau\xi} (v_x - x_\tau) \\
 & + x_\xi x_\eta y_{\tau\xi} (v_y - y_\tau) - y_{\xi\tau} (v_x - x_\tau) J + x_{\xi\tau} (v_y - y_\tau) J \\
 & + y_{\xi\tau} v_{tx} J - x_{\xi\tau} v_{ty} J] \quad (\text{A.26})
 \end{aligned}$$

$$\begin{aligned}
 (\text{I} + \text{II})_{x_{\xi\tau}y_{\xi\tau}} &= \frac{1}{J} [y_{\xi}y_{\eta}x_{\tau\xi} (v_x - x_{\tau}) - y_{\xi}x_{\eta}x_{\tau\xi} (v_y - y_{\tau}) - x_{\xi}y_{\eta}y_{\tau\xi} (v_x - x_{\tau}) \\
 &\quad + x_{\xi}x_{\eta}y_{\tau\xi} (v_y - y_{\tau}) - x_{\xi}y_{\eta}y_{\xi\tau} (v_x - x_{\tau}) + y_{\xi}x_{\eta}y_{\xi\tau} (v_x - x_{\tau}) \\
 &\quad + x_{\xi}y_{\eta}x_{\xi\tau} (v_y - y_{\tau}) - y_{\xi}x_{\eta}x_{\xi\tau} (v_y - y_{\tau}) \\
 &\quad + x_{\xi}y_{\eta}y_{\xi\tau}v_{tx} - y_{\xi}x_{\eta}y_{\xi\tau}v_{tx} - x_{\xi}y_{\eta}x_{\xi\tau}v_{ty} + y_{\xi}x_{\eta}x_{\xi\tau}v_{ty}] \quad (\text{A.27})
 \end{aligned}$$

$$\begin{aligned}
 (\text{I} + \text{II})_{x_{\xi\tau}y_{\xi\tau}} &= \frac{1}{J} [y_{\xi}x_{\tau\xi} (y_{\eta} (v_x - x_{\tau}) - x_{\eta} (v_y - y_{\tau}) - x_{\eta} (v_y - y_{\tau})) \\
 &\quad - x_{\xi}y_{\tau\xi} (y_{\eta} (v_x - x_{\tau}) - x_{\eta} (v_y - y_{\tau}) + y_{\eta} (v_x - x_{\tau})) \\
 &\quad + y_{\xi}x_{\eta}y_{\xi\tau} (v_x - x_{\tau}) + x_{\xi}y_{\eta}x_{\xi\tau} (v_y - y_{\tau}) \\
 &\quad + x_{\xi}y_{\eta}y_{\xi\tau}v_{tx} - y_{\xi}x_{\eta}y_{\xi\tau}v_{tx} - x_{\xi}y_{\eta}x_{\xi\tau}v_{ty} + y_{\xi}x_{\eta}x_{\xi\tau}v_{ty}] \quad (\text{A.28})
 \end{aligned}$$

$$\begin{aligned}
 (\text{I} + \text{II})_{x_{\xi\tau}y_{\xi\tau}} &= \frac{1}{J} [y_{\xi}x_{\tau\xi} \left(\sqrt{x_{\eta}^2 + y_{\eta}^2} \bar{u} - x_{\eta} (v_y - y_{\tau}) \right) \\
 &\quad - x_{\xi}y_{\tau\xi} \left(\sqrt{x_{\eta}^2 + y_{\eta}^2} \bar{u} + y_{\eta} (v_x - x_{\tau}) \right) \\
 &\quad + y_{\xi}x_{\eta}y_{\xi\tau} (v_x - x_{\tau}) + x_{\xi}y_{\eta}x_{\xi\tau} (v_y - y_{\tau}) \\
 &\quad + x_{\xi}y_{\eta}y_{\xi\tau}v_{tx} - y_{\xi}x_{\eta}y_{\xi\tau}v_{tx} - x_{\xi}y_{\eta}x_{\xi\tau}v_{ty} + y_{\xi}x_{\eta}x_{\xi\tau}v_{ty}] \quad (\text{A.29})
 \end{aligned}$$

$$\begin{aligned}
 &(\text{I} + \text{II})_{x_{\xi\tau}y_{\xi\tau}} = \\
 \frac{1}{J} &[y_{\xi}x_{\tau\xi} \left(\sqrt{x_{\eta}^2 + y_{\eta}^2} \bar{u} + y_{\eta} (v_x - x_{\tau}) - x_{\eta} (v_y - y_{\tau}) - y_{\eta} (v_x - x_{\tau}) \right) \\
 &- x_{\xi}y_{\tau\xi} \left(\sqrt{x_{\eta}^2 + y_{\eta}^2} \bar{u} + y_{\eta} (v_x - x_{\tau}) - x_{\eta} (v_y - y_{\tau}) + x_{\eta} (v_y - y_{\tau}) \right) \\
 &\quad + y_{\xi}x_{\eta}y_{\xi\tau} (v_x - x_{\tau}) + x_{\xi}y_{\eta}x_{\xi\tau} (v_y - y_{\tau}) \\
 &\quad + x_{\xi}y_{\eta}y_{\xi\tau}v_{tx} - y_{\xi}x_{\eta}y_{\xi\tau}v_{tx} - x_{\xi}y_{\eta}x_{\xi\tau}v_{ty} + y_{\xi}x_{\eta}x_{\xi\tau}v_{ty}] \quad (\text{A.30})
 \end{aligned}$$

$$\begin{aligned}
 (\text{I} + \text{II})_{x_{\xi\tau}y_{\xi\tau}} &= \frac{1}{J} [y_{\xi}x_{\tau\xi} \left(2\sqrt{x_{\eta}^2 + y_{\eta}^2} \bar{u} - y_{\eta} (v_x - x_{\tau}) \right) \\
 &\quad - x_{\xi}y_{\tau\xi} \left(2\sqrt{x_{\eta}^2 + y_{\eta}^2} \bar{u} + x_{\eta} (v_y - y_{\tau}) \right) \\
 &\quad + y_{\xi}x_{\eta}y_{\xi\tau} (v_x - x_{\tau}) + x_{\xi}y_{\eta}x_{\xi\tau} (v_y - y_{\tau}) \\
 &\quad + x_{\xi}y_{\eta}y_{\xi\tau}v_{tx} - y_{\xi}x_{\eta}y_{\xi\tau}v_{tx} - x_{\xi}y_{\eta}x_{\xi\tau}v_{ty} + y_{\xi}x_{\eta}x_{\xi\tau}v_{ty}] \quad (\text{A.31})
 \end{aligned}$$

$$\begin{aligned}
(I + II)_{x_{\xi\tau}y_{\xi\tau}} &= \frac{1}{J} [2\sqrt{x_{\eta}^2 + y_{\eta}^2} \bar{u} (y_{\xi}x_{\tau\xi} - x_{\xi}y_{\tau\xi}) \\
&\quad - y_{\xi}x_{\tau\xi}y_{\eta} (v_x - x_{\tau}) - x_{\xi}y_{\tau\xi}x_{\eta} (v_y - y_{\tau}) \\
&\quad + y_{\xi}x_{\eta}y_{\xi\tau} (v_x - x_{\tau}) + x_{\xi}y_{\eta}x_{\xi\tau} (v_y - y_{\tau}) \\
&\quad + x_{\xi}y_{\eta}y_{\xi\tau}v_{tx} - y_{\xi}x_{\eta}y_{\xi\tau}v_{tx} - x_{\xi}y_{\eta}x_{\xi\tau}v_{ty} + y_{\xi}x_{\eta}x_{\xi\tau}v_{ty} \\
&\quad + y_{\xi}y_{\eta}x_{\xi\tau}v_{tx} - y_{\xi}y_{\eta}x_{\xi\tau}v_{tx} \\
&\quad + x_{\xi}x_{\eta}y_{\xi\tau}v_{ty} - x_{\xi}x_{\eta}y_{\xi\tau}v_{ty}] \tag{A.32}
\end{aligned}$$

$$\begin{aligned}
(I + II)_{x_{\xi\tau}y_{\xi\tau}} &= \frac{1}{J} [2\sqrt{x_{\eta}^2 + y_{\eta}^2} \bar{u} (y_{\xi}x_{\tau\xi} - x_{\xi}y_{\tau\xi}) \\
&\quad + x_{\tau\xi}y_{\eta} (-y_{\xi} (v_x - x_{\tau} - v_{tx}) + x_{\xi} (v_y - y_{\tau} - v_{ty})) \\
&\quad - y_{\xi\tau}x_{\eta} (-y_{\xi} (v_x - x_{\tau} - v_{tx}) + x_{\xi} (v_y - y_{\tau} - v_{ty})) \\
&\quad + x_{\xi}y_{\eta}y_{\xi\tau}v_{tx} + y_{\xi}x_{\eta}x_{\xi\tau}v_{ty} \\
&\quad - y_{\xi}y_{\eta}x_{\xi\tau}v_{tx} \\
&\quad - x_{\xi}x_{\eta}y_{\xi\tau}v_{ty}] \tag{A.33}
\end{aligned}$$

Na površini aeroprofila brzina v u protoku G koja je okomita na $\eta = \text{konst.}$, je jednaka nuli i odgovara slijedećem izrazu u jednadžbi (A.33):

$$v = -y_{\xi} (v_x - x_{\tau} - v_{tx}) + x_{\xi} (v_y - y_{\tau} - v_{ty}) = 0. \tag{A.34}$$

Iz toga slijedi:

$$\begin{aligned}
(I + II)_{x_{\xi\tau}y_{\xi\tau}} &= \frac{1}{J} [2\sqrt{x_{\eta}^2 + y_{\eta}^2} \bar{u} (y_{\xi}x_{\tau\xi} - x_{\xi}y_{\tau\xi}) \\
&\quad + x_{\xi}y_{\eta}y_{\xi\tau}v_{tx} + y_{\xi}x_{\eta}x_{\xi\tau}v_{ty} - y_{\xi}y_{\eta}x_{\xi\tau}v_{tx} - x_{\xi}x_{\eta}y_{\xi\tau}v_{ty}] \tag{A.35}
\end{aligned}$$

I + II (dijelovi s $x_{\xi\xi}$ i $y_{\xi\xi}$):

$$\begin{aligned}
(I + II)_{x_{\xi\xi}y_{\xi\xi}} &= \frac{1}{J}[-y_{\eta}y_{\xi\xi}(v_x - x_{\tau})^2 + x_{\eta}y_{\xi\xi}(v_y - y_{\tau})(v_x - x_{\tau}) \\
&\quad + y_{\eta}y_{\xi\xi}(v_x - x_{\tau})v_{tx} - x_{\eta}y_{\xi\xi}(v_y - y_{\tau})v_{tx} \\
&\quad + y_{\eta}x_{\xi\xi}(v_x - x_{\tau})(v_y - y_{\tau}) - x_{\eta}x_{\xi\xi}(v_y - y_{\tau})^2 \\
&\quad - y_{\eta}x_{\xi\xi}(v_x - x_{\tau})v_{ty} + x_{\eta}x_{\xi\xi}(v_y - y_{\tau})v_{ty}] \cdot \frac{J}{J}
\end{aligned} \tag{A.36}$$

$$\begin{aligned}
(I + II)_{x_{\xi\xi}y_{\xi\xi}} &= \frac{1}{J^2}[-y_{\eta}^2x_{\xi}y_{\xi\xi}(v_x - x_{\tau})^2 + x_{\eta}y_{\eta}y_{\xi}y_{\xi\xi}(v_x - x_{\tau})^2 \\
&\quad + x_{\xi}x_{\eta}y_{\eta}y_{\xi\xi}(v_x - x_{\tau})(v_y - y_{\tau}) - y_{\xi}x_{\eta}^2y_{\xi\xi}(v_x - x_{\tau})(v_y - y_{\tau}) \\
&\quad + x_{\xi}y_{\eta}^2y_{\xi\xi}(v_x - x_{\tau})v_{tx} - y_{\xi}x_{\eta}y_{\eta}y_{\xi\xi}(v_x - x_{\tau})v_{tx} \\
&\quad - x_{\xi}x_{\eta}y_{\eta}y_{\xi\xi}(v_y - y_{\tau})v_{tx} + y_{\xi}x_{\eta}^2y_{\xi\xi}(v_y - y_{\tau})v_{tx} \\
&\quad + x_{\xi}y_{\eta}^2x_{\xi\xi}(v_x - x_{\tau})(v_y - y_{\tau}) - x_{\eta}y_{\eta}y_{\xi}x_{\xi\xi}(v_x - x_{\tau})(v_y - y_{\tau}) \\
&\quad - x_{\xi}x_{\eta}y_{\eta}x_{\xi\xi}(v_y - y_{\tau})^2 + y_{\xi}x_{\eta}^2x_{\xi\xi}(v_y - y_{\tau})^2 \\
&\quad - x_{\xi}y_{\eta}^2x_{\xi\xi}(v_x - x_{\tau})v_{ty} + y_{\xi}x_{\eta}y_{\eta}x_{\xi\xi}(v_x - x_{\tau})v_{ty} \\
&\quad + x_{\xi}x_{\eta}y_{\eta}x_{\xi\xi}(v_y - y_{\tau})v_{ty} - y_{\xi}x_{\eta}^2x_{\xi\xi}(v_y - y_{\tau})v_{ty} \\
&\quad + x_{\xi}y_{\xi\xi}x_{\eta}^2(v_y - y_{\tau})^2 - x_{\xi}y_{\xi\xi}x_{\eta}^2(v_y - y_{\tau})^2 \\
&\quad + x_{\xi}x_{\eta}y_{\eta}y_{\xi\xi}(v_x - x_{\tau})(v_y - y_{\tau}) - x_{\xi}x_{\eta}y_{\eta}y_{\xi\xi}(v_x - x_{\tau})(v_y - y_{\tau})]
\end{aligned} \tag{A.37}$$

$$\begin{aligned}
 & (I + II)_{x_{\xi\xi}y_{\xi\xi}} = \\
 & \frac{1}{J^2} [-x_{\xi}y_{\xi\xi} (y_{\eta}^2 (v_x - x_{\tau})^2 - 2x_{\eta}y_{\eta} (v_x - x_{\tau}) (v_y - y_{\tau}) + x_{\eta}^2 (v_y - y_{\tau})^2) \\
 & \quad + x_{\eta}y_{\eta}y_{\xi}y_{\xi\xi} (v_x - x_{\tau})^2 \\
 & \quad - y_{\xi}x_{\eta}^2y_{\xi\xi} (v_x - x_{\tau}) (v_y - y_{\tau}) \\
 & \quad + x_{\xi}y_{\eta}^2y_{\xi\xi} (v_x - x_{\tau}) v_{tx} - y_{\xi}x_{\eta}y_{\eta}y_{\xi\xi} (v_x - x_{\tau}) v_{tx} \\
 & \quad - x_{\xi}x_{\eta}y_{\eta}y_{\xi\xi} (v_y - y_{\tau}) v_{tx} + y_{\xi}x_{\eta}^2y_{\xi\xi} (v_y - y_{\tau}) v_{tx} \\
 & \quad + x_{\xi}y_{\eta}^2x_{\xi\xi} (v_x - x_{\tau}) (v_y - y_{\tau}) - x_{\eta}y_{\eta}y_{\xi}x_{\xi\xi} (v_x - x_{\tau}) (v_y - y_{\tau}) \\
 & \quad - x_{\xi}x_{\eta}y_{\eta}x_{\xi\xi} (v_y - y_{\tau})^2 + y_{\xi}x_{\eta}^2x_{\xi\xi} (v_y - y_{\tau})^2 \\
 & \quad - x_{\xi}y_{\eta}^2x_{\xi\xi} (v_x - x_{\tau}) v_{ty} + y_{\xi}x_{\eta}y_{\eta}x_{\xi\xi} (v_x - x_{\tau}) v_{ty} \\
 & \quad + x_{\xi}x_{\eta}y_{\eta}x_{\xi\xi} (v_y - y_{\tau}) v_{ty} - y_{\xi}x_{\eta}^2x_{\xi\xi} (v_y - y_{\tau}) v_{ty} \\
 & \quad + x_{\xi}y_{\xi\xi}x_{\eta}^2 (v_y - y_{\tau})^2 \\
 & \quad - x_{\xi}x_{\eta}y_{\eta}y_{\xi\xi} (v_x - x_{\tau}) (v_y - y_{\tau})] \quad (A.38)
 \end{aligned}$$

$$\begin{aligned}
 & (I + II)_{x_{\xi\xi}y_{\xi\xi}} = \frac{1}{J^2} [-x_{\xi}y_{\xi\xi} (x_{\eta}^2 + y_{\eta}^2) \bar{u}^2 \\
 & \quad + x_{\eta}y_{\eta}y_{\xi}y_{\xi\xi} (v_x - x_{\tau})^2 \\
 & \quad - y_{\xi}x_{\eta}^2y_{\xi\xi} (v_x - x_{\tau}) (v_y - y_{\tau}) \\
 & \quad + x_{\xi}y_{\eta}^2y_{\xi\xi} (v_x - x_{\tau}) v_{tx} - y_{\xi}x_{\eta}y_{\eta}y_{\xi\xi} (v_x - x_{\tau}) v_{tx} \\
 & \quad - x_{\xi}x_{\eta}y_{\eta}y_{\xi\xi} (v_y - y_{\tau}) v_{tx} + y_{\xi}x_{\eta}^2y_{\xi\xi} (v_y - y_{\tau}) v_{tx} \\
 & \quad + x_{\xi}y_{\eta}^2x_{\xi\xi} (v_x - x_{\tau}) (v_y - y_{\tau}) - x_{\eta}y_{\eta}y_{\xi}x_{\xi\xi} (v_x - x_{\tau}) (v_y - y_{\tau}) \\
 & \quad - x_{\xi}x_{\eta}y_{\eta}x_{\xi\xi} (v_y - y_{\tau})^2 + y_{\xi}x_{\eta}^2x_{\xi\xi} (v_y - y_{\tau})^2 \\
 & \quad - x_{\xi}y_{\eta}^2x_{\xi\xi} (v_x - x_{\tau}) v_{ty} + y_{\xi}x_{\eta}y_{\eta}x_{\xi\xi} (v_x - x_{\tau}) v_{ty} \\
 & \quad + x_{\xi}x_{\eta}y_{\eta}x_{\xi\xi} (v_y - y_{\tau}) v_{ty} - y_{\xi}x_{\eta}^2x_{\xi\xi} (v_y - y_{\tau}) v_{ty} \\
 & \quad + x_{\xi}y_{\xi\xi}x_{\eta}^2 (v_y - y_{\tau})^2 \\
 & \quad - x_{\xi}x_{\eta}y_{\eta}y_{\xi\xi} (v_x - x_{\tau}) (v_y - y_{\tau}) \\
 & \quad + y_{\xi}x_{\xi\xi}y_{\eta}^2 (v_x - x_{\tau})^2 - y_{\xi}x_{\xi\xi}y_{\eta}^2 (v_x - x_{\tau})^2 \\
 & \quad + x_{\eta}y_{\eta}y_{\xi}x_{\xi\xi} (v_x - x_{\tau}) (v_y - y_{\tau}) - x_{\eta}y_{\eta}y_{\xi}x_{\xi\xi} (v_x - x_{\tau}) (v_y - y_{\tau})] \quad (A.39)
 \end{aligned}$$

$$\begin{aligned}
(I + II)_{x_{\xi\xi}y_{\xi\xi}} &= \frac{1}{J^2} [-x_{\xi}y_{\xi\xi} (x_{\eta}^2 + y_{\eta}^2) \bar{u}^2 \\
&+ y_{\xi}x_{\xi\xi} (y_{\eta}^2 (v_x - x_{\tau})^2 - 2x_{\eta}y_{\eta} (v_x - x_{\tau}) (v_y - y_{\tau}) + x_{\eta}^2 (v_y - y_{\tau})^2) \\
&\quad + x_{\eta}y_{\eta}y_{\xi}y_{\xi\xi} (v_x - x_{\tau})^2 \\
&\quad - y_{\xi}x_{\eta}^2y_{\xi\xi} (v_x - x_{\tau}) (v_y - y_{\tau}) \\
&+ x_{\xi}y_{\eta}^2y_{\xi\xi} (v_x - x_{\tau}) v_{tx} - y_{\xi}x_{\eta}y_{\eta}y_{\xi\xi} (v_x - x_{\tau}) v_{tx} \\
&- x_{\xi}x_{\eta}y_{\eta}y_{\xi\xi} (v_y - y_{\tau}) v_{tx} + y_{\xi}x_{\eta}^2y_{\xi\xi} (v_y - y_{\tau}) v_{tx} \\
&\quad + x_{\xi}y_{\eta}^2x_{\xi\xi} (v_x - x_{\tau}) (v_y - y_{\tau}) \\
&\quad - x_{\xi}x_{\eta}y_{\eta}x_{\xi\xi} (v_y - y_{\tau})^2 \\
&- x_{\xi}y_{\eta}^2x_{\xi\xi} (v_x - x_{\tau}) v_{ty} + y_{\xi}x_{\eta}y_{\eta}x_{\xi\xi} (v_x - x_{\tau}) v_{ty} \\
&+ x_{\xi}x_{\eta}y_{\eta}x_{\xi\xi} (v_y - y_{\tau}) v_{ty} - y_{\xi}x_{\eta}^2x_{\xi\xi} (v_y - y_{\tau}) v_{ty} \\
&\quad + x_{\xi}y_{\xi\xi}x_{\eta}^2 (v_y - y_{\tau})^2 \\
&\quad - x_{\xi}x_{\eta}y_{\eta}y_{\xi\xi} (v_x - x_{\tau}) (v_y - y_{\tau}) \\
&\quad - y_{\xi}x_{\xi\xi}y_{\eta}^2 (v_x - x_{\tau})^2 \\
&+ x_{\eta}y_{\eta}y_{\xi}x_{\xi\xi} (v_x - x_{\tau}) (v_y - y_{\tau})] \tag{A.40}
\end{aligned}$$

$$\begin{aligned}
(\text{I} + \text{II})_{x_\xi y_\xi} &= \frac{1}{J^2} [-x_\xi y_\xi (x_\eta^2 + y_\eta^2) \bar{u}^2 + y_\xi x_\xi (x_\eta^2 + y_\eta^2) \bar{u}^2 \\
&\quad + x_\eta y_\eta y_\xi y_\xi (v_x - x_\tau)^2 \\
&\quad - y_\xi x_\eta^2 y_\xi (v_x - x_\tau) (v_y - y_\tau) \\
&\quad + x_\xi y_\eta^2 y_\xi (v_x - x_\tau) v_{tx} - y_\xi x_\eta y_\eta y_\xi (v_x - x_\tau) v_{tx} \\
&\quad - x_\xi x_\eta y_\eta y_\xi (v_y - y_\tau) v_{tx} + y_\xi x_\eta^2 y_\xi (v_y - y_\tau) v_{tx} \\
&\quad + x_\xi y_\eta^2 x_\xi (v_x - x_\tau) (v_y - y_\tau) \\
&\quad - x_\xi x_\eta y_\eta x_\xi (v_y - y_\tau)^2 \\
&\quad - x_\xi y_\eta^2 x_\xi (v_x - x_\tau) v_{ty} + y_\xi x_\eta y_\eta x_\xi (v_x - x_\tau) v_{ty} \\
&\quad + x_\xi x_\eta y_\eta x_\xi (v_y - y_\tau) v_{ty} - y_\xi x_\eta^2 x_\xi (v_y - y_\tau) v_{ty} \\
&\quad + x_\xi y_\xi x_\eta^2 (v_y - y_\tau)^2 \\
&\quad - x_\xi x_\eta y_\eta y_\xi (v_x - x_\tau) (v_y - y_\tau) \\
&\quad - y_\xi x_\xi y_\eta^2 (v_x - x_\tau)^2 \\
&\quad + x_\eta y_\eta y_\xi x_\xi (v_x - x_\tau) (v_y - y_\tau) \\
&\quad + x_\xi x_\eta y_\eta y_\xi (v_x - x_\tau) v_{ty} - x_\xi x_\eta y_\eta y_\xi (v_x - x_\tau) v_{ty} \\
&\quad + x_\xi x_\eta^2 y_\xi (v_y - y_\tau) v_{ty} - x_\xi x_\eta^2 y_\xi (v_y - y_\tau) v_{ty}] \tag{A.41}
\end{aligned}$$

$$\begin{aligned}
(I + II)_{x_{\xi\xi}y_{\xi\xi}} &= \frac{1}{J^2} [(x_{\eta}^2 + y_{\eta}^2) \bar{u}^2 (y_{\xi}x_{\xi\xi} - x_{\xi}y_{\xi\xi}) \\
&+ x_{\eta}y_{\eta}y_{\xi\xi} (v_x - x_{\tau}) (y_{\xi} (v_x - x_{\tau} - v_{tx}) - x_{\xi} (v_y - y_{\tau} - v_{ty})) \\
&+ x_{\eta}^2y_{\xi\xi} (v_y - y_{\tau}) (-y_{\xi} (v_x - x_{\tau} - v_{tx}) + x_{\xi} (v_y - y_{\tau} - v_{ty})) \\
&\quad + x_{\xi}y_{\eta}^2y_{\xi\xi} (v_x - x_{\tau}) v_{tx} \\
&\quad - x_{\xi}x_{\eta}y_{\eta}y_{\xi\xi} (v_y - y_{\tau}) v_{tx} \\
&\quad + x_{\xi}y_{\eta}^2x_{\xi\xi} (v_x - x_{\tau}) (v_y - y_{\tau}) \\
&\quad - x_{\xi}x_{\eta}y_{\eta}x_{\xi\xi} (v_y - y_{\tau})^2 \\
&- x_{\xi}y_{\eta}^2x_{\xi\xi} (v_x - x_{\tau}) v_{ty} + y_{\xi}x_{\eta}y_{\eta}x_{\xi\xi} (v_x - x_{\tau}) v_{ty} \\
&+ x_{\xi}x_{\eta}y_{\eta}x_{\xi\xi} (v_y - y_{\tau}) v_{ty} - y_{\xi}x_{\eta}^2x_{\xi\xi} (v_y - y_{\tau}) v_{ty} \\
&\quad - y_{\xi}x_{\xi\xi}y_{\eta}^2 (v_x - x_{\tau})^2 \\
&\quad + x_{\eta}y_{\eta}y_{\xi}x_{\xi\xi} (v_x - x_{\tau}) (v_y - y_{\tau}) \\
&\quad - x_{\xi}x_{\eta}y_{\eta}y_{\xi\xi} (v_x - x_{\tau}) v_{ty} \\
&\quad + x_{\xi}x_{\eta}^2y_{\xi\xi} (v_y - y_{\tau}) v_{ty}] \tag{A.42}
\end{aligned}$$

Iskoristivši uvjet u jednadžbi (A.34), slijedi izraz

$$\begin{aligned}
(\text{I} + \text{II})_{x_\xi x_\xi y_\xi} &= \frac{1}{J^2} [(x_\eta^2 + y_\eta^2) \bar{u}^2 (y_\xi x_{\xi\xi} - x_\xi y_{\xi\xi}) \\
&\quad + x_\xi y_\eta^2 y_{\xi\xi} (v_x - x_\tau) v_{tx} \\
&\quad - x_\xi x_\eta y_\eta y_{\xi\xi} (v_y - y_\tau) v_{tx} \\
&\quad + x_\xi y_\eta^2 x_{\xi\xi} (v_x - x_\tau) (v_y - y_\tau) \\
&\quad - x_\xi x_\eta y_\eta x_{\xi\xi} (v_y - y_\tau)^2 \\
&\quad - x_\xi y_\eta^2 x_{\xi\xi} (v_x - x_\tau) v_{ty} + y_\xi x_\eta y_\eta x_{\xi\xi} (v_x - x_\tau) v_{ty} \\
&\quad + x_\xi x_\eta y_\eta x_{\xi\xi} (v_y - y_\tau) v_{ty} - y_\xi x_\eta^2 x_{\xi\xi} (v_y - y_\tau) v_{ty} \\
&\quad - y_\xi x_{\xi\xi} y_\eta^2 (v_x - x_\tau)^2 \\
&\quad + x_\eta y_\eta y_\xi x_{\xi\xi} (v_x - x_\tau) (v_y - y_\tau) \\
&\quad - x_\xi x_\eta y_\eta y_{\xi\xi} (v_x - x_\tau) v_{ty} \\
&\quad + x_\xi x_\eta^2 y_{\xi\xi} (v_y - y_\tau) v_{ty}] \tag{A.43}
\end{aligned}$$

$$\begin{aligned}
(\text{I} + \text{II})_{x_\xi x_\xi y_\xi} &= \frac{1}{J^2} [(x_\eta^2 + y_\eta^2) \bar{u}^2 (y_\xi x_{\xi\xi} - x_\xi y_{\xi\xi}) \\
&\quad x_{\xi\xi} y_\eta^2 (v_x - x_\tau) (-y_\xi (v_x - x_\tau - v_{tx}) + x_\xi (v_y - y_\tau - v_{ty})) \\
&\quad + x_\eta y_\eta x_{\xi\xi} (v_y - y_\tau) (y_\xi (v_x - x_\tau - v_{tx}) - x_\xi (v_y - y_\tau - v_{ty})) \\
&\quad + x_\xi y_\eta^2 y_{\xi\xi} (v_x - x_\tau) v_{tx} \\
&\quad - x_\xi x_\eta y_\eta y_{\xi\xi} (v_y - y_\tau) v_{tx} \\
&\quad + y_\xi x_\eta y_\eta x_{\xi\xi} (v_x - x_\tau) v_{ty} \\
&\quad - y_\xi x_\eta^2 x_{\xi\xi} (v_y - y_\tau) v_{ty} \\
&\quad - x_\xi x_\eta y_\eta y_{\xi\xi} (v_x - x_\tau) v_{ty} \\
&\quad + x_\xi x_\eta^2 y_{\xi\xi} (v_y - y_\tau) v_{ty} \\
&\quad - y_\xi y_\eta^2 x_{\xi\xi} (v_x - x_\tau) v_{tx} \\
&\quad + y_\xi x_\eta y_\eta x_{\xi\xi} (v_y - y_\tau) v_{tx}] \tag{A.44}
\end{aligned}$$

Iskoristivši jednadžbu (A.34), slijedi

$$\begin{aligned}
(\text{I} + \text{II})_{x_{\xi\xi}y_{\xi\xi}} = & \frac{1}{J^2} [(x_\eta^2 + y_\eta^2) \bar{u}^2 (y_\xi x_{\xi\xi} - x_\xi y_{\xi\xi}) \\
& + x_\xi y_\eta^2 y_{\xi\xi} (v_x - x_\tau) v_{tx} \\
& - x_\xi x_\eta y_\eta y_{\xi\xi} (v_y - y_\tau) v_{tx} \\
& + y_\xi x_\eta y_\eta x_{\xi\xi} (v_x - x_\tau) v_{ty} \\
& - y_\xi x_\eta^2 x_{\xi\xi} (v_y - y_\tau) v_{ty} \\
& - x_\xi x_\eta y_\eta y_{\xi\xi} (v_x - x_\tau) v_{ty} \\
& + x_\xi x_\eta^2 y_{\xi\xi} (v_y - y_\tau) v_{ty} \\
& - y_\xi y_\eta^2 x_{\xi\xi} (v_x - x_\tau) v_{tx} \\
& + y_\xi x_\eta y_\eta x_{\xi\xi} (v_y - y_\tau) v_{tx}]
\end{aligned} \tag{A.45}$$

$$\underline{(I + II)_{x_\xi \tau y_\xi \tau} + (I + II)_{x_\xi \xi y_\xi \xi} + (I + II)_{\text{rest}} :}$$

$$\begin{aligned}
 I + II = & \frac{1}{J} [2\sqrt{x_\eta^2 + y_\eta^2} \bar{u} (y_\xi x_{\tau\xi} - x_\xi y_{\tau\xi}) \\
 & + x_\xi y_\eta y_{\xi\tau} v_{tx} + y_\xi x_\eta x_{\xi\tau} v_{ty} - y_\xi y_\eta x_{\xi\tau} v_{tx} - x_\xi x_\eta y_{\xi\tau} v_{ty}] \\
 & + \frac{1}{J^2} [(x_\eta^2 + y_\eta^2) \bar{u}^2 (y_\xi x_{\xi\xi} - x_\xi y_{\xi\xi}) \\
 & \quad + x_\xi y_\eta^2 y_{\xi\xi} (v_x - x_\tau) v_{tx} \\
 & \quad - x_\xi x_\eta y_\eta y_{\xi\xi} (v_y - y_\tau) v_{tx} \\
 & \quad + y_\xi x_\eta y_\eta x_{\xi\xi} (v_x - x_\tau) v_{ty} \\
 & \quad - y_\xi x_\eta^2 x_{\xi\xi} (v_y - y_\tau) v_{ty} \\
 & \quad - x_\xi x_\eta y_\eta y_{\xi\xi} (v_x - x_\tau) v_{ty} \\
 & \quad + x_\xi x_\eta^2 y_{\xi\xi} (v_y - y_\tau) v_{ty} \\
 & \quad - y_\xi y_\eta^2 x_{\xi\xi} (v_x - x_\tau) v_{tx} \\
 & \quad + y_\xi x_\eta y_\eta x_{\xi\xi} (v_y - y_\tau) v_{tx}] \\
 & \quad + \frac{1}{J} [y_\xi y_\eta v_{tx\xi} (v_x - x_\tau) \\
 & \quad - y_\xi x_\eta v_{tx\xi} (v_y - y_\tau) + J x_{\tau\tau} y_\xi + J v_{tx\tau} y_\xi] \\
 & \quad - \frac{1}{J} [x_\xi y_\eta v_{ty\xi} (v_x - x_\tau) \\
 & \quad - x_\xi x_\eta v_{ty\xi} (v_y - y_\tau) + J y_{\tau\tau} x_\xi + J v_{ty\tau} x_\xi]
 \end{aligned} \tag{A.46}$$

gradp · n̄:

$$\begin{aligned}
\text{grad}p \cdot \vec{n} &= \frac{\partial p}{\partial x} n_x + \frac{\partial p}{\partial y} n_y \\
&= \left[\frac{1}{J} \left(y_\eta \frac{\partial p}{\partial \xi} - y_\xi \frac{\partial p}{\partial \eta} \right) \right] (-y_\xi) + \left[\frac{1}{J} \left(-x_\eta \frac{\partial p}{\partial \xi} + x_\xi \frac{\partial p}{\partial \eta} \right) \right] (x_\xi) \\
&= \frac{1}{J} \left(-y_\xi y_\eta \frac{\partial p}{\partial \xi} + y_\xi^2 \frac{\partial p}{\partial \eta} \right) + \frac{1}{J} \left(-x_\xi x_\eta \frac{\partial p}{\partial \xi} + x_\xi^2 \frac{\partial p}{\partial \eta} \right) \\
&= \frac{1}{J} \frac{\partial p}{\partial \eta} (x_\xi^2 + y_\xi^2) - \frac{1}{J} \frac{\partial p}{\partial \xi} (x_\xi x_\eta + y_\xi y_\eta) \tag{A.47}
\end{aligned}$$

Prema jednadžbi (A.5) slijedi:

$$\begin{aligned}
&\rho \left[\frac{1}{J} [2\sqrt{x_\eta^2 + y_\eta^2} \bar{u} (y_\xi x_{\tau\xi} - x_\xi y_{\tau\xi}) \right. \\
&+ x_\xi y_\eta y_{\xi\tau} v_{tx} + y_\xi x_\eta x_{\xi\tau} v_{ty} - y_\xi y_\eta x_{\xi\tau} v_{tx} - x_\xi x_\eta y_{\xi\tau} v_{ty}] \\
&+ \frac{1}{J^2} [(x_\eta^2 + y_\eta^2) \bar{u}^2 (y_\xi x_{\xi\xi} - x_\xi y_{\xi\xi}) \\
&\quad + x_\xi y_\eta^2 y_{\xi\xi} (v_x - x_\tau) v_{tx} \\
&\quad - x_\xi x_\eta y_\eta y_{\xi\xi} (v_y - y_\tau) v_{tx} \\
&\quad + y_\xi x_\eta y_\eta x_{\xi\xi} (v_x - x_\tau) v_{ty} \\
&\quad - y_\xi x_\eta^2 x_{\xi\xi} (v_y - y_\tau) v_{ty} \\
&\quad - x_\xi x_\eta y_\eta y_{\xi\xi} (v_x - x_\tau) v_{ty} \\
&\quad + x_\xi x_\eta^2 y_{\xi\xi} (v_y - y_\tau) v_{ty} \\
&\quad - y_\xi y_\eta^2 x_{\xi\xi} (v_x - x_\tau) v_{tx} \\
&\quad \left. + y_\xi x_\eta y_\eta x_{\xi\xi} (v_y - y_\tau) v_{tx} \right] \\
&\quad + \frac{1}{J} [y_\xi y_\eta v_{tx\xi} (v_x - x_\tau) \\
&\quad - y_\xi x_\eta v_{tx\xi} (v_y - y_\tau) + J x_{\tau\tau} y_\xi + J v_{tx\tau} y_\xi] \\
&\quad - \frac{1}{J} [x_\xi y_\eta v_{ty\xi} (v_x - x_\tau) \\
&\quad - x_\xi x_\eta v_{ty\xi} (v_y - y_\tau) + J y_{\tau\tau} x_\xi + J v_{ty\tau} x_\xi] = \\
&\quad \frac{1}{J} \frac{\partial p}{\partial \eta} (x_\xi^2 + y_\xi^2) - \frac{1}{J} \frac{\partial p}{\partial \xi} (x_\xi x_\eta + y_\xi y_\eta) \tag{A.48}
\end{aligned}$$

$$\begin{aligned}
 \frac{\partial p}{\partial \eta} (x_\xi^2 + y_\xi^2) &= \frac{\partial p}{\partial \xi} (x_\xi x_\eta + y_\xi y_\eta) \\
 &+ \rho \{ 2 \sqrt{x_\eta^2 + y_\eta^2} \bar{u} (y_\xi x_{\tau\xi} - x_\xi y_{\tau\xi}) \\
 &+ x_\xi y_\eta y_{\xi\tau} v_{tx} + y_\xi x_\eta x_{\xi\tau} v_{ty} - y_\xi y_\eta x_{\xi\tau} v_{tx} - x_\xi x_\eta y_{\xi\tau} v_{ty} \\
 &+ \frac{1}{J} [(x_\eta^2 + y_\eta^2) \bar{u}^2 (y_\xi x_{\xi\xi} - x_\xi y_{\xi\xi}) \\
 &+ x_\xi y_\eta^2 y_{\xi\xi} (v_x - x_\tau) v_{tx} - x_\xi x_\eta y_\eta y_{\xi\xi} (v_y - y_\tau) v_{tx} \\
 &+ y_\xi x_\eta y_\eta x_{\xi\xi} (v_x - x_\tau) v_{ty} - y_\xi x_\eta^2 x_{\xi\xi} (v_y - y_\tau) v_{ty} \\
 &- x_\xi x_\eta y_\eta y_{\xi\xi} (v_x - x_\tau) v_{ty} + x_\xi x_\eta^2 y_{\xi\xi} (v_y - y_\tau) v_{ty} \\
 &- y_\xi y_\eta^2 x_{\xi\xi} (v_x - x_\tau) v_{tx} + y_\xi x_\eta y_\eta x_{\xi\xi} (v_y - y_\tau) v_{tx}] \\
 &+ y_\xi y_\eta v_{tx\xi} (v_x - x_\tau) - y_\xi x_\eta v_{tx\xi} (v_y - y_\tau) + J x_{\tau\tau} y_\xi + J v_{tx\tau} y_\xi \\
 &- x_\xi y_\eta v_{ty\xi} (v_x - x_\tau) + x_\xi x_\eta v_{ty\xi} (v_y - y_\tau) - J y_{\tau\tau} x_\xi - J v_{ty\tau} x_\xi \} \tag{A.49}
 \end{aligned}$$

$$\begin{aligned}
 \frac{\partial p}{\partial \eta} (x_\xi^2 + y_\xi^2) &= \frac{\partial p}{\partial \xi} (x_\xi x_\eta + y_\xi y_\eta) \\
 &+ \rho \{ J \left[\frac{\bar{u}^2}{(x_\xi^2 + y_\xi^2)} (y_\xi x_{\xi\xi} - x_\xi y_{\xi\xi}) + \frac{2\bar{u}}{\sqrt{x_\xi^2 + y_\xi^2}} (y_\xi x_{\tau\xi} - x_\xi y_{\tau\xi}) \right. \\
 &\quad \left. + x_{\tau\tau} y_\xi - y_{\tau\tau} x_\xi \right] \\
 &+ x_\xi y_\eta y_{\xi\tau} v_{tx} + y_\xi x_\eta x_{\xi\tau} v_{ty} - y_\xi y_\eta x_{\xi\tau} v_{tx} - x_\xi x_\eta y_{\xi\tau} v_{ty} \\
 &+ \frac{1}{J} [x_\xi y_\eta^2 y_{\xi\xi} (v_x - x_\tau) v_{tx} - x_\xi x_\eta y_\eta y_{\xi\xi} (v_y - y_\tau) v_{tx} \\
 &+ y_\xi x_\eta y_\eta x_{\xi\xi} (v_x - x_\tau) v_{ty} - y_\xi x_\eta^2 x_{\xi\xi} (v_y - y_\tau) v_{ty} \\
 &- x_\xi x_\eta y_\eta y_{\xi\xi} (v_x - x_\tau) v_{ty} + x_\xi x_\eta^2 y_{\xi\xi} (v_y - y_\tau) v_{ty} \\
 &- y_\xi y_\eta^2 x_{\xi\xi} (v_x - x_\tau) v_{tx} + y_\xi x_\eta y_\eta x_{\xi\xi} (v_y - y_\tau) v_{tx}] \\
 &+ y_\xi y_\eta v_{tx\xi} (v_x - x_\tau) - y_\xi x_\eta v_{tx\xi} (v_y - y_\tau) + J v_{tx\tau} y_\xi \\
 &- x_\xi y_\eta v_{ty\xi} (v_x - x_\tau) + x_\xi x_\eta v_{ty\xi} (v_y - y_\tau) - J v_{ty\tau} x_\xi \} \tag{A.50}
 \end{aligned}$$

$$\begin{aligned}
 \frac{\partial p}{\partial \eta} (x_\xi^2 + y_\xi^2) &= \frac{\partial p}{\partial \xi} (x_\xi x_\eta + y_\xi y_\eta) + \rho \left\{ J \left[\frac{\bar{u}^2}{(x_\xi^2 + y_\xi^2)} (y_\xi x_{\xi\xi} - x_\xi y_{\xi\xi}) \right. \right. \\
 &\quad \left. \left. + \frac{2\bar{u}}{\sqrt{x_\xi^2 + y_\xi^2}} (y_\xi x_{\tau\xi} - x_\xi y_{\tau\xi}) + x_{\tau\tau} y_\xi - y_{\tau\tau} x_\xi \right] \right. \\
 &\quad \left. + v_{tx} y_\eta (x_\xi y_{\xi\tau} - y_\xi x_{\xi\tau}) - v_{ty} x_\eta (x_\xi y_{\xi\tau} - y_\xi x_{\xi\tau}) \right. \\
 + \frac{1}{J} &\left[y_\eta^2 (v_x - x_\tau) v_{tx} (x_\xi y_{\xi\xi} - y_\xi x_{\xi\xi}) - x_\eta y_\eta (v_y - y_\tau) v_{tx} (x_\xi y_{\xi\xi} - y_\xi x_{\xi\xi}) \right. \\
 &\quad \left. + x_\eta y_\eta (v_x - x_\tau) v_{ty} (x_\xi y_{\xi\xi} - y_\xi x_{\xi\xi}) + x_\eta^2 (v_y - y_\tau) v_{ty} (x_\xi y_{\xi\xi} - y_\xi x_{\xi\xi}) \right] \\
 &\quad + y_\eta (v_x - x_\tau) (y_\xi v_{tx\xi} - x_\xi v_{ty\xi}) - x_\eta (v_y - y_\tau) (y_\xi v_{tx\xi} - x_\xi v_{ty\xi}) \\
 &\quad \left. + J (v_{tx\tau} y_\xi - v_{ty\tau} x_\xi) \right\} \quad (\text{A.51})
 \end{aligned}$$

$$\begin{aligned}
 \frac{\partial p}{\partial \eta} (x_\xi^2 + y_\xi^2) &= \frac{\partial p}{\partial \xi} (x_\xi x_\eta + y_\xi y_\eta) + \rho \left\{ J \left[\frac{\bar{u}^2}{(x_\xi^2 + y_\xi^2)} (y_\xi x_{\xi\xi} - x_\xi y_{\xi\xi}) \right. \right. \\
 &\quad \left. \left. + \frac{2\bar{u}}{\sqrt{x_\xi^2 + y_\xi^2}} (y_\xi x_{\tau\xi} - x_\xi y_{\tau\xi}) + x_{\tau\tau} y_\xi - y_{\tau\tau} x_\xi \right] \right. \\
 &\quad \left. + (x_\xi y_{\xi\tau} - y_\xi x_{\xi\tau}) (v_{tx} y_\eta - v_{ty} x_\eta) \right. \\
 + \frac{1}{J} &\left[(x_\xi y_{\xi\xi} - y_\xi x_{\xi\xi}) (y_\eta^2 (v_x - x_\tau) v_{tx} - x_\eta y_\eta (v_y - y_\tau) v_{tx}) \right. \\
 &\quad \left. + x_\eta y_\eta (v_x - x_\tau) v_{ty} + x_\eta^2 (v_y - y_\tau) v_{ty} \right] \\
 &\quad + (y_\xi v_{tx\xi} - x_\xi v_{ty\xi}) (y_\eta (v_x - x_\tau) - x_\eta (v_y - y_\tau)) \\
 &\quad \left. + J (v_{tx\tau} y_\xi - v_{ty\tau} x_\xi) \right\} \quad (\text{A.52})
 \end{aligned}$$

Literatura

- [1] Wright J.R. *Introduction to Aircraft Aeroelasticity and Loads*. John Wiley & Sons Ltd, 2007.
- [2] Voss R. Ueber die ausbreitung akustischer stoerungen in transonischen stroemungsfeldern von tragfluegeln. Rept. DFVLR-FB 88-13, DFVLR, Institut fuer Aeroelastik, Goettingen, February 1988.
- [3] Hodges D. H., Pierce G. A. *Introduction to Structural Dynamics and Aeroelasticity*. Cambridge University Press, 2002.
- [4] Schuster D.M., Liu D.D., Huttzell L.J. Computational aeroelasticity: Success, progress, challenge. *Journal of Aircraft*, 40(5):843–856, 2003.
- [5] Theodorsen T., Garrick I.E. A theoretical and experimental investigation of the flutter problem. NACA TR-685, September 1940.
- [6] Albano E., Rodden W.P. A doublet-lattice method for calculating the lift distributions on oscillating surfaces in subsonic flows. *AIAA Journal*, 7(2):279–285, 1969.
- [7] Giesing J.P., Kalman T.P., Rodden W.P. Subsonic unsteady aerodynamics for general configurations, part I—direct application of the non-planar doublet-lattice method. Rept. AFFDL-TR-71-5, Pt. 1, Air Force Flight Dynamics Lab., Air Force Systems Command, April 1972.

- [8] Rodden W.P., Taylor P.F., McIntosh S.C. Further refinement of the non-planar aspects of the subsonic doublet-lattice lifting surface method. In *Proceedings of the 20th International Council of Aeronautical Sciences Congress*, Naples, Italy, Paper ICAS-96-2.8.2, September 1996.
- [9] Batina J.T. A finite-difference approximate-factorization algorithm for solution of the unsteady transonic small-disturbance equation. NASA TP 3129, January 1992.
- [10] Drela M. *Two-Dimensional Transonic Aerodynamic Design and Analysis Using the Euler Equations*. PhD thesis, Massachusetts Institute of Technology, 1985.
- [11] Whitfield D.L., Swafford T.W., Jacocks J.L. Calculation of turbulent boundary layers with separation and viscous-inviscid interaction. *AIAA Journal*, 19(10):1315–1322, 1981.
- [12] Drela M., Giles M.B. Viscous-inviscid analysis of transonic and low reynolds number airfoils. *AIAA Journal*, 25(10):1347–1355, 1987.
- [13] Zhang Z., Liu F., Schuster D.M. An efficient euler method on non-moving cartesian grids with boundary-layer correction for wing flutter simulations. In *AIAA 2006-884*, January, 2006.
- [14] Kreiselmaier E., Laschka B. Small disturbance euler equations: Efficient and accurate tool for unsteady load prediction. *Journal of Aircraft*, 37(5):770–778, 2000.
- [15] Pechloff A., Laschka B. Small disturbance navier-stokes method: Efficient tool for predicting unsteady air loads. *Journal of Aircraft*, 43(1):17–29, 2006.
- [16] Filippone A., Sorensen J.N. Viscous-inviscid interaction using the navier-stokes equations. *AIAA Journal*, 35(9):1464–1471, 1997.
- [17] Stock H.W., Haase W. Navier-stokes airfoil computations with e^n transition prediction including transitional flow regions. *AIAA Journal*, 38(11):2059–2066, 2000.
- [18] Stock H.W. Infinite swept-wing navier-stokes computations with e^n transition prediction. *AIAA Journal*, 43(6):1221–1229, 2005.
- [19] Lighthill M.J. On displacement thickness. *Journal of Fluid Mechanics*, 4(4):383–392, 1958.

- [20] Bram Van Leer. Towards the ultimate conservative difference scheme v. a second-order sequel to godunov's method. *J. Comput. Phys.*, 135(2):229–248, 1997.
- [21] Toro E.F. *Riemann Solvers and Numerical Methods for Fluid Dynamics*. Springer, 1999.
- [22] Whitfield D.L. Analytical description of the complete turbulent boundary layer velocity profile. In *AIAA-78-1158*, July 1978.
- [23] Steger J. L., Sorenson R. L. Automatic mesh-point clustering near a boundary in grid generation with elliptic partial differential equations. *Journal of Computational Physics*, 33(3):405–410, 1979.
- [24] Carstens V. Two-dimensional elliptic grid generator for airfoils and cascades. DLR-FB 88-52, 1988.
- [25] Thompson J.E., Warsi Z.U.A., Mastin C.W. *Numerical Grid Generation*. Elsevier Science Publishing Co., 1985.
- [26] Various authors. Experimental data base for computer program assessment - report of the fluid dynamics panel working group 04. AGARD-AR 138, May 1979.
- [27] Various authors. Compendium of unsteady aerodynamic measurement. AGARD-R 702, August 1982.
- [28] Deutsches Zentrum für Luft- und Raumfahrt. *Technical Documentation of the DLR TAU-Code*.
- [29] Magnus R., Yoshihara H. Inviscid transonic flow over airfoils. *AIAA Journal*, 8(12):2157–2161, 1970.
- [30] Anderson J.D., Jr. *Modern Compressible Flow*. McGraw-Hill Publishing Company, 1990.
- [31] Soda A. Numerical investigation of unsteady transonic shock/boundary-layer interaction for aeronautical applications. Forschungsbericht 2007-03, Deutsches Zentrum für Luft- und Raumfahrt, March 2007.

- [32] Tijdeman H. Investigation of the transonic flow around oscillating airfoils. NLR TR 77090 U, October 1977.

Životopis

Ime i prezime: Frane Majić

Datum rođenja: 28.12.1977

Mjesto rođenja: Varaždin

Zaposlenje:

2003. - sada Znanstveni novak na Katedri za aerodinamiku, Zavod
za zrakoplovstvo, Fakultet strojarstva i brodogradnje
u Zagrebu, Sveučilište u Zagrebu

Školovanje:

2003. - sada Poslijediplomski studij, Fakultet strojarstva i brodogradnje,
Sveučilište u Zagrebu

1996. - 2002. Dipl. ing. zrakoplovstva, Fakultet strojarstva i brodogradnje,
Sveučilište u Zagrebu

1992. - 1996. Zrakoplovna tehnička škola Rudolfa Perešina, Velika Gorica

1984. - 1992. Osnovna škola Ivana Kukuljevića Sakcinskog, Ivanec